

**FACULTY
OF MATHEMATICS
AND PHYSICS**
Charles University

DOCTORAL THESIS

Jakub Šebesta

**Topological insulators
and magnetic order**

Department of Condensed Matter Physics

Supervisor of the doctoral thesis: doc. RNDr. Karel Carva, Ph.D.

Study programme: Physics of Condensed Matter
and Materials Research

Study branch: P4F3

Prague 2021

I declare that I carried out this doctoral thesis independently, and only with the cited sources, literature and other professional sources. It has not been used to obtain another or the same degree.

I understand that my work relates to the rights and obligations under the Act No. 121/2000 Sb., the Copyright Act, as amended, in particular the fact that the Charles University has the right to conclude a license agreement on the use of this work as a school work pursuant to Section 60 subsection 1 of the Copyright Act.

In date

Author's signature

Dedication

Dedicated to my family, who supports and encourages me during doctoral studies.

Acknowledgment

I wish to express my sincere gratitude, especially to my supervisor doc. Karel Carva for his guidance and patience. My thanks also go to my adviser doc. Ilja Turek for his critical comments. I would like to express my thanks to all co-workers on joint publications. I greatly appreciate their collaboration. Special thanks are given to the Faculty of Mathematics and Physics, especially to the Department of Condensed Matter Physics. I acknowledge the support and access to computational facilities.

Computational resources were supplied by the project “e-Infrastruktura CZ” (e-INFRA LM2018140) provided within the program Projects of Large Research, Development and Innovations Infrastructures. This work was supported by The Ministry of Education, Youth and Sports from the Large Infrastructures for Research, Experimental Development and Innovations project “e-Infrastructure CZ – LM2018140”.

Title: Topological insulators and magnetic order

Author: Jakub Šebesta

Department: Department of Condensed Matter Physics

Supervisor: doc. RNDr. Karel Carva, Ph.D.,
Department of Condensed Matter Physics

Abstract: The occurrence of various defects can strongly influence the physical properties of real materials. Depending on their type, new outstanding features can arise, but also characteristic behavior might be lost. This thesis is dedicated to the impact of diverse disorder's presence on the physical behavior of three-dimensional topological insulators, namely, the well-known Bi_2Se_3 compound. Despite possessing a band gap in the bulk, these materials host unique metallic surface states protected by the time-reversal symmetry. Thus, the surface states are robust against perturbation, which respects the protecting symmetry. Breaking the symmetry, e.g. by the magnetic field, can open the surface gaps. In this work, the influence of the magnetic as well as native chemical defects, occurring in the real samples, on the electronic structure is described. Notably, the dispersion of the surface metallic states is followed up. Since the surface gap can be opened by the magnetic field, magnetic exchange interactions and related Curie temperatures of magnetic defects are thoroughly studied. Particularly, the influence of disorder on the character of the exchange interactions and related Curie temperatures is described. Dealing with layered systems, the behavior of planar defects might be inspected. Therefore, the distribution of twin planes and their interplay with chemical defects is extensively discussed.

Keywords: topological insulators, magnetic interactions,
magnetization dynamics, numerical simulations

Contents

Introduction	3
1 Electronic Structure of Solids	7
1.1 Nonrelativistic electrons	7
1.2 Relativistic description	8
1.3 Density functional theory	10
1.4 TB-LMTO-ASA method	12
1.4.1 Bulk systems	12
1.4.2 Layered systems	14
1.5 Coherent potential approximation	14
1.6 Observables in TB-LMTO-ASA	16
2 Magnetic Interactions	19
2.1 Exchange mechanisms	19
2.1.1 Coulomb exchange	20
2.1.2 Kinetic exchange	21
2.1.3 Double exchange	24
2.1.4 Metallic exchange – Ruderman-Kittel-Kasuya-Yoshida interaction	25
2.1.5 Magnetic anisotropy	27
2.2 Magnetic exchange interactions	28
2.3 Ab-initio calculation of magnetic exchange interactions	29
2.3.1 Real-space method, Liechtenstein formula	30
3 Magnetic Ordering	33
3.1 Magnetic materials	34
3.1.1 Diamagnetics	34
3.1.2 Paramagnetics	34
3.1.3 Magnetically ordered materials	36
4 Topological Insulators Overview	39
4.1 Topological matter	39
4.1.1 Integer Quantum Hall Effect	40
4.1.2 Thouless–Kohmoto–Nightingale–den Nijs theory	41
4.1.3 Berry phase, connection and curvature	41
4.2 Edge states	43
4.3 Topological phase transition	44
4.4 2D Quantum spin Hall topological insulators	46
4.5 3D topological insulators	50
4.5.1 \mathbb{Z}_2 invariant	50
4.6 $\text{Bi}_{(1-x)}\text{Sb}_x$ – the first 3D TI	53
4.7 Second generation 3D TI	55

5	Bulk Bi₂Se₃	57
5.1	Computational details	58
5.2	Electronic structure	59
5.3	Exchange interactions	67
5.4	Curie temperatures	73
5.5	Results summary	78
6	Heisenberg Exchange Interactions	
	– Influence of the Relativistic Corrections	81
6.1	Bulk Bi ₂ Se ₃ exchange interactions	81
6.2	Transition metals alloys' exchange interactions	86
6.3	Results summary	90
7	Bi₂Se₃ Thin Layers	91
7.1	Computational details	91
7.2	Thin layers & surface states	92
7.3	Electronic structure in presence of chemical disorder	97
	7.3.1 Magnetic defects	97
	7.3.2 Native defects	103
7.4	Exchange interactions	106
7.5	Planar defects – Twin planes	110
	7.5.1 Single TP in a pristine Bi ₂ Se ₃ system	111
	7.5.2 Interaction between TPs	112
	7.5.3 Influence of chemical disorder	113
	7.5.4 Dependence of the inter-TP interaction on the dopant concentration	115
	7.5.5 Magnetic dopants	117
	7.5.6 Mixed TP orientation	119
7.6	Results summary	122
	Conclusions	123
	Bibliography	125
	List of Figures	141
	List of Tables	145
	List of Abbreviations	147
	List of Publications	151

Introduction

Material research represents an integral part of the condensed matter physics, improving and tuning properties of the known materials and smoothing the path toward designing new outstanding ones. Novel materials bearing remarkable and unforeseen physical properties allow people to create more efficient devices or incredible constructions. Their properties depend on e.g. preparation method, dimensionality, or actual composition. Besides, real materials are not pristine structure in general as they contain a wide range of defects which affect resulting properties. From the experimental point of view, it is unfeasible to cover the whole range of compositions, crystal or magnetic structures, defects, etc. Particularly, one is able to prepare a limited number of samples only, and also a sort of them might be hardly achievable or even unavailable. However, they might bear serious physical effects relevant for further development. Such a problem can be managed in a theoretical framework by ab-initio calculations. After decades of improvement, solid-state theory represents a reliable approach to describing real materials and related physical phenomena. It allows for detail studying of materials and associated physical properties beyond the scope of experimental studies. A possible continuous variation of parameters makes the analysis thoroughgoing. Then excellent comprehension of physical behavior makes the material designing easier.

In this thesis, we deal particularly with an influence of the chemical disorder on the physical properties of topological insulators, namely the Bi_2Se_3 compound. Topological insulators represent a quite novel field of solid-state physics. They are interesting from the point of view of spintronics, a new advanced branch of electronics, since hosting spin-polarized gapless surface states. Besides, the significance of topological concepts in the description of phases of matter and related phase transitions were highlighted by the Nobel Prize in Physics, which D.J. Thouless, F.D.M. Haldane, and J.M. Kosterlitz were awarded in 2016. However, upon real conditions, the formation of defects, likely modifying both surface and bulk properties, is hardly avoided. The physical properties might be modified accidentally by an occurrence of intrinsic defects, which naturally appears in the real samples. It can be challenging to control their presence during the formation of samples. Thus, calculations do not only indicate modifications of the physical properties but also they might serve to a determination of the type and amount of present defects. On the other hand, artificial doping can be introduced to control the compound's behavior. Regarding the gapless surface states, magnetic doping is important as the magnetic field breaks the time-reversal symmetry, which keeps the surface band gap closed. Then, an examination of the magnetic pair exchange interactions is essential to estimate related magnetic ordering temperatures, where nonzero net magnetization occurs. In this work, a theoretic description benefits from properties of the tight-binding linear-muffin-tin orbital method based on the Green's function formalism. It allows to include disorder in the framework of coherent potential approximation, which guarantees effective and high-performance treating, while the reliability of calculations is kept. Considering translation symmetry in the plane only, this formalism can be extended

to the description of layered systems, allowing one to calculate the physical properties of thin-layer structures as bismuth chalcogenides. Besides, thanks to the Green's function formalism, the magnetic exchange interactions are easily obtainable.

Aims of the thesis

Namely, we aim at the influences of the native and magnetic disorder on the bulk Bi_2Se_3 electronic structure in order to describe the behavior of the band gap, which significantly modify transport properties. Then, concerning magnetic doping, we try to analyze in detail the character of the magnetic pair exchange interactions there, due to an estimation of the ferromagnetic ordering temperature. Notably, the impact of the actual composition, including the type of the doping, on the strength and character of the magnetic exchange interactions. Later, we compare the observed bulk behavior to that one of the thin layered Bi_2Se_3 structures, where we focus mainly on the formation of the surface gapless states. Having performed calculations of the thin-layer system, we examine the behavior of less studied planar defects, namely twin planes.

Structure of the thesis

Initially we provide a brief introduction to used computation methods, materials and related physics (Chapters 1 to 4). Then, we proceed from an examination of the influence of the chemical disorder on Bi_2Se_3 bulk properties (Chapter 5). Studying the bulk is a great starting point as it allows one to understand the compound's behavior in presence of the disorder. Regarding the bulk properties, we discuss a possible influence of native as well as magnetic chemical disorder on the bulk transport properties based on the modification of the electronic structure (Sec. 5.2). It is shown that also the occurrence of the native defects substantially affects the magnetism of introduced magnetic dopants. Thus, one does not only discuss how the magnetic dopants behave themselves in a pristine structure but also how the behavior depends on the type and amount of native defects. A detailed study of the magnetic exchange interactions (Sec. 5.3) is employed to determine the dependence of the ferromagnetic ordering temperatures of the actual composition of the Bi_2Se_3 systems (Sec. 5.4). The influence of relativistic corrections on the exchange interactions' behavior is considered in Chapter 6.

Having studied bulk systems, we can proceed to the more complex case, discussing the impact of the partial loss of translation symmetry in thin layered systems (Chapter 7). Concerning thin layered Bi_2Se_3 systems, we verify the presence of the gapless surface states in presence of the various chemical disorder (Sec. 7.3). Besides, the influence of the reduced dimensionality on the exchange interactions is checked. Namely, a depth profile of the exchange interactions is discussed (Sec. 7.4). Additionally, employing the layered formalism, the behavior of twin planes – experimentally evidenced planar defects in Bi_2Se_3 is studied (Sec. 7.5). We focus on the distribution of twin planes in a multilayer Bi_2Se_3 slab, and their interplay with magnetic and native defects, where their preference under doping is discussed.

Overview of publications

Part of the results mentioned in this work is included in the following publications. They are divided into already published (P), or submitted (S).

- Ref. [1] (P) contains a study of the bulk Bi_2Se_3 compound in presence of the chemical disorder. The influence of magnetic and nonmagnetic defects on the electronic structure, magnetic properties as the magnetic exchange interactions are discussed there. The obtained behavior is employed to estimate Curie temperatures of Mn magnetic defects and their dependence on the composition.
- Ref. [2] (P) discussed behavior of twin planes – planar defects in thin layered Bi_2Se_3 systems. The dependence of twin planes formation and segregation in the dependence on the character of chemical doping is discussed. The impact of twin plane occurrence on the metallic Dirac surface states is appended.
- Refs. [3] (P) and [4] (S) contain calculations of the exchange interactions in the framework of the fully relativistic approach in the case of $3d$ alloys.

1. Electronic Structure of Solids

Around one hundred years of quantum theory development, which had brought a ground-breaking concept of the wave-particle duality, enabled people to describe physics on atomic and electronic scales reliably. Nonetheless, a considerable complexity of the theoretical description cause that analytical solutions of only simple systems are feasible despite using various approximations. A way-out was provided by rising computational performance in connection with a numerical solution of problems. Nowadays, a wide range of approximations suitable for various systems exists, namely, Hatry-Fock or top-notch Coupled Cluster method used mainly in quantum chemistry, Density Functional Theory (DFT), a workhorse of solid-state physics, or cutting-edge GW approximation suitable for studying electron excitation. All the above mention cases represent so-called ab-initio computational methods. The name stands for a widely used framework of methods, which avoids using any extra assumptions like phenomenological parameters or models, which break the method's generality. It relies only on physical laws and constants. Differently speaking, calculations are performed from the first principles. However, reasonable, general, and physical relevant assumptions might be used to decrease the complexity of solved problems.

This section will briefly introduce density functional theory (DFT), and an overview of the employed tight-binding linear-muffin-tin orbital method utilizing the atomic-sphere approximation (TB-LMTO-ASA) is mentioned. References [5–8] are followed mainly in this chapter.

1.1 Nonrelativistic electrons

One of the key point of non-relativistic quantum physics is description of the evolution of a particle system by the so-called Schrödinger equation (SE) having a form a wave equation,

$$i\hbar\partial_t|\psi\rangle = \hat{H}|\psi\rangle, \quad (1.1)$$

where \hbar stands for the Plank constant and the whole system is described by a many body wave-function $|\psi\rangle$. Assuming a system whose Hamiltonian \hat{H} is time independent, it yields a simplified form of the Eq. 1.1 — the stationary SE

$$\hat{H}|\psi\rangle = E|\psi\rangle \quad (1.2)$$

and a simple time evolution the stationary state

$$|\psi\rangle(t) = e^{-\frac{i}{\hbar}\hat{H}t}|\psi_0\rangle. \quad (1.3)$$

Nevertheless, electrons' behavior in a matter represents a complicated problem with a complex structure of interactions even one assumes the Born-Oppenheimer (adiabatic) approximation. It separates the motion of nuclei, which results in an external potential parametrized by nuclei positions. Then the Hamiltonian of an N-electron system reads

$$\begin{aligned} \hat{H} &= \hat{H}_0 + \hat{V}_{ee} + \hat{V}_{ej} \\ &= -\frac{\hbar^2}{2m} \sum_{i=1}^N \Delta_i + \frac{e'^2}{2} \sum_{i,j=1}^N \frac{1}{|\mathbf{r}_i - \mathbf{r}_j|} + \frac{e'^2}{2} \sum_{i=1}^N \sum_{I=1}^{N_n} \frac{Z_I}{|\mathbf{r}_i - \mathbf{r}_I|}, \end{aligned} \quad (1.4)$$

where m denotes the electron mass, e' is the reduce elementary charge ($e' = e/\sqrt{4\pi\epsilon_0}$, where ϵ_0 is the vacuum permittivity), Z_I represents the proton number of the I^{th} atom and a vector \mathbf{r} describes position of electrons or nuclei.

The solution of Eq. 1.4 with an N-electron wave function might be obtained in the framework of the single-particle description. The original wave function having real and spin part $|\psi(\mathbf{r}_1 \dots \mathbf{r}_N; \sigma_1 \dots \sigma_N)\rangle$, σ_i denotes spin polarization of an electron i , can be emphasized in the way of one-electron orbitals $|\varphi_i\rangle$, while one has to be aware of the total wave function's fermionic character, namely the Pauli exclusion principle. Then a fully antisymmetric wave-function $|\psi\rangle$ is represented by the so-called Slater determinant composed of one electron orbital wave-functions, usually orthonormal.

The Slater determinant Ψ_0 minimizing the total energy, given by the many electron Hamiltonian (Eq. 1.4), is obtainable by Hartree-Fock (HF) method. Assuming that the total energy $E_{HF}[\varphi_1, \dots, \varphi_N]$ is functional of one electron orbitals with constraint to their orthonormality, one obtains a set of one electron equations for orbitals φ_j :

$$\epsilon_j \varphi_j = \left[-\frac{\hbar^2}{2m} \Delta + \hat{V}_H + \hat{V}_{HF} + \hat{V}_{ext} \right] \varphi_j, \quad (1.5)$$

$$\hat{V}_H(\mathbf{r})\varphi_j(\mathbf{r}) = \sum_{a=1}^N \int \frac{\varphi_a^*(\mathbf{r}')\varphi_a(\mathbf{r}')}{|\mathbf{r} - \mathbf{r}'|} d\mathbf{r}' \varphi_j(\mathbf{r}) = \int \frac{n(\mathbf{r}')}{|\mathbf{r} - \mathbf{r}'|} d\mathbf{r}' \varphi_j(\mathbf{r}), \quad (1.6)$$

$$\hat{V}_{HF}(\mathbf{r})\varphi_j(\mathbf{r}) = \sum_{a=1}^N \int \frac{\varphi_a^*(\mathbf{r}')\varphi_j(\mathbf{r}')}{|\mathbf{r} - \mathbf{r}'|} d\mathbf{r}' \varphi_a(\mathbf{r}). \quad (1.7)$$

Besides the first kinetic term (Eq. 1.5) and the external potential \hat{V}_{ext} including for instance, the interaction with nuclei, there occur the Coulomb term \hat{V}_H denoting the electrostatic interaction with the electron density of all electrons $n(\mathbf{r})$ and the HF exchange term \hat{V}_{HF} representing a non-local potential arising from antisymmetric constrains on wave-functions. Finally, Lagrange multipliers ϵ_j are related to the ionization energy. The occurrence of the non-local potential \hat{V}_{HF} makes the method demanding and unsuitable for spacious systems. Moreover, the HF method neglects correlations since using a single Slater determinant.

[5, 7, 8]

1.2 Relativistic description

For certain materials, generally containing heavier elements, the above stated description is insufficient and an inclusion of relativistic corrections is inevitable to obtain correct behavior. It resides in the replacement of SE by the Dirac equation (DE)

$$\hat{H}\Psi_i = E_i\Psi_i = E_i \begin{pmatrix} \phi_i \\ \chi_i \end{pmatrix}; \quad \hat{H} = c\boldsymbol{\alpha} \cdot [\mathbf{p} - e\mathbf{A}] + (\beta - I_4) mc^2 + V(\mathbf{r})I_4, \quad (1.8)$$

where Ψ_i denotes a four-component bispinor composed of the large component ϕ_i and the small component χ_i . Both of them are spinors. Since that the Hamiltonian is composed of four-dimensional matrices. The vector of matrices $\boldsymbol{\alpha}$ is

composed of Pauli spin matrices σ

$$\boldsymbol{\alpha} = \begin{pmatrix} 0 & \boldsymbol{\sigma} \\ \boldsymbol{\sigma} & 0 \end{pmatrix}, \quad (1.9)$$

$\hat{\mathbf{p}}$ denotes the momentum operator and \mathbf{A} is the vector potential operator. The matrix β is defined as follows

$$\beta = \begin{pmatrix} I_2 & 0 \\ 0 & -I_2 \end{pmatrix}, \quad (1.10)$$

where I_n is a unity matrix of order n , mc^2 is the electron rest energy, which together with E_i produces the total relativistic energy.

However, the form of the Hamiltonian (Eq. 1.8) is problematic, since expression of the exchange-correlation (xc) part of the effective potential \mathbf{A}_{eff} . Therefore, it is replaced by coupling of an effective magnetic field \mathbf{B}_{eff} to the spin density. It results in the fully relativistic (FR) Kohn-Sham-Dirac equation defined by a Hamiltonian

$$\hat{H}_{\text{KSD}} = c\boldsymbol{\alpha} \cdot \mathbf{p} + (\beta - I_4) mc^2 + V_0(\mathbf{r})I_4 + \beta \boldsymbol{\Sigma} \cdot \mathbf{B}_{\text{eff}}, \quad (1.11)$$

$$\mathbf{B}_{\text{eff}}[n, \mathbf{m}](\mathbf{r}) = \mu_{\text{B}} \mathbf{B}_{\text{ext}}(\mathbf{r}) + \frac{\delta E_{\text{xc}}[n(\mathbf{r}), \mathbf{m}(\mathbf{r})]}{\delta \mathbf{m}(\mathbf{r})}, \quad (1.12)$$

$$\boldsymbol{\Sigma} = \begin{pmatrix} \boldsymbol{\sigma} & 0 \\ 0 & \boldsymbol{\sigma} \end{pmatrix}, \quad (1.13)$$

where potential V_0 is related to the spin independent part of the effective potential v_{S} (Eq. 1.22), \mathbf{B}_{ext} is an external magnetic field and μ_{B} is the Bohr magneton. The latter term of \mathbf{B}_{eff} (Eq. 1.12) denotes the xc-magnetic field \mathbf{B}_{xc} .

Separating and excluding the small component χ and neglecting the external magnetic field \mathbf{B}_{ext} , it yields an effective energy dependent Hamiltonian for the large component ϕ

$$\hat{H}_{\text{eff}}(E) = (\mathbf{p} \cdot \boldsymbol{\sigma}) \frac{c^2}{2mc^2 + E - V_0(\mathbf{r}) + \mathbf{B}_{\text{xc}}(\mathbf{r}) \cdot \boldsymbol{\sigma}} (\mathbf{p} \cdot \boldsymbol{\sigma}) + V_0(\mathbf{r}) + \mathbf{B}_{\text{xc}}(\mathbf{r}) \cdot \boldsymbol{\sigma}. \quad (1.14)$$

Concerning valence electrons, their energy range as well as the exchange splitting in the denominator of Eq. 1.14 can be neglected. Considering the scalar-relativistic approximation (SRA) of Eq. 1.14, one obtains a Hamiltonian

$$\hat{H}_{\text{SRA}} \Phi = E \Phi, \quad \hat{H}_{\text{SRA}} = \mathbf{p} \cdot \omega^{-1}(\mathbf{r}) \mathbf{p} + V_0(\mathbf{r}) + \mathbf{B}_{\text{xc}}(\mathbf{r}) \cdot \boldsymbol{\sigma}, \quad (1.15)$$

$$\omega(\mathbf{r}) = 2m + c^{-2} [E_0 - V_0(\mathbf{r})], \quad (1.16)$$

where E_0 is an energy inside the valence band. In the case of a constant direction of the magnetic field \mathbf{B}_{xc} , let's suppose its alignment along the z -axis, the SRA Hamiltonian \hat{H}_{SRA} (Eq. 1.15) commutes with the spin operator σ_z . Hence, one obtains two separated solutions related either to the spin up or spin down.

The neglected spin-orbit (SO) interaction, which might be significant for obtaining reliable results, can be treated in the framework of the SRA as an perturbation with a Hamiltonian

$$\hat{H}_{\text{SO}} = (\mathbf{p} \cdot \boldsymbol{\sigma}) \omega^{-1}(\mathbf{r}) (\mathbf{p} \cdot \boldsymbol{\sigma}) - \mathbf{p} \cdot \omega^{-1}(\mathbf{r}) \mathbf{p} = \left\{ \left[\boldsymbol{\nabla} \omega^{-1}(\mathbf{r}) \right] \times \mathbf{p} \right\} \cdot \boldsymbol{\sigma}. \quad (1.17)$$

Generally, it leads to a small mixing of the spin up and spin down solutions. Considering spherically symmetrical potential $V_0(\mathbf{r})$ and atomic orbitals $\phi_{\ell ms}(\mathbf{r})$, where ℓ, m and s are angular resp. spin momentum quantum numbers, the matrix elements of the SO Hamiltonian reads

$$\langle \phi_{\ell ms} | \hat{H}_{\text{SO}} | \phi_{\ell' m' s'} \rangle = \delta_{\ell \ell'} \xi_{\ell, ss'} \langle \phi_{\ell ms} | \mathbf{L} \cdot \mathbf{S} | \phi_{\ell' m' s'} \rangle, \quad (1.18)$$

$$\xi_{\ell, ss'} = 2 \int r \phi_{\ell s'}(r) \phi_{\ell s}(r) [\omega^{-1}(\mathbf{r})]' dr, \quad (1.19)$$

where \mathbf{L} resp. \mathbf{S} stand for the angular orbital and spin momentum operators.

[6, 8]

1.3 Density functional theory

The problem of the mentioned extreme complicatedness arising from the non-local potential V_{HF} (Eq. 1.7) can be overcome by focusing on the electron density $n(\mathbf{r})$ instead of wave function, where electron density resulting from the N-body wave function stands for a function of only three coordinates. It is possible thanks to the Hohenberg-Kohn theorems, which says that a potential have to be a functional of $n(\mathbf{r})$ and the total energy is minimized for the ground state density [5–7]

$$n(\mathbf{r}) = \sum_{\sigma_1 \dots \sigma_N} \int d\mathbf{r}_1 \dots d\mathbf{r}_N \sum_{i=1}^N |\psi(\mathbf{r}_1 \dots \mathbf{r}_N; \sigma_1 \dots \sigma_N)|^2 \delta(\mathbf{r} - \mathbf{r}_i). \quad (1.20)$$

Kohn-Sham (KS) equations show that an easily solvable one electron SE can be constructed

$$\left(-\frac{\hbar^2}{2m} \Delta + v_S \right) \varphi_S = \epsilon_i \varphi_S; \quad n(\mathbf{r}; \sigma) = \sum_i |\varphi_{Si}(\mathbf{r}, \sigma)|^2, \quad (1.21)$$

where φ_S is a KS orbital and v_S denotes an effective potential given by $n(\mathbf{r})$

$$v_S(\mathbf{r}) = v_{ext}(\mathbf{r}) + e'^2 \int \frac{n(\mathbf{r}')}{|\mathbf{r} - \mathbf{r}'|} d\mathbf{r}' + \frac{\delta E_{xc}[n(\mathbf{r})]}{\delta n(\mathbf{r})}. \quad (1.22)$$

The first term v_{ext} is an external potential, the second represents the Coulomb interaction, and the last one stands for an xc-potential v_{xc} , while E_{xc} denotes an xc-functional. KS equations represent a set of coupled equations. The ground state density can be obtained by iterations until a self-consistency is achieved.

The mentioned xc-functional $E_{xc}[n(\mathbf{r})]$ stands for a key point of DFT calculations. Despite being small, it has a significant impact on the obtained results. Nonetheless, its form is unknown. Therefore, several approximations are used. There are mentioned a few of them.

- Local density approximation LDA

A basic approximation of the exchange-correlation potential based on the xc-energy density $\epsilon_{xc}[n(\mathbf{r})]$ of the homogenous electron gas parameterized only by the electron density $n(\mathbf{r})$

$$E_{xc}[n(\mathbf{r})] = \int \epsilon_{xc}[n(\mathbf{r})] n(\mathbf{r}) d\mathbf{r}. \quad (1.23)$$

The xc-energy density ϵ_{xc} can be decomposed to the exchange part ϵ_x and correlation part ϵ_c since the exchange energy density has a simple form for the homogeneous electron

$$\epsilon_x = -\frac{3}{4} \left(\frac{3}{\pi} n(\mathbf{r}) \right)^{\frac{1}{3}}. \quad (1.24)$$

The correlations are more complex. Functionals based on fitting of Monte-Carlo simulations are used in general. Namely correlation functionals of Perdew-Zunger, Vosko-Wilk-Nusair etc. A general feature is the underestimation of the exchange and overestimation of correlations. For instance, it leads to underestimation of the band gap.

- Local spin density approximation (LSDA)

An extension of the LDA for systems with a spin polarized electron density $n(\mathbf{r}; s)$. Assuming a system with a collinear spin polarization along the z-axis, two likely distinct densities for the spin up ($\sigma = \uparrow$) and spin down ($\sigma = \downarrow$) channel occur there

$$n(\mathbf{r}) = n_{\uparrow}(\mathbf{r}) + n_{\downarrow}(\mathbf{r}). \quad (1.25)$$

Then a simple generalization of xc-potential appears

$$v_{xc,\sigma} = \frac{\delta E_{xc}[n_{\uparrow}(\mathbf{r}), n_{\downarrow}(\mathbf{r})]}{\delta n_{\sigma}(\mathbf{r})} = \frac{\delta \int n(\mathbf{r}) \epsilon_{xc}(n_{\uparrow}(\mathbf{r}), n_{\downarrow}(\mathbf{r})) d\mathbf{r}}{\delta n_{\sigma}(\mathbf{r})}, \quad (1.26)$$

which means solving of two sets of KS equations for different spins $\sigma = \uparrow, \downarrow$.

A difference between electron densities of spin-up and spin-down channels brings about the occurrence of the spin density \mathbf{m} , which is a vector quantity pointing along the spin polarization axis. Assuming polarization along the z-axis

$$\mathbf{m}(\mathbf{r}) = (n_{\uparrow}(\mathbf{r}) - n_{\downarrow}(\mathbf{r})) \hat{\mathbf{e}}_z. \quad (1.27)$$

It brings about an effective magnetic contribution to Hamiltonian

$$\boldsymbol{\sigma} \cdot \mathbf{B}_{\text{eff}} = \frac{\delta E_{xc}[n(\mathbf{r}), \mathbf{m}(\mathbf{r})]}{\delta \mathbf{m}(\mathbf{r})}, \quad (1.28)$$

where $\boldsymbol{\sigma}$ denotes Pauli matrices.

- Generalized gradient approximation (GGA)

L(S)DA seems to be inappropriate to a description of systems with a large spatial variation of electron densities. Therefore, a large number of functionals depending not only on the density but also on its gradient have been formulated, namely PBE, b3LYP etc. Assuming a system the spin polarization, a general formula for the xc-energy reads

$$E_{xc} = \int f(n_{\uparrow}, n_{\downarrow}, \nabla n_{\uparrow}, \nabla n_{\downarrow}) d\mathbf{r}. \quad (1.29)$$

- LDA + U

Simple LDA fails in description of strongly-correlated materials, where partially filled d - or f -shells appear. LDA+U cures correlation effects by adding an orbital dependent single-particle potential, which treats the Coulomb repulsion of well-localized orbitals in the manner of the Hubbard like Hamiltonian. Assuming a set of N localized electrons, a general total energy functional in LDA+U framework reads

$$E_{\text{LDA+U}}[n(\mathbf{r})] = E_{\text{LDA}}[n(\mathbf{r})] + E_{\text{Hub}}[\{n_{mn}^{\sigma}\}] - E_{\text{dc}}[\{n_{mn}^{\sigma}\}], \quad (1.30)$$

where $\{n_{mn}^{\sigma}\}$ denotes set of occupation numbers defined by a projection of the occupied Kohn-Sham states $\varphi_{kj\sigma}$ on the localized basis $\{\phi_{m\sigma}\}$

$$n_{mn}^{\sigma} = \sum_{kj} f_{kj}^{\sigma} \langle \varphi_{kj\sigma} | \phi_{m\sigma} \rangle \langle \phi_{n\sigma} | \varphi_{kj\sigma} \rangle, \quad (1.31)$$

the index k denotes k -points and j index energy bands. The E_{Hub} term contains electron-electron interaction modeled similarly to the Hubbard Hamiltonian and E_{dc} represents a correction for double-counting.

[5, 7, 8]

1.4 TB-LMTO-ASA method

In this section, an overview of the tight-binding linear muffin-tin orbital method in the atomic sphere approximation (TB-LMTO-ASA) is introduced. It was employed to reckon electronic structures of the studied system, which serve as grounding for presented results. Fundamental ideas, including treating disorder and calculating magnetic exchange interactions, reliability as well as strengths and weaknesses of the used approach, are mentioned. Thanks to the complexity of the method, one is referred for a thorough description to Refs. [5, 6], since it goes beyond the scope of the present work. Refs. [5, 6] are followed in this section.

1.4.1 Bulk systems

The method arises from an assumption of spherically symmetric atomic muffin-tin potentials centered at the atomic sites. The atomic spheres are only slightly over-lapped and fill the whole spaces – atomic sphere approximation. It allows one to neglect the kinetic term in the interstitial region, which leads to high performance and the effective description of various sorts of systems. However, it causes problems in materials with spatial inhomogeneity (e.g. van der Waals material), where the usage of empty spheres is desired. Besides, it does not allow the complete lattice relaxation, and there occurs a systematic total energy error.

This method enables one to treat a problem within various formalism, which includes either non-relativistic, scalar-relativistic or fully relativistic approach according to the system complexity. Solving an appropriate wave equation, mentioned in previous sections, one obtains a secular equation in the framework of the

ASA. Using the translational symmetry of solids and assuming the non-relativistic treatment, it reads in the k -space

$$\det [P_{\mathbf{B}\ell}(E) \delta_{\mathbf{B}L,\mathbf{B}'L'} - S_{\mathbf{B}L,\mathbf{B}'L'}(\mathbf{k})] = 0, \quad (1.32)$$

where k is the wave vector and $L = (l, m)$ are angular momentum quantum numbers labeling distinct solutions. In the case of relativistic treatment, they are replaced by relativistic $\Lambda = (\kappa, \mu)$ indices. A vector \mathbf{B} represents atomic basis vectors. According to the translational symmetry, an atomic site \mathbf{R} might be express by means of the translation vector \mathbf{T} as follows $\mathbf{R} = \mathbf{B} + \mathbf{T}$. The secular equation (Eq. 1.32) is composed of two principal parts, namely potential function $P_{\mathbf{B}\ell}(E)$ and structure constants $S_{\mathbf{B}L,\mathbf{B}'L'}(\mathbf{k})$. The former describes properties of the particular atomic spheres. The later refers to positions of the atomic spheres, where the lattice Fourier transformation was used according to the 3D translational symmetry

$$S_{\mathbf{B}L,\mathbf{B}'L'}(\mathbf{k}) = \sum_{\mathbf{T}} S_{\mathbf{B}L,(\mathbf{B}'+\mathbf{T})L'} e^{i\mathbf{k}\cdot\mathbf{T}}. \quad (1.33)$$

One should note that the energy independence of structure constants makes the geometrical description quite simple. By an energy linearization of LMTO orbitals it is possible to get rid of the energy dependence in the secular equation, which yields

$$\det [E\delta_{\mathbf{B}L,\mathbf{B}'L'} - H_{\mathbf{B}L,\mathbf{B}'L'}^{\text{orth}}(\mathbf{k})] = 0, \quad (1.34)$$

where the orthogonal Hamiltonian H^{orth} is parametrized by potential parameters C , Δ and γ as follows

$$H^{\text{orth}} = C + \sqrt{\Delta} S^\gamma \sqrt{\Delta}, \quad (1.35)$$

$$S^\gamma = S (1 - \gamma S)^{-1}, \quad (1.36)$$

and where potential function $P_{\mathbf{B}\ell}(E)$ has a parametric form as well. The operator notation is neglected in this section for brevity.

A great advantage of the TB-LMTO-ASA method resides in possible treatment by the Green's function formalism. It is well suitable for an inclusion of chemical disorder, final temperature, or solving electrical transport or magnetic exchange interactions. The appropriate Green's function can be written as follows

$$G(z) = \lambda(z) + \mu(z)g(z)\mu(z), \quad (1.37)$$

$$g(z) = [P(z) - S]^{-1}, \quad (1.38)$$

where $\lambda(z)$ and $\mu(z)$ are diagonal matrices in indices $(\mathbf{R}\ell)$. The non-diagonal matrix $g(z)$ is the so-called auxiliary Green's function, whose poles z corresponds to the eigenvalues of the secular equation Eq. 1.32. Assuming second order parametrization of the potential function $P(z)$, the physical Green's function $G(z)$ becomes a resolvent of the orthogonal Hamiltonian H^{orth}

$$G(z) = (z - H^{\text{orth}})^{-1}. \quad (1.39)$$

It means the physical properties of interest are available in the framework of Green's function.

1.4.2 Layered systems

The bulk TB-LMTO-ASA method concerning the Green's function formalism can be generalized for layered systems including the translational symmetry in the atomic plane only. Concerning screened tight-binding structure constants $S_{\mathbf{R}L,\mathbf{R}'L'}^\beta$ vanishing over a few nearest neighbors distance, the system might be divided into a countable set of principal layer described by an index p , where they contain a finite number of atomic layers. One can assume that structure constants $S_{\mathbf{R}L,\mathbf{R}'L'}^\beta$ are non-zero only up to nearest neighbor principal layer. Having layered structure, the two-dimensional lattice Fourier transformation of a layered translation invariant matrix $A_{\mathbf{B}L,\mathbf{B}'L'}(\mathbf{k}_\parallel)$ can be defined

$$A_{p\mathbf{B}L,p'\mathbf{B}'L'}(\mathbf{k}_\parallel) = \sum_{\mathbf{T}_\parallel} A_{p\mathbf{B}L,p'(B'+\mathbf{T}_\parallel)L'} e^{i\mathbf{k}_\parallel \cdot \mathbf{T}_\parallel}, \quad (1.40)$$

where \mathbf{B} is a basis vector in the p^{th} principal layer. \mathbf{T}_\parallel and \mathbf{k}_\parallel denote 2D translation resp. 2D wave vectors. The layered counterpart of the auxiliary Green's function g (Eq. 1.38) can be defined by a matrix equation

$$\sum_{p\mathbf{B}L} M_{p'\mathbf{B}'L',p\mathbf{B}L}(\mathbf{k}_\parallel, z) g_{p\mathbf{B}L,p''\mathbf{B}''L''}(\mathbf{k}_\parallel, z) = \delta_{p'\mathbf{B}'L',p''\mathbf{B}''L''}, \quad (1.41)$$

$$M_{p'\mathbf{B}'L',p\mathbf{B}L}(\mathbf{k}_\parallel, z) = \left[P_{p'\mathbf{B}L}(z) \delta_{p'\mathbf{B}'L',p\mathbf{B}L} - S_{p'\mathbf{B}',p\mathbf{B}L}(\mathbf{k}_\parallel) \right]. \quad (1.42)$$

Thanks to the screened structure constants S^β , the matrix M is tridiagonal in the p index. Hence, neglecting \mathbf{B}, L indices for brevity, the on-site auxiliary Green's function at the p^{th} principal layer can be obtained by the partitioning as follows

$$g_{p,p}(\mathbf{k}_\parallel, z) = \left[P_p(z) - S_{p,p}(\mathbf{k}_\parallel) - \Gamma_p^<(\mathbf{k}_\parallel, z) - \Gamma_p^>(\mathbf{k}_\parallel, z) \right]^{-1}, \quad (1.43)$$

where $\Gamma_p^<(\mathbf{k}_\parallel, z)$ and $\Gamma_p^>(\mathbf{k}_\parallel, z)$ denote embedding potentials originating from the adjacent semi-infinite blocks. They satisfy following recursion relations

$$\Gamma_p^>(\mathbf{k}_\parallel, z) = S_{p,p\pm 1}(\mathbf{k}_\parallel) \left[P_{p\pm 1}(z) - S_{p\pm 1,p\pm 1}(\mathbf{k}_\parallel) - \Gamma_{p\pm 1}^>(\mathbf{k}_\parallel, z) \right]^{-1} S_{p\pm 1,p}(\mathbf{k}_\parallel). \quad (1.44)$$

Having a system attached to semi-infinite leads, one is able to reckon the initial embedding potential $\Gamma_0^>, \Gamma_0^<$. For an semi-infinite system they satisfied a closed recursion relation

$$\Gamma_0^>(\mathbf{k}_\parallel, z) = S_{0,1}(\mathbf{k}_\parallel) \left[P_0(z) - S_{0,0}(\mathbf{k}_\parallel) - \Gamma_0^>(\mathbf{k}_\parallel, z) \right]^{-1} S_{1,0}(\mathbf{k}_\parallel), \quad (1.45)$$

where potential functions $P_0(z)$ and structure constants $S_{0,0}(\mathbf{k}_\parallel)$ are related to the semi-infinite system composed of principal layers $p = 0$.

1.5 Coherent potential approximation

For real material calculations, an influence of chemical disorder is generally highly important as it might significantly modify the properties of pristine structures. In general, there are two main approaches describing a system with a random substitutional disorder on a non-random lattice. The first is the so-called supercell

method based on configuration averaging of a (quasi-)randomly perturbed system. According to the structure size, it might require large statistical ensembles, which makes it quite computationally demanding. Having employed the Green's function formalism, one can treat the substitutional disorder in the framework of the coherent potential approximation (CPA) [9] through the construction of Green's functions describing an effective medium. CPA represents an efficient concept to include substitutional disorder since small demands in comparison to the supercell method. It suits for small perturbations concerning similar elements or small defect concentrations. In the following section, a general concept of the CPA in the TB-LMTO-ASA framework is introduced, while Ref. [6] is followed.

Let's assume a system composed of components Q , which are randomly distributed with concentrations $c_{\mathbf{R}}^Q$ obeying the relation

$$\sum_Q c_{\mathbf{R}}^Q = 1, \quad (1.46)$$

where \mathbf{R} denotes lattice site. A random configuration is described by occupation number $\eta_{\mathbf{R}}^Q$ denoting whether an atom of Q type occupies lattice site \mathbf{R} ($\eta_{\mathbf{R}}^Q = 1$) or not ($\eta_{\mathbf{R}}^Q = 0$), whilst occupation numbers satisfy relations

$$\sum_Q \eta_{\mathbf{R}}^Q = 1, \quad \langle \eta_{\mathbf{R}}^Q \rangle = c_{\mathbf{R}}^Q, \quad (1.47)$$

where $\langle \dots \rangle$ stands for the configurational averaging. Then the configurational averaged form of the physical Green's function (Eq. 1.37) can be expressed. Its site-diagonal elements reads

$$\langle G_{\mathbf{R},\mathbf{R}}(z) \rangle = \bar{G}_{\mathbf{R},\mathbf{R}}(z) = \sum_Q c_{\mathbf{R}}^Q \bar{G}_{\mathbf{R},\mathbf{R}}^Q(z), \quad (1.48)$$

$$\bar{G}_{\mathbf{R},\mathbf{R}}^Q(z) = \sum_Q c_{\mathbf{R}}^Q \left[\lambda_{\mathbf{R}}^{\alpha,Q}(z) + \mu_{\mathbf{R}}^Q(z) \bar{g}_{\mathbf{R},\mathbf{R}}^Q(z) \mu_{\mathbf{R}}^Q(z) \right], \quad (1.49)$$

$$\bar{g}_{\mathbf{R},\mathbf{R}}^Q(z) = \frac{1}{c_{\mathbf{R}}^Q} \langle \eta_{\mathbf{R}}^Q g_{\mathbf{R},\mathbf{R}}(z) \rangle, \quad (1.50)$$

where $\bar{G}_{\mathbf{R},\mathbf{R}}^Q(z)$ and $\bar{g}_{\mathbf{R},\mathbf{R}}^Q(z)$ are conditionally averaged site-diagonal elements of physical resp. auxiliary Green's functions denoting the contribution originated from the occupation of the site \mathbf{R} by an atomic type Q . Analogously, the non-diagonal elements of the configurational averaged Green's function reads

$$\bar{G}_{\mathbf{R},\mathbf{R}'}(z) = \sum_{Q,Q'} c_{\mathbf{R}}^Q \bar{G}_{\mathbf{R},\mathbf{R}'}^{Q,Q'}(z) c_{\mathbf{R}'}^{Q'}, \quad (1.51)$$

$$\bar{G}_{\mathbf{R},\mathbf{R}'}^{Q,Q'}(z) = \mu_{\mathbf{R}}^Q(z) \bar{g}_{\mathbf{R},\mathbf{R}'}^{Q,Q'}(z) \mu_{\mathbf{R}'}^{Q'}, \quad (1.52)$$

$$\bar{g}_{\mathbf{R},\mathbf{R}'}^{Q,Q'}(z) = \frac{1}{c_{\mathbf{R}}^Q} \langle \eta_{\mathbf{R}}^Q g_{\mathbf{R},\mathbf{R}'}(z) \eta_{\mathbf{R}'}^{Q'} \rangle \frac{1}{c_{\mathbf{R}'}^{Q'}}. \quad (1.53)$$

Concerning numerical application, the auxiliary Green's function $g(z)$ (Eq. 1.38) is important. The configuration averaged counterpart $\bar{g}(z)$, which reads

$$\bar{g}_{\mathbf{R},\mathbf{R}'}(z) = \sum_Q c_{\mathbf{R}}^Q \bar{g}_{\mathbf{R},\mathbf{R}}^Q(z) \delta_{\mathbf{R},\mathbf{R}'} + \sum_{QQ'} c_{\mathbf{R}}^Q \bar{g}_{\mathbf{R},\mathbf{R}'}^{QQ'}(z) c_{\mathbf{R}'}^{Q'} (1 - \delta_{\mathbf{R},\mathbf{R}'}), \quad (1.54)$$

can be for practical purpose reformulated by means of the non-random coherent potential function matrix $\mathcal{P}(z)$, which describes non-random scattering properties of “effective” atoms brought about by the configurational averaging, as follows

$$\bar{g}_{\mathbf{R},\mathbf{R}'}(z) = \left[\mathcal{P}^\alpha(z) - S^\alpha \right]_{\mathbf{R},\mathbf{R}'}. \quad (1.55)$$

In the framework of the CPA, the single-site approximation is used. It neglects the site off-diagonal elements of the coherent potential function $\mathcal{P}(z)$, which leads to a simple site-diagonal matrix form

$$\mathcal{P}_{\mathbf{R},\mathbf{R}'}(z) = \mathcal{P}_{\mathbf{R}}(z) \delta_{\mathbf{R},\mathbf{R}'}. \quad (1.56)$$

For numerical solution, a site-diagonal coherent interactor $\Omega_{\mathbf{R}}(z)$ should be introduced

$$\Omega_{\mathbf{R}}(z) = \mathcal{P}_{\mathbf{R}}(z) - [\bar{g}_{\mathbf{R},\mathbf{R}}(z)]^{-1}. \quad (1.57)$$

It represents a coupling of the atomic site \mathbf{R} described by the configurational averaged Green’s function $\bar{g}_{\mathbf{R},\mathbf{R}}(z)$ to all other atomic sites. The CPA-condition in the framework of the single-site approximation reads

$$\sum_Q c_{\mathbf{R}}^Q \bar{g}_{\mathbf{R},\mathbf{R}}^Q(z) = \bar{g}_{\mathbf{R},\mathbf{R}}(z). \quad (1.58)$$

Having defined the coherent interactor $\Omega_{\mathbf{R}}(z)$, the CPA-condition (Eq. 1.58) can be rewritten as follows

$$\sum_Q c_{\mathbf{R}}^Q \left[P_{\mathbf{R}}^{\alpha,Q}(z) - \Omega_{\mathbf{R}}^\alpha(z) \right]^{-1} = \bar{g}_{\mathbf{R},\mathbf{R}}^\alpha(z), \quad (1.59)$$

where Eq. 1.58 and Eq. 1.59 stands for a closed set of equations defining the coherent potential function $\mathcal{P}(z)$ and the coherent interactor $\Omega_{\mathbf{R}}(z)$, which can be solved by an iterative process.

1.6 Observables in TB-LMTO-ASA

The evaluation of the most important one-electron physical quantities obtainable from TB-LMTO-ASA electronic structure calculations is described in this part. Ref. [6] is followed in this section.

Charge density

One should start from the key point of electronic structure calculations – the charge density $\varrho(\mathbf{r})$. Employing complete orthonormal basis set ψ_i , a resolvent $G(z)$ related to the Hamiltonian H (Eq. 1.39) with eigenvalues ϵ_i can be written in the form of the spectral representation

$$G(z) = \sum_i |\psi_i\rangle \frac{1}{z - \epsilon_i} \langle \psi_i|. \quad (1.60)$$

The resolvent $G(z)$ is analytical in the upper half of the complex plane. Hence the energy resolved charge density $w(\mathbf{r}, E)$ can be obtained by a side-limit of the one-electron Green’s function $G(\mathbf{r}, \mathbf{r}, z)$, where $z = E + i0$, as follows

$$w(\mathbf{r}, E) = -\frac{1}{\pi} \text{Im} G(\mathbf{r}, \mathbf{r}, z = E + i0). \quad (1.61)$$

Likely, more important in the framework of the LMTO-ASA theory is the charge density $\varrho_{\mathbf{R}}(\mathbf{r})$ inside the atomic sphere \mathbf{R} . For generality, the spin-dependent charge density $\varrho_{\mathbf{R},\sigma}(\mathbf{r})$ might be defined as it arise for spin-polarized systems. It obeys relation

$$\varrho_{\mathbf{R},\sigma}(\mathbf{r}) = \sum_{LL'} \int_{-\infty}^{E_F} \varphi_{\mathbf{R}L,\sigma}(\mathbf{r}, E) n_{\mathbf{R},LL',\sigma}(E) \varphi_{\mathbf{R}L',\sigma}(\mathbf{R}, E) dE, \quad (1.62)$$

where $\varphi_{\mathbf{R}L,\sigma}(\mathbf{r}, E)$ denotes spin-dependent regular solutions in the \mathbf{R} atomic sphere. The spin-dependent local density of states $n_{\mathbf{R},LL',\sigma}(E)$ obeys a similar relation to Eq. 1.61. Employing the spin-dependent on-site physical Green's function, it yields

$$n_{\mathbf{R},LL',\sigma}(E) = -\frac{1}{\pi} \text{Im} G_{\mathbf{R}L,\mathbf{R}L',\sigma}(E + i0). \quad (1.63)$$

Assuming a system with a collinear spin polarization, for simplicity with polarization along z-axis ($\sigma = \uparrow, \downarrow$), the total charge density $\varrho_{\mathbf{R}}(\mathbf{r})$ and the total spin density obeys relations

$$\varrho_{\mathbf{R}}(\mathbf{r}) = \varrho_{\mathbf{R},\uparrow}(\mathbf{r}) + \varrho_{\mathbf{R},\downarrow}(\mathbf{r}), \quad (1.64)$$

$$m_{\mathbf{R}}(\mathbf{r}) = \varrho_{\mathbf{R},\uparrow}(\mathbf{r}) - \varrho_{\mathbf{R},\downarrow}(\mathbf{r}). \quad (1.65)$$

Density of states

The local density of states (DOS) $n_{\mathbf{R}}(E)$ at the atomic site \mathbf{R} consists of contributions represented by $\mathbf{R}L\sigma$ -projected local densities $n_{\mathbf{R}L,\sigma}(E)$. They stand for diagonal elements of the local DOS matrix. Therefore, $n_{\mathbf{R}}(E)$ reads

$$n_{\mathbf{R}}(E) = \sum_{L\sigma} n_{\mathbf{R}L,\sigma}(E) = -\frac{1}{\pi} \sum_{L\sigma} \text{Im} G_{\mathbf{R}L,\mathbf{R}L,\sigma}(E + i0). \quad (1.66)$$

Concerning atomic site \mathbf{R} , the total DOS of the occupied states is equal to the total charge at the site \mathbf{R}

$$\int_{\mathbf{R}} \varrho_{\mathbf{R}}(\mathbf{r}) d\mathbf{r} = \int_{-\infty}^{E_F} n_{\mathbf{R}}(E) dE. \quad (1.67)$$

Bloch spectral function

Assuming a system with translational symmetry, the electronic structure can be described in the Brillouin zone (BZ) by k -resolved physical quantities through the lattice Fourier transformation (Eq. 1.33). Hence, the on-site physical Green's function determining the local density of states (Eq. 1.66) obeys a relation

$$G_{\mathbf{B}L,\mathbf{B}L}(z) = \frac{1}{N} \sum_{\mathbf{k}} G_{\mathbf{B}L,\mathbf{B}L}(\mathbf{k}, z). \quad (1.68)$$

Similarly, the local density of states $n_{\mathbf{R}}(E)$ (Eq. 1.66) can be defined by means of the Bloch spectral functions (BSF's) $\mathcal{A}_{\mathbf{B}L}(\mathbf{k}, E)$ as follows

$$n_{\mathbf{R}}(E) = \frac{1}{N} \sum_{L\sigma} \sum_{\mathbf{k}} \mathcal{A}_{\mathbf{B}L,\sigma}(\mathbf{k}, E), \quad (1.69)$$

$$\mathcal{A}_{\mathbf{B}L,\sigma}(\mathbf{k}, E) = -\frac{1}{\pi} \text{Im} G_{\mathbf{B}L,\mathbf{B}L}(\mathbf{k}, E + i0, \sigma). \quad (1.70)$$

The BSF $\mathcal{A}_{\mathbf{BL}}(\mathbf{k}, E)$ stands for a distribution of the density of states in the k -space, the amplitude includes. Therefore it is suitable for description and analysis of the band structure.

The all mentioned observables can be generalized assuming a layered system in presence of substitutional disorder. Mainly, the BSF's are essential for the description of a disordered system since the poles z of the configurational averaged physical Green's function $G(z)$ (Eqs. 1.48, 1.51) do not describe the effective medium in the CPA framework properly.

2. Magnetic Interactions

Assuming for simplicity a non-relativistic system with the spin polarization along z -axis, an atomic orbital is characterized by a set of quantum numbers, namely principal q.n. n , angular q.n. l , magnetic q.n. m and spin q.n. m_s . An electron of the atomic state $|nlm; m_s\rangle$ carries two magnetic moments contributions. The first is the angular magnetic moment $\boldsymbol{\mu}_L$ (with z -projection μ_{Lz}) [10]

$$|\boldsymbol{\mu}_L| = -\mu_B \sqrt{l(l+1)}, \quad (2.1)$$

$$\mu_{Lz} = -\mu_B m, \quad (2.2)$$

which represent a quantum analogue of classical magnetic moment, where the quantum current density $\mathbf{j}(\mathbf{r})$ is assumed [10]

$$\mathbf{j}(\mathbf{r}) = -\frac{\hbar e}{2mi} [\varphi^*(\mathbf{r})\nabla\varphi(\mathbf{r}) - \nabla\varphi(\mathbf{r})\varphi^*(\mathbf{r})]. \quad (2.3)$$

The second is the spin magnetic moment $\boldsymbol{\mu}_S$ with no classical analogy [10]

$$|\boldsymbol{\mu}_S| = -g_e \mu_B m_s, \quad (2.4)$$

where $g_e \approx 2.0023\dots$ is the gyro-magnetic ratio. Finally, assuming the LS coupling, the total angular momentum \mathbf{J} and the related magnetic moment $\boldsymbol{\mu}_J$ obey relations [10]

$$\mathbf{J} = \mathbf{L} + \mathbf{S}, \quad (2.5)$$

$$\boldsymbol{\mu}_J = -g_J \mu_B \mathbf{J}, \quad (2.6)$$

where g_J is the Landé g -factor. Realizing that the atomic moments are of the order of μ_B , it is obvious, that magnetostatic dipole-dipole interaction [7, 10]

$$\Delta E = \frac{\mu_0}{4\pi} \frac{\boldsymbol{\mu}_1 \cdot \boldsymbol{\mu}_2 - ((\mathbf{R}_2 - \mathbf{R}_1) \cdot \boldsymbol{\mu}_1)((\mathbf{R}_2 - \mathbf{R}_1) \cdot \boldsymbol{\mu}_2)}{|\mathbf{R}_2 - \mathbf{R}_1|^3}, \quad (2.7)$$

where μ_i and \mathbf{R} are magnetic moment and position of the i^{th} atom, is not sufficient to reach observed high magnetic ordering temperatures. Therefore, additional magnetic interactions have to be introduced. The constant μ_0 denotes the vacuum permeability.

In solid, an effective coupling between magnetic moments arises from the Coulomb repulsion and electron hopping, considering the Pauli exclusion principle forbidding the occupation of a particular quantum state by more than one fermion.

2.1 Exchange mechanisms

In this section, several model exchange mechanisms characterizing electron coupling in real systems are introduced employing small model systems. Concerning the exchange mechanisms, one follows Refs. [7, 11]. Besides regarding the Ruderman-Kittel-Kasuya-Yoshida interaction Refs. [12–17] are employed and Refs. [10, 18] in the case of the magnetic anisotropy are used.

2.1.1 Coulomb exchange

The Pauli exclusion principle states that a permutation of fermions changes the many-body fermionic wave function sign. Therefore, electrons of the same spin are not allowed to occupy the same orbital simultaneously. It makes the Coulomb energy spin-dependent as the exchange hole occurs.

Let's consider for brevity two electron model, with two one electron orbitals $\varphi_\alpha(\mathbf{r})$, where $\alpha = a, b$, and the Coulomb repulsion

$$H_U = \sum_{i < j} \frac{1}{|\mathbf{r}_i - \mathbf{r}_j|} \quad (2.8)$$

setting $e' = 1$. Using the second quantization formalism, the two-electron state $\Psi_{a\sigma; b\sigma'}$ reads

$$\Psi_{a\sigma; b\sigma'} = |a\sigma; b\sigma'\rangle = c_{a\sigma}^\dagger c_{b\sigma'}^\dagger |0\rangle, \quad (2.9)$$

where σ, σ' denote electron spins, c^\dagger, c are fermionic creation and annihilation operators and $|0\rangle$ stands for the empty state. Similarly, the Coulomb interaction is defined in the second quantization as follows

$$V = \frac{1}{2} \sum_{ijkl} \mathcal{V}_{ijkl} c_i^\dagger c_j^\dagger c_k c_l, \quad (2.10)$$

$$\mathcal{V}_{ijkl} = \iint \varphi_i^*(\mathbf{r}_1) \varphi_j^*(\mathbf{r}_2) \frac{1}{|\mathbf{r}_1 - \mathbf{r}_2|} \varphi_k(\mathbf{r}_2) \varphi_l(\mathbf{r}_1) d\mathbf{r}_1 d\mathbf{r}_2. \quad (2.11)$$

Considering the two-electron state $|a\sigma; b\sigma\rangle$, two contributions to the Eq. 2.11 can be distinguished. First, the direct Coulomb integral

$$U_{ab} = \iint |\varphi_a(\mathbf{r}_1)|^2 |\varphi_b(\mathbf{r}_2)|^2 d\mathbf{r}_1 \frac{1}{|\mathbf{r}_1 - \mathbf{r}_2|} d\mathbf{r}_2 \quad (2.12)$$

and second, the exchange integral

$$J_{ab} = \iint \varphi_a^*(\mathbf{r}_1) \varphi_b^*(\mathbf{r}_2) \varphi_a(\mathbf{r}_2) \varphi_b(\mathbf{r}_1) \frac{1}{|\mathbf{r}_1 - \mathbf{r}_2|} d\mathbf{r}_2. \quad (2.13)$$

Assuming various orientations of the electron spins σ, σ' , one obtains the basis set $\{\Psi_{\uparrow\uparrow}, \Psi_{\uparrow\downarrow}, \Psi_{\downarrow\uparrow}, \Psi_{\downarrow\downarrow}\}$, where the Coulomb term matrix reads

$$H_U = \begin{pmatrix} U_{ab} - J_{ab} & 0 & 0 & 0 \\ 0 & U_{ab} & -J_{ab} & 0 \\ 0 & -J_{ab} & U_{ab} & 0 \\ 0 & 0 & 0 & U_{ab} - J_{ab} \end{pmatrix}. \quad (2.14)$$

Diagonalizing it, one obtains two sort of the eigenstates, namely triplet states $\Psi_{\uparrow\uparrow}, \Psi_{\downarrow\downarrow}$ and $\frac{1}{\sqrt{2}}(\Psi_{\uparrow\downarrow} + \Psi_{\downarrow\uparrow})$ bearing the eigenenergy $\Delta\epsilon_t = U_{ab} - J_{ab}$ and a singlet state $\frac{1}{\sqrt{2}}(\Psi_{\uparrow\downarrow} - \Psi_{\downarrow\uparrow})$ with the eigenenergy $\Delta\epsilon_s = U_{ab} + J_{ab}$. One can show that both integrals U_{ab} and J_{ab} are positive, therefore triplet states lie below the singlet states. Let's φ_α are degenerate atomic orbitals, then the Coulombs exchange maximize the spin of the atomic shell.

2.1.2 Kinetic exchange

An exchange mechanism where the electron hopping is dominant is called the kinetic exchange. The Coulomb interaction plays there only a role of the local on-site electron repulsion U . Let's consider a system with two spatially separated orthogonal orbitals (φ_i , $i = 1, 2$). The system is occupied by two electrons with opposite spins, which are allowed to move between the orbitals. The electron hopping is described by the matrix element $-t$ when electrons' order is maintained. Otherwise, a change of the sign is needed according to the Pauli exclusion principle. Then, assuming the basis

$$\{|\uparrow, \downarrow\rangle, |\downarrow, \uparrow\rangle, |\uparrow\downarrow, \cdot\rangle, |\cdot, \uparrow\downarrow\rangle\}, \quad (2.15)$$

the Hamiltonian describing the mentioned toy model of the H_2 molecule reads

$$H = \begin{pmatrix} 0 & 0 & -t & -t \\ 0 & 0 & t & t \\ -t & t & U & 0 \\ -t & t & 0 & U \end{pmatrix}. \quad (2.16)$$

It is related to the following eigenstates and energy eigenvalues

$$\begin{aligned} \Psi_{\text{cov}} &= \frac{1}{\sqrt{2}} (|\uparrow, \downarrow\rangle + |\downarrow, \uparrow\rangle), \quad \epsilon_{\text{cov}} = 0; \\ \Psi_{\text{ion}} &= \frac{1}{\sqrt{2}} (|\uparrow\downarrow, \cdot\rangle - |\cdot, \uparrow\downarrow\rangle), \quad \epsilon_{\text{ion}} = U; \\ \Psi_{\pm} &= \frac{[|\uparrow, \downarrow\rangle - |\downarrow, \uparrow\rangle - \frac{\epsilon_{\pm}}{2t} (|\uparrow\downarrow, \cdot\rangle + |\cdot, \uparrow\downarrow\rangle)]}{\sqrt{2 + \frac{\epsilon_{\pm}^2}{2t^2}}}, \quad \epsilon_{\pm} = \frac{U}{2} \pm \frac{\sqrt{U^2 + 16t^2}}{2}. \end{aligned} \quad (2.17)$$

One should be aware that states with parallel spins are neglected in the basis set since electron hopping is forbidden there. Their eigenenergy would be zero, similar to the covalent states Ψ_{cov} .

Direct exchange

Recalling the eigenstates and eigenenergies (Eq. 2.17) of the model Hamiltonian (Eq. 2.16), one can notice that the lowest energies are achieved for the states with dominant contribution of the ‘‘covalent states’’, $|\uparrow, \downarrow\rangle$ and $|\downarrow, \uparrow\rangle$, especially in the large- U limit. Therefore, let's focus on the covalent states and project out the ionic ones out of the Hamiltonian (Eq.: 2.16) by the partitioning technique. It yields an effective Hamiltonian

$$H_{\text{dir}}(\epsilon) = \begin{pmatrix} -t & -t \\ t & t \end{pmatrix} \begin{pmatrix} \epsilon - U & 0 \\ 0 & \epsilon - U \end{pmatrix}^{-1} \begin{pmatrix} -t & t \\ -t & t \end{pmatrix}, \quad (2.18)$$

where the energy ϵ can be approximate by a characteristic eigenenergy of the covalent states Ψ_{cov} and Ψ_{-} , which is roughly zero. It leads to the occurrence of an effective spin-spin interaction in the effective Hamiltonian, which reads

$$H_{\text{dir}} \approx \frac{2t^2}{U} \begin{pmatrix} -1 & 1 \\ 1 & -1 \end{pmatrix} = \frac{4t^2}{U} \left(\mathbf{S}_1 \cdot \mathbf{S}_2 - \frac{n_1 n_2}{4} \right), \quad (2.19)$$

where \mathbf{S}_i is the spin operator and n_i is the occupation number. The related eigenstates are singlet state Ψ_s and triplet state Ψ_t

$$\begin{aligned}\Psi_s &= \frac{1}{\sqrt{2}} (|\uparrow, \downarrow\rangle - |\downarrow, \uparrow\rangle), & \varepsilon_s &= -\frac{4t^2}{U}, \\ \Psi_t &= \frac{1}{\sqrt{2}} (|\uparrow, \downarrow\rangle + |\downarrow, \uparrow\rangle), & \varepsilon_t &= 0,\end{aligned}\quad (2.20)$$

where the other triple states were excluded due to parallel spins as it has been mentioned. Concerning the effective Hamiltonian, it is obvious that the direct kinetic exchange favors the antiparallel ordering.

Superexchange

Localized orbitals might require an improvement of the previous exchange mechanism since their overlap can be negligible, and therefore the electron hopping is supposed to be unlikely. Although the direct coupling of localized orbitals can be negligible, there might appear an indirect coupling for specific compounds. For instance, considering transition metal oxides, there occurs an indirect coupling of the localized metallic d -states intermediated by oxygen p -states. According to the geometry, one can distinguish the antiferromagnetic and ferromagnetic superexchange.

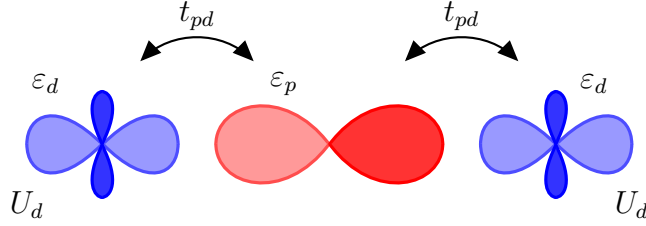


Figure 2.1: Antiferromagnetic superexchange geometry. (Adapted after [19])

- Antiferromagnetic superexchange

Initially, let's consider inline coupling of two d -orbitals mediated by a single p -orbital (Fig. 2.1). Assuming hopping between p - and d -orbitals t_{pd} and the Coulomb repulsion U_d within d -orbitals, while the repulsion is neglected for simplicity at the p -orbital, the Hamiltonian of the model system (Fig. 2.1) in the second quantization reads

$$H = \varepsilon_d \sum_{i\sigma} n_{i\sigma} + \varepsilon_p \sum_{\sigma} n_{p\sigma} - t_{dp} \sum_{i\sigma} (c_{i\sigma}^\dagger c_{p\sigma} + c_{p\sigma}^\dagger c_{i\sigma}) + U_d \sum_i n_{i\uparrow} n_{i\downarrow}, \quad (2.21)$$

where ε_d and ε_p denote the electron energy in the d - resp. p -orbital, and $i = 1, 2$ describes particular d -orbitals. Let's consider an initial state of the system with two p -electrons and a single electron at each d -orbital. Then, one can set $2(\varepsilon_p + \varepsilon_d)$ as the zero-energy level. The Hilbert spaces related to the initial states either with parallel or antiparallel d -electron spin are disjoint. Hence, one can treat them separately. Particular Hilbert spaces can be constructed by acting of the third term in the Hamiltonian (Eq.: 2.21),

describing the electron hopping, on the initial states. Focusing on the initial states and projecting out the rest of the related Hilbert space by the partitioning technique analogously to the Direct exchange, one obtains for parallel d -electron spins ($c_{1\uparrow}^\dagger c_{p\downarrow}^\dagger c_{p\uparrow}^\dagger c_{2\uparrow}^\dagger |0\rangle$) an effective Hamiltonian

$$H_{\text{eff}} = \begin{pmatrix} t_{pd} & t_{pd} \end{pmatrix} \begin{pmatrix} \varepsilon - U_d + \Delta_{pd} & 0 \\ 0 & \varepsilon - U_d + \Delta_{pd} \end{pmatrix} \begin{pmatrix} t_{pd} \\ t_{pd} \end{pmatrix} \approx -\frac{2t_{pd}^2}{U_d + \Delta_{pd}}, \quad (2.22)$$

where $\Delta_{pd} = \varepsilon_d - \varepsilon_p$ denotes a difference of d - and p - energy levels. According to the zero-energy level position, one can assume $\varepsilon = 0$. The same relation (Eq. 2.22) is valid for the state with two spin down d -electron states.

Analogously, one can derive an effective Hamiltonian concerning the antiparallel d -electron spins. The related Hilbert space is quite large, containing nine distinct states. Therefore, for brevity, only the final result is mentioned

$$H_{\text{eff}} \approx -\frac{2t_{pd}^2}{U_d + \Delta_{pd}} \begin{pmatrix} 1 & 0 \\ 0 & 1 \end{pmatrix} - \frac{2t_{pd}^4}{(U_d + \Delta_{pd})^4} \left(\frac{1}{U_d} + \frac{1}{U_d + \Delta_{pd}} \right) \begin{pmatrix} 1 & -1 \\ -1 & 1 \end{pmatrix}. \quad (2.23)$$

The first term is similar to the previous effective Hamiltonian (Eq.: 2.22). However, according to the Direct exchange (Eq. 2.19), the second term, the sign included, represents an effective spin coupling described by a Hamiltonian

$$H_{\text{eff}} = \frac{2t_{pd}^4}{(U_d + \Delta_{pd})^4} \left(\frac{1}{U_d} + \frac{1}{U_d + \Delta_{pd}} \right) \left(\mathbf{S}_1 \cdot \mathbf{S}_2 - \frac{n_1 n_2}{4} \right), \quad (2.24)$$

which shows that an antiparallel spin order is favored as well.

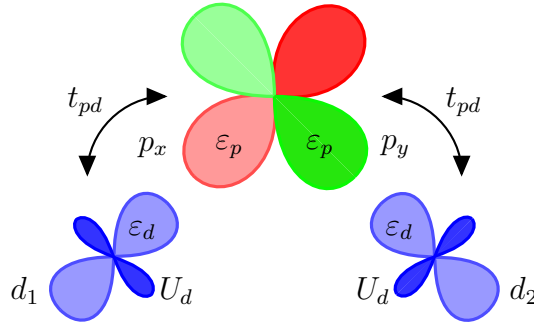


Figure 2.2: Ferromagnetic superexchange geometry. (Adapted after [19])

- Ferromagnetic superexchange

Actually, the character of the spin coupling strongly depends on the assumed geometry. Let's consider a site bearing two p -orbitals, namely p_x and p_y , which form a right-angled bridge between two d -orbitals (Fig. 2.2). According to the right-angled geometry the Slater-Coster integrals allow electron hopping only between d_1 and p_x resp. d_2 and p_y orbitals. Concerning the electron hopping, it gives rise to the occurrence of two separated

electron system. However, the energy depends on the mutual spin orientation. Let's consider two initial states, namely $c_{1\uparrow}^\dagger c_{p_x\downarrow}^\dagger c_{p_x\uparrow}^\dagger c_{p_y\downarrow}^\dagger c_{p_y\uparrow}^\dagger c_{2\uparrow}^\dagger |0\rangle$ and $c_{1\uparrow}^\dagger c_{p_x\downarrow}^\dagger c_{p_x\uparrow}^\dagger c_{p_y\downarrow}^\dagger c_{p_y\uparrow}^\dagger c_{2\downarrow}^\dagger |0\rangle$, which are related to disjoint Hilbert spaces. Similarly to the previous case, only d -orbital on-site repulsion U_d is include. However, the Coulomb exchange between p_x and p_y has to be taken into account. It is described by the the exchange J_{xy} according the Eq. 2.14. Then, for the first state bearing parallel d -spins, a triplet state, the effective Hamiltonian reads

$$H_{\text{eff}} \approx -\frac{2t_{pd}^2}{U_d + \Delta_{pd}} - \left(\frac{2t_{pd}^4}{(U_d + \Delta_{pd})^2} \frac{1}{2(U_d + \Delta_{pd}) - J_{xy}} \right). \quad (2.25)$$

Concerning the set of states related to the second initial state, the antiparallel d -spins effective Hamiltonian follows

$$H_{\text{eff}} \approx -\frac{2t_{pd}^2}{U_d + \Delta_{pd}} - \frac{2t_{pd}^4}{(U_d + \Delta_{pd})^2} \frac{1}{2(U_d + \Delta_{pd}) - J_{xy}} + \frac{4t_{pd}^4}{(U_d + \Delta_{pd})^2} \frac{J_{xy}}{4(U_d + \Delta_{pd})^2 - J_{xy}^2} \begin{pmatrix} 1 & -1 \\ -1 & 1 \end{pmatrix}, \quad (2.26)$$

where the last term describes an extra energy contribution related to the singlet states with respect to the triplet ones. It denotes the singlet-triplet splitting. Then, it is obvious that the 90° superexchange has a ferromagnetic character.

2.1.3 Double exchange

Most commonly it can be ascribe to mixed valence compounds. They possess a non-integer number of electrons per site, therefore the occupations of particular site can differ. It means that an electron might hop between sites without a cost of the extra Coulomb interaction U . Let's consider two sites with two orbital of the type used in the description of the Coulomb exchange (Eq. 2.9). Orbitals φ_a are occupied by one electron per site, however only one of φ_b orbitals is occupied by a single electron, which can hop between φ_b orbitals with the rate t_{bb} . According to the Coulomb exchange, there occurs the exchange coupling J_{ab} , while Coulomb repulsion U_{ab} is set as the zero energy level. Assuming the basis of states with total spin $S_z^{\text{tot}} = \frac{3}{2}$, one obtains eigenstates which couple φ_a orbitals into triplet states

$$\Psi_{\pm}^{\frac{3}{2}} = \frac{1}{\sqrt{2}} (|\uparrow, \uparrow\rangle_1 |\cdot, \uparrow\rangle_2 \pm |\cdot, \uparrow\rangle_1 |\uparrow, \uparrow\rangle_2) = \frac{1}{\sqrt{2}} (|\cdot, \uparrow\rangle_b \pm |\cdot, \uparrow\rangle_b) |\uparrow, \uparrow\rangle_a, \quad (2.27)$$

$$\varepsilon_{\pm}^{\frac{3}{2}} = -J_{ab} \pm t_{bb}. \quad (2.28)$$

Similarly, regarding the total spin $S_z^{tot} = \frac{1}{2}$, the eigenstates acquire a form of equally weighted linear combination of the basis states. It reads

$$\begin{aligned}\Psi_{\pm}^{\frac{1}{2}} &= \frac{1}{\sqrt{6}} (|\uparrow, \uparrow\rangle_1 |\cdot, \downarrow\rangle_2 \pm |\cdot, \uparrow\rangle_1 |\uparrow, \downarrow\rangle_2 \\ &\quad + |\cdot, \uparrow\rangle_1 |\downarrow, \uparrow\rangle_2 \pm |\downarrow, \uparrow\rangle_1 |\cdot, \uparrow\rangle_2 + |\uparrow, \uparrow\rangle_1 |\cdot, \downarrow\rangle_2 \pm |\cdot, \downarrow\rangle_1 |\uparrow, \downarrow\rangle_2) \\ &= \frac{1}{\sqrt{2}} (|\uparrow, \cdot\rangle_b \pm |\cdot, \uparrow\rangle_b) \frac{1}{\sqrt{2}} (|\uparrow, \downarrow\rangle_a + |\downarrow, \uparrow\rangle_a) + \frac{1}{\sqrt{2}} (|\downarrow, \cdot\rangle_b \pm |\cdot, \downarrow\rangle_b) |\uparrow, \uparrow\rangle_a, \\ \varepsilon_{\pm}^{\frac{1}{2}} &= -J_{ab} \pm t_{bb}.\end{aligned}\tag{2.29}$$

$$\tag{2.30}$$

It reveals that the electron hopping in the φ_b orbitals leads to the spin alignment in the orbitals φ_a .

2.1.4 Metallic exchange – Ruderman-Kittel-Kasuya-Yoshida interaction

In metals, so-called Ruderman-Kittel-Kasuya-Yoshida (RKKY) interaction occurs. It stands for an indirect exchange mediated by the electron gas. It represents a second-order scattering process. Simply speaking, an electron is scattered by a moment to an intermediate state initially. Afterward, another scattering by a different moment causes a return from the intermediate state.

In the RKKY framework, the exchange interaction between two localized spin moments is effectively mediated by virtual particle-hole excitations in the Fermi sea, which arise from the electrons' interaction with a spin moment. The excitations change the electron gas's polarization modifying its dielectric properties.

The RKKY interaction can be formally derived in terms of the Kubo response theory. Let's consider an interaction Hamiltonian H_{int} between conduction electrons and spin moment, which reads

$$H_{int} = -A \sum_i \mathbf{s}_i(\mathbf{r}_i) \cdot \mathbf{S}_\alpha(\mathbf{R}_\alpha) \delta(\mathbf{r}_i - \mathbf{R}_\alpha) \tag{2.31}$$

$$= g\mu_B \sum_i \mathbf{H}_{\text{eff}}(\mathbf{r}_i) \cdot \mathbf{s}_i(\mathbf{r}_i),$$

$$\mathbf{H}_{\text{eff}}(\mathbf{r}) = -\frac{A}{g\mu_B} \mathbf{S}_\alpha(\mathbf{R}_\alpha) \delta(\mathbf{r} - \mathbf{R}_\alpha), \tag{2.32}$$

where A is a scaling parameter, s_i and \mathbf{r}_i are conduction electrons' spin and position. Analogously \mathbf{R}_α describes the position of a spin \mathbf{S}_α . \mathbf{H}_{eff} represents the effective molecular field acting on the conduction electrons' spins. Then, one can evaluate the electron gas magnetization $m(\mathbf{r})$ introduced by the effective molecular field \mathbf{H}_{eff} through the electron gas susceptibility χ_0 . Let's $\mathbf{R}_\alpha = 0$ for brevity, then

$$\mathbf{m}(\mathbf{r}) = \int \chi_0(\mathbf{r} - \mathbf{r}') \mathbf{H}_{\text{eff}}(\mathbf{r}') d\mathbf{r}' = -\frac{A}{g\mu_B} \chi_0(\mathbf{r}) \mathbf{S}_\alpha. \tag{2.33}$$

Let's suppose another localized spin $\mathbf{S}_\beta(\mathbf{R}_\beta)$, where $\mathbf{R}_\beta = \mathbf{r}$. Then, according to Eq. 2.31, it interacts with the electron gas magnetization, which is related to

an induced spin density $\mathbf{s}(\mathbf{r})$, as follows

$$H_{\alpha\beta} = \frac{A}{g\mu_B} \mathbf{m}(\mathbf{r}) \mathbf{S}_\beta(\mathbf{r}), \quad (2.34)$$

$$\mathbf{m}(\mathbf{r}) = -g\mu_B \mathbf{s}(\mathbf{r}). \quad (2.35)$$

Finally, one obtains the RKKY interaction Hamiltonian proportional to the susceptibility of the electron gas

$$H_{\text{RKKY}} = -\frac{A^2}{g^2\mu_B^2} \frac{1}{(2\pi)^3} \int \chi_0(\mathbf{q}) e^{-i\mathbf{q}\mathbf{r}} d\mathbf{q} \mathbf{S}_\alpha(0) \cdot \mathbf{S}_\beta(\mathbf{r}). \quad (2.36)$$

The noninteracting electron gas susceptibility in the atomic units reads

$$\chi_0(\mathbf{q}, \omega) = \frac{2}{(2\pi)^3} \sum_{n,n'} \int \frac{f(\varepsilon_{n,\mathbf{k}+\mathbf{q}}) - f(\varepsilon_{n',\mathbf{k}})}{\varepsilon_{n',\mathbf{k}+\mathbf{q}} - \varepsilon_{n,\mathbf{k}+\mathbf{q}} - (\omega + i\eta)} d\mathbf{k}, \quad (2.37)$$

where n, n' denotes energy band indices and ε is the related energy. The integration is performed in the first Brillouin zone, $f(\varepsilon_{n,\mathbf{k}})$ stands for the Fermi-Dirac distribution and ω is the frequency. A small quantity ($\eta \rightarrow 0$) is related to the analytical continuation. Assuming the static limit, one obtains the real static susceptibility

$$\chi_0(\mathbf{q}, 0) = \frac{2}{(2\pi)^3} \sum_{n,n'} p.v. \int \frac{f(\varepsilon_{n,\mathbf{k}+\mathbf{q}}) - f(\varepsilon_{n',\mathbf{k}})}{\varepsilon_{n',\mathbf{k}+\mathbf{q}} - \varepsilon_{n,\mathbf{k}+\mathbf{q}}} d\mathbf{k}. \quad (2.38)$$

One should be aware of the properties of the electron gas susceptibility in the real space. In the case of the 3D electron gas the static susceptibility reads

$$\chi_0(\mathbf{q}, 0) = -\frac{mk_F}{(2\pi)^3} F\left(\frac{2k_F}{q}\right), \quad (2.39)$$

$$F(x) = 1 - \frac{1-x^2}{2x} \ln\left|\frac{x+1}{x-1}\right|, \quad (2.40)$$

where m is the electron mass and k_F denotes the Fermi wave vector. Performing the inverse Fourier transformation, one obtains an oscillation function in the real space

$$\chi_0(\mathbf{r}, 0) = \frac{m}{(2\pi)^3} \frac{(2k_F r) \cos(2k_F r) - \sin(2k_F r)}{r^4}. \quad (2.41)$$

The amplitude of the oscillations decays as (r^{-3}) – so-called Friedel oscillation (Fig. 2.3). It is obvious that the character of the RKKY-interaction depends on the mutual distance of the localized spins.

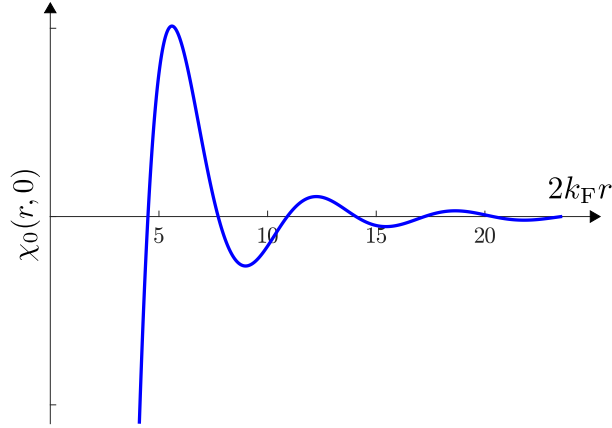


Figure 2.3: Friedel oscillations

2.1.5 Magnetic anisotropy

To explain the existence of the hard and easy magnetic axes, which are essential for much practical application, one has to introduce the anisotropic interactions. They bring about the magnetic anisotropy energy, an orientation-dependent energy contribution, giving rise to the favored magnetization direction.

One can distinguish two origins of the magnetic anisotropy. The first one is the dipole magnetic interaction (Eq. 2.7) of the local magnetization density $\mathbf{m}(\mathbf{r})$.

Shape anisotropy

Let's evaluate the dipolar field \mathbf{H}_{dip} acting on a certain magnetic moment μ_i . One can consider the Lorentz decomposition method dividing a sample to a spherical cavity around the moment μ_i and the rest part. In the cavity, microscopic moments are considered. Otherwise, a continuous distribution of the macroscopic magnetization $M(\mathbf{r})$ is assumed. Then, the magnetic pseudo-charge density $\rho_M(\mathbf{r})$ can be defined

$$\rho_M(\mathbf{r}) = -\nabla \cdot M(\mathbf{r}). \quad (2.42)$$

Considering a uniform magnetization M , magnetic pseudo-charges exist only at boundaries. The dipole field due to dipoles in the cavity and magnetic pseudo-charge at the Lorentz cavity boundary rapidly converges and slightly contributes to the magnetocrystalline anisotropy discussed later. The most important in the sense of the shape anisotropy is the demagnetizing field \mathbf{H}_d caused by pseudo-charges at the surface. The related magnetic energy contribution reads

$$U_{sh} = -\frac{1}{2} \int \mathbf{M} \cdot \mathbf{H}_d. \quad (2.43)$$

Concerning the bulk the demagnetizing field \mathbf{H}_d is described by a demagnetizing tensor D as follows

$$\mathbf{H}_d = -\mathbf{D} \cdot \mathbf{M}. \quad (2.44)$$

On the other hand, concerning thin films the surface shape anisotropy energy follows a simple relation

$$E = \frac{1}{2} \mu_0 M \cos^2 \theta, \quad (2.45)$$

where θ denotes the angle to the plane normal.

Magnetocrystalline anisotropy

The second origin of the magnetic anisotropy bears in the SO interaction (Eq. 1.18). According to the crystal field theory, the angular momentum \mathbf{L} in a crystal field is being quenched, in general. The crystal field potential is real, which means that pure real eigenstates can be found. Since the angular momentum operator is imaginary, it leads to its zero expectation values. Hence, only spin magnetic moments remains. The SO interaction partly removes the quenching of the angular momentum, nevertheless the effect is tiny since the SO coupling ξ (Eq. 1.19) is generally much smaller than the bandwidth. Thus, higher order perturbation theory is used. Considering the second order, for an unknown spin state the magnetic anisotropy obeys a relation

$$H_{\text{MCA}}^{(2)} = |\xi|^2 \sum_n \frac{\langle 0|L_\mu|n\rangle\langle n|L_\nu|0\rangle}{E_0 - E_n} S_{\mu\nu} = -S_\mu \Lambda_{\mu\nu} S_\nu. \quad (2.46)$$

where μ, ν denotes Cartesian components and $\Lambda_{\mu\nu}$ stands for a general 3×3 real symmetric tensor \mathbf{R} . Rotating Λ into principal axis, one obtains the anisotropy constants K

$$\Lambda_{\mu\mu} = K_\mu \delta_{\mu\mu}. \quad (2.47)$$

Concerning frequent cubic symmetry, using of the 4th order perturbation theory is needed.

2.2 Magnetic exchange interactions

In this paragraph, a general form of magnetic exchange interactions is described, while Refs. [19, 20] are followed. Considering various exchange mechanisms, the spin-spin exchange interactions up to the second-order can be described by a Hamiltonian, which obeys relation

$$H = \sum_i K(\mathbf{S}_i) - \sum_{i \neq j} \mathbf{S}_i \mathbb{J}_{ij} \mathbf{S}_j. \quad (2.48)$$

The first term stands for the on-site anisotropy energy and the second one describes inter-site magnetic exchange interactions represented by a bilinear form with 3×3 matrices \mathbb{J}_{ij} . One can decomposed the inter-site exchange interactions' bilinear form into three distinct contributions as follows

$$\mathbb{J}_{ij} = J_{ij} \mathbb{I} + \mathbb{J}_{ij}^{\text{A}} + \mathbb{J}_{ij}^{\text{S}}, \quad (2.49)$$

$$J_{ij} = \frac{1}{3} \text{Tr} \mathbb{J}_{ij}, \quad (2.50)$$

$$\mathbb{J}_{ij}^{\text{A}} = \frac{1}{2} (\mathbb{J}_{ij} - \mathbb{J}_{ij}^{\text{T}}), \quad (2.51)$$

$$\mathbb{J}_{ij}^{\text{S}} = \frac{1}{2} (\mathbb{J}_{ij} + \mathbb{J}_{ij}^{\text{T}}) - J_{ij} \mathbb{I}, \quad (2.52)$$

where \mathbb{I} is the unity matrix and \mathbb{J}^{T} denotes the transpose of the of \mathbb{J}_{ij} . The first contribution represents the isotropic Heisenberg exchange interactions J_{ij} . The second one describes the antisymmetric or Dzyaloshinskii-Moriya interaction (DMI) $\mathbb{J}_{ij}^{\text{A}}$ and the last one stands for the anisotropic exchange $\mathbb{J}_{ij}^{\text{S}}$ being

a trace less symmetric part of the \mathbb{J}_{ij} . Defining the Dzyaloshinskii-Moriya vector $D_{ij}^x = \epsilon_{xyz} J_{ij}^{Axy}$, where the ϵ_{xyz} stands for the Levi-Civita symbol, the general Hamiltonian (Eq. 2.48) reads

$$H = \sum_i K(\mathbf{S}_i) - \sum_{i \neq j} J_{ij} \mathbf{S}_i \cdot \mathbf{S}_j - \sum_{i \neq j} \mathbf{D}_{ij} (\mathbf{S}_i \times \mathbf{S}_j) - \sum_{i \neq j} \mathbf{S}_i \mathbb{J}_{ij}^S \mathbf{S}_j. \quad (2.53)$$

Concerning this work, one deals with the Heisenberg exchange interactions J_{ij} . They stand for the most essential interactions as they represent the energy leading term with the most considerable energy contribution. They are responsible for the parallel or antiparallel spin ordering considering the collinear magnetic structure, or they might give arise to noncollinear spin spiral structures. According to the form of the Hamiltonian (Eq.: 2.53) and concerning a simple structure, the parallel spin alignment is related to the positive values of the Heisenberg exchange interactions J_{ij} and *vice versa*. Mostly, the absolute values of the J_{ij} decay exponentially with the distance. However, it depends on the considered system. Concerning the metals, exchange interactions' oscillations might occur thanks to the RKKY-interaction.

The presence of the DMI strongly depends on the crystal symmetry. Namely, it vanishes in the case of high symmetry structures containing the inversion symmetry. However, it naturally occurs at interfaces and surfaces. DMI exists only between two distinct atoms without mirror or inversion symmetry. The SO interaction's presence brings it about, and the DMI's magnitude is of the first-order in the SO interaction. DMI gives rise to the noncollinear chiral magnetic structures or weak ferromagnetism as a net magnetization in the antiferromagnets.

2.3 Ab-initio calculation of magnetic exchange interactions

The knowledge of the magnetic exchange interactions is essential in the description of the magnetic atoms' interplay or the evaluation of magnetic ordering temperatures. Generally, there exist two approaches to reckon the Heisenberg exchange interactions J_{ij} (Eq. 2.53) discussed in this work. Both of them are able to describe chemical disorder, which is important to treat magnetic doping [21, 22]. The first one is called the frozen magnon approach. It relies on calculations of the total energy of spin spiral structures described by the spin vector q , in the reciprocal space [23]. The generalized Bloch theorem allows a direct evaluation of the total energies $E(q)$ [24]. The second approach is based on the Liechtenstein formula [22, 25, 26]. It evaluates the exchange interactions J_{ij} in the real space according to energy changes related to a constrained rotation of the spin polarization axis. In the present work, the last approach is adopted. It allows direct calculating of the exchange interactions concerning particular constituents, including their types and positions, which is suitable e.g. for nontrivial layer structures.

2.3.1 Real-space method, Liechtenstein formula

In the real-space approach, the description of exchange interactions arises from the multiple scattering theory. Initially, let's assume the effective Heisenberg Hamiltonian [22]

$$H = - \sum_{i \neq j} J_{ij} \mathbf{e}_i \cdot \mathbf{e}_j, \quad (2.54)$$

where \mathbf{e}_i denotes a unit vector pointing along the direction of the spin moment \mathbf{S}_i (Eq. 2.53). The exchange interactions J_{ij} include the local moments' $\mathbf{S}_{i,j}$ magnitudes. The adiabatic approximation is considered there. It allows one to neglect the magnetization's precession caused by spin waves in calculations of related energy changes. It means that the magnetization's precession is much slower than the electron motion, namely, the electron hopping. It says that spin-wave energy is small with respect to the band width and the exchange splitting [7, 22, 23]. It is valid for long-wavelength magnons, which are mostly a scope of thermodynamic calculations.

According to the effective Heisenberg Hamiltonian (Eq. 2.54), the exchange interactions are related to a rotation of the local moments spin-polarization axis. Therefore, the energy change associated to local moment deviations is calculated. Considering infinitesimal deviations, the magnetic force theorem can be applied [25, 27]. It states that the energy change is related to the change of the one-particle energies. Assuming the first order perturbation of the spin and charge density the energy variation δE reads

$$\begin{aligned} \delta E &= -\delta \left(\sum_i \varepsilon_i \right) \\ &= \iint \frac{n(\mathbf{r})n(\mathbf{r}')}{|\mathbf{r} - \mathbf{r}'|} d\mathbf{r} d\mathbf{r}' + \text{Tr} \left(\hat{\rho} \delta \hat{V}_{\text{exc}} \right), \end{aligned} \quad (2.55)$$

where ε_i denotes the one-electron energies, ρ is the density matrix and \hat{V}_{exc} stands for the xc-potential operator. Considering the multiple scattering approach [25, 28], the energy variation δE obeys a relation

$$\delta E = \frac{1}{\pi} \int^{E_F} d\varepsilon \text{Im Tr} \ln \left[1 - \left(1 + \delta \hat{t}_i^{-1} \hat{T}^{ii} \right)^{-1} \delta \hat{t}_i^{-1} \hat{T}^{ij} \left(1 + \delta \hat{t}_j^{-1} \hat{T}^{jj} \right)^{-1} \right], \quad (2.56)$$

where \hat{T} is the scattering path operator and \hat{t} denotes single site scattering matrix. Indices i and j denote the spin moment sites. Using the second order perturbation in the deviation angle and spin polarization along the z -axis, the exchange interactions J_{ij} reads [25]

$$\begin{aligned} J_{ij} &\simeq \frac{1}{4\pi} \int^{E_F} d\varepsilon \text{Im Tr}_L \left[\Delta_i \hat{T}_{\uparrow}^{ij} \Delta_j \hat{T}_{\downarrow}^{ji} \right], \\ \Delta_i &= \delta \hat{t}_{i,\uparrow}^{-1} - \delta \hat{t}_{i,\downarrow}^{-1}. \end{aligned} \quad (2.57)$$

Finally in terms of the TB-LMTO-ASA method the exchange interactions J_{ij} reads [23, 26]

$$\begin{aligned} J_{ij} &\simeq \frac{1}{4\pi} \text{Im} \int_{E_F}^{E_B} \text{Tr}_L \left[\Delta_i (E + i0) g_{ij}^{\uparrow} (E + i0) \Delta_j (E + i0) g_{ji}^{\downarrow} (E + i0) \right] dE, \\ \Delta_i(z) &= P_i^{\uparrow}(z) - P_i^{\downarrow}(z), \end{aligned} \quad (2.58)$$

where, according to the TB-LMTO-ASA formalism (Eq. 1.4), $g_{ij}^\sigma(z) = g_{\mathbf{R}L, \mathbf{R}'L'}^\sigma(z)$ denotes the spin-resolved auxiliary Green's function (Eq. 1.38) and $P_i^\sigma(z) = P_{\mathbf{R}L}^\sigma(z)$ stands for the potential function. The energy integration is performed along a contour in the upper part of the complex plane involving the occupied part of the valence band, where E_B denotes the bottom of the valence band.

According to the vertex cancellation theorem [29], one is able to directly extend the last formula to disorder systems in the framework of the CPA [22, 23]. It yields

$$J_{ij}^{\alpha\beta} = \frac{1}{4\pi} \text{Im} \int_{E_F}^{E_B} \text{Tr}_L \left[\Delta_i^\alpha(z) \bar{g}_{ij}^{\alpha\beta, \uparrow}(z) \Delta_j^\beta(z) \bar{g}_{ji}^{\beta\alpha, \downarrow}(z) \right] dz, \quad (2.59)$$

where $\bar{g}_{ij}^{\alpha\beta\sigma}$ denotes the conditionally averaged spin polarized auxiliary Green's functions (Eq. 1.53). Besides, it is possible to evaluate directly the on-site average pair exchange interactions J_i^0 defined as follows [22]

$$J_i^{0,\alpha} = \sum_j J_{ij}^{\alpha\beta} c_j^\beta, \quad (2.60)$$

where c_j^β denotes concentration of the element β at the site j . Considering the multiple scattering approach, the exchange interactions J_i^0 in the framework of the TB-LMTO-ASA method reads [21, 22]

$$J_i^{0,\alpha} = -\frac{1}{4\pi} \text{Im} \int_{E_F}^{E_B} \text{Tr}_L \left\{ \Delta_i^\alpha(z) \left[\bar{g}_{ii}^{\alpha, \uparrow}(z) - \bar{g}_{ii}^{\alpha, \downarrow}(z) \right] + \left[\Delta_i^\alpha(z) \bar{g}_{ii}^{\alpha, \uparrow}(z) \Delta_i^\alpha(z) \bar{g}_{ii}^{\alpha, \downarrow}(z) \right] \right\} dz. \quad (2.61)$$

3. Magnetic Ordering

In this chapter, a brief overview of the magnetic materials' types and their characteristic behavior are mentioned. It includes a fundamental division of magnetic materials as well as fundamental approaches describing magnetic ordering. Refs. [10, 22, 30] are mostly followed here.

Let's introduce basic physical quantities describing magnetic properties initially.

Magnetization

Magnetization M denotes a density of the magnetic moment in the studied system. It stands for an important quantity in the description of magnetic ordering as it belongs among the ordering parameters by means of the Landau theory of phase transitions. Assuming a system in presence of the magnetic field H , the magnetization obeys a relation

$$M_\mu(H) = -\frac{1}{V} \frac{\partial E_0(H)}{\partial H_\mu}, \quad (3.1)$$

where V denotes the volume of the system, $E_0(H)$ is the magnetic field dependent ground-state energy, and μ describes a vector component. In the case of a system in thermal equilibrium, the temperature-dependent magnetization can be expressed by means of the Helmholtz free energy F

$$M(H, T) = -\frac{1}{V} \left(\frac{\partial F}{\partial H} \right)_T, \quad (3.2)$$

$$F = -k_B T \ln \left(\sum_n e^{-E_n(H)/k_B T} \right) = -\frac{1}{\beta} \ln \left(\sum_n e^{-\beta E_n(H)} \right), \quad (3.3)$$

where k_B denotes the Boltzmann constant, T is the thermodynamic temperature and $E_n(H)$ stands for the energies of excited states.

[10]

Magnetic susceptibility

Magnetic susceptibility describes the response of a system to the magnetic field. It is defined by the change of the magnetization as follows

$$\chi_{\mu\nu} = \frac{\partial M_\mu}{\partial H_\nu} = -\frac{1}{V} \left(\frac{\partial^2 F}{\partial H_\mu \partial H_\nu} \right)_T, \quad (3.4)$$

where μ, ν denote Cartesian coordinates. According to the Kubo linear response theory, the magnetic susceptibility tensor $\chi_{\xi\zeta}^{(ij)}$ reads

$$\chi_{\mu\nu}^{(ij)} = \frac{i}{\hbar} \Theta(t - t_0) \left\langle \left[\hat{S}_\mu^{(i)}(t), \hat{S}_\nu^{(j)}(t_0) \right] \right\rangle, \quad (3.5)$$

where $\hat{S}_\mu^{(i)}$ stands for the μ component of the spin operator at the site i . It means, that the susceptibility is related to spin-spin correlations of a quantum-mechanical system.

[10, 13, 31, 32]

3.1 Magnetic materials

According to the interaction of magnetic materials with the external magnetic field and the magnetic order character, one can distinguish several types of magnetic behavior. Special magnetic behavior as the super-paramagnetism occurring in nano-particles is neglected.

3.1.1 Diamagnetics

Diamagnetism is related to the effort of a matter to repel the external magnetic field by changes in its electronic structure. They lead to the induction of the opposite magnetic field to the external one repelling the matter from it. It can be described as a screening of the external magnetic field by a motion of the electron charge, which represents an electric current inducing a magnetic field counteracting the external one. Diamagnetism is present in all kinds of material. However, being relatively weak, it is overcome by other effects if they are present. In the case when diamagnetism is the sole contribution, we are talking about diamagnetics. It includes metals like copper, silver, selenium, bismuth, or most of the organic compound. Diamagnetics bear a negative magnetic susceptibility, and their relative magnetic permeability is less than one.

Considering closed shell atoms, the angular \mathbf{L} and spin \mathbf{S} magnetic moments vanish. Hence the total magnetic moment \mathbf{J} is zero as well. Assuming a spherically symmetric atoms, the so-called Langevin diamagnetic susceptibility reads

$$\chi_{\text{Langevin}} = -\frac{e^2 N}{6mcV} \langle r^2 \rangle, \quad (3.6)$$

where N is number of electron of the mass m , V denoted the volume and $\langle r^2 \rangle$ stands for the quantum-mechanical mean square value of the electron radii.

In the case of metals, one describes the diamagnetism by the Landau susceptibility which is based on the behavior of the Fermi electron gas. The susceptibility reads

$$\chi_{\text{Landau}} = -\frac{\mu_{\text{B}}^2}{3} g(E_{\text{F}}), \quad (3.7)$$

where $g(E_{\text{F}})$ denotes the density of states at the Fermi level. [10]

3.1.2 Paramagnetics

Paramagnetism represents the opposite behavior in the previous case. It is related to the attraction of a matter to the external magnetic field and the induction of the internal magnetic field in the external one's direction. Therefore, paramagnetic susceptibility as well as the magnetic permeability of paramagnetic materials are greater than the one.

Free electron paramagnetism – Pauli paramagnetism

Pauli paramagnetism arises from an extra spin dependent energy contribution $\pm\mu_{\text{B}}H$ in presence of the external field H . In the absence of the external field, the occupation of both electron gas spin channels is same ($g_{\uparrow\downarrow}(E) = \frac{1}{2}g(E)$). Applying the external field, the states with the opposite spin to the external

field are shift to higher energies acquiring an extra energy contribution $\mu_B H$ and *vice versa*, while a collinear spin polarization along the external field direction is concerned. Since $\mu_B \sigma H$ is small with respect to the Fermi energy E_F , it yields

$$g_{\uparrow\downarrow}(E) = \frac{1}{2}g(E \pm \mu_B H) \approx \frac{1}{2}g(E) \pm \frac{1}{2}\mu_B H \frac{\partial g(E)}{\partial E}. \quad (3.8)$$

Then, recalling that the magnetization M is proportional to the difference of the spin channels' occupations $n_{\uparrow\downarrow}$

$$M = \mu_B(n_{\uparrow} - n_{\downarrow}) = \mu_B \left(\int g_{\uparrow}(E)f(E)dE - \int g_{\downarrow}(E)f(E)dE \right), \quad (3.9)$$

where $f(E)$ denotes the Fermi-Dirac distribution, the conduction electrons' susceptibility χ_{Pauli} at the zero temperature $T = 0$ reads

$$\chi_{\text{Pauli}} = \frac{\partial M}{\partial H} = \frac{\partial}{\partial H} \left(-\mu_B^2 H \int g(E) \left(\frac{\partial f(E)}{\partial E} \right) dE \right) = \mu_B^2 g(E_F). \quad (3.10)$$

Temperature corrections are quite negligible being of order $\left(\frac{k_B T}{E_F}\right)^2$. [10]

Bound electrons paramagnetism – Curie Law

Also net magnetic moments can exhibit paramagnetic behavior. Let's consider the lowest-lying spin multiplet. Since the zero-field ground state is degenerated for a nonzero total magnetic moments \mathbf{J} , one has to calculate the susceptibility by the statistical mechanics. Thermodynamic behavior is described by the Helmholtz free energy F calculated over the $(2J + 1)$ lowest lying states, where J is the total momentum quantum number. Assuming the spin polarization along the z -axis, it follows

$$e^{-\beta F} = \sum_n e^{-\beta E_n(H)} = \sum_{J_z=-J}^J e^{-\beta g_J \mu_B J_z H}, \quad (3.11)$$

where the total magnetic moment $\mu_{J,z} = -g_J \mu_B J_z$ (Eq. 2.6) is used. It stands for a simple summation of a geometric series (Eq. 3.11). According to the Eq. 3.2, the magnetization of the studied system reads

$$M = -\frac{N}{V} \frac{\partial F}{\partial H} = \frac{N}{V} g_J \mu_B J B_J(\beta g_J \mu_B J H), \quad (3.12)$$

where the function $B_J(x)$ is the so-called Brillouin function defined as follows

$$B_J(x) = \frac{2J+1}{2J} \coth\left(\frac{2J+1}{2J}x\right) - \frac{1}{2J} \coth\left(\frac{1}{2J}x\right). \quad (3.13)$$

Assuming small fields and high temperatures, actually ($g_J \mu_B H \ll k_B T$), one can expand the Brillouin function around zero, which yields the magnetic susceptibility

$$\chi = \frac{C}{T} = \frac{N}{V} \frac{g^2 \mu_B^2}{3} \frac{J(J+1)}{k_B T}. \quad (3.14)$$

The last equation (Eq. 3.14) is called the Curie's law, describing paramagnetic behavior of a system containing permanent magnetic moments. [10]

3.1.3 Magnetically ordered materials

There occur materials, called magnetically ordered, possessing a non-vanishing mean vector of magnetic moments below a certain critical temperature. According to the existence of the macroscopic magnetization density, one can distinguish ferromagnetic (FM) materials, where the individual magnetic moments merge into non-zero so-called spontaneous magnetization, antiferromagnetic (AFM) ones missing the spontaneous magnetization as the magnetic moments cancel each other out, and ferrimagnetic ones, representing an uncompensated AFM case, simply put. Usually, the ferromagnets stand only for materials possessing magnetic moments aligned along a particular direction, as in this work. Then ferrimagnetic materials are introduced. They contain antiparallel alignment of magnetic moments while they bear non-vanishing spontaneous magnetization. The simplest magnetic structure is the FM one consisting of magnetic moments of the same direction and the same magnitude. However, various types of magnetic ordering occur, including complicated FM, AFM, or ferrimagnetic structures, namely helical structures or spin density waves. Concerning metals, the magnetic ordering is described by means of the spin density $\mathbf{m}(\mathbf{r})$ along an appropriate direction $\hat{\mathbf{e}}_z$ (Eq. 1.27). In the case of the ferromagnets and ferrimagnets, there exist a direction, where $\int \mathbf{m}(\mathbf{r})d\mathbf{r}$ is non-zero. However, for antiferromagnets, the integral vanishes for any direction [10, 30].

Assuming individual spins at Bravais lattice sites \mathbf{R}_i , it is possible to describe their low lying excitations by the Heisenberg Hamiltonian

$$H_{ex} = - \sum_{ij} J_{ij}(\mathbf{R}_i - \mathbf{R}_j) \mathbf{S}(\mathbf{R}_i) \cdot \mathbf{S}(\mathbf{R}_j) - g\mu_B \sum_i \mathbf{S}(\mathbf{R}_i) \cdot \mathbf{H}, \quad (3.15)$$

where $\mathbf{S}(\mathbf{R}_i)$ denotes the vector spin operator, J_{ij} stands for the magnetic pair exchange interactions and \mathbf{H} is the external magnetic field [10, 30].

Mean Field Approximation

The simplest way to analyze the behavior and magnetic phase transition of a system described by the Heisenberg Hamiltonian (Eq. 3.15) is represented by the mean-field approximation (MFA). Although it fails in describing the critical region as the description is quantitatively incorrect, it stands for a starting point suitable for a brief overview of the system behavior. Critical exponents obtained by the MFA differ from experimental values. The MFA completely neglects spin correlation, which leads to overestimated critical temperatures. Finally, the MFA is valid only in the high-temperature limit [10, 22, 30].

The heart of the MFA is replacing the many-body problem (Eq. 3.15) by a one-body system in presence of an effective field originating from the remaining particles. The effective ‘‘Weiss’’ field $\mathbf{H}_i^{\text{eff}}$ is determined as follows

$$\mathbf{H}_i^{\text{eff}} = \frac{1}{g\mu_B} \sum_j J_{ij} \mathbf{S}(\mathbf{R}_j) + \mathbf{H}, \quad (3.16)$$

which stands for an operator with a complex dependence on the actual spin configuration. Thus, it is replaced by its thermodynamic mean value. It yields the appropriate MFA Hamiltonian [10, 30]

$$H = -g\mu_B \sum_i \mathbf{S}(\mathbf{R}_i) \cdot \langle \mathbf{H}_i^{\text{eff}} \rangle = - \sum_{ij} J_{ij} \mathbf{S}(\mathbf{R}_i) \langle \mathbf{S}(\mathbf{R}_j) \rangle - g\mu_B \sum_i \mathbf{S}(\mathbf{R}_i) \cdot \mathbf{H}. \quad (3.17)$$

Considering ferromagnets, each spin has the same mean value, which can be expressed by means of the magnetization \mathbf{M}

$$\langle \mathbf{S} \rangle = \frac{V}{N} \frac{M}{g\mu_B}. \quad (3.18)$$

Then the effective ‘‘Weiss’’ field reads

$$\mathbf{H}^{\text{eff}} = \mathbf{H} + \frac{J^0}{(g\mu_B)^2}, \quad (3.19)$$

where J^0 denotes the on-site average pair exchange interactions (Eq. 2.60). Employing the Eq. 3.12, one obtains the MFA critical temperature

$$T_C^{\text{MFA}} = \frac{J(J+1)}{3k_B} J^0, \quad (3.20)$$

where J is the total momentum quantum number. Considering the effective Heisenberg Hamiltonian (Eq. 2.54), the MFA critical temperature acquires a simple form

$$k_B T_C^{\text{MFA}} = \frac{2}{3} J^0. \quad (3.21)$$

[10, 22, 30]

4. Topological Insulators

Overview

Topological insulators (TI) represent a remarkable kind of solids, possessing unique physical behavior. It emerges from their unusual band structure regarding their topologically protected metallic surface states. In the present chapter, a brief introduction to the field of topological matter and TIs is provided. Initially, the topology in the solids is introduced. Then, basic concepts describing the topological matter are mentioned. The last part is dedicated to 3D TIs, which are studied in the present work. Regarding this chapter, one follows mostly Refs. [19, 33, 34].

4.1 Topological matter

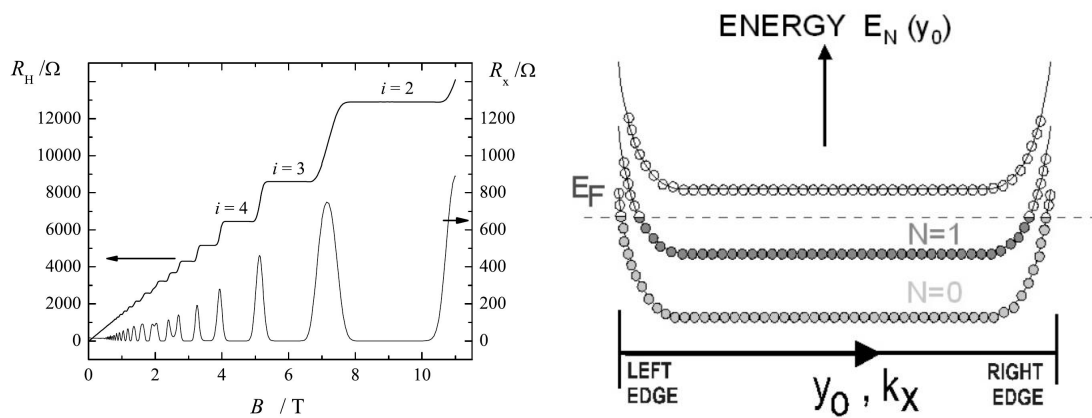
Inclusion of the topological description stands for a milestone in the characterization of solids concerning their classification, physical states, or physical properties, which brings about a new perspective to experiments as well as to the theoretical description [33, 35]. Exceptional physical properties of topological matter arise from a complex nontrivial topology either in the momentum- or real-space. It includes the topology of the band structure or the topology of real structures as magnetic structures are [19, 33]. In the present work, one deals with materials possessing a nontrivial band structure. The real space topology concerning e.g. skyrmions being vertices in magnetic structures is out of the scope. Unlike common phases of matter, topological phases are described by non-local ordering parameters describing the system's global character and its stability [19]. Each topological phase is characterized by the so-called topological invariant, which represents quantities robust against smooth system's modification similarly to the topology of the system. In general, the topology invariance arises, and it is protected by certain symmetries, where one of the most important is the time-reversal symmetry (TRS) or the inversion symmetry [33, 36]. The topological description not only does provide a new approach to known physical phenomena but also leads to the discovery of new physical phenomena with a strong application potential [19, 33, 37].

4.1.1 Integer Quantum Hall Effect

The birth of the topological band theory can be ascribed to attempts to describe the quantum Hall effect (QHE) regarding its integer form, which had been discovered a couple of decades ago (Klitzing, Dorda, and Peper; 1988 [38]). For brevity, we would call it simply QHE. It was observed that the Hall resistance ϱ_{xy} of the 2D electron gas (2DEG) exhibits a discrete quantization in units of the inverse quantum conductance $G_0 = e^2/\hbar$ as follows [39]

$$\varrho_{xy} = \frac{1}{n} \frac{\hbar}{e^2}, \quad (4.1)$$

where n is an integer, and e denotes the elemental charge. Besides, the constant Hall resistance ϱ_{xy} is associated with the vanishing longitudinal resistance ϱ_{xx} (Fig. 4.1a).



(a) DC measurement of the longitudinal resistance and Hall resistance in GaAs heterostructures. (adapted from [40]) (b) Ideal Landau levels for a device with boundaries. (adapted from [39])

Figure 4.1: Quantum Hall effect.

Traditionally, the observed behavior can be explained by a simple model of the free electrons' cyclotron motion in the homogeneous magnetic field. Assuming non-relativistic electrons, one can describe the electrons by a harmonic-oscillator like Hamiltonian providing k independent energy levels, so-called Landau levels

$$\varepsilon_n = \hbar\omega_c \left(n + \frac{1}{2} \right), \quad (4.2)$$

where ω_c stands for the cyclotron frequency. Nonetheless, close to boundaries, the electron motion is restricted and the electrons bouncing along the interface. It can be described by an additional potential, which bends the Landau levels in the interface's vicinity (Fig. 4.1b). One finds that for the increasing chemical potential, a larger number of dispersive edge channels are obtained. Recalling the group velocity

$$v_{n,k_x} = \frac{dE_n}{dk_x}, \quad (4.3)$$

one can observe that a set of channels with the same velocity direction at a certain edge is obtained. [39, 40]

4.1.2 Thouless–Kohmoto–Nightingale–den Nijs theory

Closely after the QHE discovery a link between the quantized Hall conductivity σ_{xy} and the topology of the related band structure were introduced by the Thouless–Kohmoto–Nightingale–den Nijs (TKNN) theory [41]. It reformulates the Kubo formula for the conductivity by means of band structure topological properties. The conductivity of a non-interacting system with a respect to an external uniform field $\mathcal{E}e^{-i\omega t}$ reads [8, 19, 42]

$$\sigma_{\mu\nu}(\omega) = -\frac{ie^2\hbar}{a} \sum_{nn'} \frac{f(E_{n'}) - f(E_n)}{E_{n'} - E_n} \frac{\langle n' | \hat{v}_\mu | n \rangle \langle n | \hat{v}_\nu | n' \rangle}{\hbar\omega - i\eta + E_{n'} - E_n}, \quad (4.4)$$

where μ, ν stands for real coordinates, a is the system area, $f(E)$ denotes the Fermi-Dirac distribution and \hat{v}_μ is the μ -projection of the velocity operator

$$\hat{v}_\mu = \frac{1}{i\hbar} (\hat{x}_\mu \hat{H} - \hat{H} \hat{x}_\mu). \quad (4.5)$$

Considering a direct current (DC) conductivity at the zero temperature, one obtains a simple formula for the Hall conductivity σ_{xy} [19]

$$\sigma_{xy} = -\frac{ie^2\hbar}{a} \sum_{\substack{E_{n'} < E_F, \\ E_n > E_F}} \frac{\langle n' | \hat{v}_x | n \rangle \langle n | \hat{v}_y | n' \rangle - \langle n' | \hat{v}_y | n \rangle \langle n | \hat{v}_x | n' \rangle}{(E_{n'} - E_n)^2}. \quad (4.6)$$

Transforming the coordinate operator \hat{x} into the k -space and employing the periodic boundary conditions, it yields [19, 33, 34]

$$\sigma_{xy} = -\frac{ie^2}{\hbar} \int_{\text{BZ}} \frac{dk_x dk_y}{2\pi} \sum_{E_n < E_F} \left[\langle \partial_{k_x} n | \partial_{k_y} n \rangle - \langle \partial_{k_y} n | \partial_{k_x} n \rangle \right], \quad (4.7)$$

which shows that the conductivity is related to the character of the band structure in the k -space.

4.1.3 Berry phase, connection and curvature

The matrix elements (Eq. 4.7) contain an effective vector potential in the momentum space, the so-called Berry connection A_k . Considering the Berry connection of the all occupied bands defined as follows [19]

$$A_{\mathbf{k}}^{(\mu)} = -i \sum_{E_n < E_F} \langle n | \partial_{k_\mu} | n \rangle, \quad (4.8)$$

the conductivity (Eq. 4.7) reads [19, 34]

$$\sigma_{xy}(\omega) = \frac{e^2}{\hbar} \int_{\text{BZ}} \frac{dk_x dk_y}{2\pi} (\partial_{k_x} A_{\mathbf{k}}^{(y)} - \partial_{k_y} A_{\mathbf{k}}^{(x)}) = \frac{e^2}{\hbar} \int_{\text{BZ}} \frac{dk_x dk_y}{2\pi} (\nabla_{\mathbf{k}} \times \mathbf{A}_{\mathbf{k}})_z \quad (4.9)$$

$$\mathbf{\Omega} = (\nabla_{\mathbf{k}} \times \mathbf{A}_{\mathbf{k}}). \quad (4.10)$$

The curl of the Berry connection is called Berry curvature $\mathbf{\Omega}$ (Eq.4.10). It stands for an effective magnetic field originating from the band structure topology, which acts on the electron states. Both quantities \mathbf{A} and $\mathbf{\Omega}$, are related to the geometrical (Berry) phase γ , which occurs in systems depending of external parameters.

Let's consider a system described by a time independent Hamiltonian depending on a parameter λ

$$H(\lambda)|n\lambda\rangle = E_n(\lambda)|n\lambda\rangle, \quad (4.11)$$

$$|\varphi(t)\rangle = e^{-i\theta(t)}|n\lambda(t)\rangle, \quad (4.12)$$

where the phase θ gives rise to the time evolution of the wave function $|\varphi(t)\rangle$ [19, 34]. Assuming the adiabatic approximation considering well-separated and slowly varying states and employing the time dependent SE (Eq. 1.1), one finds that the time dependent phase $\theta(t)$ obeys a relation [19]

$$\theta(t) = \frac{1}{\hbar} \int_0^t E_n \lambda(t') dt' - i \int_0^t \langle n\lambda(t') | \partial_{t'} | n\lambda(t') \rangle dt', \quad (4.13)$$

where the first term denotes the common dynamical phase whereas the second one represents the Berry phase γ .

To demonstrate the integer quantization of the QHE, let's assume a square BZ. It can be easily map on a torus, which allows one to divide the BZ into two closed areas with a common boundary C . Since Berry connections along C can differ only by a gradient of the phase $A_{\mathbf{k}}^1 - A_{\mathbf{k}}^2 = \nabla_{\mathbf{k}}\theta$, the Hall conductivity follows a relation [19, 34]

$$\sigma_{xy} = \frac{e^2}{\hbar} \frac{1}{2\pi} \left(\oint_C A_{\mathbf{k}}^1 \cdot d\mathbf{k} - \oint_C A_{\mathbf{k}}^2 \cdot d\mathbf{k} \right) = \frac{e^2}{\hbar} \frac{1}{2\pi} \oint_C \nabla_{\mathbf{k}}\theta \cdot d\mathbf{k} = \frac{e^2}{\hbar} n, \quad (4.14)$$

where one uses the Stoke's theorem in the Eq. 4.9 and where the winding number n is an integer for a uniquely defined wave function.

We recall that the bulk states cannot contribute to the conductivity in the case of the Fermi level E_F lying in between the 2DEG Landau levels (Fig. 4.1b). Hence, the Hall conductivity relies on the states at the sample edges. However, one should be aware that the evaluation of the edge conductivity (Eq. 4.14) is based on the bulk band structure. The relation between the edge properties and the bulk band structure is called the bulk-boundary correspondence [19, 33, 34].

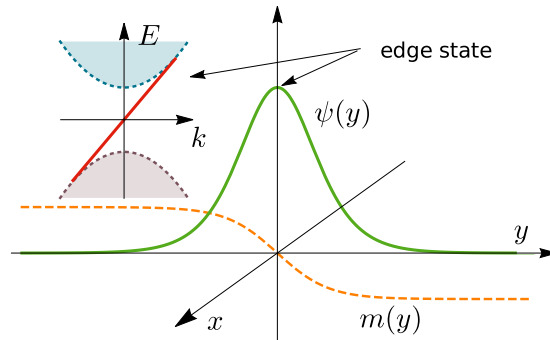


Figure 4.2: Chern insulator edge state. Orange dashed curve depicts the particle mass distribution, green curve is the related wave function of the edge state. The inset depicts the model band structure with a red edge state. (adapted after [19, 43])

4.2 Edge states

A model of the so-called Chern insulator describes the QHE occurrence without the external field presence (quantum anomalous Hall effect – QAHE). In 1988, Haldane [44] described a honeycomb model of the graphene with the broken TRS introduced by the QAHE arising from a nontrivial band structure.

A Hamiltonian of a simple Chern insulator in 2D can be written as follows

$$H = \hbar v (\sigma_x k_x + \sigma_y k_y) + m \sigma_z, \quad (4.15)$$

where v denotes the particle velocity, σ_i stands for Pauli matrices and m is the mass of particles [19]. One should note that for $m = 0$, the Eq. 4.15 describes mass-less “Dirac fermions” with a linear band dispersion, They are represented *e.g.* by Dirac cones occurring at the K and K' reciprocal points in the graphene [45–47].

Considering an arbitrary m and a basis of the helicity matrix

$$\boldsymbol{\sigma} \cdot \mathbf{u}, \quad \begin{cases} \boldsymbol{\sigma} &= (\sigma_x, \sigma_y, \sigma_z) \\ \mathbf{u} &= \frac{(\hbar v k_x, \hbar v k_y, m)}{|(\hbar v k_x, \hbar v k_y, m)|} \end{cases}, \quad (4.16)$$

the Eq. 4.15 has corresponding eigenvalues [19]

$$\varepsilon_{\mathbf{k}s} = s \sqrt{(\hbar v)^2 \mathbf{k}^2 + m^2}, \quad (4.17)$$

where $s \pm 1$ denotes the conduction resp. valence bulk bands. In order to describe the edge states, let's write the Dirac equation (Eq. 4.15) in the real space

$$[-i\hbar v (\sigma_x \partial_x + \sigma_y \partial_y) + m \sigma_z] \psi(x, y) = E \psi(x, y) \quad (4.18)$$

and consider an interface at $y = 0$ between two systems describes by Eq. 4.15 but with different signs of the m . These two systems possess mutually inverted bulk band structures and represent different states of the Chern insulator [43, 44].

The localized edge states can be found though mapping the present problem (Eq. 4.18) with the varying mass term $m \equiv m(y)$ to the Jackiw-Rebbi 1D edge models [48]. It leads to localized modes at the edge $y = 0$. The obtained modes decay in bulk, whilst they propagate along the edge as a plane wave. Considering a mass distribution $m(y < 0) > 0$ and $m(y > 0) < 0$, where naturally it is set $m(0) = 0$, one obtains a single physical solution (Fig. 4.2) [19, 48]

$$\psi(x, y) = \exp(i k_x x) \exp\left(+\frac{1}{\hbar v} \int_0^y m(y') dy'\right) |\chi_+\rangle. \quad (4.19)$$

Whereas, in the case of the opposite mass distribution the solution reads

$$\psi(x, y) = \exp(i k_x x) \exp\left(-\frac{1}{\hbar v} \int_0^y m(y') dy'\right) |\chi_-\rangle, \quad (4.20)$$

where $|\chi_{\pm}\rangle$ denotes eigenstates of the spin operator σ_x , ($\sigma_x |\chi_{\pm}\rangle = \pm |\chi_{\pm}\rangle$). Assuming $m(y)$ described by a step-like function ($m(y) = \pm \text{sgn}(y) m$), it yields the decay length λ of the edge mode ψ as follows [19]

$$\psi = e^{i k_x x} e^{y/\lambda} |\chi\rangle; \quad \lambda = \frac{\hbar v}{|m|}. \quad (4.21)$$

Regardless of the form of $m(y)$ the edge-state spectrum reads [19]

$$\varepsilon(k) = s \hbar v k, \quad (4.22)$$

where s_{\pm} denotes eigenvalues of the operator σ_x . Unlike the bulk band structure, the edge states are gapless and they span the bulk gap (Fig. 4.2). Thanks to the non-vanishing mass term, the TRS is broken and the edge states are chiral. Only a single edge state moving in a given direction occurs. According to the edge-state spectrum, the appropriate group velocity follows a relation

$$v_g = s \hbar v. \quad (4.23)$$

[19, 43, 49]

4.3 Topological phase transition

In topological matters, one can observe so-called topological transitions related to modifications of the system topology. It was mentioned that topological phases, *e.g.* differing by the topology of the band structure, are classified by topological invariants. They distinguish topological phases between each other and denote whether the phase is topologically nontrivial or not. Regarding the introduced Chern insulators, one deals with the topological Chern invariant [19, 33] defined as follows

$$C = \frac{1}{2\pi} \int_{BZ} \mathbf{\Omega} d^2\mathbf{k}, \quad (4.24)$$

which occurs in the TKNN formula (Eq. 4.9) and where $\mathbf{\Omega}$ denotes the Berry curvature (Eq. 4.10).

To introduce a simple model of a topological transition, let's consider a thin slab represented by the top and bottom 2D electronic systems in xy -direction, which are similar to the introduced one in the previous section and separated by an insulating spacer. Reducing the spacer's thickness, one obtains a quasi 2D system effectively, with overlapping top and bottom surface states. The coupling between the surfaces is described by a parameter Δ . Thus, one can construct the Hamiltonian as follows [19]

$$H = \begin{pmatrix} -i\hbar v (\sigma_x \partial_x + \sigma_y \partial_y) + m\sigma_z & \Delta \sigma_0 \\ \Delta \sigma_0 & +i\hbar v (\sigma_x \partial_x + \sigma_y \partial_y) + m\sigma_z \end{pmatrix}, \quad (4.25)$$

where σ_0 denote a unit matrix. Different signs in the diagonal elements are related to the inversion symmetry between the surfaces. Particularly, it reflects the swapping of the z axis. The Hamiltonian's form (Eq. 4.25) satisfies the fermion doubling principle [50] stating that Dirac fermions in the lattice crystals structures occurs in pairs. Related wave functions are described by bispinors composed of the top and bottom surface spinors. The Hamiltonian (Eq. 4.25) can be mapped to the Chern insulator's Hamiltonian (Eq. 4.15) by an unitary transformation. The transformed Hamiltonian is block diagonal being composed of two Chern insulators with different mass terms [19]

$$H_0 = \begin{pmatrix} -i\hbar v (\sigma_x \partial_x + \sigma_y \partial_y) + (m + \Delta) \sigma_z & 0 \\ 0 & +i\hbar v (\sigma_x \partial_x + \sigma_y \partial_y) + (m - \Delta) \sigma_z \end{pmatrix}. \quad (4.26)$$

Considering of the helicity matrix eigenstates (Eq. 4.16) and employing the formula of the Chern number (Eq. 4.24) together with the TKNN formula of the edge conductivity (Eqs. 4.9 and 4.8), one can find that the Chern number C and the Hall conductivity σ_{xy} follow relations [19]

$$C = -\frac{1}{2} (\text{sgn}(m + \Delta) + \text{sgn}(m - \Delta)) , \quad (4.27)$$

$$\sigma_{xy} = \frac{e^2}{\hbar} C . \quad (4.28)$$

It is obvious, one obtains three different topological phases classified by the Chern numbers $C = \{-1, 0, +1\}$ which are related to distinct Hall conductivity. One should note that the case $m = \Delta$ violates the fermion doubling principle. It is evident that the nonzero Hall conductivity depends on the ratio m/Δ . It describes the state of the TRS breaking, which is needed to give rise the QAHE. In the case of a small m with respect to the coupling Δ , the Hall conductivity vanish [19].

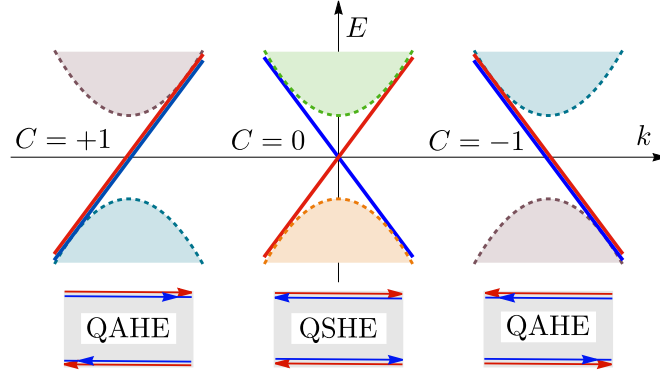


Figure 4.3: Quasi 2D-model edge spectra. (adapted after [19])

To depict the difference between these topological phases, one can evaluate the edge state spectra (Eq. 4.22). Edge states similar to the states at the interface of two systems with mutual inverted band structure can be obtained for a vacuum interface [19]. Considering a boundary along the x -axis ($y = 0$) with the vacuum in the positive semi-space, the eigenvalues s of the spin operator σ_x (Eq. 4.22) can be assign to the sign of the mass term m (Eq. 4.18) ($\sigma_x|\chi\rangle = \text{sgn}(m)|\chi\rangle$). Thus, in the present case the edge spectrum follows a relation [19]

$$\varepsilon_{\pm}(k) = \text{sgn}(m \pm k)\hbar vk , \quad (4.29)$$

and one can distinguish several cases:

$ m > \Delta \quad (\text{QAHE})$ $\varepsilon_{\pm}(k) = +\hbar vk, C = -1, \begin{matrix} m > 0, \Delta > 0 \\ m > 0, \Delta < 0 \end{matrix}$ $\varepsilon_{\pm}(k) = -\hbar vk, C = +1, \begin{matrix} m < 0, \Delta > 0 \\ m < 0, \Delta < 0 \end{matrix}$	$ m < \Delta \quad (\text{QSHE})$ $\varepsilon_{\pm}(k) = \pm\hbar vk, C = 0$, (4.30)
--	--	----------

where QSHE denotes the quantum spin Hall effect. The topological transition between the QAHE and the QSHE is located at $m = \Delta$. Regardless of the

topological phase, there occur two edge modes at each surface. However, the phases differ in the mutual orientation of the edge modes (Fig. 4.3). In the case of the QAHE, both edge modes move within the same direction (chiral states), whereas in the other case, they have opposite directions (helical states). Therefore, the Hall conductivity is zero concerning the QSHE. The model presented in this section represents a simple model of 2D topological insulators [19, 33].

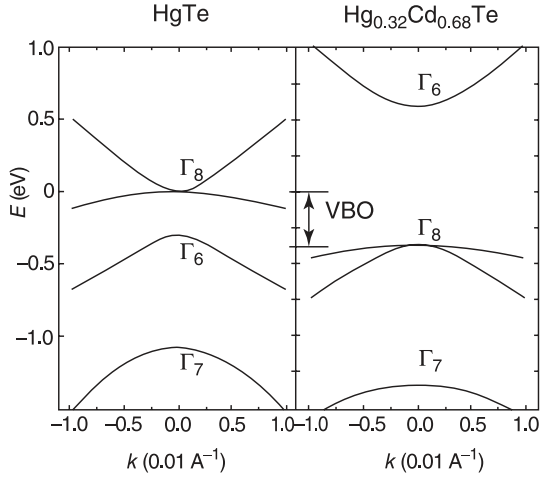


Figure 4.4: HgTe and $\text{Hg}_{0.32}\text{Cd}_{0.68}\text{Te}$ band structures obtained by the Kane-Mele model. (adapted from [33])

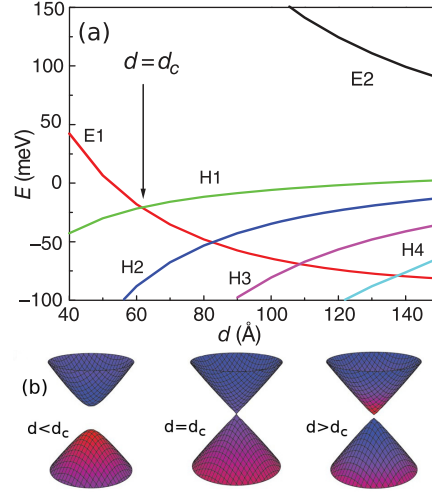


Figure 4.5: HgTe topological phase transition. (a) Electron-(E) and hole-(H) subbands as a function of the quantum well thickness. (b) Dispersion relations of E1 and H1 subbands. (adapted from [33, 51])

4.4 2D Quantum spin Hall topological insulators

Although the mentioned quantum Hall effect (Sec. 4.1.1) represents the first discovered topological state of the matter, the topological band theory's boom is related to the coming of quantum spin Hall topological insulators. Let's call them for brevity 2D topological insulators. They launched a strong development of the solid-state topological theory, which led to new proposed topologically non-trivial compounds. Also, a huge experimental effort was made. The origin of the topologically nontrivial states is discussed there by the Bernevig–Hughes–Zhang (BHZ) model [51]. It proposes an occurrence of the topological surface states, protected against weak perturbation, unlike common surface states [45], in materials possessing strong spin-orbit coupling (SOC) and the inverted band gap. The BHZ model represents a generalization of the Kane-Mele model [49, 51, 52]. It considers the honeycomb lattice and describes the occurrence of the QSHE in systems following the TRS and bearing strong SOC. The SOC represents a key ingredient of TIs. It keeps the inverted bulk band structure gapped, and it allows the QSHE without breaking the TRS, since the SOC brings about a new effective mass term, allowing new topological states of an insulating system with unbroken TRS [19, 49, 51–55]. In the Section 4.2, the Dirac edge states' formation at the interface between two topologically different materials with mutually inverted bands was shown through the simple model Hamiltonian (Eq. 4.15). The band

inversion and the related change of the topology are possible only by the level crossing, which is accompanied by the emergence of metallic in-gap states at the interface. Considering a material with an inverted band order, the origin of the topological surface states at the vacuum interface can be explained similarly, since the vacuum can be regarded as an effective matter with a normal band order possessing the infinite band gap [56]. Let's introduce the essence of the BHZ theory, which is a prediction of the topological phase transition and the occurrence of the QSHE in HgTe quantum well by a band inversion. HgTe stands for a suitable compound to observe the QSHE. It bears strong SOC thanks to relatively heavy Hg atoms and possesses an inverted band structure, which is the central feature. Its Γ_8 band has higher energy than the Γ_6 band (Fig. 4.4). Replacing Hg by Cd, the normal band order structure can be restored. Thus, placing HgTe in between CdTe slabs, a quantum phase transition is able to be demonstrated by changing the HgTe well thickness (Fig. 4.5). Depending on the quantum confinement, the quantum well is either in the normal regime for a small its small width, where CdTe is predominant, or in the inverted regime for the width above a critical value [33, 51, 53], which was experimentally verified [57] (Fig. 4.6).

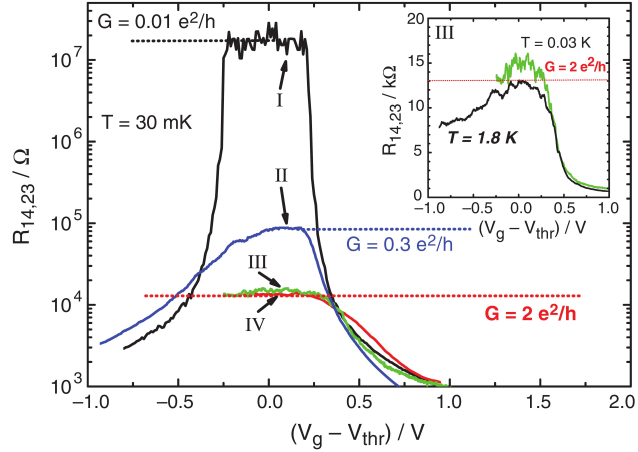


Figure 4.6: Experimental evidence of QSHE in HgTe quantum well. (I) normal regime, (II–IV) inverted regime. (adapted from [57])

Similar to the Chern insulators, where the topology is classified by the Chern invariant (Eq. 4.24), one needs to identify the nontrivial topology of surface states in the case of TIs. The robustness of the surface states is protected by certain symmetries, which includes TRS, crystal symmetries, or their combinations. Concerning the BHZ model of 2D TIs, the TRS symmetry is essential. Assuming the spin 1/2, it is described by the time-reversal operator Θ [19, 33]

$$\Theta = -i\sigma_y K, \quad (4.31)$$

where σ_y is a Pauli matrix, and K denotes the complex conjugate operator. The operator notation is neglected for brevity. The TRS inverts the momentum and the spin. Therefore, regarding systems respecting the TRS, their Hamiltonian H commutes with Θ

$$[H, \Theta] = 0, \quad (4.32)$$

and the energy bands occur in pairs, so-called Kramer's pairs [45]

$$\Theta H(\mathbf{k}, \uparrow) \Theta^{-1} = H(-\mathbf{k}, \downarrow). \quad (4.33)$$

Thus, the Kramer's pairs become degenerate at time-reversal invariant momenta (TRIM) points Γ_i in the BZ following a relation [33]

$$\Gamma \equiv -\Gamma(\text{mod } \mathbf{G}), \quad (4.34)$$

where \mathbf{G} stands for the reciprocal lattice vector. It leads to an unavoidable crossing of the surface states at the TRIM points [33, 49, 58]. Due to the SOC presence, the degeneracy of Kramer's pairs is lifted out of TRIM points. The topology of surface states can be classified by the number of times the Fermi surface intersects the surface states between two TRIM points (Fig. 4.7). One distinguishes two cases. An even number of intersections indicates a topologically trivial surface structure. The gapless states are vulnerable as a continuous transformation can remove them. On the other hand, an odd number denotes robust topologically nontrivial surface states, which are protected by the TRS [33].

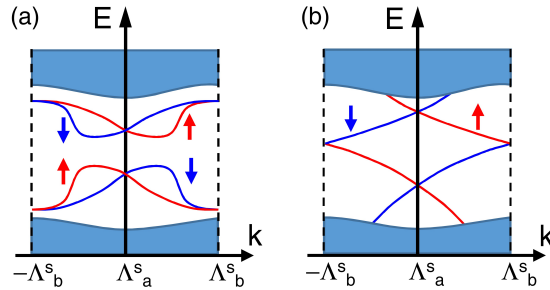


Figure 4.7: Schematic surface states. Λ points stands for the TRIM points. (a) Topologically trivial and (b) topologically nontrivial case. (adapted from [58])

The gapless helical surface states bear extraordinary transport properties. Not only is the QSHE observed in 2D TIs, but also a suppression of the electron backscattering occurs. The chiral surface states cannot be backscattered there due to the TRS presence. Let's consider a backscattering of a forward-moving spin-up electron by a nonmagnetic impurity (unbreak TRS). In general, there are two types of scattering paths – clockwise and anticlockwise turn around the impurity whilst the spin direction is being changed (Fig. 4.8). According to the SOC, only the opposite spins can move backward. Therefore, the spin has to rotate adiabatically during the scattering around the impurity. The clockwise and anticlockwise spin rotations differ by 2π . It means that the related wave functions differ by the phase factor of -1 and their interference is destructive [59]. However, in reality, the experiments show that the ballistic transport is limited by the length of the edge channels. Regarding longer ones, the theoretical conductivity $G = \frac{2e^2}{h}$ is being reduced and several scattering mechanisms have been proposed [60–62].

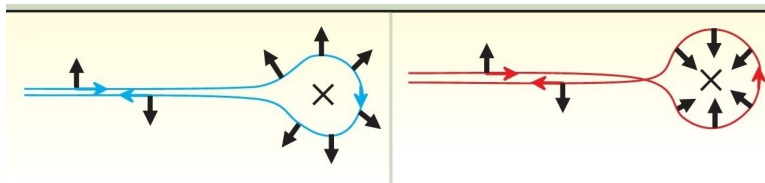


Figure 4.8: Edge scattering. Destructive interference of the backscattered electrons. (adapted from [63])

The mentioned backscattering suppression is related to the so-called weak anti-localization (WAL), a physical feature characteristic for TIs. Let's start with a common topologically trivial material and the weak localization (WL) (Fig. 4.9). The natural presence of disorder leads to the electron motion's scattering. Considering a weak disorder, the electron motion obeys the so-called quantum diffusive regime. The conductivity is related to the probability of the motion from the source to the drain, assuming all possible scattering paths. Unlike the Boltzmann transport, the coherent superposition of the scattered wave functions is taken into account. The interference of the scattered electrons is relevant for closed electron paths. Assuming 2D transport, there exist two sorts of these electron loops. One is the propagation of an electron pair in the same sense around a closed path. In the other case, the electrons propagate in the opposite directions around the close loop representing the time-reversal counterpart (Fig. 4.10). The constructive interference of both cases contributes to the backscattering. Applying a weak perpendicular magnetic field, the WL is suppressed due to the TRS breaking. The WAL occurs in presence of the SOC. Moving an electron adiabatically around the Fermi surface of TIs, the electron acquires π Berry phase for a closed path. It is related to 2π rotation of the spin, and it yields destructive interference and suppression of the backscattering. Unlike the WL, the applied magnetic field enhances the backscattering. [64–67]

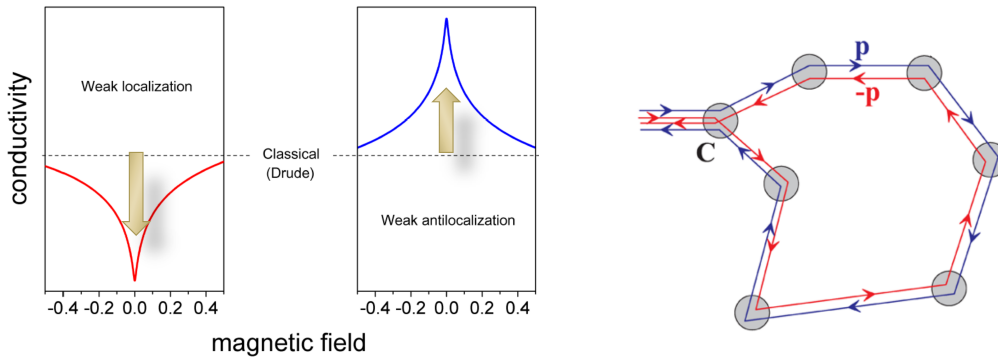


Figure 4.9: Weak (anti-)localization magnetoconductivity sketch. (adapted from [68]) Figure 4.10: Clockwise – counterclockwise trajectory giving a backscattering contribution. (adapted from [69])

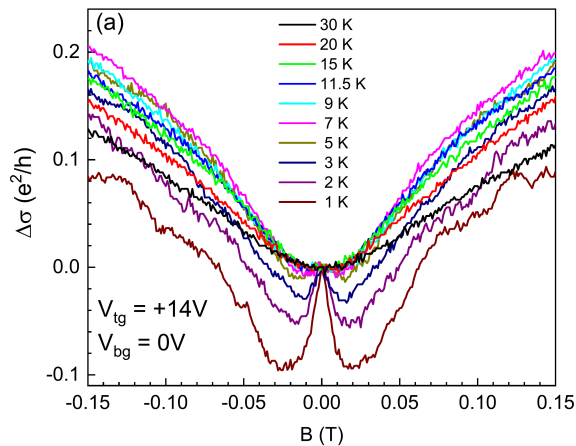


Figure 4.11: Temperature-induced WAL/WL crossover in a disordered InAs/GaSb double quantum well. (adapted from [58])

4.5 3D topological insulators

Great progress in the field of TIs was made by a discovery of the topologically nontrivial phase in 3D insulators [70]. Unlike the 2D TIs where topological states are obtained at edges of buried quantum well, the nontrivial surface states occur in 3D TIs also at the bare surface. It makes the experiments more feasible. It allows not only charge transport measurements but also *e.g.* the photoemission spectroscopy, which probes the band structure and provides information about optical or transport properties. Besides, doping or interfacing of the 3D TIs can lead to a realization of magnetic or superconductive behavior [19, 33]. Finally, the 3D TIs paved the way to discovering new topologically distinct materials, namely topological crystal insulators (TCI), topological Kondo insulators, or Dirac and Weyl semimetals [35, 45, 59, 71–73].

The topological state of 3D TIs is topologically distinct from the 2D analogs since 3D TIs do not represent a simple generalization of the 2D case. In general, it is not possible to compose them of multiple adiabatically connected 2D quantum spin Hall topological insulators (QSH TI) [33, 45]. Let's introduce the appropriate topological invariant. In both cases, 2D QSH TIs as well as 3D TIs, one deals with the so-called \mathbb{Z}_2 invariant [49, 74–76]. One should be aware that the 3D TIs protected by the TRS are taken into account since the TRS is needed to define the \mathbb{Z}_2 invariant. In the 2D case, it is only a binary quantity ν resolving the topologically trivial ($\nu = 0$) and nontrivial ($\nu = 1$) states. Whereas, in the 3D case, the situation is more complicated as so-called strong and weak TIs are distinguished, and the \mathbb{Z}_2 invariant acquires a vector form being composed of one so-called strong topological index and three weak indices.

4.5.1 \mathbb{Z}_2 invariant

In the following abstract model, one shows that the topological properties, including the occurrence of the spin-polarized surface (edge) states, can be derived from the bulk band structure properties similar to the Chern insulators (Eq. 4.14). Initially, let's consider a bulk insulating ribbon and assume that electron wave functions have a form of the Bloch waves in the y direction, whereas they are represented by Wannier states localized at lattice sites in the x direction (Fig. 4.12). Since bulk is insulating, a Wannier state's spin can be transferred without adding the energy by an adiabatic change of the Hamiltonian only if there exist spin-polarized edge states. To avoid the charge movement, one interchanges the opposite spins between the edges. The realization by a thought experiment is sketched in the Fig. 4.13, where the Wannier states moving through the ribbon's 1D BZ is depicted. The k -points $k_y = n\pi/a$, where n is an integer and a is the y -direction lattice constant, stands for TRIM points, where the spin states have to become degenerate. If a spin states switch its spin partner between the TRIM points, the spin-polarized Wannier states move toward the particular edge according to their spin, which leads to uncompensated spin edge states (Fig. 4.13). The mentioned process can be realized adiabatically by moving the spins along a hollow cylinder with the circumference of the y lattice parameter, which follows the periodicity of the ribbon (Fig. 4.12). Besides, an adjustable field pointing in the x -direction is applied. A change of the one magnetic flux quantum is related to the 2π phase

shift, which modified the k_y vector by the required value of $2\pi/a$. The 2π phase shift does not change the electronic band structure, and the process is adiabatic since the energy of the 2D states is not influenced by the field parallel to the ribbon plane. For an insulating bulk, the transfer is impossible without edge states switching of the spin partner, which represents a topological property related to the connectivity. In 2D, the switching of the spin partners is simply related to the nontrivial topology ($\nu = 1$). References [19, 74, 77] have been followed.

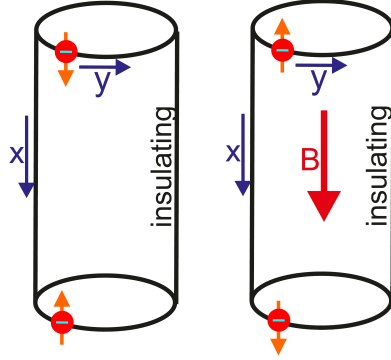


Figure 4.12: Transfer of the Wannier states along an insulating cylinder. (adapted from [19])

The presence of the spin partner switching originates from bulk properties. Switching from the Wannier states to Bloch waves in both direction, the variation of k_y between 0 and π/a etc. stands for a transition between states represented by two line segments in the 2D BZ (Fig. 4.13). To describe the partner switching, one needs to describe the partner configuration at the particular segment. It is possible by evaluating the so-called time reversal polarization (TRP) $\pi = \pm 1$ [75, 76]. Thus, if the TRP π varies between these segments the Wannier states change the partner. Moreover, the TRP is express only by properties at TRIM points by means of the product of quantities $\delta(\mathbf{\Gamma}_i)$ [19, 59, 77]

$$\delta_i = \frac{\sqrt{\det[w(\mathbf{\Gamma}_i)]}}{\text{Pf}[w(\mathbf{\Gamma}_i)]} = \pm 1, \quad (4.35)$$

$$w_{ij}(\mathbf{k}) = \langle u_i(-\mathbf{k}) | \Theta | u_j(\mathbf{k}) \rangle, \quad (4.36)$$

where $\text{Pf}[w]$ denotes the Pfaffian of a unitary matrix w , $|u(\mathbf{k})\rangle$ is a Bloch state and Θ stands for the time-reversal operator (Eq. 4.31).

Simply, it yields that if the product of $\delta(\mathbf{\Gamma}_i)$ at the all four irreducible TRIM points in the 2D BZ is negative, the Wannier states switch the spin partner, which indicates a topologically non-trivial state ($\nu = 1$) [59, 77]

$$(-1)^{\nu_{2D}} = \prod_{i=1}^4 \delta_i. \quad (4.37)$$

The TRP and $\delta(\mathbf{\Gamma}_i)$ depend solely on the bulk properties. They depends on the properties of the occupied bands and they do not change till the E_F reach another band [19, 75, 77].

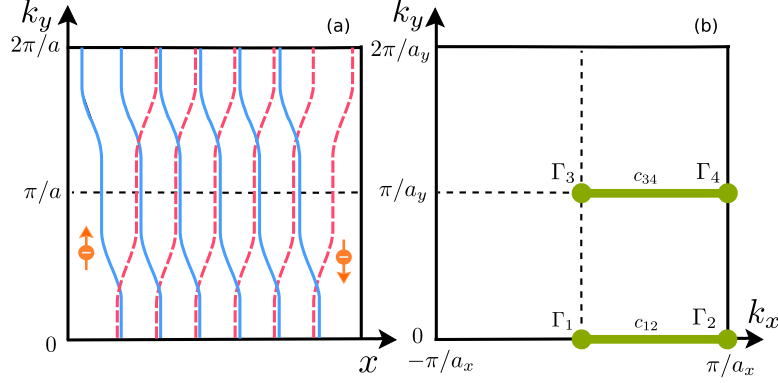


Figure 4.13: Switching of the spin partner. (a) Sketch of the spin resolved paths of the Wannier states. (b) 2D Brillouin zone, where Γ_i stand for TRIM points. c_{ij} denotes line segments where the time reversed polarization is evaluated. (adapted after [19, 77])

Assuming a rectangular lattice for brevity, one can extend the formulation of the \mathbb{Z}_2 invariant to 3D. It was shown that the edge states occur if the TRP given by the projection of $\delta(\Gamma_i)$ to the edge changes its sign (Fig. 4.13). Regarding the 3D case, such projection represents a cut-out plane of the surface, and the edge states become a part of the surface. One has to deal effectively with all the possible cut-offs giving the surface states. Therefore, it is needed to evaluate the TRS at all the line segments perpendicular to the surface, which stands for the projections of $\delta(\Gamma_i)$ at the bulk TRIM points to the selected surface (Fig. 4.14)

$$(-1)^{\nu_0} = \prod_{i=1}^8 \delta_i. \quad (4.38)$$

If the TRS product is negative (one different sign in Fig. 4.14c), the surface states occur on any surface since the TRS change between all possible line segments, which were defined for the edge states. Such topological phase is called a strong TI (STI) ($\nu_0 = 1$) (Fig 4.14). In the other case, there exists a plane where the projections of $\delta(\Gamma_i)$ lead to the same signs of the TRS. It means that in this plane, there absent the topologically protected surface states, and one talks about weak TI (WTI) ($\nu_0 = 0$). One describes the plane by weak indices ν_i denoting the surface plane normal (Fig 4.14)

$$(-1)^{\nu_{k=1,2,3}} = \prod_{n_j \neq k=0,1;n_k=1} \delta_{i=(n_1 n_2 n_3)}. \quad (4.39)$$

If both the strong as well as weak indices are zero, no topologically protected states occur in the material. References [19, 74–76] have been followed.

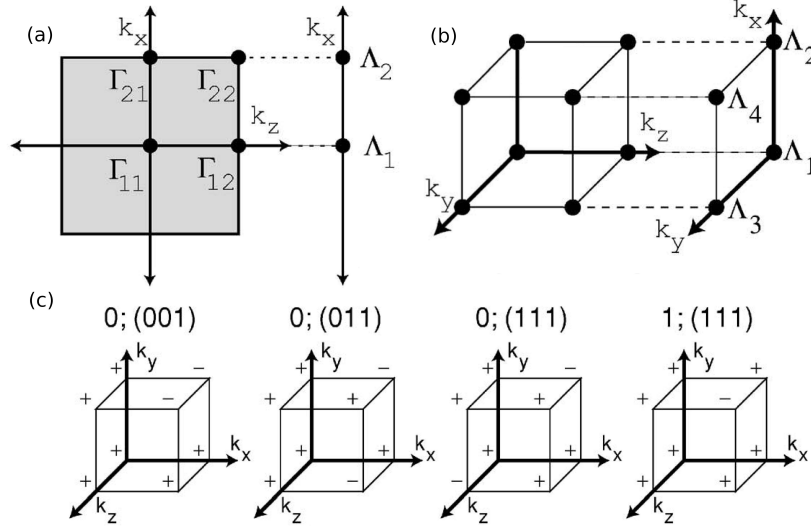


Figure 4.14: Time reversal polarization - projection of the TRIM points. (a) projection from a 2D BZ to the edge, (b) projection from a 3D BZ to the surface, (c) examples of the TRS in the 3D BZ and related \mathbb{Z}_2 invariants. (adapted from [76])

4.6 $\text{Bi}_{(1-x)}\text{Sb}_x$ – the first 3D TI

The topological band theory's importance was manifested by the prediction of 3D materials where nontrivial topology emerges. Employing the theoretical predictions [75, 78], the $\text{Bi}_{(1-x)}\text{Sb}_x$ alloy became the first experimentally prepared 3D TI [70]. The theory had supposed that the interplay of heavy Bi and Sb elements should lead to the occurrence of topologically nontrivial surface states. Both elements bear strong SOC. Moreover, the Sb band structure possesses a band inversion at the T -point, which makes it topologically nontrivial according to the \mathbb{Z}_2 theory [33, 74]. Nonetheless, the bulk band gap is partly close, as Sb is a semimetal. Bi is also a semimetal. However, an opening of the band gap by substituting is expected [33]. Concerning tiny Sb concentrations ($x < 0.07$) as well as much significant ones ($x > 0.22$), $\text{Bi}_{(1-x)}\text{Sb}_x$ stay semimetallic (Fig. 4.15). However, for intermediate compositions, a bulk band gap opens. Meanwhile, the band inversion occurs at the L point. Thus, $\text{Bi}_{(1-x)}\text{Sb}_x$ becomes topologically nontrivial in the semiconductor regime [70, 79] (Fig. 4.16). The surface band structure of the experimentally probed $\text{Bi}_{0.99}\text{Sb}_{0.01}$ is quite complicated [70]. Important are states around the surface \bar{M} point (the bar denotes the surface BZ point), where the band gap occurs. The \bar{M} point is the projection of the bulk L point with the inverted band structure [35, 70] (Fig. 4.15). The angle-resolved photoemission spectroscopy (ARPES) measurements revealed that the spin-polarized bands cross five times the Fermi level on the path between the $\bar{\Gamma}$ and \bar{M} points, which indicates topologically nontrivial surface states (Fig. 4.16). Considering the three-fold symmetry, it can be shown that an odd number of Fermi surface pockets enclose the surface TRIM points, which suggest the π Berry phase also related to topologically nontrivial surfaces (Fig. 4.16). Finally, it is confirmed by the bulk boundary correspondence as it corresponds to the calculated TRP [33, 35, 70, 76].

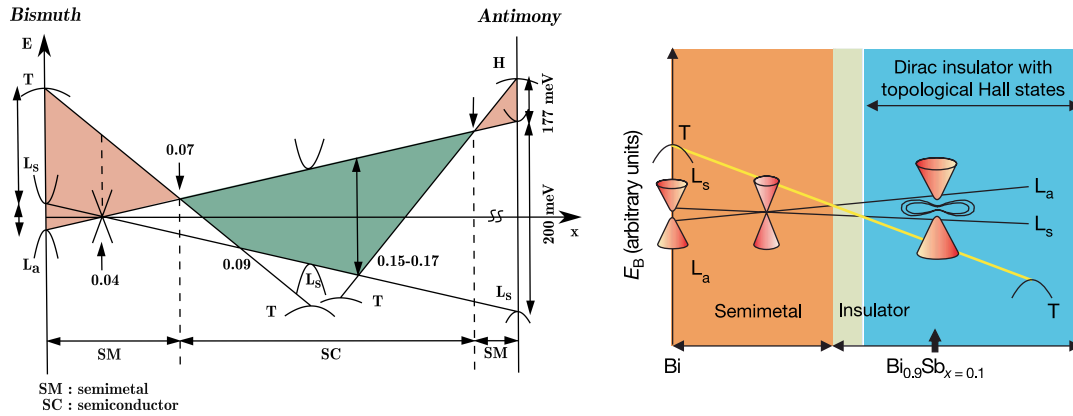


Figure 4.15: Bulk band gap evolution and topological phase in $\text{Bi}_{(1-x)}\text{Sb}_x$ systems as a function of the composition. (adapted from [70, 79])

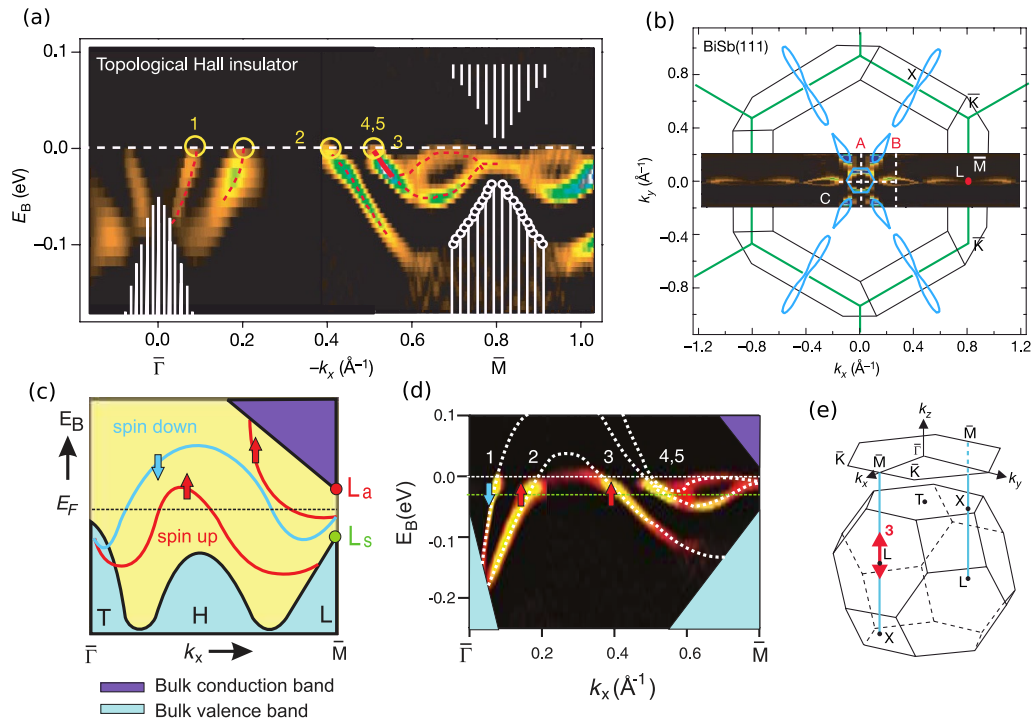


Figure 4.16: $\text{Bi}_{0.99}\text{Sb}_{0.01}$ surface states. (a),(d) experimentally measured spin polarized surface states. (c) sketch of the surface states between the $\bar{\Gamma}$ and \bar{M} points, switching of the spin partner is visible (b),(e) projection to the bulk BZ. (adapted from [70, 80])

4.7 Second generation 3D TI

The band structure of $\text{Bi}_{(1-x)}\text{Sb}_x$ is complicated to study the physics of topological surface states. Furthermore, the bulk band gap is relatively small (≤ 50 meV comp. Fig. 4.15), which does not suit well real applications. Thus, people focus on tetradymid semiconductors, namely Bi_2Se_3 , Bi_2Te_3 and Sb_2Te_3 compounds. These so-called second-generation TIs bear a rather large band gap. Particularly, the largest is Bi_2Se_3 bulk band gap (0.3 meV) promising the occurrence of the surface states up to room temperatures [35]. However, especially, an extremely simple surface band structure had been theoretically predicted [81] and confirmed by the experiments [82–85]. They revealed, regarding this family of compounds, that there is only a single Dirac cone at the $\bar{\Gamma}$ point, in the center of the surface BZ. These three mentioned compounds have the same \mathbb{Z}_2 invariant (1;000), which makes the surface states robust. Bi_2Se_3 possesses the simplest surface band structure among these compounds, and having an almost ideal Dirac cone, [82, 83, 86] it became a prototype of the 3D TIs (Fig. 4.18). According to the spin-momentum locking, the surface states are spin-polarized with a helical spin texture possessing certain chirality by means of the spin texture rotation. It is characteristic for TIs as it is related to the π Berry phase and nontrivial topology [87, 88]. Compared to $\text{Bi}_{(1-x)}\text{Sb}_x$, the clear stoichiometry of the second generation TIs is a great advantage. Since these compounds possess an additional mirror symmetry, the chirality is well defined, and is related to the positive velocity (Eq. 4.29) [33]. Not only the TRS but also crystal symmetries can protect the surface states – *e.g.* TCI [73]. In that case, the topology is described by the so-called mirror Chern number n_M representing a topological invariant characterizing the connection of surface states to the valence and conduction bands along the mirror plane [89]. The mentioned compounds have nonzero mirror Chern number ($n_M = -1$). Therefore, they bear a dual topological character. It results in the protection of the gapless surface states for a magnetic field perpendicular to the mirror plane, although the TRS is broken by the magnetic field [90]. These TIs crystallize in a rhombohedral crystal structure of the $R\bar{3}m$ space group (Fig. 4.17) [35, 81]. It consists of hexagonal layers gathered into quintuples (so-called quintuple layers – QL), where Se and Bi layers alternate. These QLs interact only by van der Waals (vdW) forces, and the structural vdW gap between QLs occurs. The stacking of the hexagonal layers through the structure resembles the face-centered cubic (FCC) stacking as three stacking positions alternate there. Considering z axis as the normal to the hexagonal layers, there exist three mirror planes, according to the three-fold symmetry, parallel to the z axis, which are responsible for the nonzero mirror Chern number [35, 81, 90, 91]. Naturally, the real structure is hardly pristine and several kinds of defect occur there, namely vacancies, antisites or stacking faults as twin planes or Bi double-layers *etc.* [91–99].

The breaking of the TRS can be realized *e.g.* by a nonzero net magnetization of magnetic dopants employing, for instance, transition metals (Fe, Cr, Mn) or proximity of magnetic material [35]. It can lead to the surface gap opening and modification of the surface conductivity. Considering a sufficiently small concentration of magnetic dopant, a temperature-driven surface conductivity can occur by employing the magnetic ordering of magnetic dopants [87, 100, 101]. A nonzero magnetization and the induced magnetic surface gap can lead to the

presence of the QAHE. The Kramer's degeneracy is lifted, and chiral edge states occur for the Fermi level E_F within the opened gap [33, 35, 102, 102–104]. Besides control of the magnetization direction in magnetically doped TIs is also interesting. Considering a strong SOC, switching the magnetization direction by an electric current through the spin-orbit torque has been demonstrated [105]. These mentioned examples of the uncommon magnetically doped TIs' behavior indicate why one is involved in their study in this work, particularly in their exchange interactions.

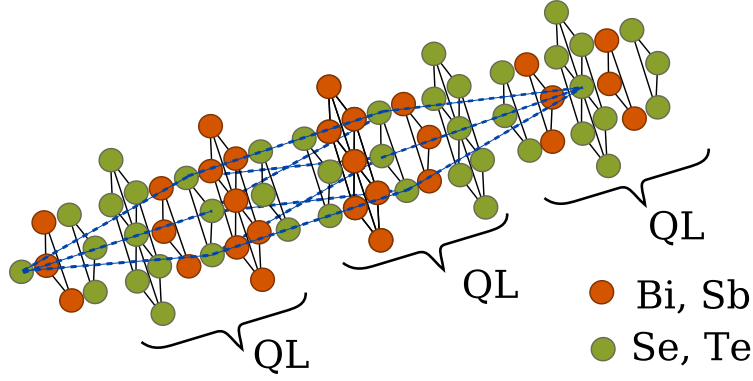


Figure 4.17: Sketch of the crystal structure of Bi_2Se_3 , Bi_2Te_3 and Sb_2Te_3 compounds.

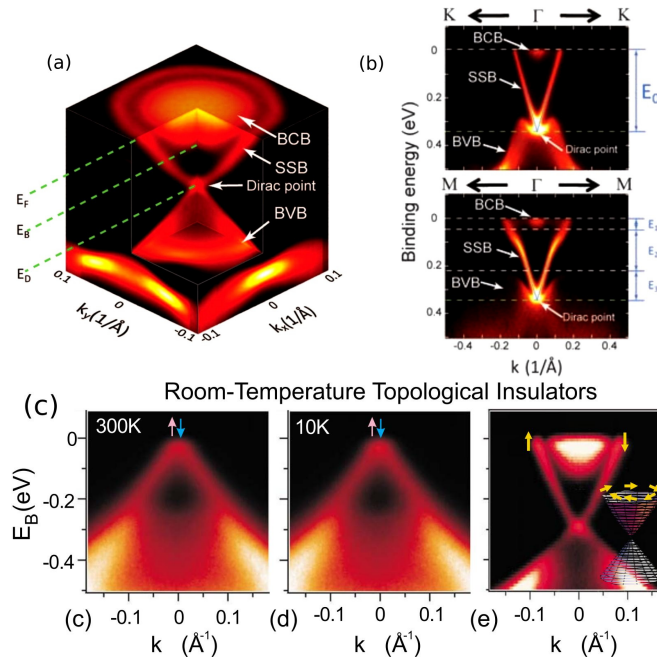


Figure 4.18: Surface band structure of Bi_2Se_3 and Bi_2Te_3 experimentally measured by ARPES. (a) 2D structure of the Bi_2Se_3 Dirac cone, (b) surface Dirac states in Bi_2Te_3 , (c) temperature robustness of gapless surface states in Bi_2Se_3 . (adapted from [45, 84, 86])

5. Bulk Bi_2Se_3

The previous section showed that magnetic doping could significantly change the physical properties of TIs. In this work, we focus on their influence on their electronic structure and behavior of the magnetic exchange interactions, including magnetic ordering temperatures, of well-known Bi_2Se_3 compound, the prototype of the 3D TI. However, we do not concentrate only on magnetic dopants itself, but native defects are also taken into account. They naturally occur in the real samples, and they are able to modify the physical properties of the ideal TIs as the band gap width, surface states, or exchange interactions. The thin-layer structures of 3D TIs are important due to the occurrence of the surface Dirac states. However, we do not deal with Bi_2Se_3 slabs right now, but initially, we focus on the bulk structures' behavior. It allows one to learn a lot about the Bi_2Se_3 behavior, and later it enables one to compare the bulk behavior to the surface one. Besides, it is evident that the layered calculations are more complex, and thus, the bulk calculations are a great starting point. This chapter aims to describe the interplay of the magnetic and native dopants and their influence on the ground state properties of the bulk Bi_2Se_3 . Most of the results have been published in the Ref. [1].

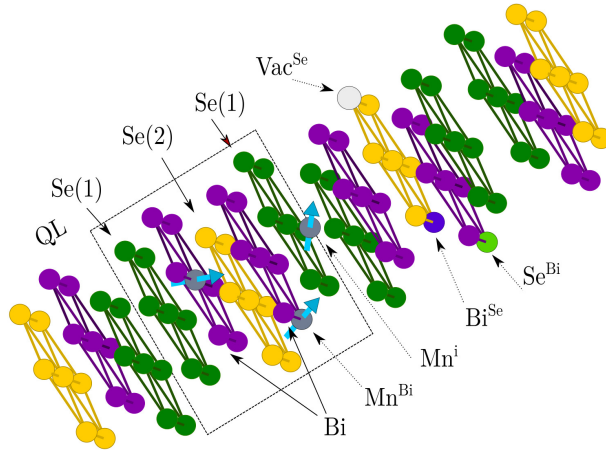


Figure 5.1: Examples of chemical disorder in the Bi_2Se_3 structure. QL – quintuple layer, Mn^{Bi} – substitutional Mn defect, Mn^{Bi} – interstitial Mn defect, Bi^{Se} and Se^{Bi} – Bi resp. Se antisites, Vac^{Se} – Se vacancies.

In the following calculation, experimental lattice parameters and inner coordinates are employed [106] ($a = 4.138 \text{ \AA}$ and $c = 28.640 \text{ \AA}$). In order to minimize the number of atomic sites, the rhombohedral unit cell is used. It consists of two Bi and three Se sites. To improve the filling of the structure in the TB-LMTO-ASA framework, an empty sphere (ES) is placed in the vdW gap as an extra site [107]. Besides, it stands for a possible host of magnetic atoms. In the present work, we occupy with Mn magnetic doping widely used in the experiments [108–112]. It does not represent such strong magnetic perturbation as *e.g.* Fe doping and it seems to be more suitable to ab-initio calculation than *e.g.* Cr one. In the crystal structure, there occur several sites, which can be possibly occupied by magnetic

dopants. According to the experimental and theoretical studies [95, 100, 113], the most probable position is related to replacing of Bi atoms, so-called substitutional position Mn^{Bi} (Fig. 5.1). However, Mn doping can lead to the occurrence of Mn atom at the interstitial position Mn^{i} in the vdW gap [113–115]. Therefore, we take it into account in the present work as well. Additionally, recent work points to the formation of the septuple layer (SL) in bismuth chalcogenides [116] induced by magnetic doping. However, concerning Bi_2Se_3 compound, it is shown that the formation of the SLs is negligible for small concentrations of magnetic defects, unlike Bi_2Te_3 .

In real materials, intrinsic defects occur [82, 94, 117, 118]. It is hard to avoid them and their formation depends on the used growth method and growth conditions [119, 120]. According to the experiments, the measured samples are mostly n -type. It is believed, that the increased Fermi level stems from the occurrence of Se vacancies (Vac^{Se}) [92, 94, 121]. It corresponds to theoretical works calculating the formation energy of native defects and revealing that Vac^{Se} defects are likely the most favorable intrinsic defects in Bi_2Se_3 compound [93, 95, 122]. Besides, there exist other native defects as Bi and Se antisites (Bi^{Se} resp. Se^{Bi}), which are also considered there. They represent a substitution of the Se atoms by Bi ones (Bi^{Se}) and vice versa (Fig. 5.1). According to the preparation, stoichiometric as well as nonstoichiometric samples can occur [96].

Usually, people do not pay attention to the intrinsic defects studying magnetically doped TIs. However, the presence of native defects modifies the electronic structure. It influences the bulk conductivity [93] and therefore has a significant impact on the indirect exchange interactions. Considering typical low concentrations of the magnetic dopants in samples, the importance of the superexchange [123–125], and RKKY [126, 127] interactions arises, where mainly the later one strongly depends on the carrier density. Besides, the native defects move the Fermi level and modify the band gap width, which is important from the surface states' point of view [128].

5.1 Computational details

Electronic structure calculations are performed in the framework of the scalar relativistic TB-LMTO-ASA method (Sec. 1.2) with the included SO interaction, which is essential for a good description of the band structure as it modifies the band structure significantly in the proximity of the Fermi level [33]. We employ the *spd* atomic model with the LSDA xc-potential of Vosko-Wilk-Nusair [129]. Besides, a basic screened impurity model was involved in order to improve the electrostatics in the calculated disordered systems [130]. Calculations are performed in the full BZ of $36 \times 36 \times 36$ k -points, which appeared to be sufficient to obtain a great convergence of the calculated data. The energy convergence criterion of the self-consistent cycle is less than $10 \mu\text{Ry}$. The calculated band gap width (313 meV, Fig. 5.2) corresponds well with the experimental ARPES measurements [82, 131, 132] as well as to theoretical calculations [81, 132, 133]. Further increasing of the k -mesh density leads to only small negligible modifications of the band structure, namely a change of the band gap width is less than 0.5 %. Concerning the calculated magnetically doped structures, the related change of magnitudes of magnetic moments has an order of $10^{-3} \mu_{\text{B}}$ and

the ordering temperatures estimated in the framework of the mean-field approximation differ less than 1 % of their magnitude. Chemical disorder is treated by means of the CPA, which is suitable for the studied small concentrations of defects. The CPA stands for a highly efficient approach with substantially small computational demands compared to the supercell method [134]. The magnetic defects, as well as the native ones, are treated with the same concentration at the appropriate sublattices.

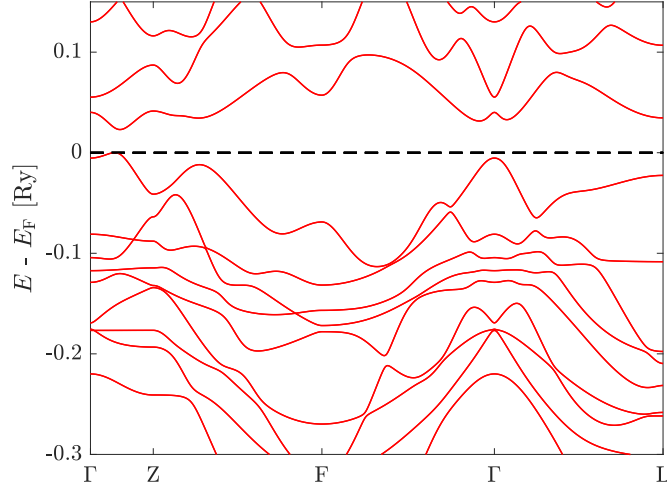


Figure 5.2: Band structure of the pure Bi_2Se_3 compound.

5.2 Electronic structure

Initially, the electronic structure of the pure Bi_2Se_3 compound is evaluated to compare our approach to the literature. The obtained large band gap width of 313 meV (Figs. 5.2 and 5.3) corresponds well to the experimental and theoretical works [82, 131, 132] as it was mentioned in the previous paragraph. The DOS calculations reveal that the valence band is dominated by the Se-6*p* states, while Bi-4*p* states predominate in the conduction band, which agrees with the already published calculations [135, 136].

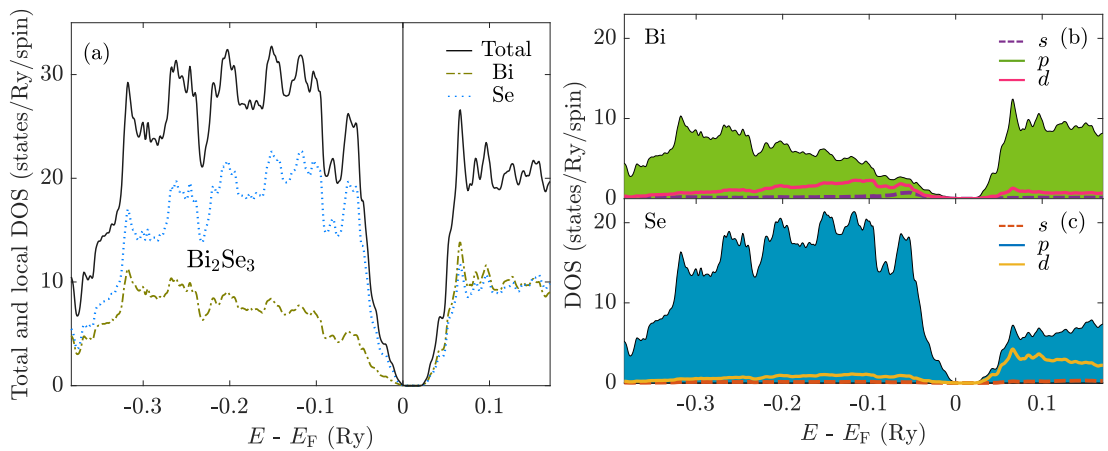


Figure 5.3: Density of states of pure Bi_2Se_3 . (a) Total DOS with Bi and Se resolved contributions. (b), (c) *s*, *p*, *d*-orbital resolved DOS of the Bi resp. Se contributions.

Magnetic disorder

Having verified the behavior of the pristine Bi_2Se_3 , we can focus on the influence of the chemical disorder on the electronic structure. First, magnetic Mn disorder is discussed. Previous works show that the inclusion of the disorder-induced local relaxation in CPA calculation might be essential to achieve reliable electronic structure [107, 137]. Since the TB-LMTO-ASA method does not allow for a calculation of the structure relaxation, the relaxation of the dopant neighborhood is studied by super-cell calculations using the Vienna ab initio Simulation Package (VASP) [138] (performed by Dr. F. Máca at the Institute of Physics of the Czech Academy of Sciences). It employs the spin-polarized DFT based on projector augmented wave (PAW) potentials implemented in the VASP [139] with a large enough cutoff energy of 500 eV and xc-potential in the GGA of Perdew, Burke, and Ernzerhof [140], where only small modifications of the electronic structure are observed in comparison with calculations using the LSDA. The electronic structure calculations are performed using the BZ consisting of $10 \times 10 \times 2$ k-point and energy convergence criterion of 10^{-4} eV. The structure optimization is treated by the conjugated gradient technique with the residual force criterion of $2.5 \text{ meV} \cdot \text{\AA}^{-1}$. The calculation used the hexagonal unit cell consisting of 60 atoms resp. 61 atoms in the case of Mn^i defects. Only a single Mn defect (either Mn^{Bi} or Mn^i) is incorporated in the unit cell. It is related to the nominal concentration of $1/24$ ($\sim 4.2\%$), which corresponds to the considered concentration range of the magnetic defects. It is important due to reaching the appropriate Fermi level position as it significantly influences dopants' behavior [120]. Concerning the substitutional Mn^{Bi} defect, a non-negligible lattice relaxation is obtained as the Mn-Se distance is reduced from the initial symmetric one of 2.97 \AA to 2.60 \AA resp. 2.70 \AA , depending on the Se sublattice, while the Mn-Bi distance remains unchanged (4.14 \AA). On the contrary, no significant structure distortion is observed in the case of the interstitial Mn^i defects.

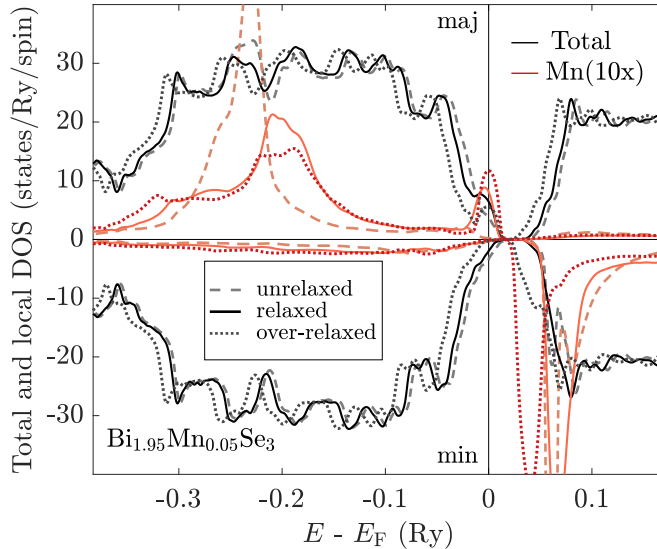


Figure 5.4: Dependence of the spin-resolved density of states of Bi_2Se_3 doped by Mn^{Bi} acceptors on the structure relaxation. Solutions related to three different local Mn Wigner-Seitz radii are depicted. Mn- Se_1 distance: (unrelaxed) 2.97 \AA , (relaxed) 2.70 \AA , (overrelaxed) 2.61 \AA . Concentration of Mn^{Bi} is $x = 0.05$ per f.u.

In the TB-LMTO-ASA method framework, the structure relaxation obtained by the super-cell calculations can be reflected by corrections of the species-dependent Wigner-Seitz radii [107, 141]. Their modification leads to a change of the structure constants in the LMTO method, which influences the associated hopping integrals and changes the potential parameters through the self-consistent calculations [6] (Sec. 1.4). Altogether, it can significantly modify the resulting Green's function and electronic structure. There exist two sorts of Wigner-Seitz radii, the global one w^{all} , which defines the structure volume and the local radii w^Q related to the atomic species Q . To reflect the structural distortion, the Wigner-Seitz radii are changed locally for $Q = \text{Bi}, \text{Mn}$, while the total volume of the Bi-sublattice is preserved. It is defined as follows $V^{\text{Bi}} = 4\pi/3 [(x-1)(w^{\text{Bi}})^3 + x(w^{\text{Mn}})^3]$, where x denotes the Mn concentration. We point out that small volume changes related to magnetic doping or native defects are neglected in our calculation. Concerning the Mn Wigner-Seitz radius w^{Mn} , the native value of the solid-state Mn $w^{\text{Mn}} = 2.80$ a.u. is used to replace the original Wigner-Seitz radii related to the Bi-sublattice (Fig. 5.4 – relaxed solution). We note that the structural distortion is studied only for the magnetic doping. No further modifications are performed concerning the native defects discussed later.

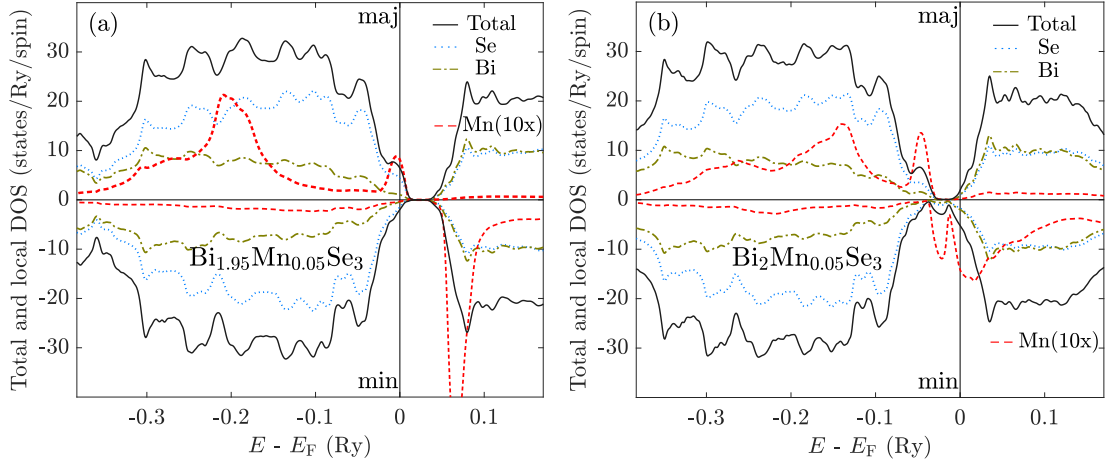


Figure 5.5: Spin-resolved densities of states of magnetically doped Bi_2Se_3 . Concentration of Mn atoms is $x = 0.05$ per f.u. (a) Doping with Mn^{Bi} acceptors. (b) Doping with Mn^{I} donors.

Regarding the Mn^{Bi} dopants, it is found that the DOS is highly sensitive to the structure relaxation (Fig. 5.4). Notably, the character of the Mn^{Bi} local DOS. Mn^{Bi} dopants stand for electron acceptors, which moves the Fermi level position inside the valence band (Fig. 5.5a). At the Fermi level, a small majority spin impurity Mn peak working as a virtual bound state occurs. Depending on the state of the relaxation, its intensity and relative position to the valence band edge change. Mostly, Mn^{Bi} majority spin $3d$ -states lie more in-depth in the valence band, and they are also sensitive to the amount of the structure distortion as their energy localization strongly depends on the introduced relaxation. Concerning the minority spin channel, there appears a significant Mn^{Bi} impurity peak at the edge of the conduction band. The position of the calculated Mn^{Bi} peaks corresponds to the ab-initio calculation performed by the Korringa-Kohn-

Rostoker method [142]. Also, the band gap width strongly depends on structural distortion. It is reduced with the increasing amount of local relaxation (Fig. 5.4). However, concerning the employed relaxation determined by $w^{\text{Mn}} = 2.80$ a.u., the band gap is maintained (Fig. 5.5a), despite the presence of the ingap states. Besides the dependence on the relaxation, the band gap width is influenced by the concentration of the Mn^{Bi} defects as well (Fig. 5.6a). Increasing the concentration of magnetic Mn^{Bi} dopants, the bulk band gap is being closed, particularly by the Mn impurity states and Se states, which strongly hybridize with the Mn one. The occurrence of the majority spin Mn impurity peak and the related hybridization leads to a predominance of majority spin states at the Fermi level. Regarding the used small Mn^{Bi} concentration, the reduction of the bulk band gap is nearly linear with respect to the dopant concentration (Fig. 5.7). Concerning the magnetic doping, the magnetocrystalline anisotropy is calculated. Studying the hexagonal layer structure (Fig. 5.1) a weak out of plane anisotropy of the order of $0.1 \mu\text{Ry}$ is found. Thus, the out of plane spin polarization in the calculation is used.

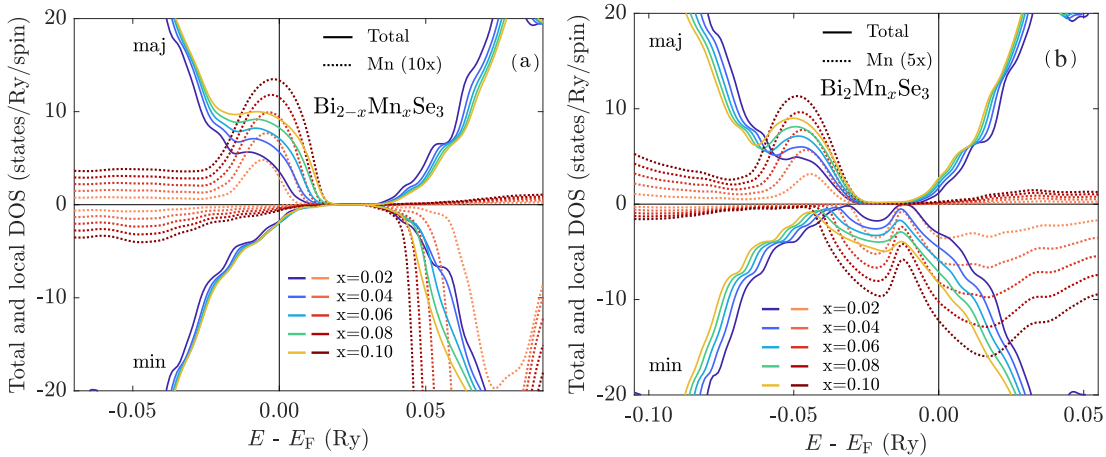


Figure 5.6: Bulk band gap in magnetically doped Bi_2Se_3 . (a) Doping with Mn^{Bi} acceptors. (b) Doping with Mn^{I} donors.

Since the VASP supercell calculations reveal only little relaxation concerning the interstitial Mn^{I} dopant, no additional relaxation similar to the previous case of Mn^{Bi} dopants is included in the TB-LMTO-ASA method framework. Unlike the substitutional Mn defects, the Mn^{I} dopants act as electron donors placing the Fermi level at the bottom of the conduction band (Fig. 5.5b). The presence of Mn^{I} dopants gives rise to the occurrence of Mn impurity peaks in the former Bi_2Se_3 band gap. They strongly hybridize with Bi and Se states, and they act as the virtual bound states. These states fill the band gap in the minority spin channel even for small Mn^{I} concentration, while for the majority spin channel, the width is reduced only (Fig. 5.6b). It removes the insulating character and brings about half-metallic behavior.

The obtained Mn^{Bi} magnetic moments around $4.0 \mu_{\text{B}}$ (Fig. 5.8) correspond to values obtained elsewhere [143] and they resemble to magnitudes of magnetic moments founded in magnetically doped Bi_2Te_3 compounds [107, 144] similarly to the Mn^{I} moments ($3.1 - 3.2 \mu_{\text{B}}$). The Mn^{Bi} magnetic moments' magnitudes strongly depend on the amount of the included relaxation, which is obvious from the change of the DOS (Considering the Fig. 5.4: unrelaxed system $4.59 \mu_{\text{B}}$,

relaxed system $4.03 \mu_B$ and over-relaxed system $3.52 \mu_B$). However, they are not influenced by the type of magnetic order. Comparing the used FM order with the paramagnetic state represented by the disordered local moment (DLM) model, almost no change is found. The FM and DLM states represent the limiting cases of the magnetic order. The first describes a perfectly ordered system, the second absolutely disordered one. Nevertheless, it is observed that magnetic moments' magnitudes decrease with increasing concentrations of magnetic dopants (Fig. 5.8), regarding both defect types. It stems from the shifting of the Fermi level Mn impurity peaks with respect to the Mn impurity peaks (Fig. 5.6).

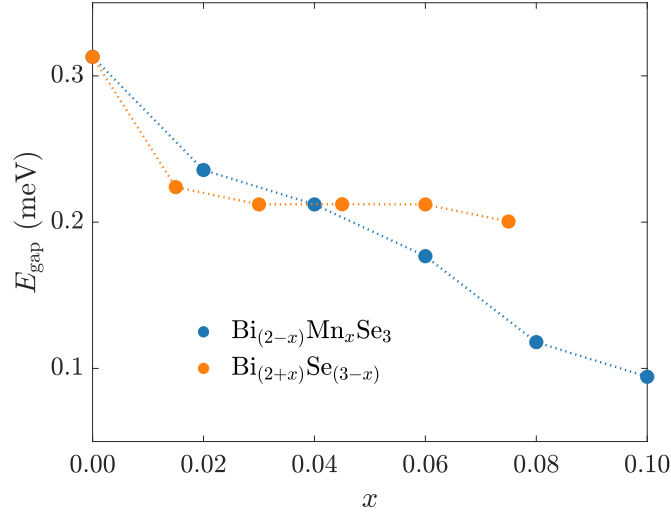


Figure 5.7: Bulk band gap width as a function of the chemical defects' concentration.

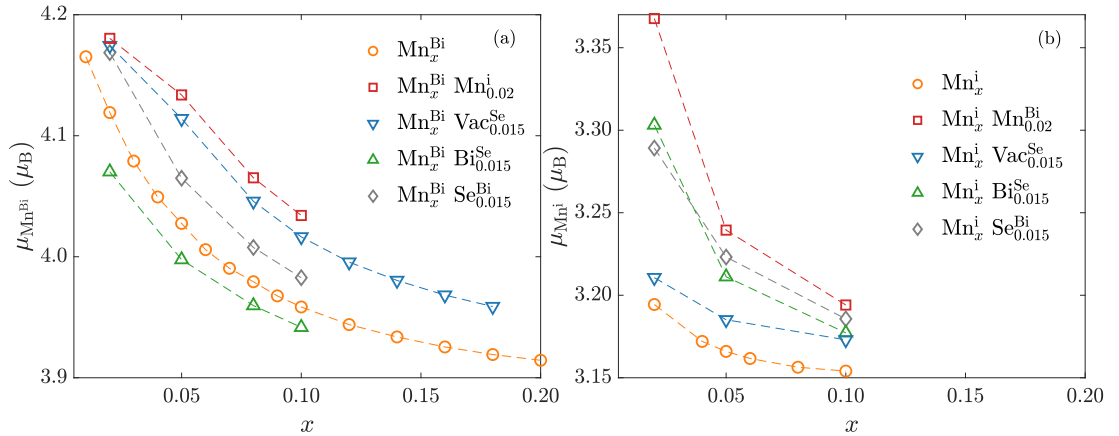


Figure 5.8: Dependence of the Mn magnetic moments' magnitude on the Mn concentration x and the presence of other chemical defects. (a) Magnitudes of Mn^{Bi} magnetic moments as a function of the Mn^{Bi} dopant concentration. (b) Magnitudes of Mn^i magnetic moments as a function of the Mn^i dopant concentration. Subscripts of dopants' labels specify dopant concentration per f.u.

Native defects

The most common native defects in the Bi_2Se_3 compound, the Se vacancies (Vac^{Se}), act in the Bi_2Se_3 system as electron donor moving the Fermi level upwards with the respect to the ideal system (Fig 5.9a). These defects induce shallow mid-gap states filling the whole gap irrespective of the dopant concentration. Thus, one can expect tiny conductivity in presence of Vac^{Se} . Their occurrence in magnetically doped systems (Fig 5.9b, c) induces mid-gap states similar to the original case. It results in gap closing in the both spin channel. Concerning Mn^{i} dopants the position of the Fermi level is nearly unchanged. However, in the case of Mn^{Bi} dopants, the Fermi level is fixed at the mid-gap states. Besides, the positions of the Mn impurity peaks are almost unchanged (Fig. 5.7).

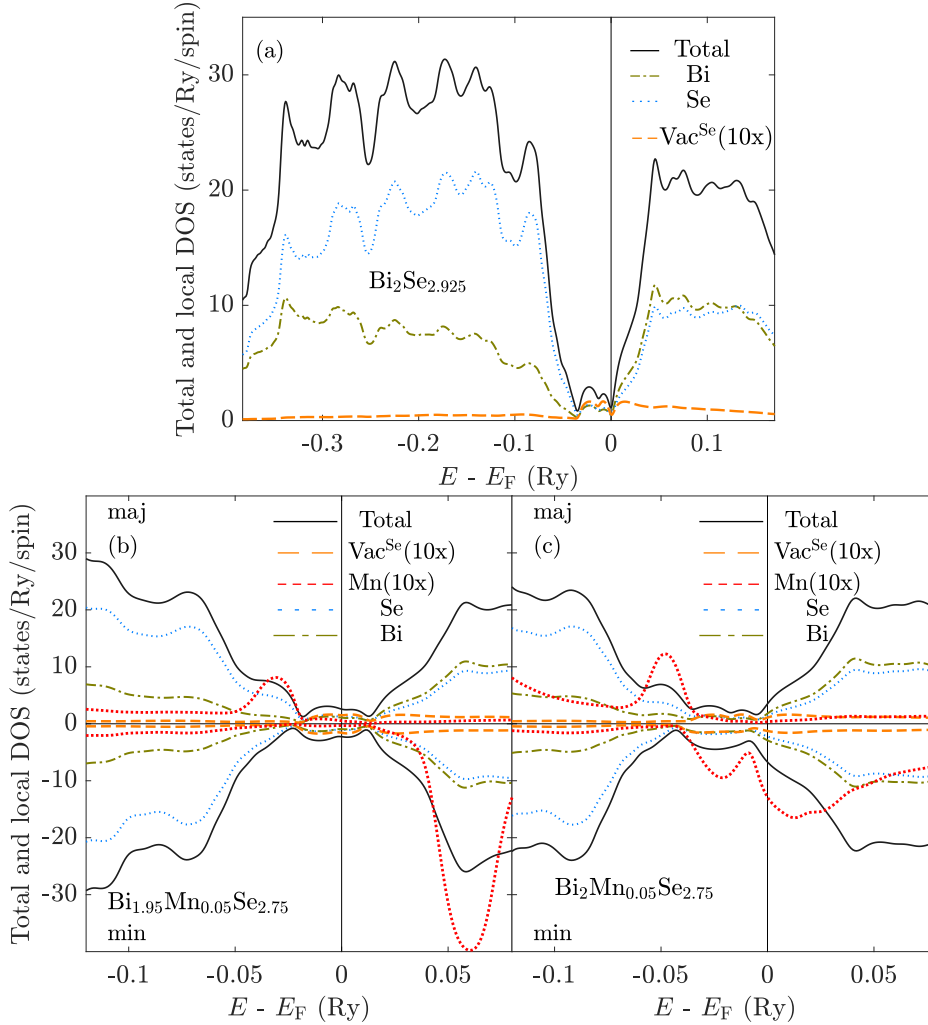


Figure 5.9: Bi_2Se_3 system densities of states in presence of Se vacancies (Vac^{Se}) with the total concentration 0.075 per f.u.: (a) native defects only, (b) native defects together with the magnetic substitutional Mn^{Bi} dopants, (c) native defects together with the magnetic interstitial Mn^{i} dopants.

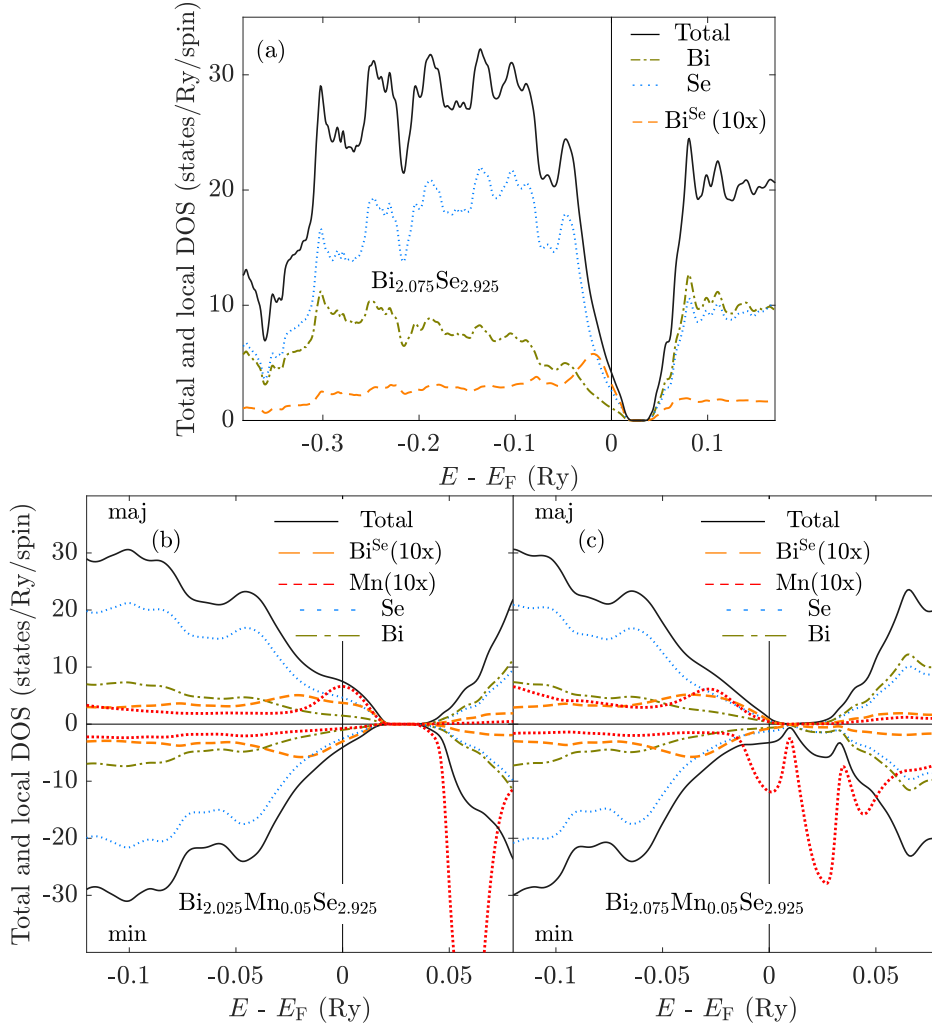


Figure 5.10: Bi_2Se_3 system densities of states in presence of Bi antisites (Bi^{Se}) with the total concentration 0.075 per f.u.: (a) native defects only, (b) native defects together with the magnetic substitutional Mn^{Bi} dopants, (c) native defects together with the magnetic interstitial Mn^{I} dopants.

Another kind of possible native defect is Bi antisite (Bi^{Se}). They behave as electron acceptors shifting the Fermi level to the valence band, while they form a slight Bi^{Se} impurity peak nearby the Fermi level (Fig. 5.10a). Unlike the Vac^{Se} defects, the band gap survives in presence of Bi^{Se} ones, although the gap width is partly reduced. However, the width depends only weakly on the Bi^{Se} concentration (Fig. 5.7). In presence of the Mn^{Bi} dopants, the gap is further reduced (the gap width E_{gap} is about 130 meV concerning the system depicted in the (Fig. 5.10b). The position of the Fermi level within the valence band is nearly kept since both defects behave as electron donors. Besides, the weak majority spin Bi^{Se} impurity peak strongly hybridizes with the Mn^{Bi} impurity peak, which is suppressed by the presence of the Bi antisites. Concerning the Mn^{I} magnetic dopants, the minority spin channel band gap remains closed (Fig. 5.10c). The position of the Fermi level depends on the concentrations of defects as both electron acceptors, and electron donors are introduced. Similarly to the Mn^{Bi} defects, there occurs a hybridization of the impurity peak in the majority spin channel. Furthermore, an additional splitting of Mn^{I} impurity peaks around the Fermi level appears in the other spin channel.

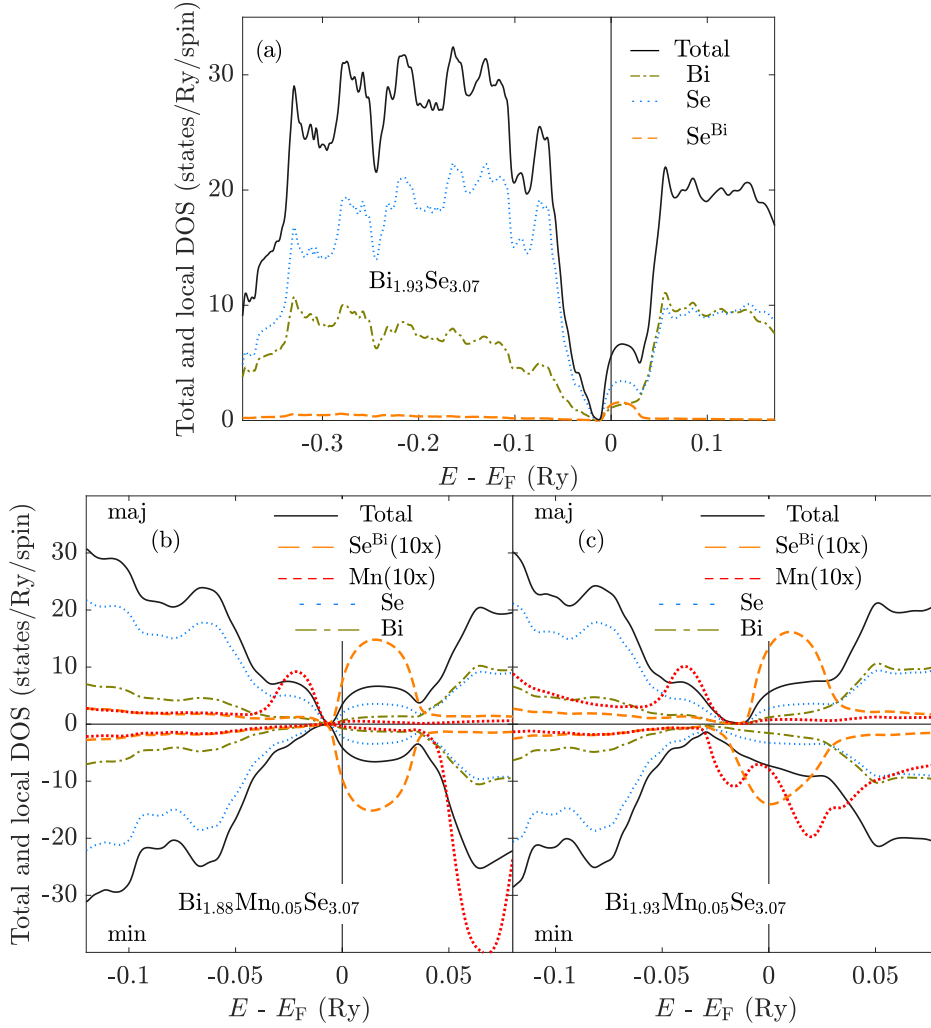


Figure 5.11: Bi_2Se_3 system densities of states in presence of Se antisites (Se^{Bi}) with the total concentration 0.075 per f.u.: (a) native defects only, (b) native defects together with the magnetic substitutional Mn^{Bi} dopants, (c) native defects together with the magnetic interstitial Mn^{I} dopants.

To be complete, the Se^{Bi} defects are appended. Unlike the Bi^{Se} counterparts, the Se^{Bi} defects work naturally as electron donors placing the Fermi level at the conduction band edge (Fig. 5.11a). The Se^{Bi} impurity peak behaves as a virtual bound state, where it strongly hybridizes particularly with the Se states. The Se^{Bi} defects cause band gap closing as the valence band and the conduction band almost touch nearly regardless of the Se^{Bi} concentration. Similarly, the band gap is about to be closed concerning additional substitutional Mn^{Bi} co-doping (Fig. 5.11b), whereas a small band gap in the majority spin channel seems to be maintained regarding Mn^{I} magnetic dopants (Fig. 5.11c). There, a significant hybridization of minority spin Mn^{Bi} impurity peaks with the Se^{Bi} occurs.

Naturally the native defects influence the Mn^{Bi} and Mn^{I} magnetic moments' magnitudes (Fig. 5.8). Concerning the later ones, all the mentioned native defects bring about increasing of their magnitude. It is related to shape modification of the minority spin Mn impurity peaks (Fig. 5.9c) or to a downwards shift of the relative Fermi level position (Figs 5.10c and 5.11c). In the case of Mn^{Bi} dopants, Vac^{Bi} and Se^{Bi} defects increase the magnitudes of magnetic moments since they

place the Fermi level into the former Bi_2Se_3 gap above the majority state Mn impurity peak (Figs. 5.9b and 5.11b). By contrast, a small reduction is observed regarding Bi^{Se} defects as the Fermi level slightly moves downwards (Fig. 5.10b). Finally, also the magnetic Mn^{Bi} and Mn^{i} defects increase the magnitude of magnetic moments of the counterpart (Fig. 5.8) since they act as electron acceptors resp. donors, which changes the spins polarization as it has been mentioned before.

5.3 Exchange interactions

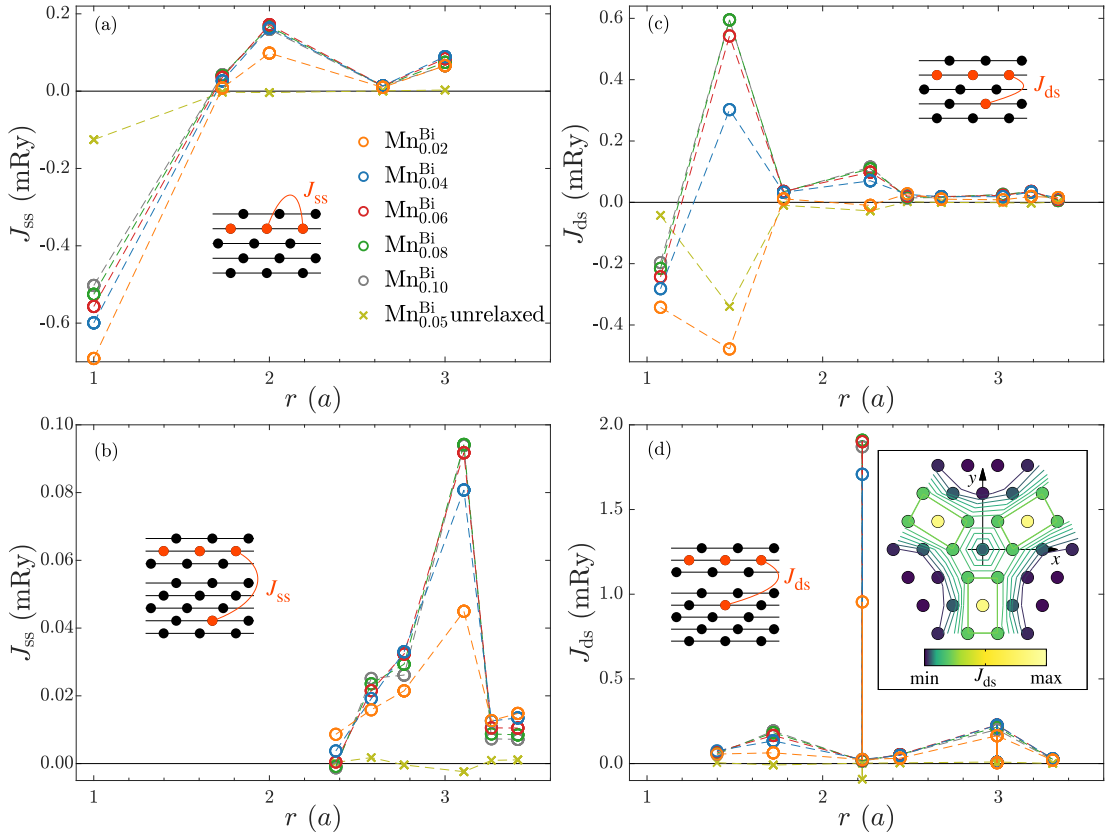


Figure 5.12: Magnetic exchange interactions between Mn^{Bi} magnetic moments as a function of the mutual distance r . The dependence of the exchange interactions on the dopant concentration is depicted. The distance is expressed in terms of the lattice parameter a . (a) Magnetic moments belonging to the same sublattice at the same hexagonal layer. (b) Magnetic moments belonging to the same sublattice, but in neighboring QLs. (c) Magnetic moments belonging to the different sublattice in the same QL. (d) Magnetic moments belonging to the different sublattices and neighboring QLs. The inset in (d) depicts a planar distribution of the exchange interaction strength between moments at depicted atomic sites and the magnetic moment at the other sublattice's origin. Subscripts of dopants' labels specify dopant concentration per f.u.

Knowledge of the magnetic exchange interactions is essential to describe the magnetic ordering of the studied system. The TB-LMTO approach employing Liechtenstein formula (Eq. 2.59) is used. It applies a pure scalar-relativistic framework neglecting the SO interactions in the Hamiltonian (Eq. 1.15). It makes the method high efficient with small computation demand as it allows for the calculation only in the irreducible part of the BZ. The evaluation of magnetic exchange interactions demands a high density of the k -points. Actually, the previously calculated electronic structures within the scalar relativistic framework allowing for the SO interactions are employed. Using the known potential parameters (Eq. 1.38) the CPA self-consistent configuration averaged Green's function is evaluated (Eqs. 1.55) while the SO interaction is neglected. The presence of the SO interaction leads to the loss of the invariance against a global rotation of spins, which makes the mapping (Eq. 2.57) of the energy variations δE (Eq. 2.56) on the effective Heisenberg Hamiltonian (Eq. 2.54) unfeasible [145, 146]. The Green's function is constructed by using the $20 \times 20 \times 20$ k -mesh in the BZ. A substantially larger density of k -points ($100 \times 100 \times 100$) is adopted to obtain reliable real space magnetic exchange interactions based on the inverse Fourier transform.

The exchange interactions are depicted as functions of the magnetic moment distances $J(r) = J(|\mathbf{R}_2 - \mathbf{R}_1|)$ (Figs. 5.12, 5.14, 5.15, 5.16). They are divided by the types of the interacting Mn defects and related sublattices. Namely, subplots (a, b) describe interactions related to magnetic atoms occupying the same atomic sublattice, whereas (c, d) ones are related to different sublattices. Besides, concerning Mn^{Bi} moments (Figs. 5.12, 5.14), (a,c) subplots contain interaction within the same QL, while (b, d) ones belong to neighboring QLs. In the Fig. 5.16, subplots (c, d) depict interactions between Mn^{Bi} and Mn^{i} moments.

In the description, we begin with the Mn^{Bi} interactions. Considering no other defects (Fig. 5.12), the exchange interactions are rather positive, except for the two nearest ones. However, in the diluted magnetic system, a wide range of neighbors has to be considered. There exist other stronger positive interactions, which are able to overcome the nearest neighbor ones. Besides, the impact of the nearest neighbor interaction in diluted systems is suppressed by means of the percolation effect [124]. It is evident that the strength of the exchange interactions evolves with the increasing Mn^{Bi} concentration, while their sign is almost unchanged. Based on the calculated data, it appears that the exchange interactions are converged above the concentration $x = 0.08$. Naturally, one of the most robust exchange interactions occurs within the same QL (Fig. 5.12a,b). With increasing distance, these interactions turn from significant negative values to positive ones. The interactions at the same sublattice (Fig. 5.12a) seem to vigorously oscillate with increasing distance, while the inter-sublattice ones (Fig. 5.12b) strongly decay above the distance of $2.4 a$.

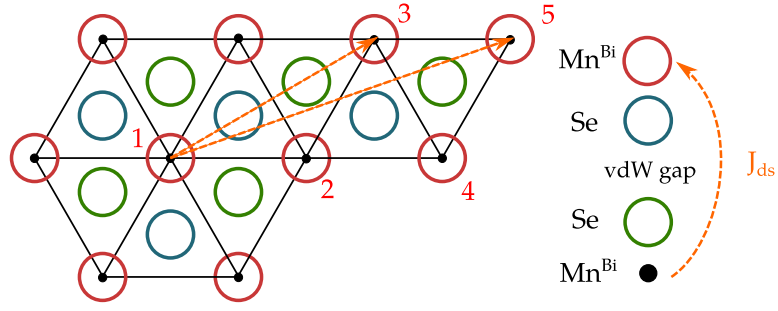


Figure 5.13: Relation of the Mn^{Bi} exchange interactions across the vdW gap and the crystal structure. The numbers denote the nearest neighbor atomic shells according to the Fig. 5.12d.

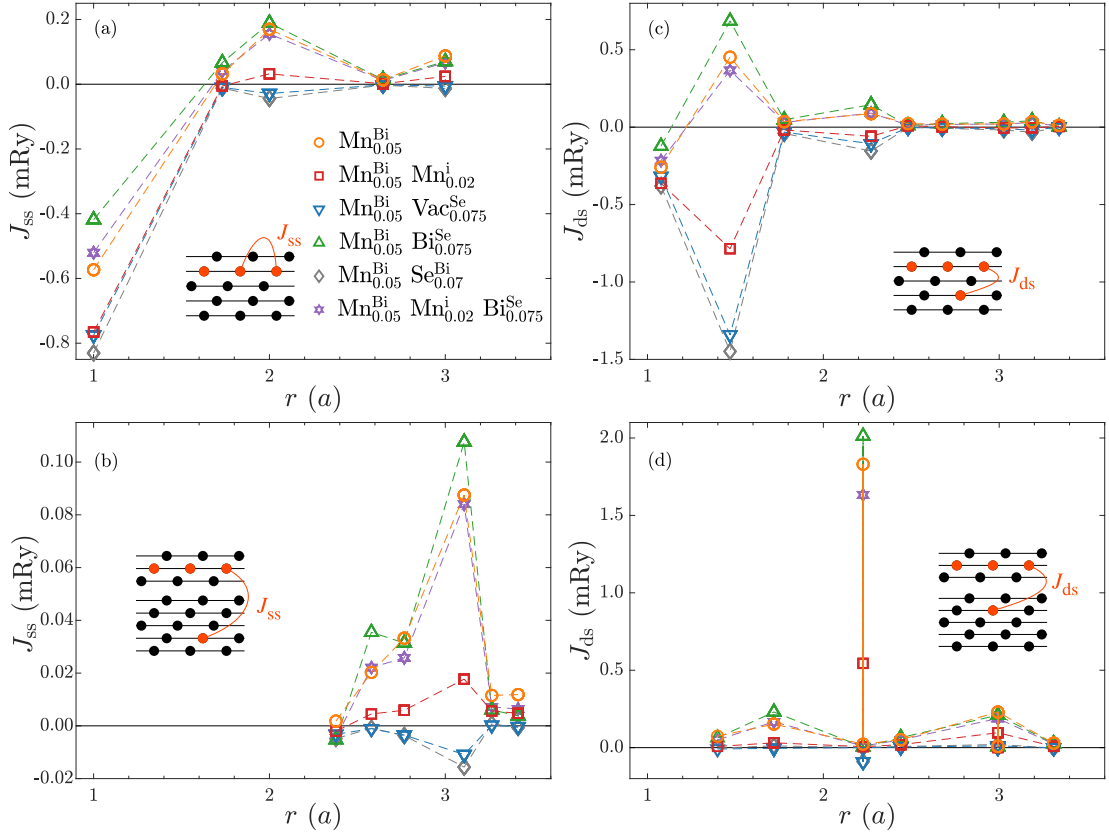


Figure 5.14: Magnetic exchange interactions between Mn^{Bi} magnetic moments as a function of the mutual distance r in presence of other defects. The distance is expressed in terms of the lattice parameter a . (a) Magnetic moments belonging to the same sublattice at the same hexagonal layer. (b) Magnetic moments belonging to the same sublattice, but in neighboring QLs. (c) Magnetic moments belonging to the different sublattice in the same QL. (d) Magnetic moments belonging to the different sublattices and neighboring QLs. Subscripts of dopants' labels specify dopant concentration per f.u.

The interactions between different sublattices (Fig. 5.12c,b) are mostly weak except for the unexpected colossal exchange interactions belonging to different Bi sublattices separated by the vdW gap. It stands for the far strongest interaction, considerably overcoming the other calculated ones. The position of the interacting partner site in the counter-sublattice is depicted in the inset of the Fig. 5.12d, which fulfills the three-fold symmetry in agreement with the $R\bar{3}m$ space group. Analyzing the crystal structure, we find interestingly that the connection between the appropriate Mn^{Bi} positions meets the Se atom closely in the intermediate atomic layers forming an $\text{Mn}^{\text{Bi}}\text{-Se-Se-Mn}^{\text{Bi}}$ chain (Fig. 5.13). The inter-atomic distances within the chain are relatively small: the $\text{Mn}^{\text{Bi}}\text{-Se}$ distance is of $0.7a$, and the Se-Se distance across the vdW gap is of $0.85a$. Hence, it appears that the Se atoms substantially enhance the $\text{Mn}^{\text{Bi}}\text{-Mn}^{\text{Bi}}$ exchange interactions by mediating them (super-exchange). It is likely suit also to exchange interactions near $r = 3a$ (compare Figs. 5.12d and 5.13).

The character of the Mn^{Bi} exchange interactions is strongly affected by the occurrence of other chemical defects (Fig. 5.14). Their presence not only does significantly modify the strength of the exchange interactions but also it is able to change their sign. Based on the calculated data, we observe that only Bi^{Se} defects from the all considered defects renders the Mn^{Bi} exchange interactions more positive, namely the most intensive ones. The other defects shift the exchange interactions to negative values. Significantly, the Vac^{Se} and Se^{Bi} makes the exchange interactions purely antiparallel.

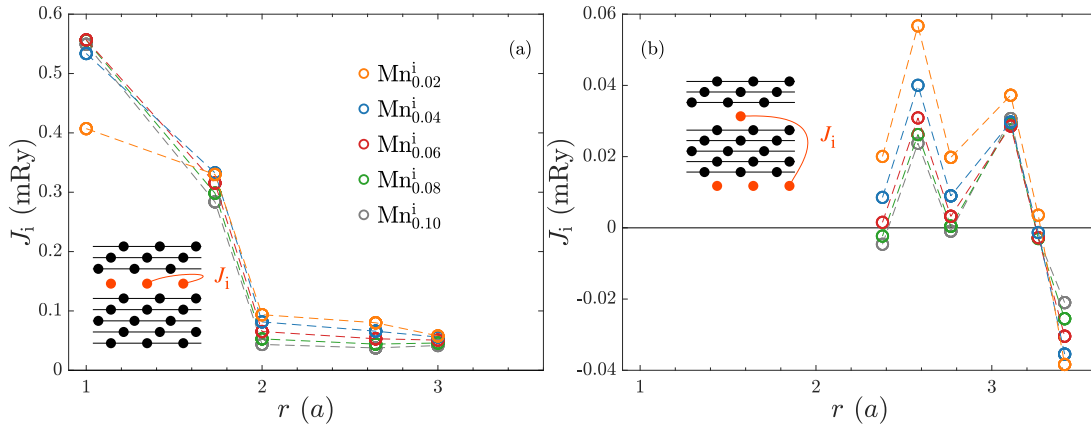


Figure 5.15: Magnetic exchange interactions between Mn^i magnetic moments as a function of the mutual distance r . Dependence of the exchange interactions on the dopant concentration is depicted. The distance is expressed in term of the lattice parameter a . (a) Magnetic moments belonging to the same sublattice at the same hexagonal layer. (b) Magnetic moments belonging to the same sublattice, but in neighboring QLs. Subscripts of dopants' labels specify dopant concentration per f.u.

Similar to the previous case, Mn^i exchange interactions are influenced by the concentration of the magnetic dopants as well (Fig. 5.15). By contrast, their magnitudes are decreased, except that one of the nearest neighbor Mn^i atom. Moreover, some of them acquire the opposite sign (Fig. 5.15b). However, the solely Mn^i exchange interactions are positive, especially the same sublattice (Fig. 5.15a). The presence of other defects shifts the intra-sublattice Mn^i exchange interac-

tions towards the negative values (Fig. 5.16a), namely the Se^{Bi} ones and also the Bi^{Se} antisites, which induce the opposite behavior concerning the Mn^{Bi} exchange interactions. The dependence of the Mn^{i} exchange interactions across the QL (Fig. 5.16b) on the disorder is more complex as there occur modifications of the original oscillations of the interactions' magnitudes. Finally, the mixed $\text{Mn}^{\text{i}}\text{-Mn}^{\text{Bi}}$ exchange interactions are rather antiparallel. Only the nearest neighbor ones are positive. They are sensitive to the presence of native defects as the Se^{Bi} ones can introduce extremely robust antiparallel exchange interactions (Fig. 5.16c). It has been shown that the magnetic exchange interactions are highly sensitive to the presence of the chemical disorder as well as the concentration of the magnetic atoms. In agreement with the modification of the magnetic moments (Fig. 5.8), it reveals that the magnetic properties of the Mn-doped Bi_2Se_3 compound strongly depend on its actual composition. Besides, it enables one to modify the properties in the case of a well controllable growth method.

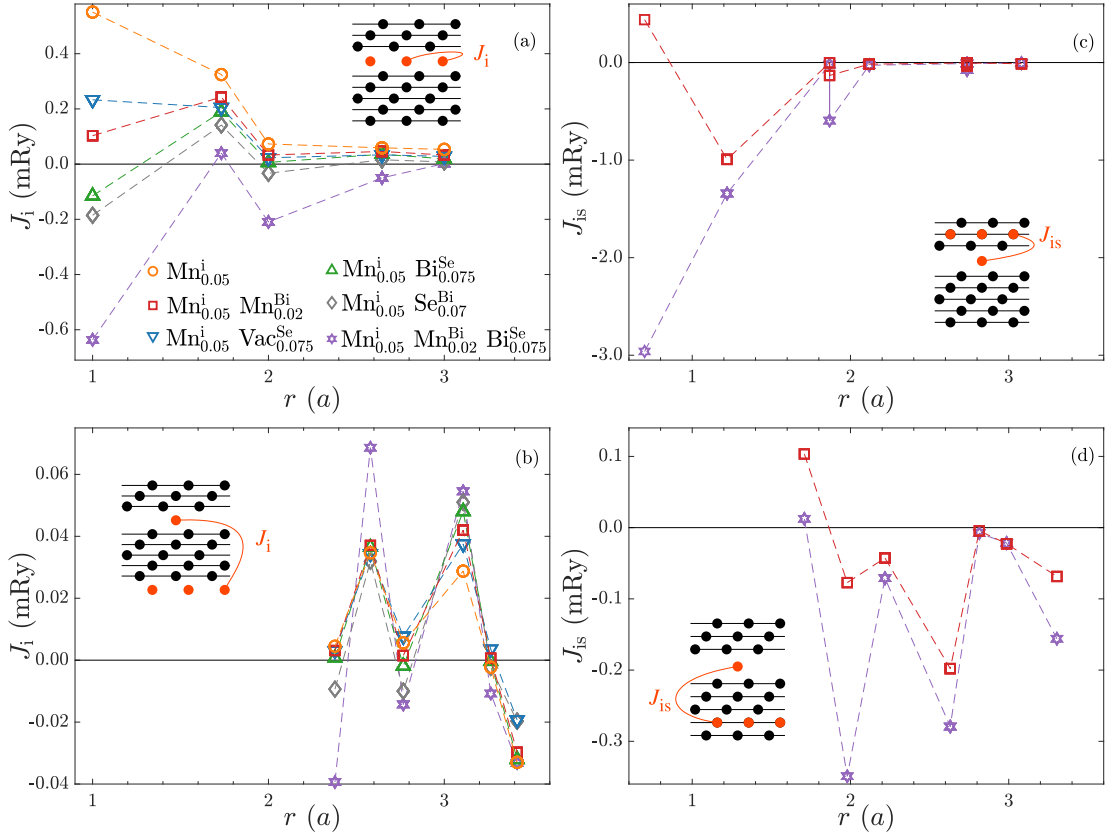


Figure 5.16: Magnetic exchange interactions between Mn^{i} magnetic moments as a function of the mutual distance r in presence of other defects: (a) magnetic moments belonging to the same sublattice at the same hexagonal layer, (b) magnetic moments belonging to the same sublattice, but in neighboring QLs. Exchange interactions between Mn^{i} magnetic moments and Mn^{Bi} magnetic moments as a function of the mutual distance r , (c) Mn^{Bi} moments in the adjacent Bi sublattice, (d) Mn^{Bi} moments in the opposite Bi sublattice. The distance is expressed in term of the lattice parameter a . Subscripts of dopants' labels specify dopant concentration per f.u.

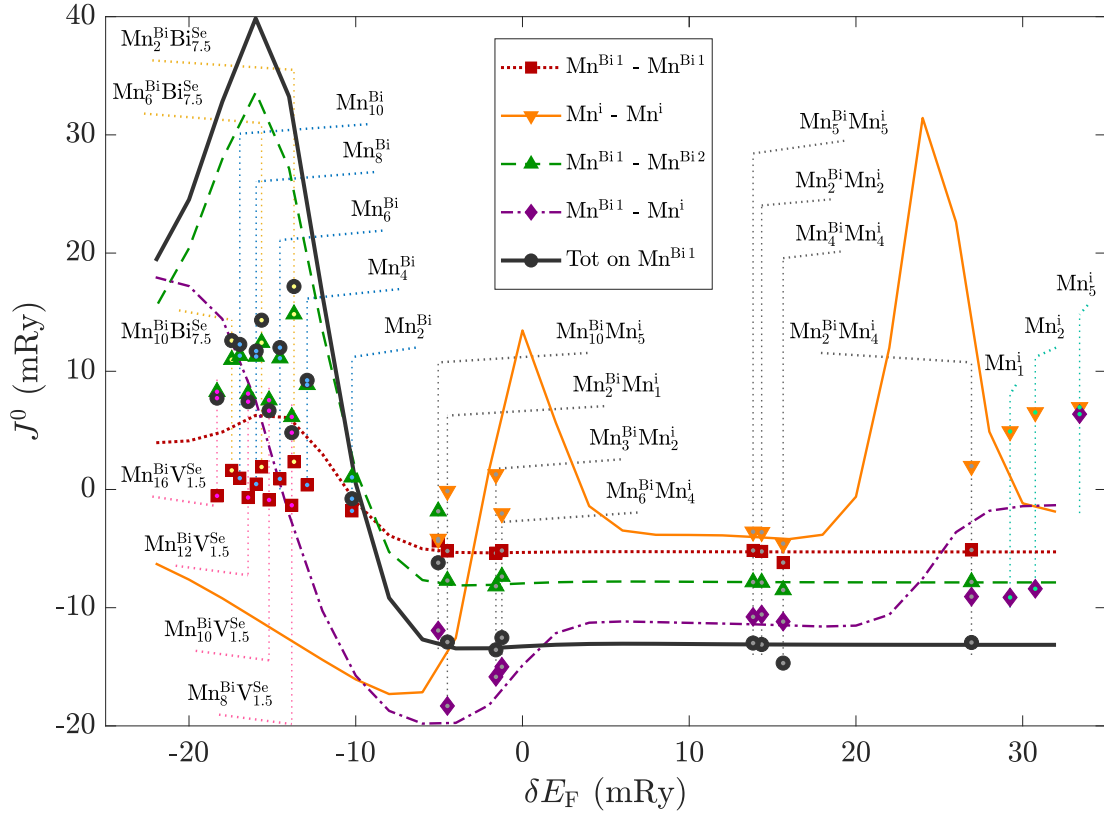


Figure 5.17: Relation between the Fermi level shift and magnitudes of magnetic exchange interactions. (lines) Exchange interactions between different magnetic dopants summed over all considered shells in the reference system with concentrations of magnetic dopants limiting to zero as a function of the Fermi level position relative to the Fermi level of pure Bi_2Se_3 . (points) Exchange interactions between different magnetic dopants calculated for a specific combination of dopants and depicted at the energy corresponding to its own Fermi level. They are also summed over all considered shells. Subscripts of dopants' labels specify dopant concentrations per f.u.

Obviously, one cannot describe the magnetic exchange interactions' behavior in detail since it is so complex, and the configuration space is enormous, considering all possible defects. Still, one can study the relationship between the Fermi level position and the exchange interactions' character as it might be partly related to the conduction electrons. This contribution is influenced by the Fermi level position, and one has observed that the defects are able to shift its position strongly. To evaluate the influence of the Fermi level position on the magnetic exchange interactions, we calculate the exchange interactions as a function of the Fermi level shift δE_F with respect to the unperturbed system employing just two magnetic defects in the pristine Bi_2Se_3 system (Fig. 5.17). In the CPA framework, it can be mimicked by limiting the concentration of magnetic defects to zero. The exchange interactions are evaluated for the same number of neighboring shells similar to the previous cases (Figs. 5.14, 5.16). However, for brevity, their sums $J_{A,B}^0$ related to particular magnetic sublattices A, B are depicted only. We restrict to the interactions within the same QL (Fig. 5.14a,c) or the same vdW gap (Fig. 5.16a) and the nearest Mn^{Bi} and Mn^{i} sublattices (Fig. 5.15c). The evaluated sums are depicted as functions of the Fermi level shift δE_F . It is determined

either by self-consistent calculation of systems containing various types of defects in comparison to the Fermi level of the unperturbed system or by the modified Fermi level position of the reference effective system (Fig. 5.17).

Comparing the disordered systems to the reference ones, we reveal a quite good agreement. Although the exchange interactions in the disordered systems are mostly weaker, which might arise from the increased electron scattering, there occurs a great qualitative correspondence with the reference system concerning the shape of dependencies. It suggests that the conduction electrons and the related RKKY exchange interactions substantially influence the observed magnetic behavior. The analysis also reveals that the n - resp. p -typed doping likely strongly influences the FM order's stability. It shows that below the Fermi level shift δE_F of -10 mRy strong positive Mn^{Bi} related interactions arise. It can be achieved just by the Mn^{Bi} doping or using the Bi^{Se} defects, which both represent the electron acceptors.

5.4 Curie temperatures

Having found almost positive magnetic exchange interactions concerning both Mn^{Bi} and Mn^{i} magnetic defect, we are encouraged to evaluate the FM ordering temperatures. It can be briefly estimated by means of the MFA, employing the on-site average pair exchange interactions $J_i^{0,\alpha}$. They are directly obtainable by Eq. 2.61. The MFA stands for the basic approximation in the description of the critical temperatures. Although it yields overestimated T_C 's due to complete neglecting of spin correlations, the MFA critical temperatures serve as the upper limit. It enables one not only to estimate the upper T_C limit but also to determine the influence of particular defects on its value briefly. Regarding studied diluted systems, the critical temperature can be evaluated through a simple modification of the original MFA formula (Eq. 3.21) considering the magnetic dopants concentration x as follows [21, 147]

$$k_B T_C^{\text{MFA}} = \frac{2x}{3} \sum_{i \neq 0} J_{0i}^{\text{Mn,Mn}}. \quad (5.1)$$

Employing the Eq. 2.61 and related averaged $J_i^{0,\alpha}$ interactions one can avoid the summation of $J^{\text{Mn,Mn}}$ interactions, which directly yields

$$k_B T_C^{\text{MFA}} = \frac{2}{3} J^{0,\text{Mn}}. \quad (5.2)$$

Neglecting tiny concentrations of the magnetic dopants, calculations reveal that the Mn^{Bi} T_C^{MFA} 's are higher the Mn^{i} ones (Fig. 5.18a, b). Regarding the concentration $x = 0.10$, the relative difference is about 15 %. Concerning small concentrations, approximately up to $x=0.05$, and no other defect, the ferromagnetic behavior is stronger in the case of Mn^{i} systems. However, a strong dependence on the occurrence of extra chemical defects appears. According to the calculated influence of chemical disorder on the exchange interactions' character (Figs. 5.14 and 5.16), the T_C^{MFA} 's are influenced by the actual composition. Concerning the Mn^{Bi} dopants (Fig. 5.18a), it is observed that only Bi^{Se} defects are possibly able to enhance the T_C little bit. Importantly, it is revealed that especially the Mn^{i} counterparts strongly suppress T_C 's. However, their occurrence is

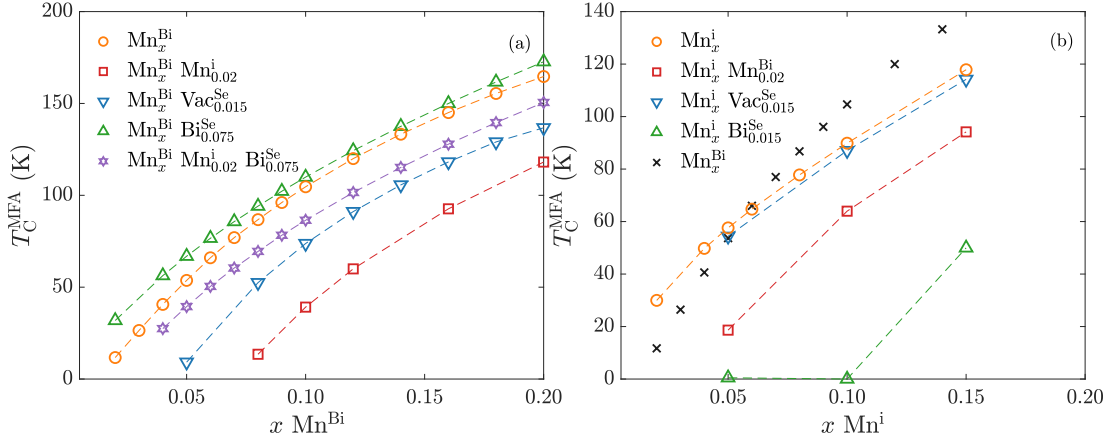


Figure 5.18: MFA magnetic ordering temperature as a function of the concentration x of Mn magnetic defects in dependence on the presence of other chemical defects: (a) Mn^{Bi} dopants (b), Mn^{I} dopants. Subscripts of dopants' labels specify dopant concentration per f.u.

far less probable than that one of the Mn^{Bi} dopants [113]. Also the Vac^{Se} 's cannot be omitted as the most probable intrinsic defects in Bi_2Se_3 systems [93, 95, 122]. It was shown that they suppress FM exchange interactions (Figs. 5.14), and thus, they decrease the T_C of Mn^{Bi} . The observed behavior corresponds to the described enhanced FM character of the Mn^{Bi} exchange interactions in the case of p -type doping, *e.g.* Bi^{Se} (Fig. 5.17). A similar influence of the Fermi level shift on Curie temperature values was observed *e.g.* in the MFA calculations of diluted magnetic semi-conductors as $(\text{Ga},\text{Mn})\text{N}$ or $(\text{Ga},\text{Mn})\text{As}$ [148].

A quite different effect of chemical disorder on the T_C^{MFA} is observed in the case of Mn^{I} dopants (Fig. 5.18b). Similarly to previous case, these T_C^{MFA} 's are suppressed in presence of the other type of Mn dopants (*i.e.* Mn^{Bi}). By contrary, the influence Bi^{Se} defects is opposite. Both studied native defects Bi^{Se} and Vac^{Se} suppress the T_C^{MFA} 's. However, it is hardly surprising thanks to the calculated Mn^{I} magnetic exchange interactions (Fig. 5.16). The observed modification of T_C^{MFA} 's qualitatively corresponds to the influence of the magnetic pair exchange interaction by the presence of extra chemical disorder (Figs. 5.14 and 5.16). Namely, regarding the in-plane Mn^{I} interactions, it has been found that their FM character is suppressed by co-doping.

One of the most reliable method to estimate the Curie temperature T_C is the Monte-Carlo (MC) simulation method [149–151]. Unlike the MFA, it does not neglect spin correlations. Thus it should provide nearly exact values of T_C in principle. Also, it allows for the chemical disorder in a more sophisticated way by means of a set of sufficiently large random supercell structures. In practice, however, the MC method's precision is limited by including a small finite number of the neighboring shells of interacting magnetic atoms due to computational demands. It leads to neglecting the long-range magnetic interactions. To evaluate the MC critical temperatures T_C^{MC} , we employ the Metropolis algorithm as implemented in Uppsala Atomistic Spin Dynamics (UppASD) package [152, 153].

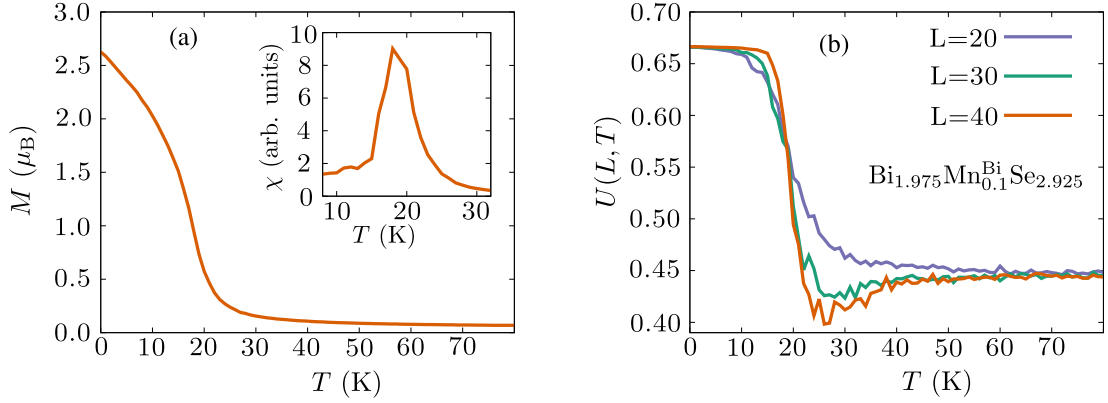


Figure 5.19: Temperature dependence of MC simulations calculated quantities for a Bi-rich Mn-doped Bi_2Se_3 system. (a) magnetization $M(T)$, and magnetic susceptibility χ in the inset, (b) Binder cumulants $U(L, T)$ for different sizes of simulated supercell: $L = 20, 30,$ and 40 .

The critical temperature in the MC simulations' framework is evaluated by means of the Binder cumulant [154]. It stands for the most reliable way, since it takes account of the finite size effects originating from the supercell approach. Thus, it provides a better reliability than approaches based on the evaluation of *e.g.* the magnetic susceptibility χ . Binder cumulant U is defined through the second and the fourth moment of the system magnetization M . It reads

$$U \equiv U(L, T) = 1 - \frac{\langle M^4 \rangle}{3\langle M^2 \rangle^2}, \quad (5.3)$$

where L characterize the dimension of the three-dimensional $L \times L \times L$ supercell. It denotes the number of elemental cells along one its side. $\langle \dots \rangle$ stands for averaging over MC step at the constant temperature T . The critical temperature T_C^{MC} is determined based on the characteristic critical behavior of the Binder cumulant as a function of the temperature T [154]:

$$\begin{aligned} \lim_{T \rightarrow 0} U(L, T) &= \frac{2}{3}, \\ \lim_{T \rightarrow \infty} U(L, T) &= \frac{1}{L}, \\ \lim_{T \rightarrow T_C} U(L, T) &= U^*, \end{aligned} \quad (5.4)$$

where U^* denotes an invariant independent of the supercell size L . It describes the point where the $U(L, T)$ curves as a function of the temperature T intersect and also it determines the critical temperature T_C^{MC} (Fig. 5.19).

The temperature dependence of magnetization $M(T)$ is determined by the simulated annealing technique, where a system initially thermalized at a sufficiently high temperature above the T_C is slowly cooled down toward the zero temperature. The MC simulations consist of more than 10^5 MC steps per each temperature point. For each considered combination of chemical defects and their particular concentrations, which is reflected by a unique set of pair exchange interactions, ten random distributions of Mn dopants in the supercell are generated. Besides, five independent parallel simulations for a certain Mn

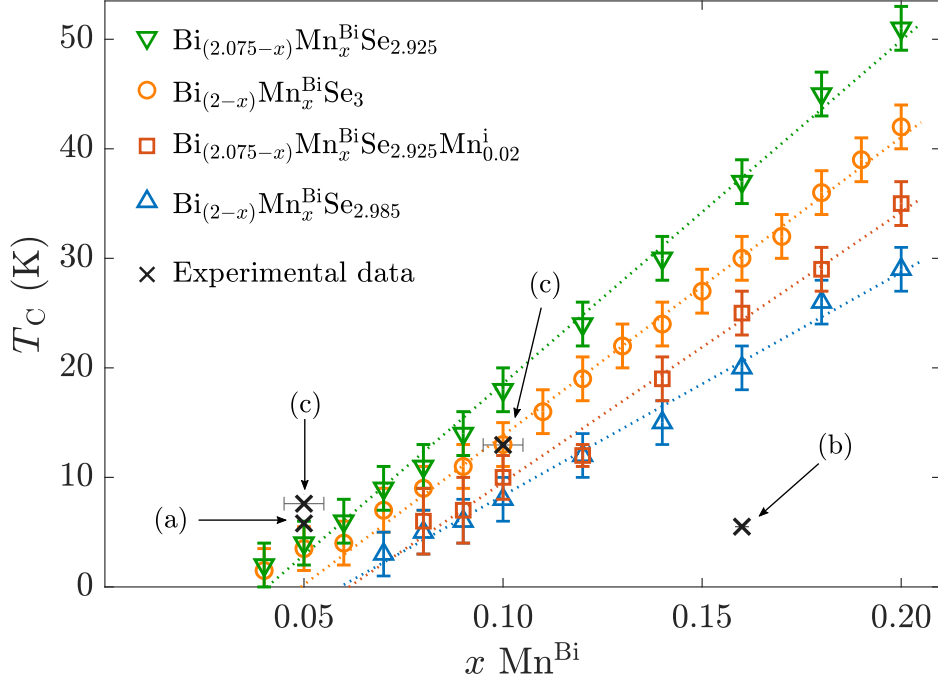


Figure 5.20: Dependence of the MC Curie temperature on the concentration x of substitutional Mn^{Bi} atoms and the inclusion of extra chemical defects. Depicted data: (\circ) Mn^{Bi} defects only, (\square) Mn^{Bi} and Bi^{Se} defects, (\triangle) previous case together with Mn^{i} , (∇) Mn^{Bi} defects with Vac^{Se} , (\times) experimental results originating from the following references: a [155], b [143], c [156].

dopant configuration are performed to improve the statistics. Also, large supercell ($L = \{20, 30, 40\}$) are considered to obtain correct intersections of Binder cumulant curves $U(L, T)$ with respect to T . We point out that only the T_C^{MC} of Mn^{Bi} dopants is evaluated as they are much more probable than the Mn^{i} one. A wide range of Mn^{Bi} magnetic pair exchange interactions, up to the mutual distance of 3.5 \AA of the Mn dopants, is included. It stands for eleven nearest neighbor atomic shells concerning the same Bi sublattice and fifteen shells in the case of distinct Bi sublattices. Overall, 175 distinct possible Mn neighbors can be considered.

Since the MFA provides only the upper limit for Curie temperatures, MC simulations are needed due to the estimation of their real values. The simulations show that the Mn^{Bi} Curie temperatures are far below the room temperature (Fig. 5.20). The obtained T_C^{MC} 's correspond for small Mn^{Bi} concentrations to the experimentally determined values [143, 155, 156]. However, the amount of defects as Vac^{Se} or Bi^{Se} is undetermined there. Therefore, concerning the chemical disorder, we provide a dependence of the Mn^{Bi} MC Curie temperatures (Fig. 5.20) on the presence of p - resp. n -type doping similar to the previous MFA calculations (Fig. 5.18a). It corresponds to the prediction made by Fermi level position manipulations (Fig. 5.17). It displays that the p -type doping (Bi^{Se}) enhances T_C of Mn^{Bi} whereas n -type doping (Vac^{Se} , Mn^{i}) suppresses them. Thus one might assume that the negligible dependence of the experimental T_C 's [143, 155, 156] on the Mn defect concentration arise from simultaneous presence of both Mn^{Bi} and Mn^{i} defects or alternatively from the influence of the native defects as Vac^{Se} [157, 158].

One should point out that an onset of the ferromagnetic order with the sample conductivity changing from n -type to p -type has been observed in certain experiments [156]. Finally, one can notice that in the case of MC simulations, the FM ordering is suppressed for small Mn^{Bi} concentrations. It likely originates from percolation effects. Besides, the nearly linear evolution of the T_C 's with increasing Mn^{Bi} corresponds to foregoing calculations [159].

5.5 Results summary

The scope of this chapter has been a chemical disorder in bulk Bi_2Se_3 . The influence of intrinsic as well as magnetic defects on the electronic structure has been inspected. Particularly, magnetic doping has been studied, where the character of Mn magnetic pair exchange interactions has been thoroughly discussed, including the estimation of the related magnetic pair exchange interactions. In the following, the main conclusions are stated.

- Both magnetic and nonmagnetic defects can substantially influence transport properties. It has been found that mid-gap states induced by most common intrinsic Bi_2Se_3 defect – Vac^{Se} fill the entire band gap. Similarly, the presence of the interstitial magnetic Mn^{i} defects brings about the closing of the minority spin channel. Besides, the occurrence of Se^{Bi} antisites cause also a significant reduction of the band gap width.
- The importance of the local relaxations in the case of the substitutional Mn doping is demonstrated as the sensitivity of the Bi_2Se_3 system to the relaxations is discussed.
- It has been found that actual composition, regarding magnetic as well as intrinsic defects, substantially influences magnitudes of magnetic moments and magnetic exchange interactions. Concerning magnetic moments' magnitudes, a significant enhancement of the Mn^{Bi} magnetic moments by Mn^{i} counterparts and Vac^{Se} has been observed. In the case of the Mn^{i} moment, they are strengthened by the Mn^{Bi} defects likewise, but the Se^{Bi} antisites appears to be ones of the most important regarding intrinsic defects.
- Concerning the magnetic exchange interactions, the ferromagnetic character of the interactions prevails, particularly for a higher amount of Mn defects, regarding the positive values of MFA Curie temperatures. However, strong antiparallel nearest neighbor Mn^{Bi} interactions there occur. Besides, considering inter atomic layer Mn^{Bi} pair interactions, likely Se atoms induced striking exchange interactions' enhancement has been observed.
- The revealed correspondence between the magnitudes of exchange interactions and the Fermi level shift indicates the RKKY character of the exchange interactions
- Regarding Mn^{Bi} dopants, a substantial enhancement of the stability of the FM order given by p-doping has been found. Electron acceptors, Mn^{Bi} defects as well as Bi^{Se} antisites, likely strengthen ferromagnetic exchange interactions for small negative Fermi level shifts.

- Predictions of the FM ordering temperatures, assuming a wide range of chemical defects, based on the MC simulation has been made. A nearly linear dependence of T_C 's on the Mn^{Bi} concentration has been observed. Substantial reduction of T_C 's by magnetic Mn^{i} counterpart and Vac^{Se} defect, the most probable native defects, has been found. It has been shown that the p-type counter-doping by e.g. Bi^{Se} might be required to enhance T_C in correspondence to the relation of the magnetic exchange strength and Fermi level shift.

6. Heisenberg Exchange Interactions – Influence of the Relativistic Corrections

So far, we calculated magnetic pair exchange interactions while the SO-interaction (Eq. 1.17) was neglected in the Hamiltonian during their evaluation by the Liechtenstein formula (Sec. 5.3) due to breaking of the global spin rotation invariance. Regarding the occurrence of a strong SO interaction within Bi_2Se_3 system, let's examine a possible influence of the modified Hamiltonian on the obtained Curie temperatures. Part of the presented results is included in the Refs. [3, 4].

In the TB-LMTO-ASA method's framework, the SO parameters $\xi_{\mathbf{R}\ell,ss'}$ arising from the SO matrix elements $\langle \phi_{\ell m s} | \hat{H}_{\text{SO}} | \phi_{\ell' m' s'} \rangle$ (Eq. 1.19) can be included as a perturbation in the orthogonal Hamiltonian H^{orth} (Eq. 1.35) via the modification of the matrix of the potential parameters C [6]

$$H^{\text{orth}} = \tilde{C} + \sqrt{\Delta} S^\gamma \sqrt{\Delta}; \tilde{C} = C + \xi. \quad (6.1)$$

Subsequently, it changes the potential parameters P (Eq. 1.38)

$$P^\alpha(z) = \left[\sqrt{\Delta} (z - \tilde{C})^{-1} \sqrt{\Delta} + \gamma - \alpha \right], \quad (6.2)$$

where an α LMTO representation is used [6]. Thus, it influences the auxiliary Green's function $g(z)$ and matrices Δ occurring in the Liechtenstein formula (Eq. 2.59). Therefore, one can ask how the neglected SO perturbation can modify the calculated T_C^{MFA} . However, even for the used collinear structure [25, 145, 146] the isotropic Heisenberg exchange interactions cannot be defined properly by employing the Eqs. 2.56 and 2.57 since the breaking of the global spin rotation invariance.

6.1 Bulk Bi_2Se_3 exchange interactions

Calculating the exchange interactions despite that fact, we obtain modifications of the exchange interactions' magnitudes and an artificial splitting of the exchange interactions as a function of the radial distance (Figs. 6.1, 6.2). It is related to a spatial modification of the exchange interactions' magnitudes as it is depicted for the in-plane pair exchange interaction in Fig. 6.3a. The symmetry of the texture is not exactly three-fold since slight asymmetry occurs in the x direction [146]. The modification of pair exchange interactions can be ascribed to the SO interaction. Regarding the inplane interactions, there exist a mirror crystal structure symmetry (we recall that Bi_2Se_3 is a dual TIs, Sec. 4.7). Thus, the interactions should respect the mirror symmetry without the SO interaction (Fig. 5.12d–inset). The modification of the exchange interactions leads to an underestimation of the MFA Curie temperatures (Eq. 5.2). Depending on the amount of Mn dopants, the MFA T_C is underestimated about 5 % – 6 %, except tiny concentrations below 4 % where the mismatch is relatively more massive.

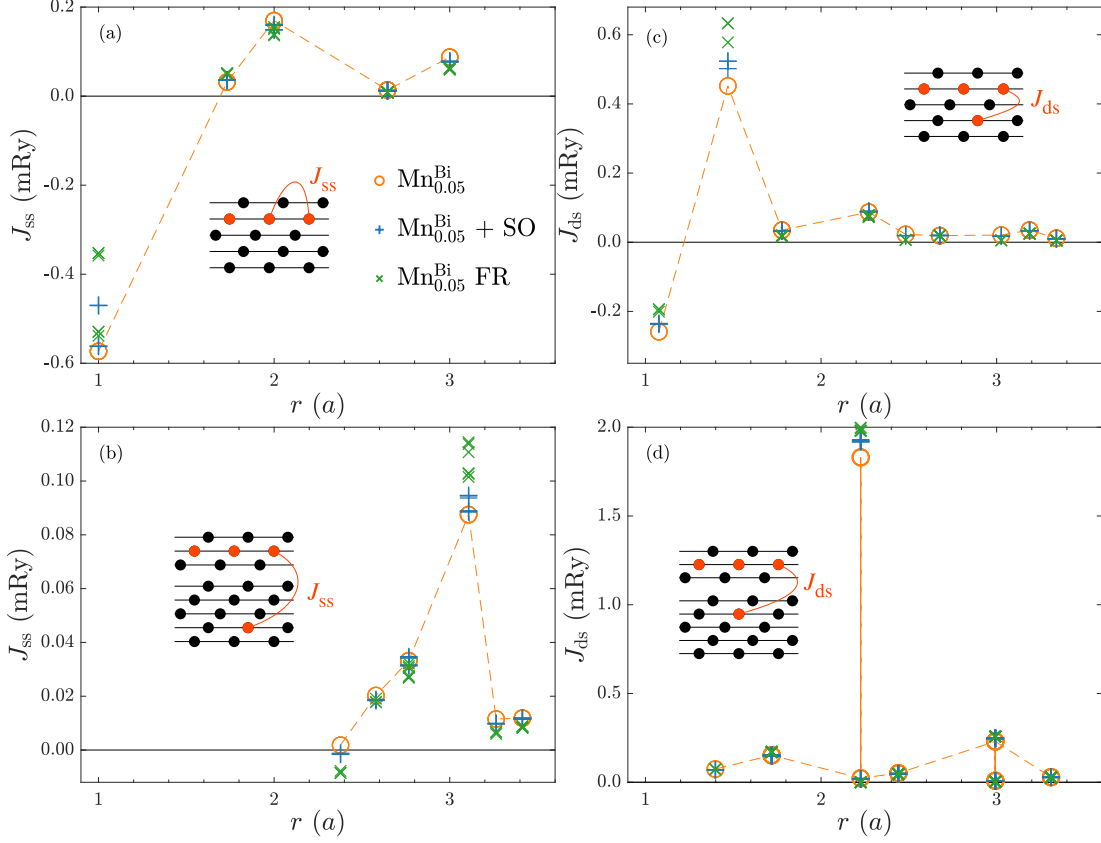


Figure 6.1: Deviation of the Mn^{Bi} magnetic exchange interactions caused by the inclusion of the SO coupling as a function of the mutual distance r . A $\text{Bi}_{1.95}\text{Mn}_{0.05}\text{Se}_3$ system is considered: (\circ) scalar relativistic approach with the neglected SO interaction, ($+$) scalar relativistic approach with the included SO interaction, (\times) fully relativistic approach. The distance is expressed in terms of the lattice parameter a . (a) Magnetic moments belonging to the same sublattice at the same hexagonal layer. (b) Magnetic moments belonging to the same sublattice, but in neighboring QLs. (c) Magnetic moments belonging to the different sublattices in the same QL. (d) Magnetic moments belonging to the different sublattices and neighboring QLs.

It shows that the neglected SO in the exchange interactions' calculations do not significantly influence the obtained data.

We have discussed the calculation in the framework of the scalar relativistic approach yet. A question might occur, what happens if one would work within the fully relativistic framework and how the observed modulation would change. We tried to implement the calculation of the magnetic exchange interactions through the Liechtenstein formula in this way. Concerning the fully relativistic framework, the LMTO canonical potential parameters P^0 are defined by relativistic potential parameters γ , C , W [6]. The Λ -th block of P^0 , reads

$$P_{\Lambda}^0(z) = \left(\gamma_{\Lambda} + W_{\Lambda}^T (EI_2 - C_{\Lambda})^{-1} \right)^{-1}, \quad (6.3)$$

where the index Λ is composed of relativistic quantum numbers μ, κ_1, κ_2 . However, considering the spin polarization along the z -axis, the spin resolved auxiliary Green's function can be constructed from the output of the fully relativistic calcu-

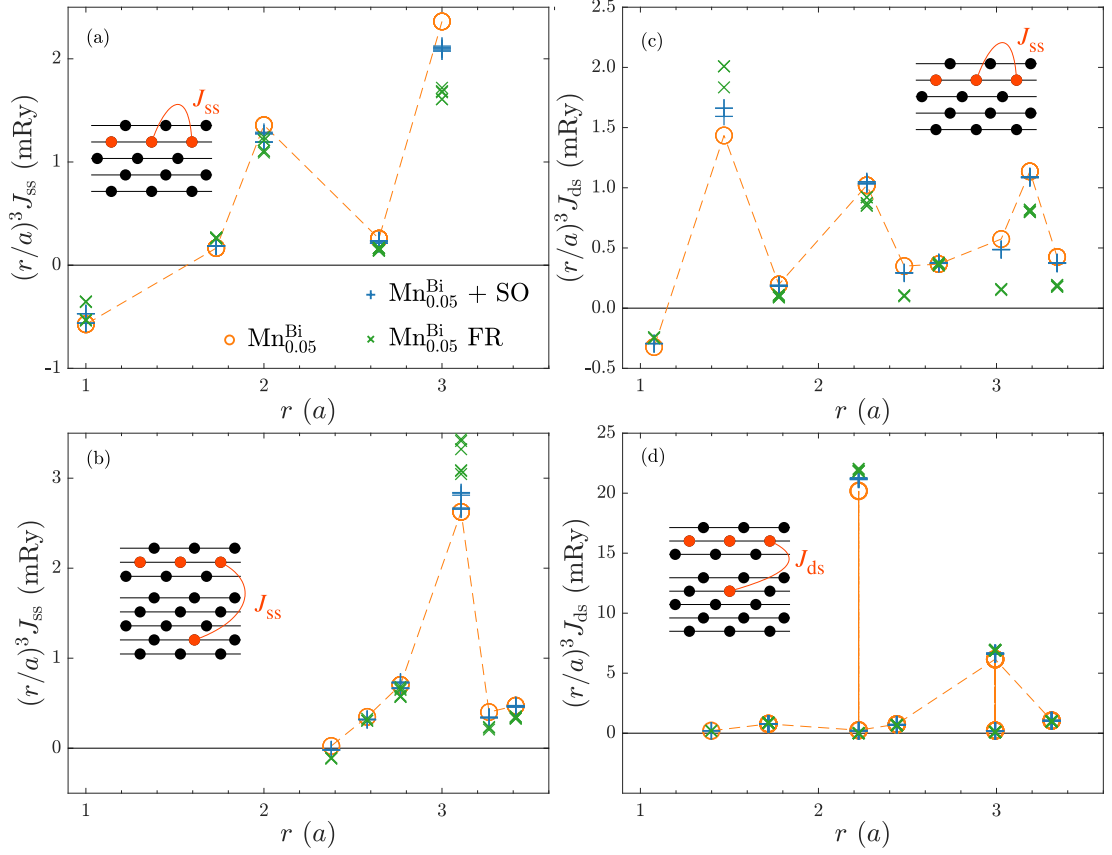


Figure 6.2: Deviation of the Mn^{Bi} magnetic exchange interactions caused by the inclusion of the SO coupling and scaled by the factor $(r/a)^3$ a function of the mutual distance r in units of the lattice parameter a . A $\text{Bi}_{1.95}\text{Mn}_{0.05}\text{Se}_3$ system is considered: (○) scalar relativistic approach with the neglected SO interaction, (+) scalar relativistic approach with the included SO interaction, (×) fully relativistic approach. (a) Magnetic moments belonging to the same sublattice at the same hexagonal layer. (b) Magnetic moments belonging to the same sublattice, but in neighboring QLs. (c) Magnetic moments belonging to the different sublattice in the same QL. (d) Magnetic moments belonging to the different sublattices and neighboring QLs.

lation by means of a transformation of the spin spherical harmonics' basic set to the non-relativistic one employing the appropriate Clebsh-Gordon coefficients $\langle \kappa\mu | \ell m s \rangle$ [6, 8]. They are defined as follows

$$\langle \kappa\mu | \ell m s \rangle^{\mathcal{C}} = \delta_{|2\kappa+1, 2\ell+1} \delta_{\mu, m+s} \text{sgn}(|\kappa| - \kappa - 2s) \sqrt{\frac{1}{2} - \frac{2s\mu}{2\kappa+1}}; \quad (6.4)$$

$$(m > 0)$$

$$\langle \kappa\mu | \ell - m s \rangle^{\mathcal{R}} = i \left[\langle \kappa\mu | \ell - m s \rangle^{\mathcal{C}} - (-1)^m \langle \kappa\mu | \ell m s \rangle^{\mathcal{C}} \right] / \sqrt{2},$$

$$\langle \kappa\mu | \ell m s \rangle^{\mathcal{R}} = i \left[\langle \kappa\mu | \ell - m s \rangle^{\mathcal{C}} + (-1)^m \langle \kappa\mu | \ell m s \rangle^{\mathcal{C}} \right] / \sqrt{2}, \quad (6.5)$$

$$(m = 0)$$

$$\langle \kappa\mu | \ell m s \rangle^{\mathcal{R}} = \langle \kappa\mu | \ell m s \rangle^{\mathcal{C}}, \quad (6.6)$$

where the superscript \mathcal{C} denotes coefficient related to the complex spherical har-

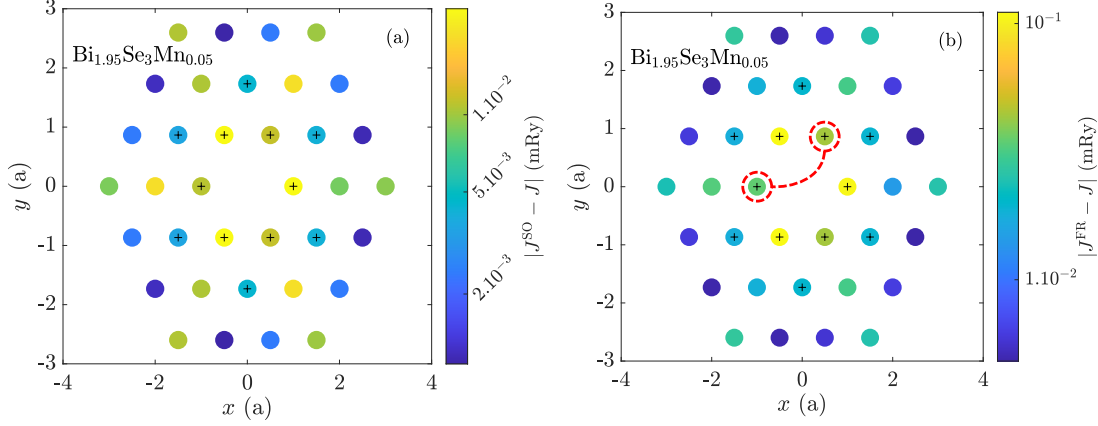


Figure 6.3: Spatial distribution of the exchange interaction modification caused by the inclusion of SO interaction: (a) within the scalar relativistic approach, (b) fully relativistic approach, both compared to the unperturbed scalar relativistic one. Exchange interactions within the same hexagonal Bi layer are depicted only. Dashed line indicates anisotropy along the x axis. The plus sign denotes positive difference $J^{\text{SO}} - J$.

monics and superscript \mathcal{R} for the real ones [160]. Then the structure constants S can be evaluated as in the scalar relativistic case [6]. It enables one to obtain the conditionally averaged auxiliary Green's function using the CPA self-consistent loop (Eq. 1.59). Similar to the case of the scalar relativistic approach, we deal only with their spin diagonal blocks to examine the behavior of the corrupted exchange interactions. It allows us to compare partly the result obtained either by the scalar relativistic to the fully relativistic approach, where the SO coupling is present directly in the Hamiltonian not only as a perturbation. Relativistic calculations provide a little bit smaller magnitudes of Mn magnetic moments (Fig. 6.5) and slightly changed exchange interactions' magnitudes. However, the shape of the radial dependence of the exchange interactions remains nearly unchanged (Figs. 6.1, 6.2). One can observe that the splitting of the data points in the radial dependence becomes more pronounced. It likely arises from a more sophisticated treatment of the SO coupling, which supports the origin of the splitting. Besides, the anisotropy along the x direction is better visible (Fig. 6.3b). The value of the MFA T_C 's are reduced in the range of 3 % – 14 % compared to the original SRA values for the studied Mn concentrations, where the difference increases with the increasing concentration (Fig. 6.4). Partly, the observed difference might arise from slightly distinct calculated spin splitting (Fig. 6.5). However, the strong artificial splitting of the exchange interactions corrupts the estimated MFA T_C 's as well (Figs. 6.1, 6.2). Finally, the calculations show that the improper evaluation could lead to a substantial error in magnitudes of particular of the exchange interactions, for instance, the nearest neighbor interactions' splitting (Figs. 6.1). Still, in total, the estimated MFA Curie temperatures are not too distinct compared to the original calculation (Sec. 5.4), notably considering the related scalar relativistic approaches with and without included SO interaction.

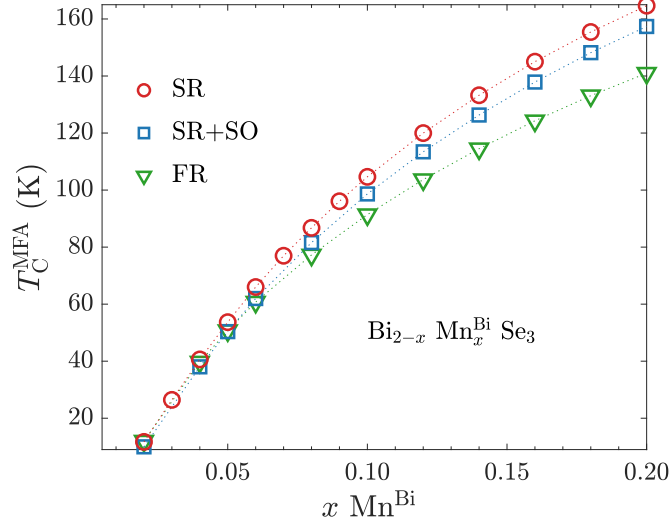


Figure 6.4: MFA magnetic ordering temperature as a function of the Mn^{Bi} dopants concentration x depending of the inclusion of the SO interaction: (\circ) scalar relativistic approach with the neglected SO interaction, (\square) scalar relativistic approach with the included SO interaction, (∇) fully relativistic approach.

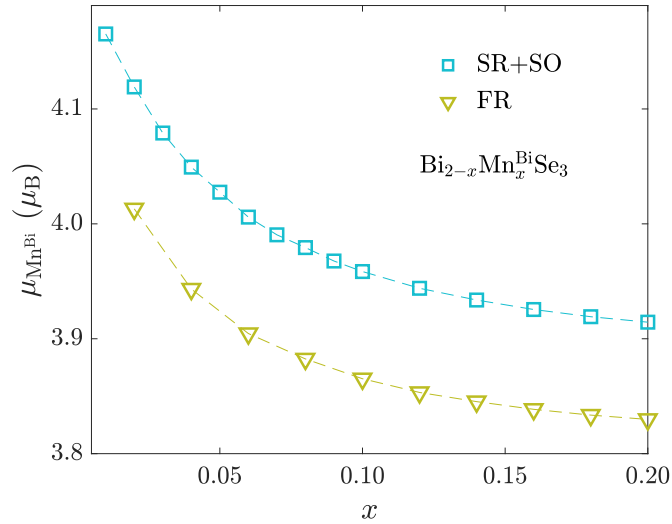


Figure 6.5: Comparison of Mn^{Bi} magnetic moments' magnitudes in the case of scalar and fully relativistic approaches as a function of the dopants concentration: (\square) scalar relativistic approach with the included SO interaction, (∇) fully relativistic approach.

6.2 Transition metals alloys' exchange interactions

So far, we have discussed the error in the case of the compound possessing a significant SO interaction. Now, let's focus on systems where the SO interaction's influence is not such significant such as $3d$ -metals and compare the obtained results. Actually, we study the behavior of the exchange interactions in multi principal element alloys based on the $3d$ -metals (Cr, Mn, Fe, Co, Ni) [3, 4]. Disordered systems should be suitable as the exchange interactions should decay fast as a function of the radial distance due to the alloying [22]. Thus, one likely does not have to pay much attention to long-range interactions. The mentioned alloys are called high-entropy alloys since a substantial stabilization of the high-temperature phase is provided by the entropy term [161]. They represent an interesting sort of material as they possess high application potential concerning the engineering [162–164]. However, the CrMnFeCoNi alloy bears only a paramagnetic behavior despite being composed of magnetic elements [165]. Therefore, it is worthy of studying the exchange interactions there, for instance, by using a non-magnetic substitution. Concerning the CrMnFeCoNi derivatives, we estimate the distortion of the magnetic exchange interactions caused by the non-neglected SO interaction within the scalar relativistic approach's framework. Comparing the results with and without the SO interaction, we find that the splitting of the exchange interactions is irrelevant there even for long-range interaction (Fig. 6.6), based on the analysis of the RKKY oscillation [22] rescaling the data by the factor $(r/a)^3$ (Eq. 2.41). Moreover, the calculations employing the SO interaction follow well the original data, where it is neglected (Fig. 6.6). It suggests a weak importance of the SO interaction for such alloys. To evaluate the difference, let's estimate the FM MFA Curie temperatures [4]. Since we are not concerned with diluted magnetic atoms, we have to employ a more sophisticated approach to evaluate the MFA T_C . Regarding the multi-sublattice system, it can be obtained by solving a eigenvalue problem considering a symmetric matrix $\mathbb{J}^{\alpha\beta}$ [22]. It is defined as follows

$$\mathbb{J}^{\alpha\beta} = c^\beta \sum_i J_{0i}^{\alpha\beta}, \quad (6.7)$$

where $J_{0i}^{\alpha\beta}$ is the pair exchange interaction related to an atom of the- α -type at the origin and the other one of the β -type at the site i , c^β stands for the appropriate concentration. Then, the MFA T_C is defined by the maximal eigenvalue j_{\max} of the matrix $\mathbb{J}^{\alpha\beta}$, which yields

$$k_B T_C = \frac{2}{3} j_{\max}. \quad (6.8)$$

We discuss the body-centered cubic (BCC) crystal structure as it provides enhanced magnetic behavior compared to the closed pack structures as FCC or hexagonal close-packed (HCP) [3]. To obtain great convergence of the MFA T_C values, a large number of atomic shells N_{sh} is taken into account. Namely, we use $N_{\text{sh}} = 70$, which is related to distances $r < 7.2 a$, where a is the appropriate lattice parameter. It stands for 110 different neighbors in the irreducible part of the space concerning the calculations without SO interaction and over 3000 neighbors in the whole space regarding the other case. Comparing the MFA T_C 's

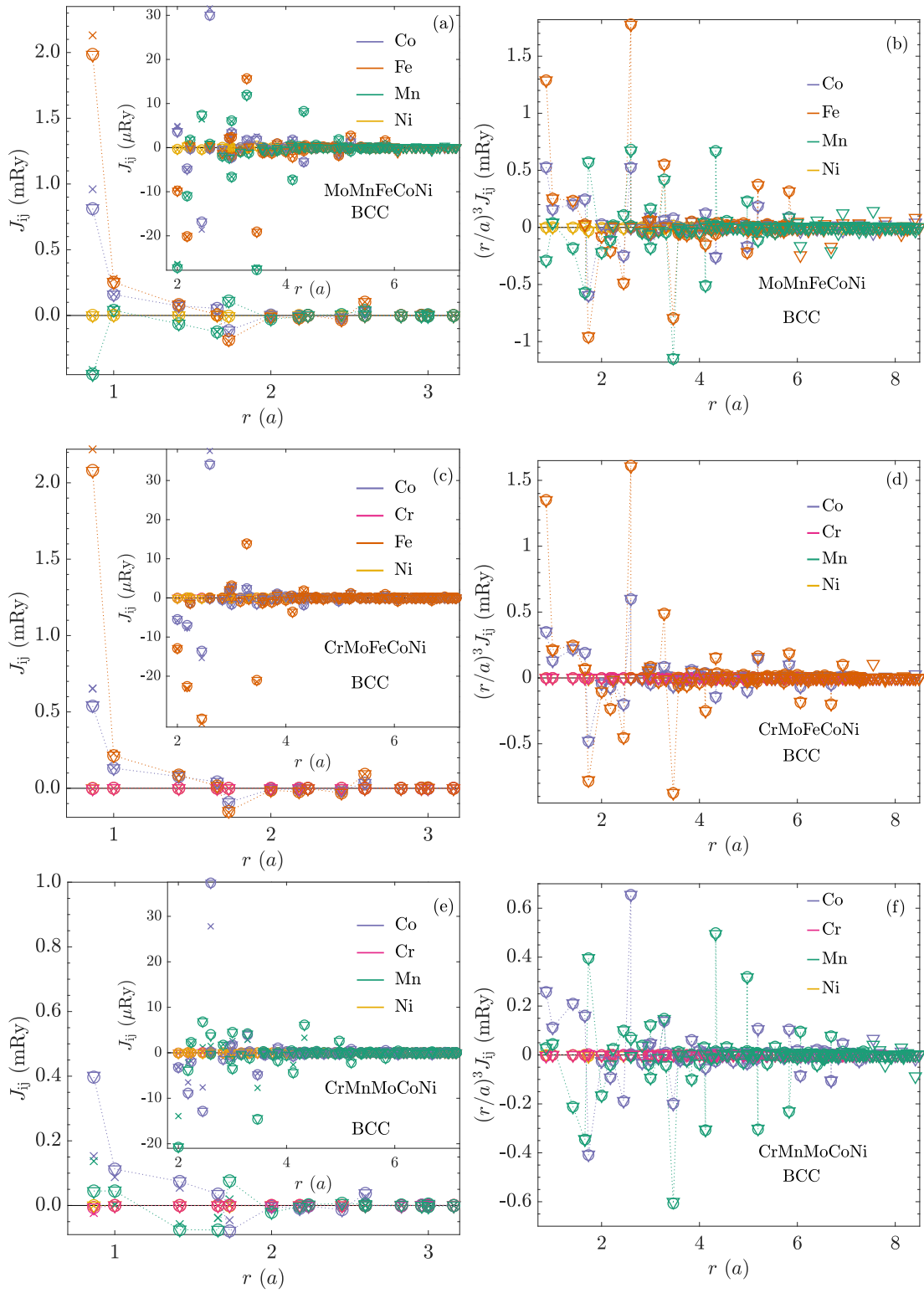
alloy	T_C (K)		
	SR	SR + SO	FR
<i>MoMnFeCoNi</i>	686	685	762
<i>CrMoFeCoNi</i>	553	553	608
<i>CrMnMoCoNi</i>	265	265	164
<i>CrMnFeMoNi</i>	470	469	499
<i>CrMnFeCoMo</i>	754	754	834

Table 6.1: MFA ferromagnetic Curie temperatures of Mo-based CrMnFeCoNi derivatives: SR - scalar relativistic approach, SR+SO - scalar relativistic approach with included SO interaction, FR - fully relativistic approach.

alloy		magnetic moments per element					(μ_B)
		<i>MoMnFeCoNi</i>	SR	-0.218	1.970	2.221	
	FR	-0.191	1.921	2.223	1.438	0.300	
<i>CrMoFeCoNi</i>	SR	0.037	-0.078	2.145	1.226	0.117	
	FR	0.062	-0.063	2.147	1.278	0.132	
<i>CrMnMoCoNi</i>	SR	-0.116	1.584	-0.083	1.144	0.107	
	FR	-0.195	1.004	-0.043	-0.798	0.074	
<i>CrMnFeMoNi</i>	SR	-0.217	1.376	2.024	-0.122	0.176	
	FR	-0.206	1.384	2.057	-0.115	0.195	
<i>CrMnFeCoMo</i>	SR	-0.042	1.642	2.122	1.383	-0.120	
	FR	-0.025	1.706	2.179	1.476	-0.112	

Table 6.2: Element resolved magnetic moments magnitudes of Mo-based CrMnFeCoNi derivatives: SR - scalar relativistic approach, FR - fully relativistic approach.

estimated in terms of the neglected and included SO interaction (Tab. 6.1), we find that the difference is negligible approximately up to 1 K (error up to 0.2 %), which corresponds to coinciding exchange interactions (Fig. 6.6). Small differences concerning the magnetic moments' magnitudes caused by the neglecting of the SO interaction might contribute. Having observed the negligible effect of the SO interaction, one can think about the impact of the fully relativistic treatment. However, even there, the splitting of the exchange interaction values as a function of the distance is insignificant (Figs. 6.6 and 6.7). Thus, it suggests a negligible corruption of the exchange interactions regarding these 3d-metals alloys. The enhanced magnitudes of the MFA T_C 's (Tab. 6.1) likely arise from modified magnitudes of magnetic moments concerning the FR approach (Tab. 6.2) [3]. Their relative change is about a few percent there.



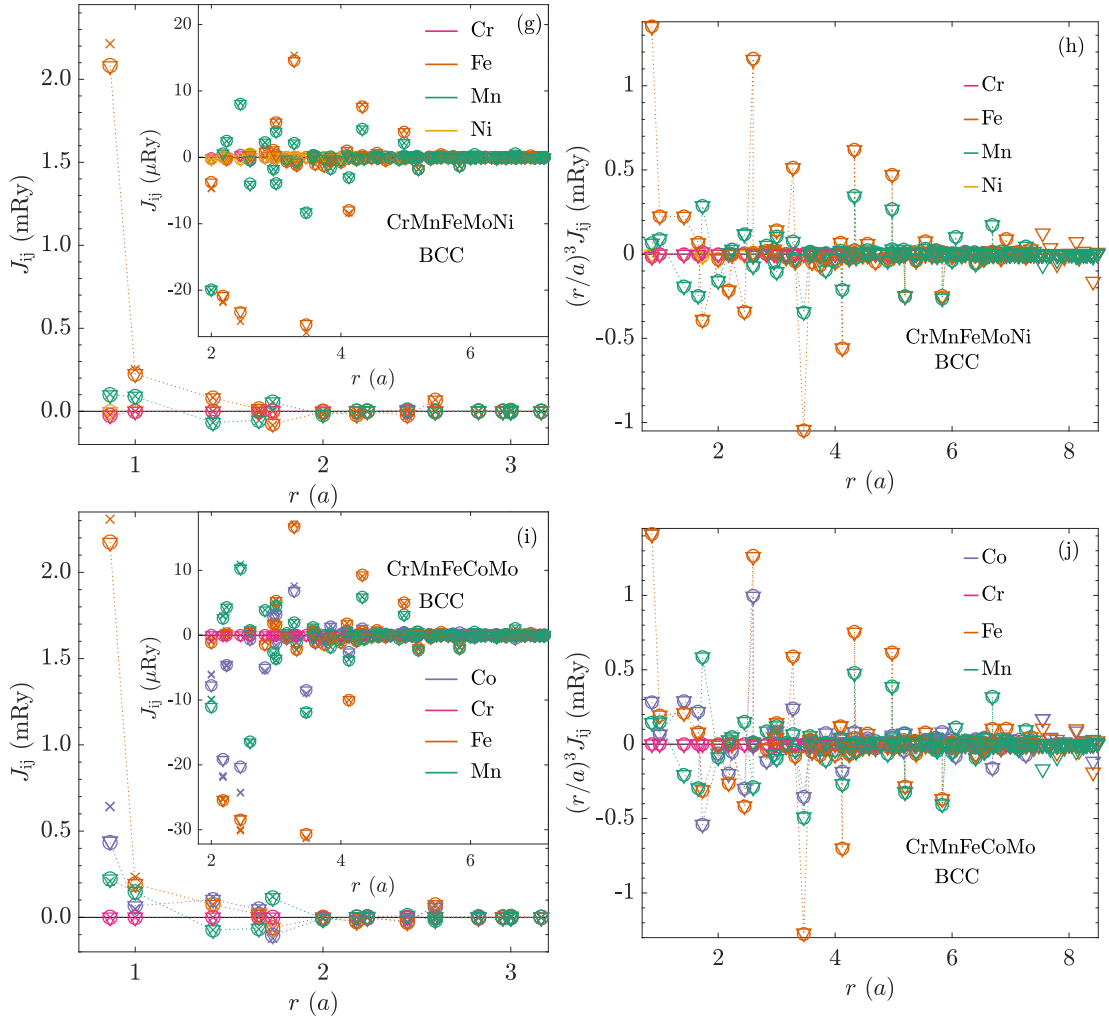


Figure 6.6: Exchange interactions of the Mo-based CrMnFeCoNi derivatives. (a,c,e,g,i) Radial distribution of the pair exchange interactions. (b,d,f,h,j) Radial distribution of the pair exchange interactions rescaled by $(r/a)^3$ – RKKY oscillations. (○) Scalar relativistic approach with the neglected SO interaction, (▽) scalar relativistic approach with the included SO interaction, (×) fully relativistic approach.

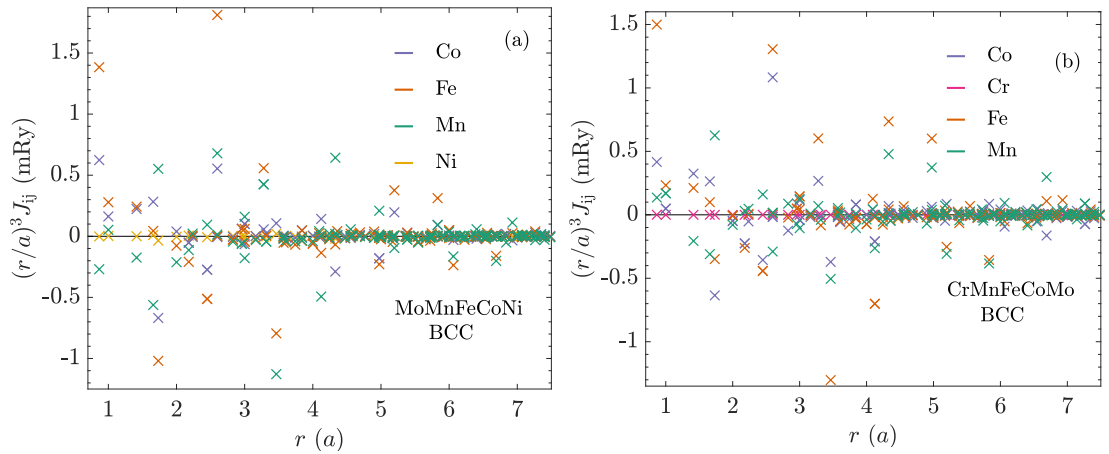


Figure 6.7: RKKY-like oscillations of the Mo-based CrMnFeCoNi derivatives' exchange interactions calculated in the framework of the fully relativistic approach.

6.3 Results summary

This chapter focuses on the impact of the missing SO interaction in calculations of Heisenberg exchange interactions as they were introduced in Sec. 5. Implementing the exchange interaction calculation in the SRA framework allowing for the SO as well as in the FR treatment, the modification of the exchange interactions' character and their magnitudes are discussed. It includes the modification of Curie temperatures likewise. In the following, the main conclusions are stated.

- Regarding Bi_2Se_3 possessing strong SO coupling, we have observed small deviations of exchange interaction's magnitudes residing at the nearest neighbor shells. They are accompanied by magnitudes' splitting due to the SO induced anisotropy. Concerning the SRA, we have shown that the character of the exchange interactions is nearly unchanged and the MFA Curie temperatures are only slightly suppressed. The comparison of the scalar and fully relativistic approaches indicates that more substantial are the preceding electronic structure calculation as different spin splitting has been obtained.
- Considering light elements and their alloys, it has been demonstrated that the SO interaction hardly influence the character of the exchange interactions irrespective of the employed approach as no visible data points splitting has been observed.

7. Bi₂Se₃ Thin Layers

So far, the properties of Bi₂Se₃ bulk structure have been discussed (Chapter 5). However, this compound belonging among 3D TIs attracts attention, particularly by the occurrence of gapless surface states (Sec. 4.7). Thus, in the following chapter, we examine the chemical disorder's influence, concerning the magnetic dopants and native defects, on the surface electronic structure properties similar to the bulk case. In order to describe the surface effects, one has to tackle multilayered structures, which can be solved through the layered Green's function LMTO method (Sec. 4.7). It enables us to study the layered resolved electronic structure, including the surface states, in presence of the mentioned chemical disorder. Moreover, not only the point defects can be treated, but also the impact of stacking fault as twin planes (TPs) [97–99] can be possibly discussed. Presented results mostly concerning the TP behavior are included in the Ref. [2].

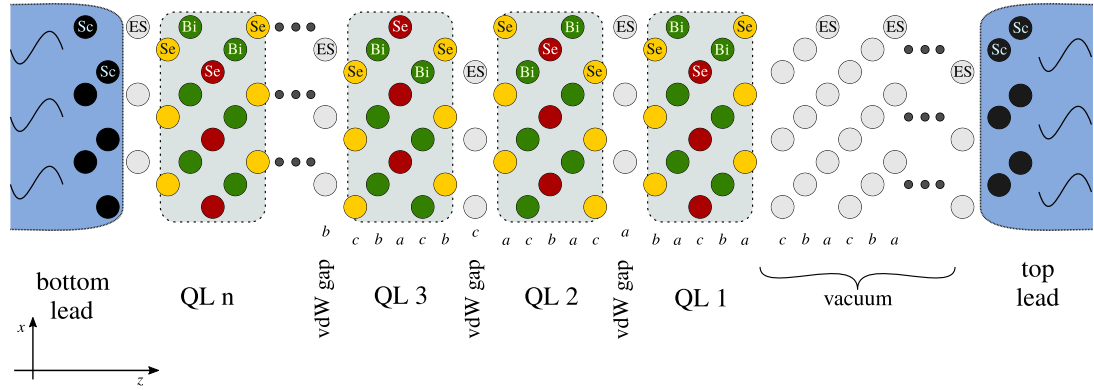


Figure 7.1: Layout of the calculated multilayer Bi₂Se₃ structure with a top vacuum surface.

7.1 Computational details

To compose a thin layer Bi₂Se₃ structure (Fig. 7.1), the previously used bulk lattice parameters and inner coordinates are employed (Chapter 5). In agreement with the bulk calculations, a local lattice relaxation related to Mn^{Bi} dopants is reflected through modifications of the Wigner-Seitz radii in the same way as in bulk (Sec. 5.2). To simulate a vacuum interface, where the gapless surface states can occur, we build a multilayer Bi₂Se₃ system as follows. It is placed in between two same semi-infinite Sc leads, which are needed to perform self-consistent calculations (Sec. 1.4.2). Besides, leads also set the Fermi level position in the whole simulated slab. Sc is chosen since its HCP crystal structure, and its lattice parameters nearly suit the Bi₂Se₃ structure. Lattice parameters are not too distinct, and the crystal structure fits the FCC-like stacking of Bi₂Se₃ QLs. A vacuum interface is created by placing a vacuum spacer between the top lead and the Bi₂Se₃ slab. It consists of several ES layers in a similar sense to the vdW gap. The ES layers extend Bi₂Se₃ slab following an FCC-like stacking and respecting the three-fold symmetry of the Bi₂Se₃ structure. Focusing on the surface states, we increase the k -mesh density for a better description of the

electronic structure, where almost 5000 k -points in the 1st BZ are used. In the layered TB-LMTO calculations framework, a multilayer structure is divided into principal layers (Sec. 1.4.2). Regarding the present work, each principal layer consists of two atomic layers. It is found to be adequate for the surface states' description, whereas calculations using smaller principal layers fail there. On the other hand, larger blocks make the calculation extremely time demanding.

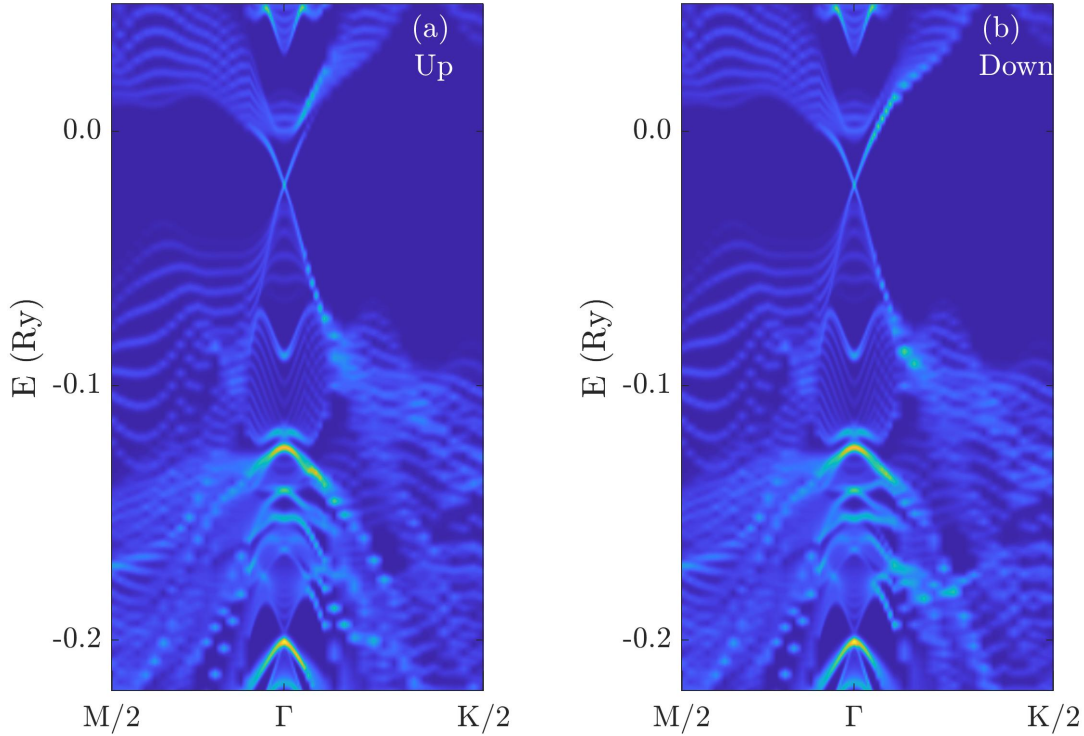


Figure 7.2: Bloch spectral functions related to the top QL of a Bi_2Se_3 slab consisting of 10 QLs employing a 10 ES layer thick vacuum spacer: (a) spin up channel, (b) spin down channel.

7.2 Thin layers & surface states

A sufficient thickness of the vacuum spacer and the Bi_2Se_3 slab to obtain gapless surface states is thoroughly checked. We perform an analysis of the BSF (Fig. 7.2a) in the vicinity of the Γ calculated at the path in between high symmetrical M and K points of the appropriate hexagonal 2D BZ (Fig. 4.16e). However, the BSF is hardly convenient for comparison of different multilayer structures. Therefore, we deal with a BSF projection along the k -path to the energy-intensity plane (Fig. 7.3), where the maximal intensity of the BSF over the considered k -path in the vicinity of the Γ point is ascribed to particular energy points

$$\text{PBSF}(E) = \max_k (\text{BSF}(E, k)) . \quad (7.1)$$

It results in easily handled line plots. One can simply compare the projected Bloch spectral function (PBSF) curves related to particular studied cases and

detect a formation of gapless Dirac states. It is indicated by band gap closing and presence of a striking intensity at the Dirac point where the surface states intersect (Fig. 7.4). Evaluating the obtained PBSF curves, we find that the surface Dirac states appear with increasing thickness of the Bi_2Se_3 slab (Fig. 7.4a). The initial band gap (~ 93 meV concerning 3 QLs Bi_2Se_3 slab) is being closed around the Bi_2Se_3 slab thickness of 7 QL, and gapless Dirac surface states occur there. One can notice a nice monotonous dependence of PBSF in the vicinity of the Dirac point denoted by an intensity peak. It proves that the thickness of 10 QLs chosen for further calculations is sufficient to form the surface Dirac states. Besides, the obtained results correspond well to the experimental evidence and theoretical models. Regarding the thinnest Bi_2Se_3 slab (3 QL), only Rashba-like splitting occurs [166] (Compare Figs. 7.4b and 7.5c). The non-existence of Dirac states can be explained by hybridization between the top and bottom edge states due to their non-negligible overlap originating from the insufficient thickness of the slab [19, 33]. Increasing the thickness, the overlap vanishes, and the Dirac states are formed [166] (Figs. 7.4c and 7.5e), where the obtained surface band structure corresponds well to ARPES measurements [167, 168]. One can notice that there occurs a shift of the Fermi level position towards the conduction band in comparison to the bulk results (compare Fig. 7.4 and Fig. 5.3). It likely arises from a small observed artificial charge transfer out of the semi-infinite leads toward the simulated slab.

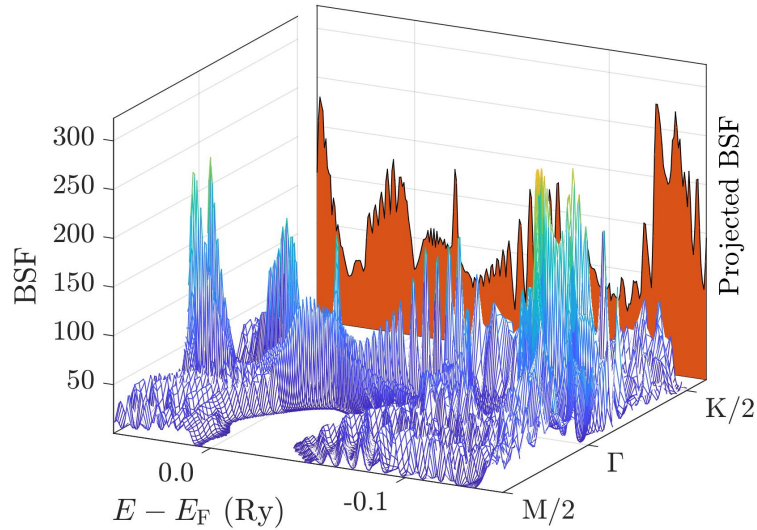


Figure 7.3: Projected Bloch spectral function.

Similarly, we estimate a sufficient thickness of the vacuum spacer (Fig. 7.6). A small number of used ES's layers leads to an artificial corruption of the surface band structure (Fig. 7.6b), likely due to hybridization with the electronic states of the top lead. For instance, one can observe a Rashba-like splitting in the conduction band. It vanishes with the increasing vacuum spacer thickness, while the shape of the surface electronic structure near the Γ point converges (Figs. 7.6a,c and 7.4c). It follows that the used vacuum spacer thickness of 10 ES's is large enough to a reliable description of the surface states. We point out the difference

between PBSF curves in Fig. 7.4 and Fig. 7.6. It stems from the usage of distinct k -meshes, where the first one (Fig. 7.2) is finer.

Finally, we examine the behavior of the inner QLs (Fig. 7.7). Regarding larger Bi_2Se_3 slab thicknesses, the bulk-like QLs seems to be hardly influenced by the surface states and the band gap width ($E_{\text{gap}} = 332$ meV, considering 10 QLs thick slab and vacuum spacer of 10 ES's layers.) approaches to the bulk value (Sec. 5.2). Concerning the Bi_2Se_3 slab composed of 3 QLs, the modification of the electronic structure and related reduction of the gap width arises from the proximity to the bottom interface. Considering larger multi-layered structures, the influence of the interface is ebbing. Besides, only slight penetration of the surface states to 3rd QL is observed.

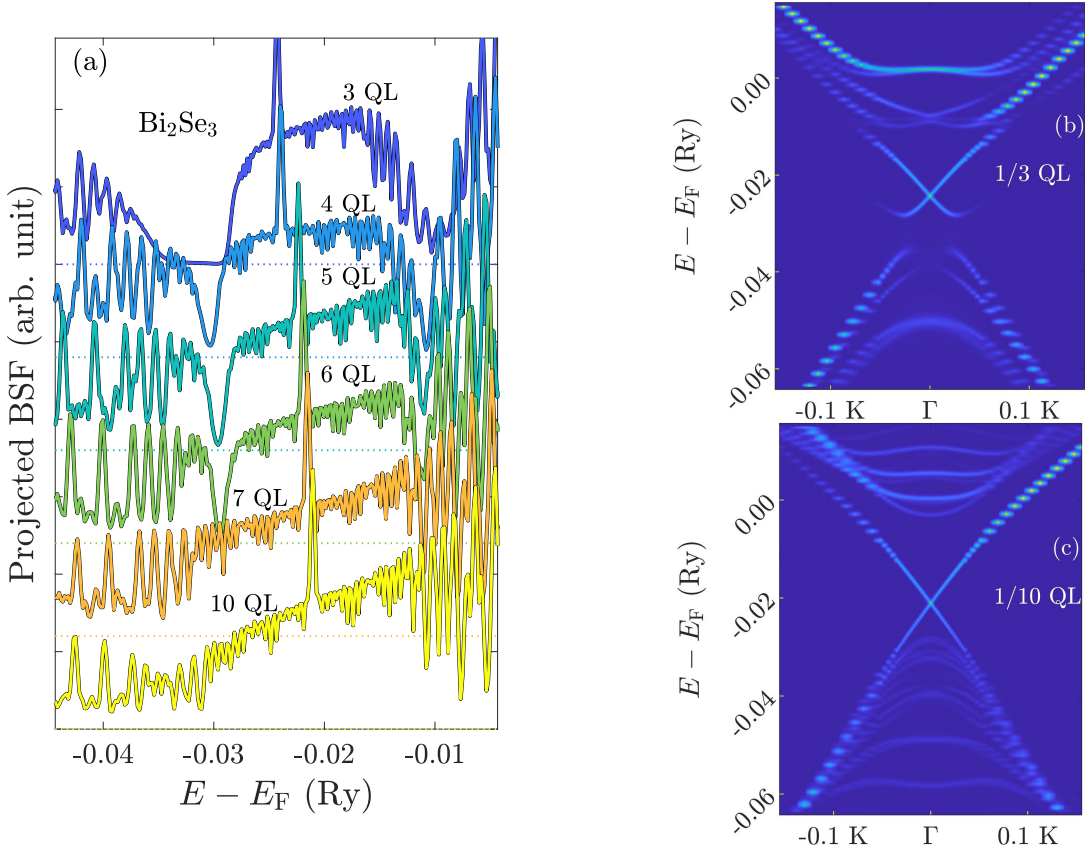


Figure 7.4: Formation of surface states with increasing thickness of the simulated Bi_2Se_3 slab. Ten ES layers thick vacuum spacer is used. (a) Projected Bloch spectral function of the surface QLs. Dispersions related to Bi_2Se_3 slabs composed from 3 QLs to 10 QLs are depicted. Curves are labeled by the Bi_2Se_3 slab thickness. Dotted lines denote zero levels. (b,c) Bloch spectral functions of the surface QL in the vicinity of the Γ point. Either 3 QLs or 10 QLs Bi_2Se_3 slabs are considered.

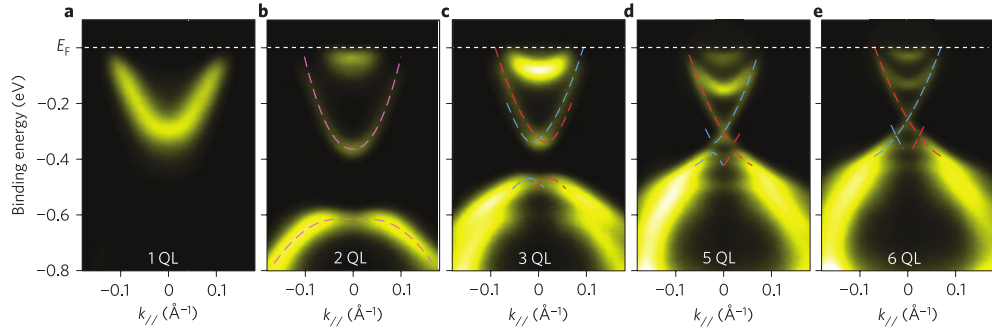


Figure 7.5: Experimental Bi_2Se_3 thin-film ARPES spectra in dependence on the film thickness. (adapted from [166])

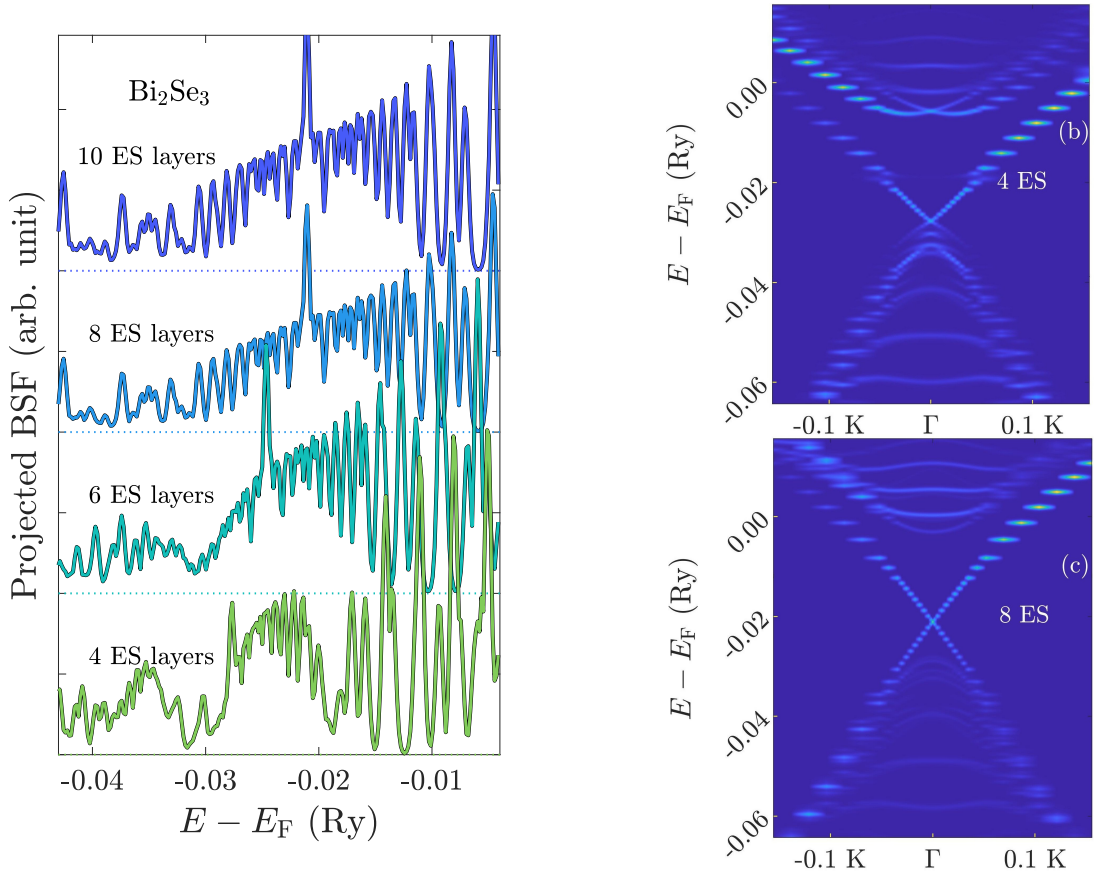


Figure 7.6: Surface states' dispersion as a function of the vacuum spacer thickness. Bi_2Se_3 slab composed of 10 QLs is used. (a) Projected Bloch spectral function of the surface QLs. Dispersions related to the various thickness of the vacuum spacer are depicted. The number of used ES layers labels curves. Dotted lines denote zero levels. (b,c) Bloch spectral functions of the surface QL in the vicinity of the Γ point. Vacuum spacers of 3 ES's resp. 8 ES's are employed.

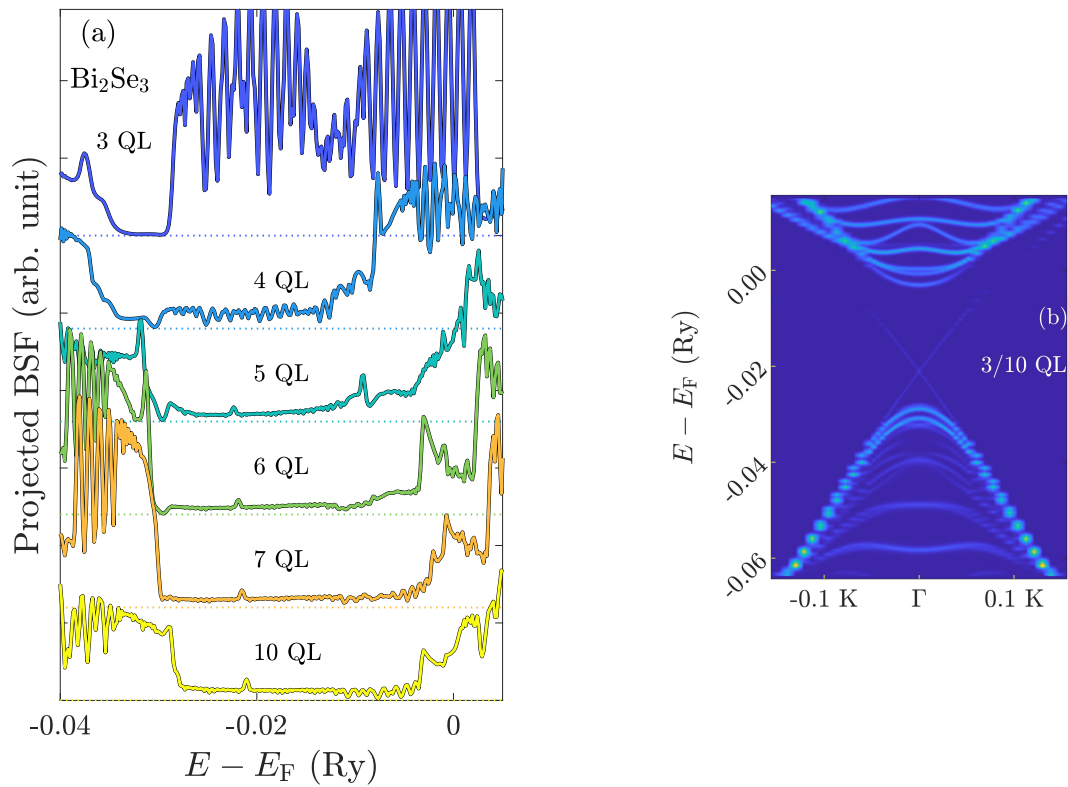


Figure 7.7: Evolution of the band gap at the 3rd QL of the Bi₂Se₃ slab. A vacuum spacer of 10 ES layers is used. (a) Projected Bloch spectral function of the 3rd QL. Curves are labeled by the Bi₂Se₃ slab thickness. Dotted lines denote zero levels. (b) Band gap at the Γ point in the BSF of the 3rd QL of the Bi₂Se₃ slab composed of 10 QLs.

7.3 Electronic structure in presence of chemical disorder

This section examines the influence of native and magnetic defects on the character of the electronic structure of the surface and inner Bi_2Se_3 QLs and compares it to the previously obtained bulk results. Notably, we focus on the occurrence of the surface states. In the layered calculations, we generally assume homogeneous doping, which resembles the bulk case. Dopants occupy sites of the same type in the multilayer structure with the same probability. Regarding the magnetic defects, the homogeneous disorder is supported by synchrotron experiments [169]. They indicate that Mn dopants are not metallic there, and therefore, they do not segregate there. Finally, we deal with the spin polarization along the z -axis similar to the bulk calculations.

However, initially, comparing the bulk and thin layer DOS's of the pure Bi_2Se_3 , we focus on the different dimensionality impact on the DOS character (Fig. 7.8). Actually, we compare the bulk DOS to the DOS's of the surface and 5th QLs (Fig. 7.1), where the later one stands for a representative of inner QLs. For a better description, particularly of the states near the band gap, we use a finer energy mesh compared to previous DOS plots. The energy axis is scaled to the bulk Fermi level E_F^{bulk} . The bulk and thin layer DOS's are placed to fit the same valence band edge position. Thus, the Fermi level position E_F^{layer} in a thin layer structure is depicted by a vertical line. We recall that the E_F^{layer} is placed near the conduction band edge irrespective of the QL number. Regarding the surface QL, both total and local DOS's are unsurprisingly modified by the interface proximity (Fig. 7.8a). Comparing the DOS curves, there occurs a larger separation of the valence and conduction bands. In the Fig. 7.8, one can observe a shift of peaks in the conduction band with respect to the bulk DOS. Besides, particularly the Se DOS is strongly modified in the valence band. Focusing on an inner QL (Fig. 7.8b), namely the 5th QL, the thin layer DOS converges to the bulk one, and the thin layer band gap width approaches to that of the bulk counterpart as one would expect (Fig. 7.8b). It indicates consistency between the bulk and thin layer structure calculations. Besides, it is evident that the DOS is not suitable for studying the surface states as other states overshadow them. It also demands a high density of the k -mesh.

7.3.1 Magnetic defects

Similarly to the pure Bi_2Se_3 structure, the surface proximity substantially modifies the surface QL DOS (Fig. 7.9). However, the Mn impurity peaks, concerning their shape and position, are nearly unchanged except the Mn^{Bi} states in the conduction band of the surface layers (Fig. 7.9a). As in bulk, there appears a hybridization of Bi and Se states with Mn impurity peak for both types of Mn dopants. Regarding an inner QL (Figs. 7.9b,d), the DOS's almost resemble the previously calculated bulk ones. Regardless of the QL position, the Mn impurity states' occurrence leads to a reduction of the band gap similar to bulk one concerning the Mn^{Bi} . Considering Mn^{i} defect, it appears that a tiny gap is maintained in the minority spin channel, unlike the bulk case. Finally, the Fermi levels are located in similar positions to the bulk calculation. Altogether,

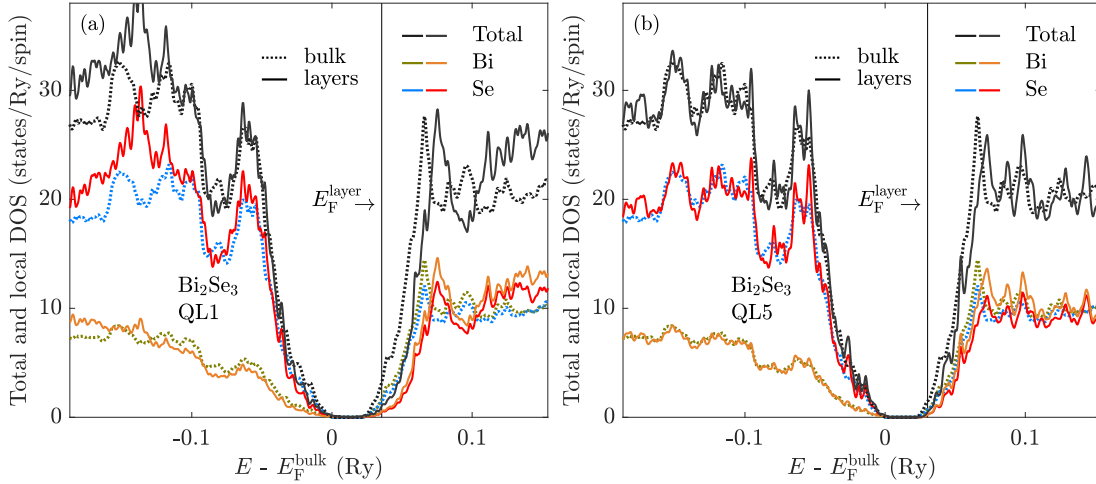


Figure 7.8: Densities of states of the thin layer Bi_2Se_3 system. Vacuum spacer of 10 ES layers and 10 QLs thick Bi_2Se_3 slab are used. (solid line) Thin layered system, (dotted line) bulk system. (a) Surface QL DOS, (b) 5th QL DOS.

it shows that despite the interface proximity, the magnetic Mn dopants' influence on the electronic structure resembles the bulk behavior, particularly concerning non-surface QLs.

The magnitudes on Mn magnetic moments follow similar dopant concentration dependencies as in bulk, and they approach magnitudes of bulk moments (Fig. 7.10). The Mn moments' magnitudes in the surface QL are either enhances concerning Mn^{Bi} defects or suppressed in the case of Mn^{i} ones compared to magnitudes of magnetic moments in inner QLs, which nearly fast converge as the function of the layer depth. Unlike the bulk, the Mn^{Bi} moment also differs for a particular Bi-sublattice within a QL. The Mn in the top Bi sublattice bears the strongest magnetic moments, while the magnitudes at the second Bi-sublattice almost reach values related to inner QLs. The observed difference between the surface and inner QLs arise from the discussed interface proximity induced modification of the electronic structure through the simulated Bi_2Se_3 slab. (Fig. 7.9). A mismatch between the bulk and inner QLs values likely resides on the calculated systems' distinct dimensionality. One can notice that the DOS inside the Bi_2Se_3 slab approaches to the bulk one. However, small deviations still survive (Fig. 7.9). It seems that the impact of the discussed shift of the Fermi level (Fig. 7.9) between thin layers and the bulk system is negligible as the Fermi level shift is insignificant concerning the bulk-like QLs.

Analyzing the BSF (Fig. 7.11) as functions of the QL position and related PBSFs plots (Figs. 7.12, 7.13), we find that the surface states in the Bi_2Se_3 system are highly sensitive to the presence of magnetic defects. Regarding the Mn^{Bi} defects, the bulk band gap is well preserved. However, the calculations reveal that the surface states near the Γ point become likely gapped already for tiny Mn^{Bi} concentrations (Fig. 7.12a). Calculations indicate a splitting of the high-intensity peaks, originally related to the Dirac point, for the Mn^{Bi} concentration $x = 0.04$ and opening of a surface gap with an increasing amount of Mn^{Bi} defects. The surface gap is well presented for the larger Mn^{Bi} concentrations. Concerning the smaller ones, only a sudden drop in the intensity occurs, which might indicate a gap. One can suggest that the surface gap is beyond the energy resolution of

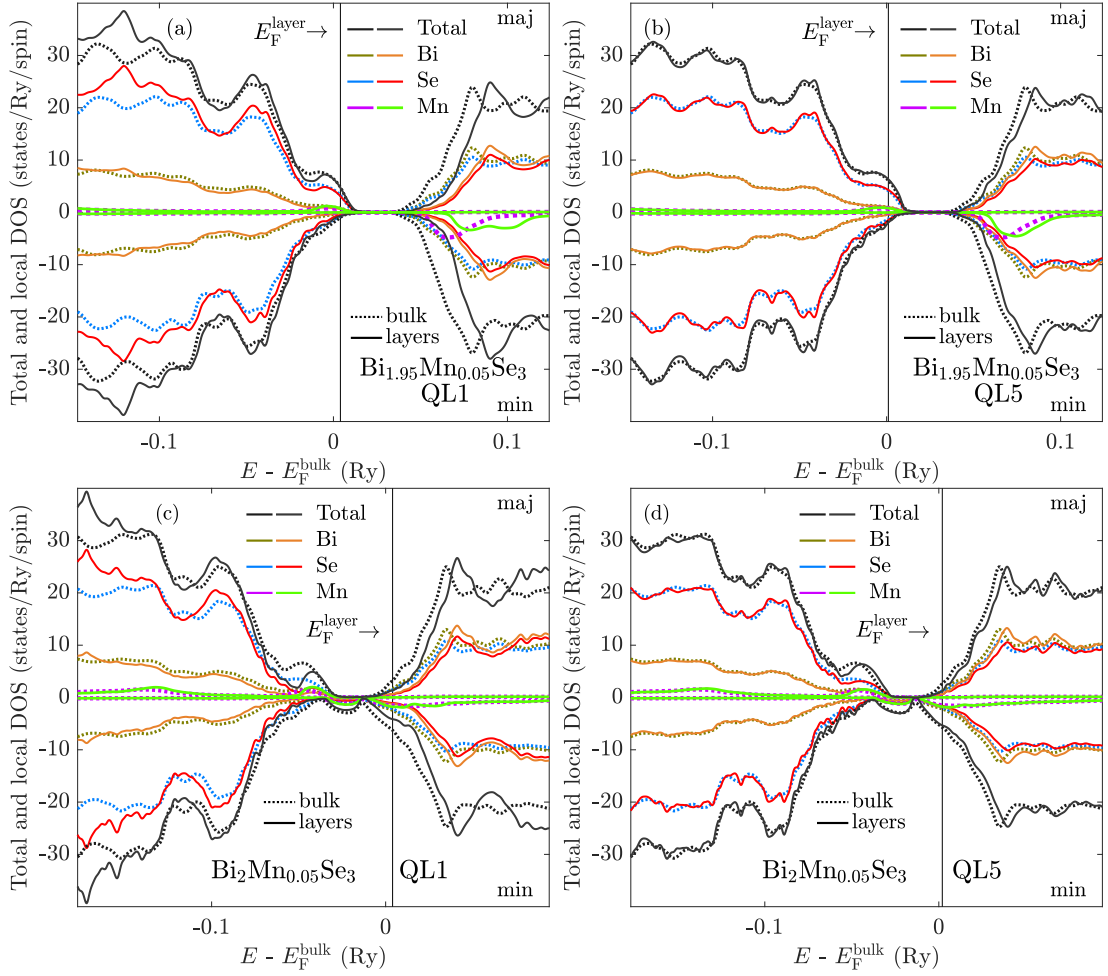


Figure 7.9: Densities of states of magnetically doped layered Bi_2Se_3 systems. (a,b) Substitutional Mn^{Bi} defects. (c,d) Interstitial Mn^{i} defects. Vacuum spacer of 10 ES layers and 10 QLs thick Bi_2Se_3 slab are used. (solid line) Thin layered system, (dotted line) bulk system. (a,c) Surface QL DOS, (b,d) 5th QL DOS.

the calculated BSFs. For an inner QL (Fig. 7.12b), a reduction of the band gap width occurs due to Mn^{Bi} states similar to the bulk results. In the band gap a small intensity of the PBSF is maintained. It appears it is an artifact of the strong surface states as the intensity disappears in the region of the surface band gap (Fig. 7.12a).

Unlike the previous case of the Mn^{Bi} defects, the interstitial Mn^{i} ones strongly modified the surface states' dispersion even for tiny concentrations (Fig. 7.13a). The PBSF dependencies indicate an occurrence of the surface gap for the 1 % Mn occupation of the interstitial positions. Concerning the PBSF spectrum, the intensity peak near the assumed band gap is related to the top of the conduction band (Fig. 7.11b). Regarding the inner QL (Fig. 7.13b), there appears a nonzero PBSF intensity in the former band gap with the increasing Mn^{i} amount, similarly to the Mn^{Bi} defects. By contrast, it does not stand for a surface state relic, but it seems that it originates from Mn impurity states and their hybridization with Bi and Se (Figs. 7.11b, 7.9d). Calculations reveal that the Dirac states might survive only for really tiny concentrations of Mn^{Bi} defects ($x < 0.01$).

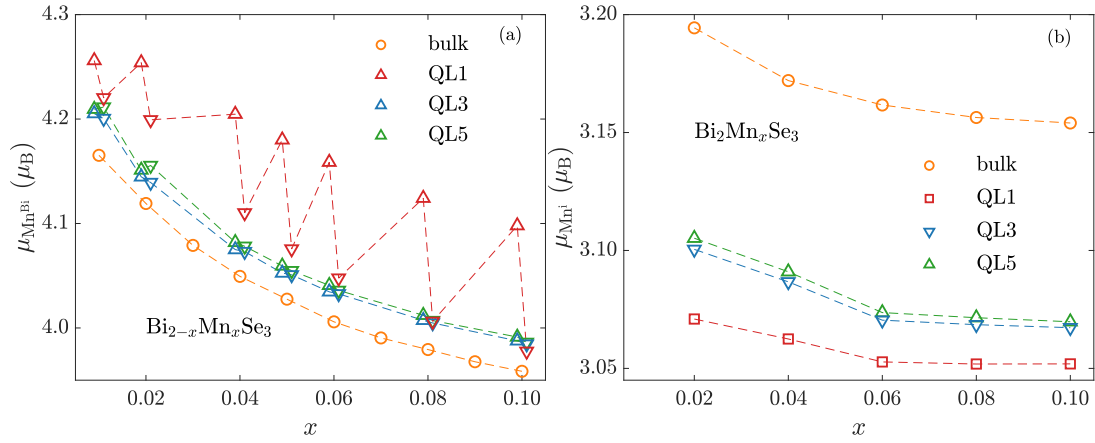


Figure 7.10: Dependence of the Mn magnetic moments' magnitude on the Mn defects concentration x and the position of defects within the thin layer structure. (a) Magnitudes of Mn^{Bi} magnetic moments as a function of the Mn^{Bi} dopant concentration. (b) Magnitudes of Mn^{i} magnetic moments as a function of the Mn^{i} dopant concentration. Vacuum spacer of 10 ES layers and 10 QLs thick Bi_2Se_3 slab are used. Bulk results are depicted for comparison. Concerning thin layer structures, magnitudes of Mn^{Bi} magnetic moments at both Bi-sublattices are shown: (Δ) top and (∇) bottom Bi-sublattices with respect to the top vacuum interface.

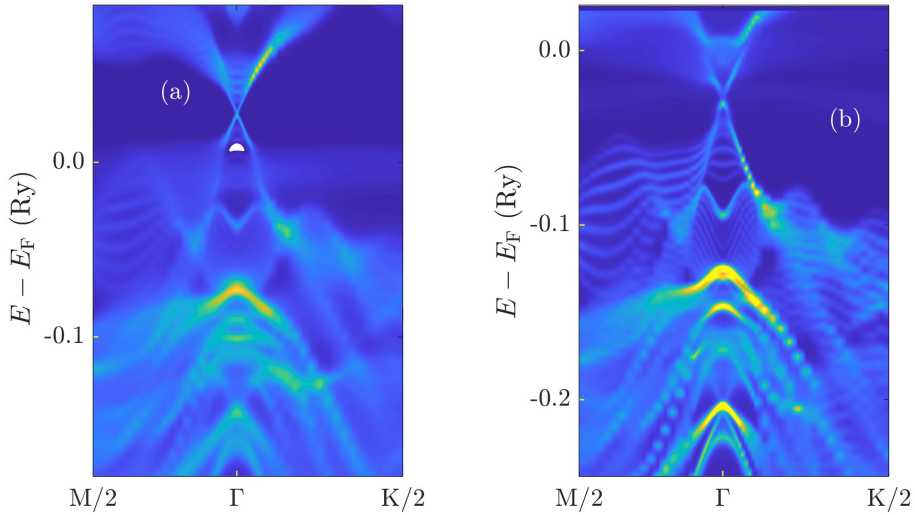


Figure 7.11: Surface QL BSFs of magnetically doped Bi_2Se_3 systems. (a) Substitutional Mn^{Bi} doping ($\text{Bi}_{1.9}\text{Mn}_{0.1}\text{Se}_3$), majority spin channel is depicted. (b) Interstitial Mn^{i} doping ($\text{Bi}_2\text{Mn}_{0.1}\text{Se}_3$), minority spin channel is depicted.

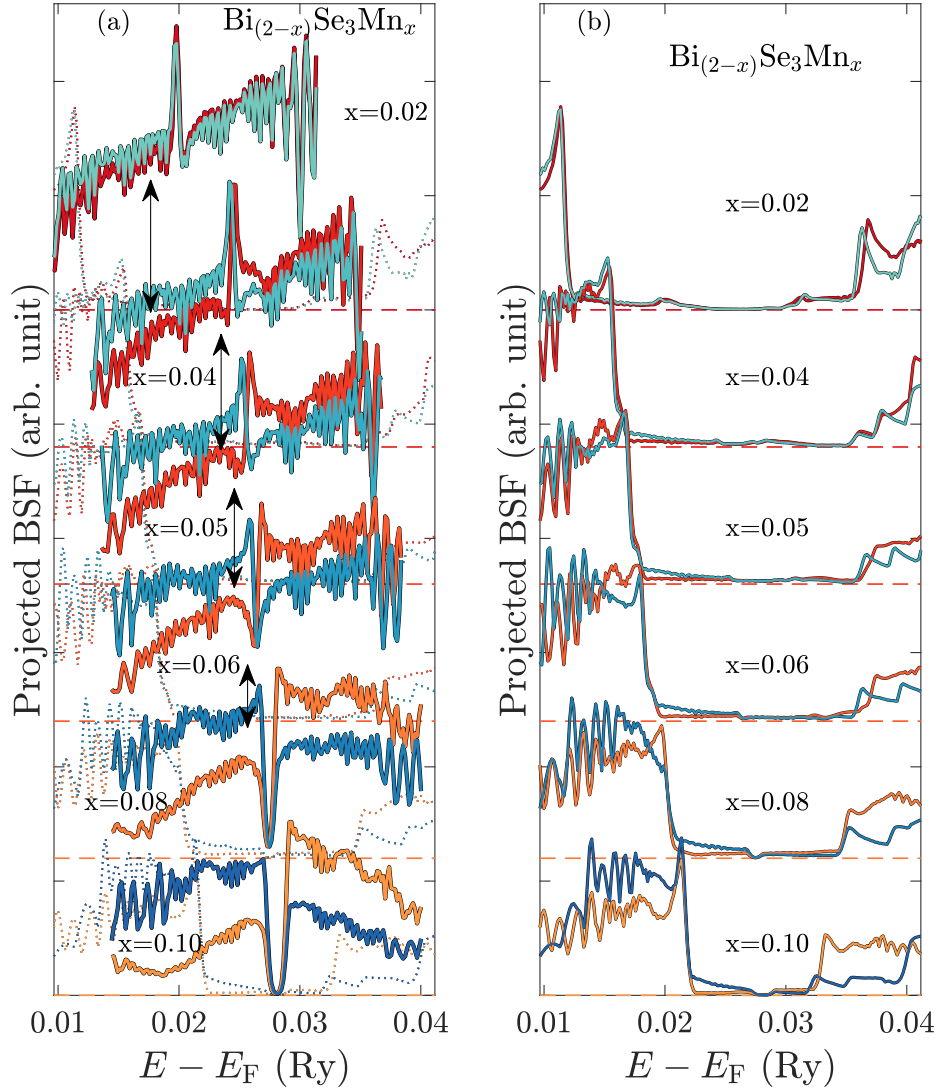


Figure 7.12: Surface states in terms of the PBSF in presence of magnetic Mn^{Bi} defects. (a) The surface QL PBSFs and (b) the 5th QL PBSFs. The later ones are also depicted in the subplot (a) by dotted lines for a better comparison. (bluish spectra) majority spin channel, (reddish spectra) minority spin channel.

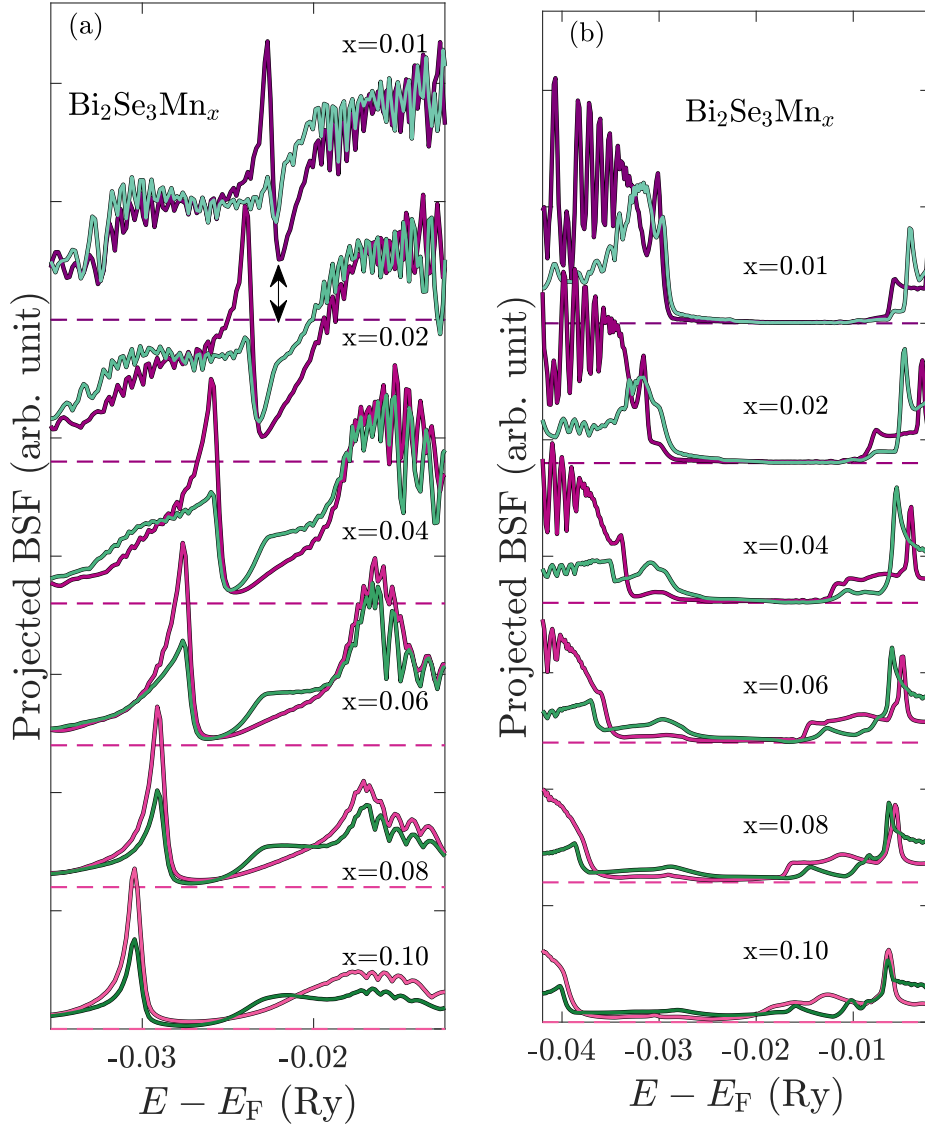


Figure 7.13: Surface states in terms of PBSF in presence of magnetic Mn^i defects. (a) The surface QL PBSFs and (b) the 5th QL PBSFs. The later ones are also depicted in the subplot (a) by dotted lines for a better comparison. (greenish spectra) majority spin channel, (mauve spectra) minority spin channel.

7.3.2 Native defects

Naturally, native defects occur also in the thin layer Bi_2Se_3 systems and influence their physical properties. To be consistent with the bulk study, we focus on the same type of intrinsic defects. Similar to the previous case of magnetic defects, the thin layer DOS's are not too distinct from the bulk one (Figs. 7.14, 7.15). Particularly concerning inner QLs, they nearly resemble. Also, the position of the Fermi level is almost the same except for the artificial shift discussed above.

Concerning Vac^{Se} defects, the presence of the induced mid-gap states is kept (Fig. 7.14). They occur irrespective of the QL position and close the band gap. It leads to loss of Dirac states (Figs. 7.16a, 7.17a). An increasing amount of Vac^{Se} defects rapidly ruins signs of the gapless surface states. Only their trace is indicated in the mid-gap state saddle.

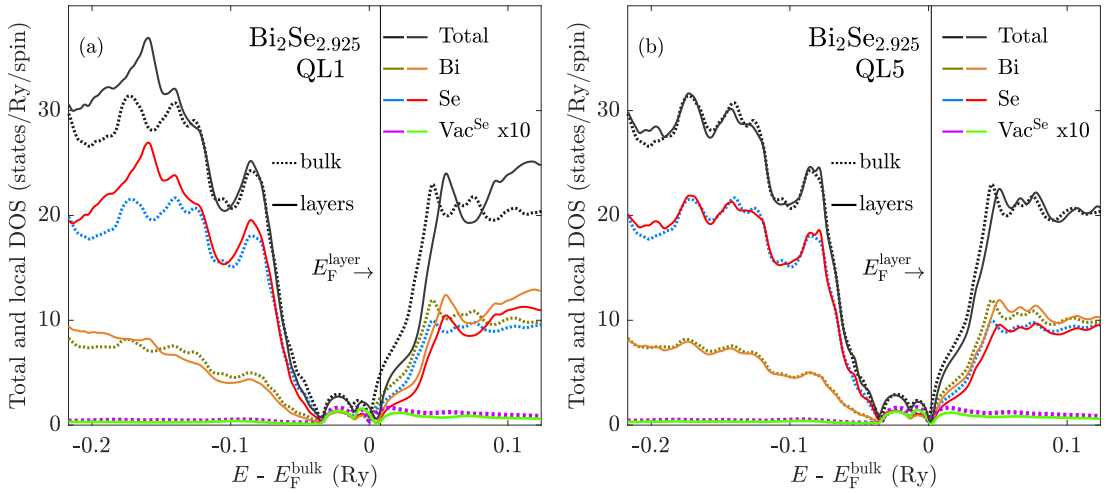


Figure 7.14: Densities of states of Bi_2Se_3 systems in presence of Vac^{Se} defects. (solid line) Thin layer system, (dotted line) bulk system. (a,c) Surface QL DOS (b,d) 5th QL DOS. Vacuum spacer of 10 ES layers and 10 QLs thick Bi_2Se_3 slab are used concerning thin layer systems.

Also, a thin layer structure hardly modifies the impact of the presence of Bi^{Se} and Se^{Bi} antisites (Fig. 7.15). The Bi^{Se} impurity peak is still located nearby the Fermi level, and the Bi^{Se} defects give rise to only shrinking of the band gap width. Furthermore, the Se^{Bi} impurity states stand for virtual bound states likewise and strongly hybridize with Se state as in bulk. Also, only a tiny band gap is maintained. All the mentioned features are kept regardless of the QL position. A non-vanishing band gap has a significant impact on the surface states (Fig. 7.15). Concerning the Bi^{Se} defects, the character of the surface states is hardly influenced compared to the pristine structure as a large band gap is maintained (Figs. 7.16b, 7.17b). Regarding the Se^{Bi} defects (Figs. 7.16c, 7.17c), the Dirac surface states seem to be maintained despite the narrow band gap and smeared states at the bottom of the conduction band, which is induced by the Se^{Bi} virtual bound states (Fig. 7.15c). The surface states mostly lack a linear dispersion character, which is likely caused by the narrow gap. However, it appears that the linearity is kept in the close vicinity of the Dirac point. The results naturally show that the closing of the band gap induced by native defects is crucial. A mere presence of weak mid-gap states induced by Vac^{Se} defects is sufficient to

lose the Dirac states. Thus, one should be aware of not only the magnetic defects but also the native one as they modify bulk band gap properties, which also has an impact on the surface states. Finally, one should take into account the Fermi level shift induced by the disorder presence, particularly the Bi^{Se} electron acceptors. It is obvious that an additional co-doping is needed to place the Fermi level E_{F} in the band gap [170].

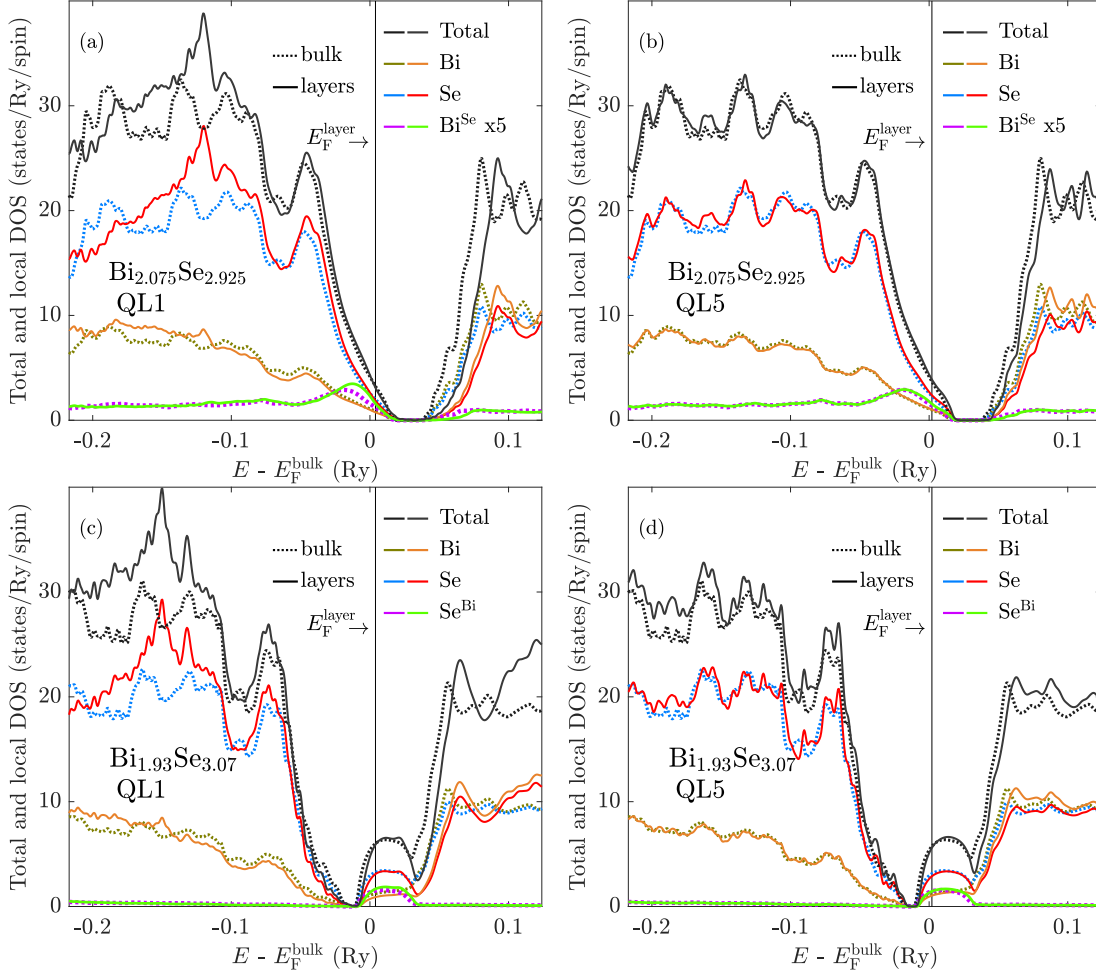


Figure 7.15: Densities of states of Bi_2Se_3 systems in presence of Bi^{Se} and Se^{Bi} antisites: (a,b) Bi^{Se} antisites, (c,d) Se^{Bi} antisites. (solid line) Thin layer system, (dotted line) bulk system. (a,c) Surface QL DOS, (b,d) 5th QL DOS. Vacuum spacer of 10 ES layers and 10 QLs thick Bi_2Se_3 slab are used concerning thin layer systems.

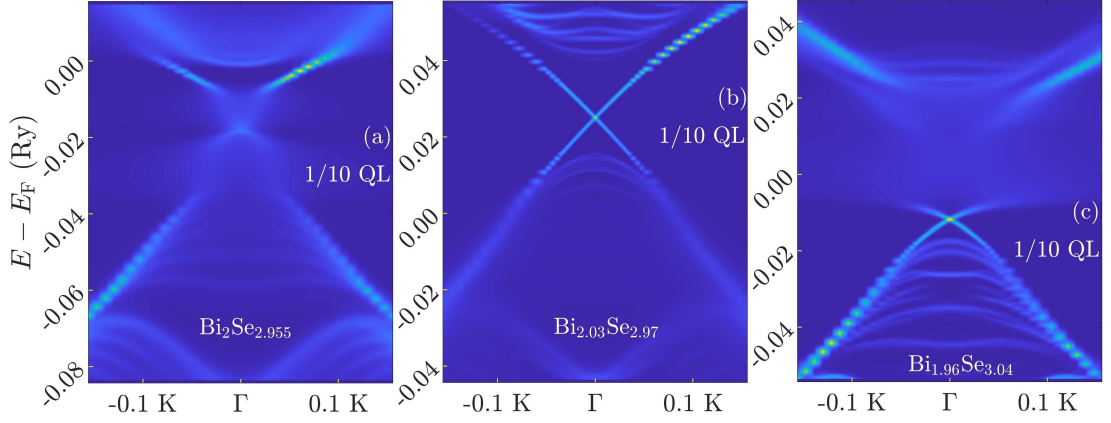


Figure 7.16: BSFs of the surface QL in presence of native defects. (a) Vac^{Se} defects, (b) Bi^{Se} defects, (c) Se^{Bi} defects.

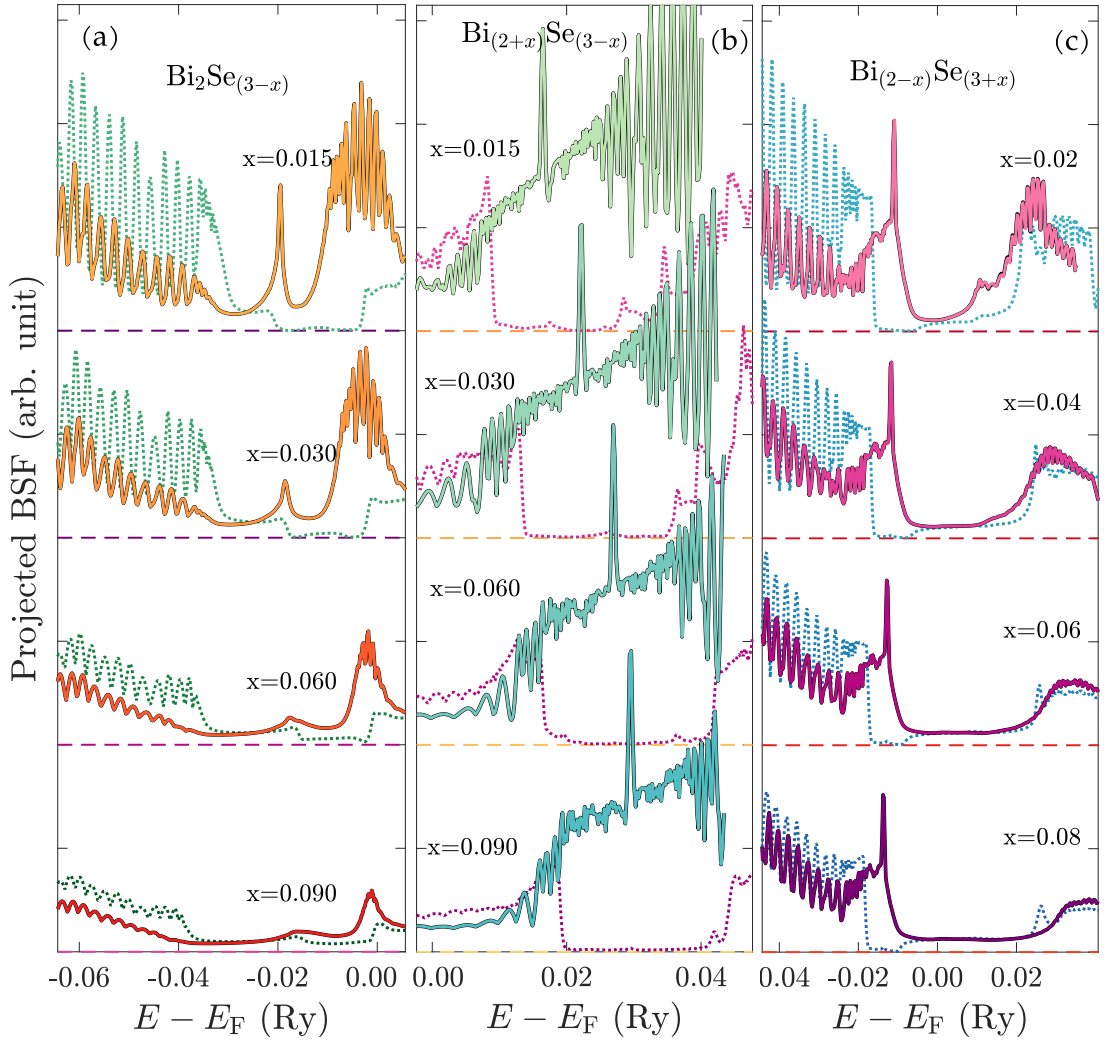


Figure 7.17: Surface states in terms of PBSF in presence of native defects: (a) Vac^{Se} defects, (b) Bi^{Se} defects, (c) Se^{Bi} defects. (solid lines) The surface QL, (dotted lines) the 5th QL.

7.4 Exchange interactions

To better analyze the behavior of magnetic dopants in Bi₂Se₃ thin layers, we try to describe their magnetic pair exchange interactions and compare them to the previously obtained bulk ones. It also includes the determination of MFA magnetic ordering temperatures.

To evaluate the magnetic exchange interactions, we transform the bulk codes based on the Liechtenstein formula (Eq. 2.59) into the layered Green's function formalism (Sec. 1.4.2). The site non-diagonal elements of the auxiliary Green's function beyond the region of the single principal layer $g_{p,q}(z, \mathbf{k}_{\parallel})$ (Eq. 1.43) can be obtained by the inversion of a finite block tridiagonal matrix $T(z, \mathbf{k}_{\parallel})$ [6]

$$g_{p,q}(z, \mathbf{k}_{\parallel}) = \left[T(z, \mathbf{k}_{\parallel}) \right]^{-1}_{(p,q)}, \quad (7.2)$$

where the indices p and q denote appropriate principal layers in the intermediate region between leads. The matrix T is defined in term of the elements of the matrix M (Eq. 1.42), composed of the potential parameters $P_p(z)$ and structure constants $S_{p,p'}(\mathbf{k}_{\parallel})$, and embedding potentials $\Gamma_p^<(z, \mathbf{k}_{\parallel})$, $\Gamma_q^>(z, \mathbf{k}_{\parallel})$ (Eq. 1.45) as follows

$$T = \begin{pmatrix} M_{p,p} - \Gamma_p^< & M_{p,p+1} & 0 & \dots & 0 \\ M_{p+1,p} & M_{p+1,p+1} & M_{p+1,p+2} & 0 & \vdots \\ 0 & & \ddots & & 0 \\ \vdots & 0 & M_{q-1,q-2} & M_{q-1,q-1} & M_{q-1,q} \\ 0 & \dots & 0 & M_{q,q-1} & M_{q,q} - \Gamma_q^> \end{pmatrix}. \quad (7.3)$$

Employing the inverse two-dimensional Fourier transformation, the real space auxiliary Green's function g_{ij} can be obtained, and the magnetic pair exchange interactions J_{ij} can be evaluated analogously to the bulk calculations (Eq. 2.59). Due to computational demands arising from the evaluation of the matrix inversion (Eq. 7.2), we restrict only to exchange interactions between close atomic layers. Namely, we investigate inplane and neighboring magnetic plane Mn^{Bi} exchange interactions and in-plane Mnⁱ ones. To obtain better bulk-like behavior of inner QLs, we enlarge the Bi₂Se₃ slab to 20 QL in order to screen the influence of the vacuum and substrate interfaces.

Regarding the Mn^{Bi} pair exchange interactions (Fig. 7.18), a strong interface proximity effect is evident. Restricting to Mn defects within the same QL (Fig. 7.18a,b), magnitudes of the FM exchange interactions in the vicinity of the surface (Fig. 7.18a,b - purple circles) are significantly suppressed in comparison to interactions within deep QLs and the nearest neighbor interactions become more antiferromagnetic. Then, around the second QL, numbered from the vacuum surface, the exchange interactions reach the maximal values and converge to the lower intensities of the inner QLs. Similarly, the strength of exchange interactions across the vdW gap culminates at the vdW between the top and second QLs. The observed oscillations of the magnitudes of exchange interactions as a function of the QL position correspond to the charge transfer modulations in the vacuum interface's vicinity. The charge of the elements in the surface QL is strongly modified due to the presence of the interface, which leads to charge oscillations at the top atomic layers. The calculated exchange interactions follow

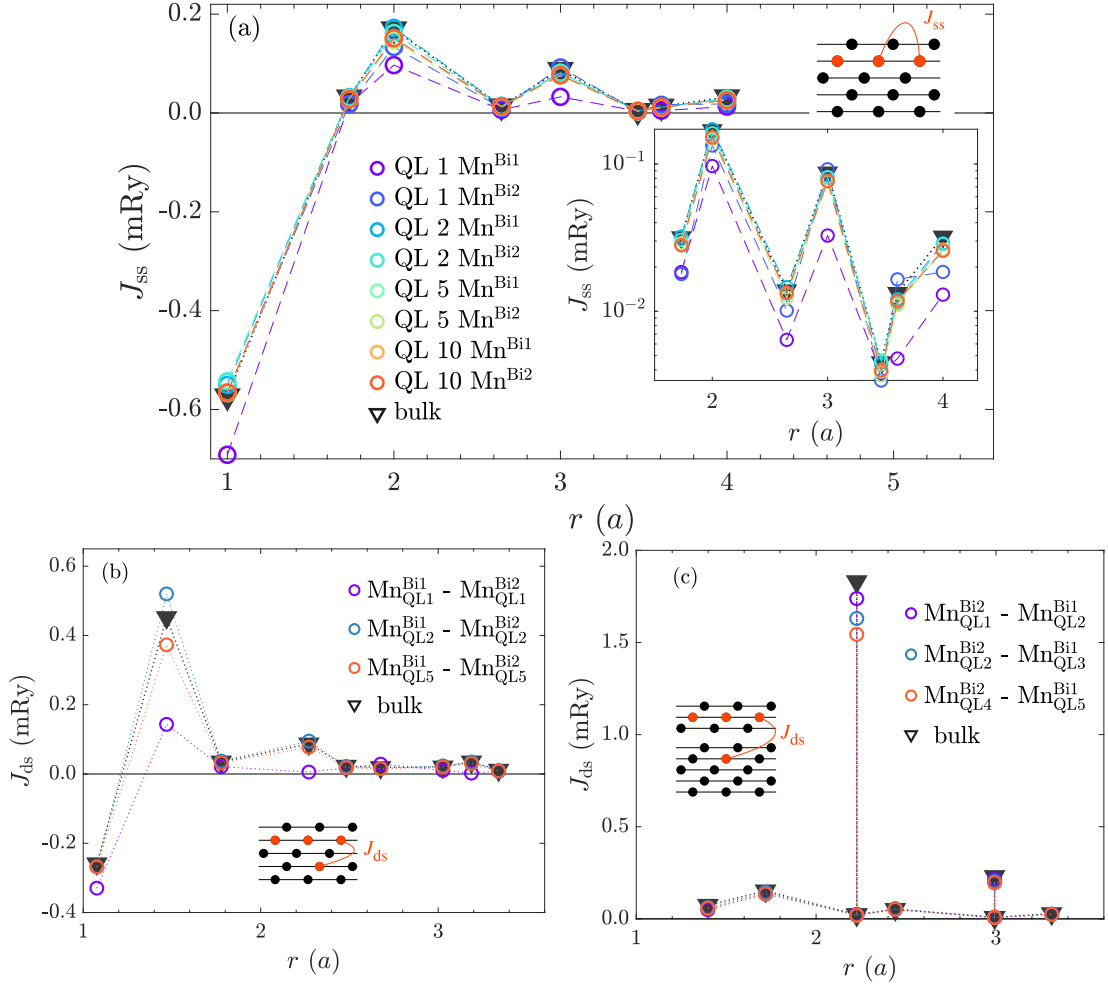


Figure 7.18: Magnetic Mn^{Bi} pair exchange interactions in thin layer systems as a function of the Mn^{Bi} position in a doped Bi₂Se₃ slab. A system consists of 10 ES layer vacuum spacer and homogeneously doped Bi_{1.95}Mn_{0.05}Se₃ slab of 20 QL. Bi layers are numbered from the vacuum interface. Bulk results are depicted for comparison. (a) In-plane exchange interactions. (b) Interactions within the same QL between different magnetic sublattices. (c) Interactions between different magnetic sublattices across the vdW gap.

the previously calculated bulk curves, particularly in the inner QL case. However, these interactions are weaker than pure bulk ones. It is pronounced mainly at the strong exchange interaction values (Fig. 7.18b,c). The actual modification of the exchange interaction magnitudes at deep QLs with respect to the bulk result is stated in the Tab. 7.1. Mostly, the Mn^{Bi} magnetic exchange interactions are reduced by 10 – 20 %.

The impact of the thin layer structure on the Mnⁱ pair exchange interactions (Fig. 7.19) is not too much different. They still resemble the calculated bulk exchange interactions. Only the proximity of the vacuum surface enhances their magnitudes, unlike the previously discussed Mn^{Bi} interactions (compare Fig. 7.19 to Fig. 7.18a). Besides, the thin layer Mnⁱ exchange interactions at inner atomic layers are not entirely reduced in comparison with the bulk values as the in-plane next-nearest neighbor interactions remain enhanced (Fig. 7.19, Tab. 7.1). However, one should be aware that the Mnⁱ defects are located further from

N_{sh}	Mn^{Bi}		Mn^{i}	
	ΔJ_{ss} (%) (in-plane)	ΔJ_{ds} (%) (within QL)	ΔJ_{ds} (%) (across vdW gap)	ΔJ_{ss} (%) (in-plane)
1	-1.3	3.7	-23.0	-4.1
2	-11.5	-17.5	-11.3	12.9
3	-10.7	-9.3	-17.6 / -15.6*	-7.1
4	-3.7	-11.0	-0.1	-4.0
5	-12.4	-21.2	-7.4 / -15.0*	-22.0
6	-11.9	-18.9	-17.4	
7	-12.1	-4.8		
8	-19.6	-15.0		

Table 7.1: Relative difference of exchange interactions' strength at the inner QL with respect to bulk magnitudes as a function of the atomic shell number N_{sh} ($\Delta J = (J_{\text{layer}} - J_{\text{bulk}})/J_{\text{bulk}}$). Exchange interactions evaluated at the 5th QL are employed. (*) denotes values related to enhanced values of J_{ds} in the Fig. 7.18c.

the surface. Thus, suppression of the exchange interactions as a function of the atomic layer position is likely not observed. The top vdW gap, where occurs the Mn^{i} defect occurs, meets the atomic position related to the culmination of magnitudes of Mn^{Bi} exchange interactions.

To evaluate better the difference between the bulk and thin layer magnetic exchange interactions, we determine the appropriate MFA Curie temperatures $T_{\text{C}}^{\text{MFA}}$ resolved by the Mn dopant positions similarly to the bulk case (Sec. 5.4). Regarding the Mn^{Bi} dopants (Fig. 7.20a), the on-site average pair exchange interactions J_0 (Eq. 2.61) at the top QL are significantly suppressed with respect to the deeper QL values or in comparison to the bulk, which leads to less than half the value of the MFA Curie temperature. Concerning small amount of the Mn^{Bi} dopants, antiparallel interactions prevail (compare Fig. 5.12) and J_0 becomes negative. By contrast, the mentioned enhancement of the exchange interactions toward more positive magnitudes at the following QLs is indicated by the culmination of the $T_{\text{C}}^{\text{MFA}}$'s as a function of the QL position. It is manifested particularly in the case of higher Mn^{Bi} concentrations, where the estimated $T_{\text{C}}^{\text{MFA}}$ nearly reach the bulk values. However, inside the Bi_2Se_3 slab, the $T_{\text{C}}^{\text{MFA}}$ is reduced in comparison to the bulk one due to weaker exchange interactions. Concerning a $\text{Bi}_{1.9}\text{Mn}_{0.1}\text{Se}_3$ system, the reduction is about 8 K. Concerning the Mn^{i} dopants (Fig. 7.20b), the surface $T_{\text{C}}^{\text{MFA}}$'s are enhanced, and they are able to overcome the bulk values slightly. However, they are suppressed concerning the inner QLs. Regarding the Mn^{Bi} and Mn^{i} defects' positions in the slab, the behavior of the $T_{\text{C}}^{\text{MFA}}$ as a function of the Mn dopant atomic layer position nearly resemble each other.

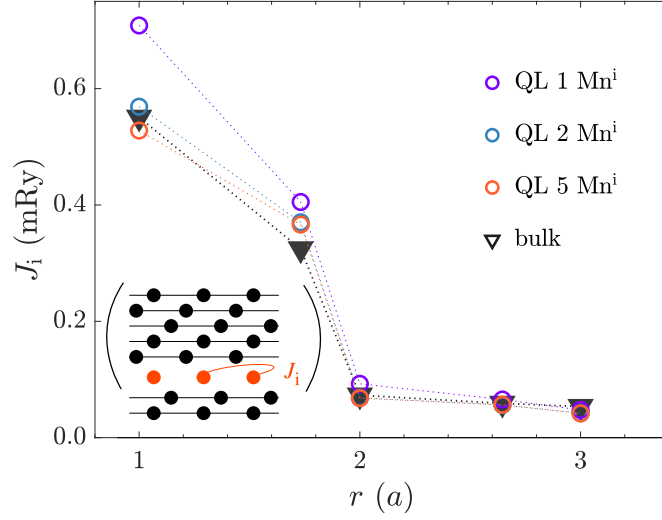


Figure 7.19: Magnetic Mnⁱ pair exchange interactions in thin layer systems as a function of the Mnⁱ position in a doped Bi₂Se₃ slab. A system consists of 10 ES layer vacuum spacer and homogeneously doped Bi₂Mn_{0.05}Se₃ slab of 20 QL. Bi layers are numbered from the vacuum interface. Bulk results are depicted for comparison. In-plane exchange interactions are depicted only.

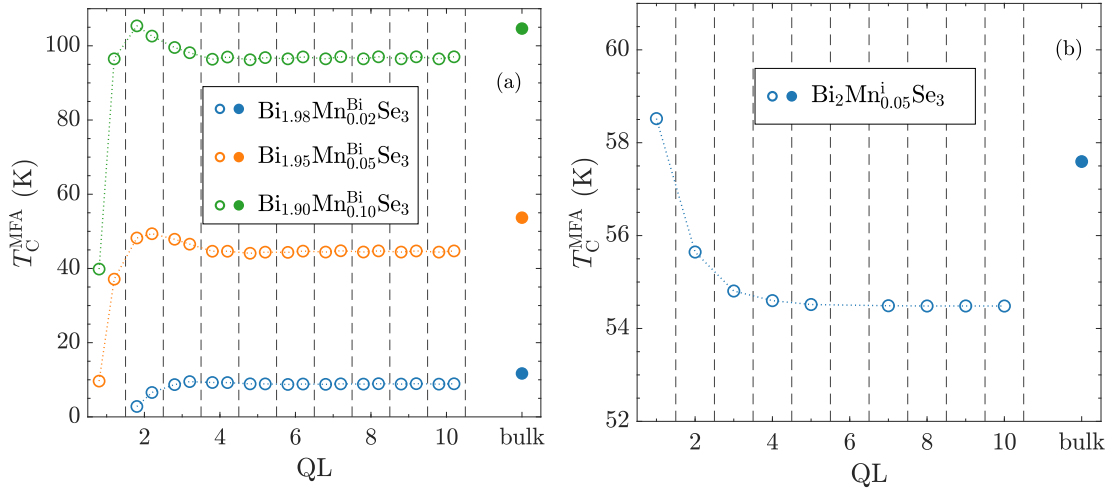


Figure 7.20: MFA Curie temperatures as a function of the position of Mn dopants in a Bi₂Se₃ slab. A system consists of 10 ES layer vacuum spacer and homogeneously doped 10 QLs. (a) Substitutional Mn^{Bi} dopants. Bi sublattices within a QL are resolved. (b) Interstitial Mnⁱ defects. Bulk results are depicted for comparison.

7.5 Planar defects – Twin planes

Having dealt with thin layers, one is able to take into account not only the point defects as the introduced native and magnetic ones but also planar defects, which naturally occur in experimental samples [171]. Namely, in this section, we tackle behavior of TPs, which are one of the experimentally evidenced planar defects [98, 99, 171] in Bi_2Se_3 multilayers. TPs stand for stacking faults, where their occurrence resides in breaking the FCC-like stacking sequence of three alternating stacking positions of hexagonal atomic layers. During the growth process, two possible stacking positions arise, which can be occupied by a new atomic layer. Thus, the mirroring of the stacking sequence could appear. It is based on the 60-degree rotation of new build atomic layers with respect to the ideal growth [99]. It gives rise to the inverse order of the stacking sequence with a TP as an interface of two adjacent twin domains. Concerning studied chalcogenides, TPs can be possibly located at several positions. However, it has been found that the most probable TP position is located at chalcogenide sites nearby the vdW gap [172], which stands for the form of TPs assume in this work. Also, TPs can modify the physical properties of TIs [173]. Thus, in this section, we focus on their segregation in the multilayer structure, while an interplay with point defects is considered. Particularly, we concentrate on the magnetic defects.

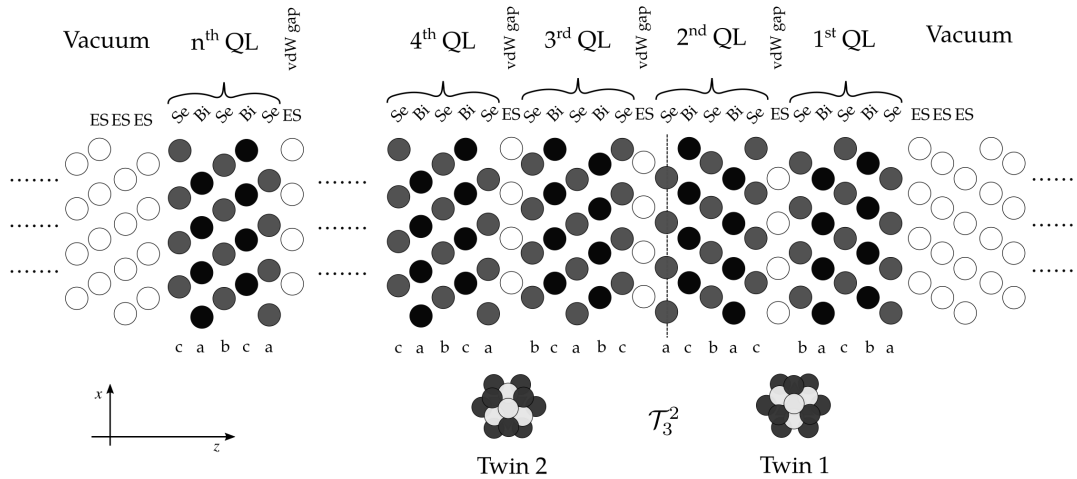


Figure 7.21: Sketch of the simulated multilayer Bi_2Se_3 slab including twin planes. Proportions of atoms are neglected. QL – quintuple layer, ES – empty sphere, \mathcal{T}_3^2 – twin plane between the second QL and the third QL.

Unlike the previous sections, we build a multilayer structure consisting of a Bi_2Se_3 slab surrounded by vacuum spacers at both sides to avoid an artificial influence of the substrate (Fig. 7.21). The vacuum spacers have the same thickness of 10 ES layers, as in the previous sections. For brevity, the position of a particular TP within a Bi_2Se_3 slab is described by the notation \mathcal{T}_{x+1}^x , where the indices denote QLs adjoining the TPs. Actually, QLs are numbered from the top surface, as in the previous case.

7.5.1 Single TP in a pristine Bi₂Se₃ system

Initially, we examine behavior of a single TP in the Bi₂Se₃ structure with no other defect. For simplicity, a not large slab of 10 QLs is employed. Since there exist two position where TPs can be located (Fig. 7.21) – above or below the vdW gap, we use TPs placed at QLs close to the top vacuum interface (lower QL number). Varying the TP position, we obtain a monotonous dependence of the TP relative formation energy ΔE_{form} (Fig. 7.22). We point out that the employed TB-LMTO-ASA framework does not allow to evaluate the absolute TP formation energy. Based on the vacuum spacer composed of ES layers (Figs. 7.1, 7.21), there occurs an artificial coupling to the lead structure, which makes the calculated absolute formation energies $E_{\text{form}}^{\mathcal{T}} = E_{\text{total}}^{\mathcal{T}} - E_{\text{total}}$ of extra TPs unreliable. The \mathcal{T} sign in the superscript denotes a structure including TPs. Consequently, we consider only systems with the same type and same number of stacking faults, where relative formation energies ΔE_{form} are used for comparison instead of the absolute ones. The later TP formation energies were studied elsewhere, we refer to Ref. [97, 172]. The relative TP formation energy is defined with a respect to the default formation energy $E_{\text{form}}^{\mathcal{T}(z_0)}$ as follows

$$\begin{aligned}\Delta E_{\text{form}}(z) &= E_{\text{form}}^{\mathcal{T}(z)} - E_{\text{form}}^{\mathcal{T}(z_0)} \\ &= \left(E_{\text{total}}^{\mathcal{T}(z)} - E_{\text{total}} \right) - \left(E_{\text{total}}^{\mathcal{T}(z_0)} - E_{\text{total}} \right) \\ &= E_{\text{total}}^{\mathcal{T}(z)} - E_{\text{total}}^{\mathcal{T}(z_0)},\end{aligned}\quad (7.4)$$

where z describes the position of a TP. It ensures the cancellation of the artificial energy contributions. Mostly, the $E_{\text{total}}^{\mathcal{T}(z_0)}$ is related to the structure bearing the minimal total energy $E_{\text{total}}^{\mathcal{T}}$. Analogously, regarding multiple TPs, their relative TP formation energy reads

$$\Delta E_{\text{form}}(z^A, z^A, \dots) = E_{\text{total}}^{(\mathcal{T}^A(z^A)\mathcal{T}^B(z^B)\dots)} - E_{\text{total}}^{(\mathcal{T}^A(z_0^A)\mathcal{T}^B(z_0^B)\dots)}. \quad (7.5)$$

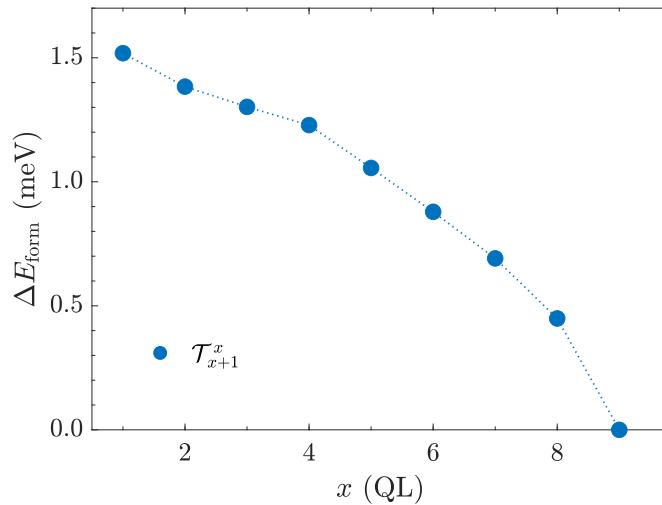


Figure 7.22: Relative formation energy of a single TP as a function of its position within the Bi₂Se₃ slab.

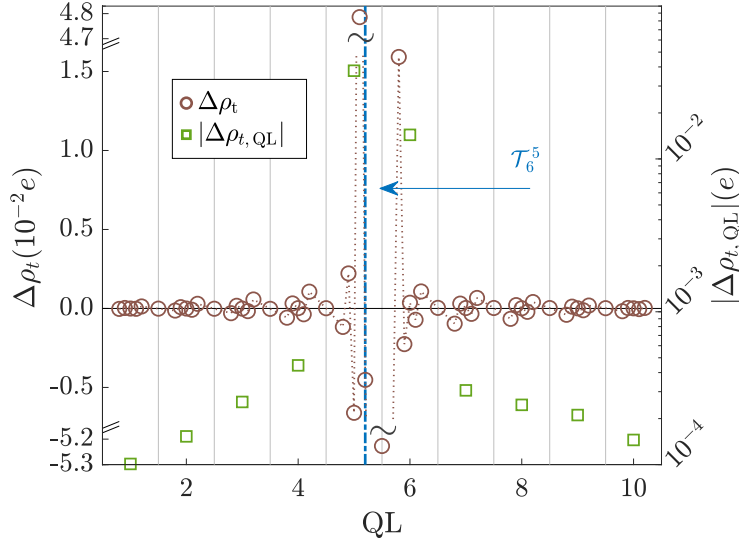


Figure 7.23: Single TP induced charge transfer. (left axis) Charge transfer distribution. (right axis) Absolute charge transfer per QL.

The shape of the obtained relative formation energy's dependence is asymmetric relating to the simulated structure. It arises from the non-symmetric position of TPs lying at the edge of QLs, which is incommensurable with the structure composed of QLs. Let's divide the Bi_2Se_3 structure into two twin domains composed of entire QLs. It is not usual since one domain would contain the TP, but it is more appropriate to simulated structure (Fig. 7.21). Having placed a TP in the top domain, the obtained dependence (Fig. 7.22) favors increasing the thickness of this domain at the expense of the bottom one. It indicates an interplay of the TP with surface vacuum interfaces, which depends on the orientation of the TP with respect to the particular interface. One can study the charge transfer ρ_t caused by the occurrence of a TP (Fig. 7.23). Particularly, it modifies the charge at TP adjacent Bi and ES atomic layers, where the charge flows from ES to Bi. Concerning more distant atomic layers, there occur charge oscillations propagating out of the TPs. Calculating the absolute charge transfer per QL $\sum_{QL} |\Delta\rho_t|$, it can be shown that the more substantial charge modulation takes place at the top domain, where the TP is localized. It suggests that its thickness maximization is energetically favorable (Fig. 7.22).

7.5.2 Interaction between TPs

Having regarded the interface induced shape of the relative formation energy of a single TP (Fig. 7.22), one can think about mutual interaction between multiple TPs as the vacuum interface can be regarded as a sort of stacking fault. For simplicity, one can assume an extra TP in the system and examine the relative formation energy with respect to their mutual position. For instance, one can fix the position of one TP and modified the distance of the other one. However, concerning multiple TPs, one has to take into account their mutual orientations. It means whether TPs lie on the same side of the vdW gap or not. According to the Fig. 7.24, let's denote the position above vdW gap α (lower QL number) and the other below the vdW gap β (higher QL number). Initially, we focus on the

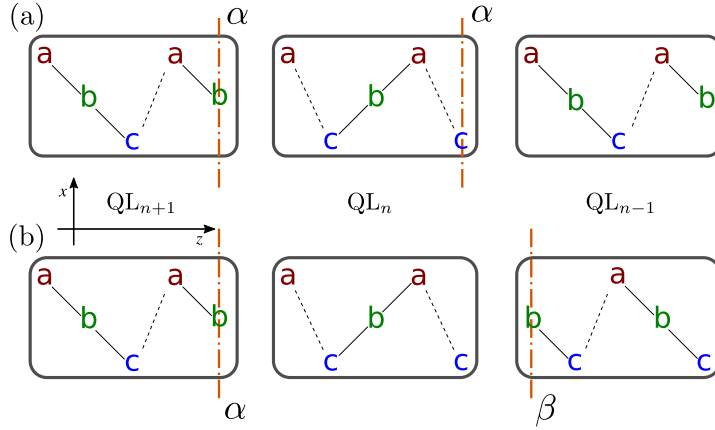


Figure 7.24: Mutual twin plane orientation. (a) Same sides of the vdW gaps resp. QLs. (b) Distinct sides of QLs.

simplest case, where all TPs are of the same type. Let's choose the α -type, for instance.

Concerning the simplest case of 2 TPs in the slab composed of 10 QLs, we observe that the obtained relative formation energy dependencies with one fixed TP position (Fig. 7.25) nearly resemble the dependence related to a single TP in the system (Fig. 7.22). Having subtracted the later from the 2 TPs dependencies, extra energetic contribution related to an interaction between adjacent TPs occurs. However, it is evident that such a small Bi_2Se_3 slab is inappropriate to study the inter TP interactions as interface proximity effects strongly influenced the calculated dependencies (Fig. 7.25). To suppress the surface-related effects, we employ a large slab composed of 20 QLs, where 3 TPs are introduced (Fig. 7.26a). Only the position of the middle one is variable as the rest two border ones are fixed. Concerning this structure, the relative formation energy is influenced principally by modification of the inter TP interactions. The larger Bi_2Se_3 slab provides a flatter single TP relative formation energy dependence (Fig. 7.26a). Furthermore, all the TPs are quite distant from vacuum interfaces (\mathcal{T}_5^4 , \mathcal{T}_{x+1}^x , and \mathcal{T}_{17}^{16} ; $5 \leq x \leq 15$) and one can compare the interplay related either to the top or bottom TP. Calculations reveal that TPs in a pure Bi_2Se_3 system clearly repel each other over a distance of 3 QLs at least (Fig. 7.26a). It corresponds to experiments which show that the observed TPs are several 10 nm apart [98, 99, 174]. According to the used lattice parameters [106], the thickness of a QL is about 1 nm. However, one should notice that one confronts samples grown by the molecular beam epitaxy, a method far from equilibrium conditions, with ab-initio ground-state calculations.

7.5.3 Influence of chemical disorder

Having dealt with chemical defects, either magnetic or nonmagnetic in the previous parts, we focus on their impact on the inter TP interactions. Similar to the preceding calculations, homogeneous doping is used. Initially, we examine the influence of magnetic Mn^{Bi} dopants (Fig. 7.26b) as the substitution position of magnetic defects is preferential [95, 100, 113]. The presence of Mn^{Bi} dopants induces a significant modification of the relative formation energy curves. Unlike

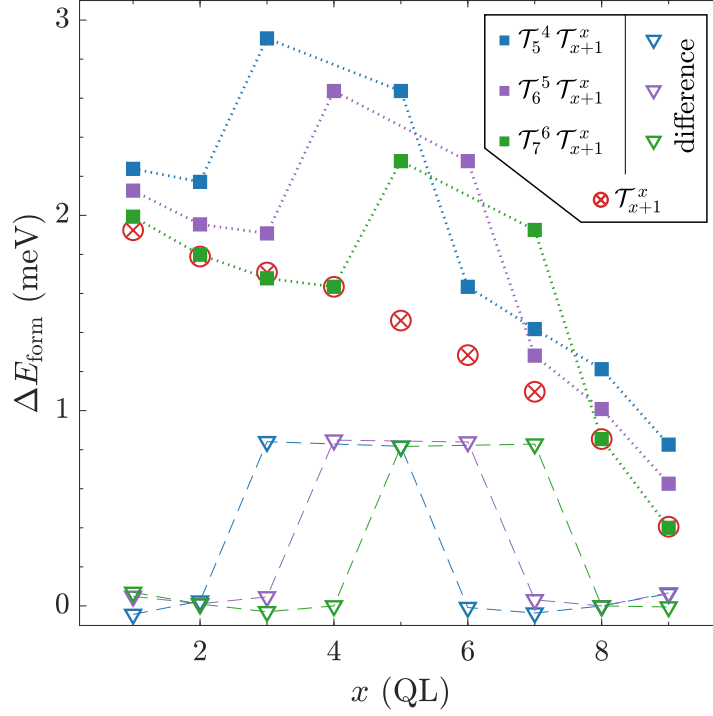


Figure 7.25: Relative formation energy of two TPs as a function of their position. (■) Relative formation energy of two TPs. (⊗) Relative formation energy belonging single TP. (□) Relative formation energy of two TPs with subtracted single TP relative energy contribution. Relative formation energies of systems containing different numbers of TPs are related to distinct absolute energies. The Bi_2Se_3 slab consists of 10 QLs.

the pure Bi_2Se_3 system (Fig. 7.26a), TPs in presence of magnetic disorder tend to be gathered here. Changing the magnetic Mn^{Bi} defects to nonmagnetic Se^{Bi} ones (Fig. 7.26c), the TP repulsion is slightly restored. It occurs only for the adjacent TPs. One can notice that disorder suppresses inter TP interactions in general. The observed changes of relative formation energies are about one order of magnitude smaller. Besides, also the influence of the vacuum interfaces on the single TP relative formation energy dependence is strongly diminished (Fig. 7.26c). The dependence becomes almost flat in the intermediate region. It indicates that the relevance of a TP as a perturbation is reduced in disordered systems in comparison to the pure regular one (Fig. 7.26a). The observed difference in TPs' behavior in presence of either magnetic or nonmagnetic defects suggests that magnetism-related effects are important there. Nevertheless, the influence of different chemistry originating from different doping cannot be ruled out.

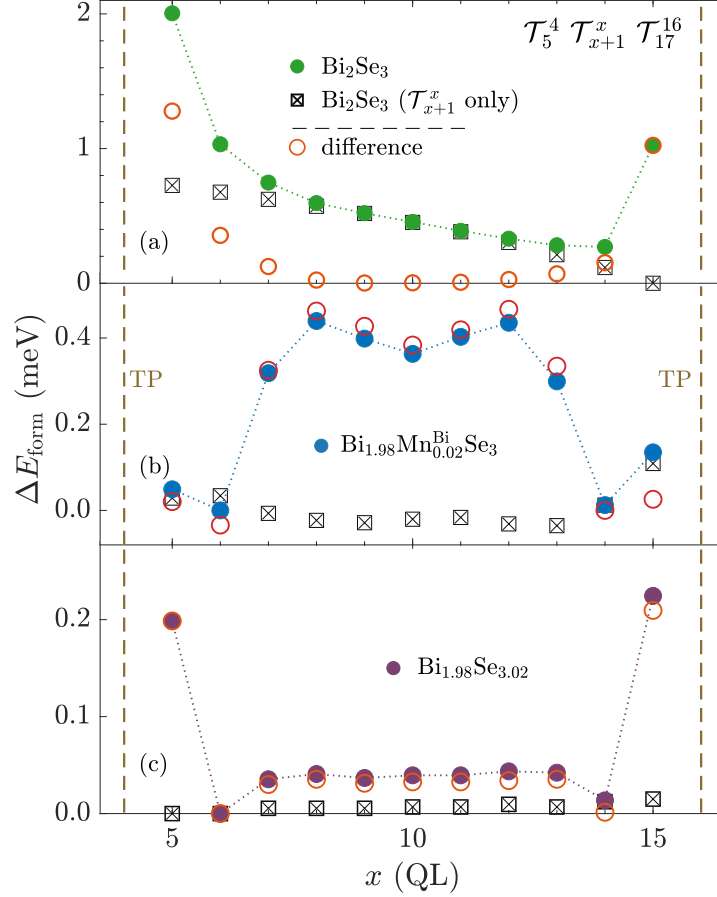


Figure 7.26: Relative formation energy of three TPs as a function of the middle TP position. (a) No chemical disorder. (b) System with magnetic Mn^{Bi} defects. (c) System with Se^{Bi} antisites. (●) Relative formation energy of systems with three TPs. (⊠) Relative formation energy related to the presence of a single TP. (○) Three TP relative formation energy with the subtracted single TP dependence. Particular relative formation energy curves are related to different absolute energies. The Bi_2Se_3 slab consists of 20 QLs.

7.5.4 Dependence of the inter-TP interaction on the dopant concentration

To reveal more details about the influence of magnetism, we examine the dependence of the TP relative formation energy on the chemical defects' concentration (Fig. 7.27). According to the Eq. 7.4 and using fixed TP positions, the relative formation energy in the case of varying composition can be defined as follows

$$\begin{aligned}
 \Delta \tilde{E}_{\text{form}}(x) &= E_{\text{form}}^{\mathcal{T}}(x) - E_{\text{form}}^{\mathcal{T}}(0) \\
 &= [E_{\text{total}}^{\mathcal{T}}(x) - E_{\text{total}}(x)] - [E_{\text{total}}^{\mathcal{T}}(0) - E_{\text{total}}(0)] \\
 &= [E_{\text{total}}^{\mathcal{T}}(x) - E_{\text{total}}^{\mathcal{T}}(0)] - [E_{\text{total}}(x) - E_{\text{total}}(0)] ,
 \end{aligned} \tag{7.6}$$

where the argument x denotes the dopant concentration. Regarding the last line of the Eq. 7.6, the artificial energy contributions are still eliminated.

We employ Bi_2Se_3 slabs of 20 QLs containing either two or three TPs in presence of homogeneous either magnetic (Mn^{Bi} or Fe^{Bi}) or nonmagnetic (Se^{Bi}) doping. It yields nearly linear concentration dependencies of the TP relative formation energy. Concerning magnetic doping, they grow irrespective of the used magnetic defects, which indicates suppressing the TP formation with an increasing amount of magnetic defects. By contrast, the calculations reveal that the increasing concentration of Se^{Bi} defects decreases TP formation energy. It likely corresponds to the obtained TP relative formation energies as functions of the TP distribution. It was mentioned that nonmagnetic disorder seems to suppress the impact on the electronic structure induced by TPs' presence. It agrees with the observed reduction of the TP formation energy (Fig. 7.26c). On the other hand, we suppose that the observed gathering of TPs (Fig. 7.26b) may be in accordance with the decreasing preference of TPs in a Bi_2Se_3 slab with an increasing amount of magnetic defects (Fig. 7.27). One might assume that the gathering of TPs leads to the minimization of the perturbation's influence on the system. Interestingly, we find that the concentration dependence of TP formation energy is almost proportional to the number of introduced TPs (Fig. 7.27: (+) and (\times) data points).

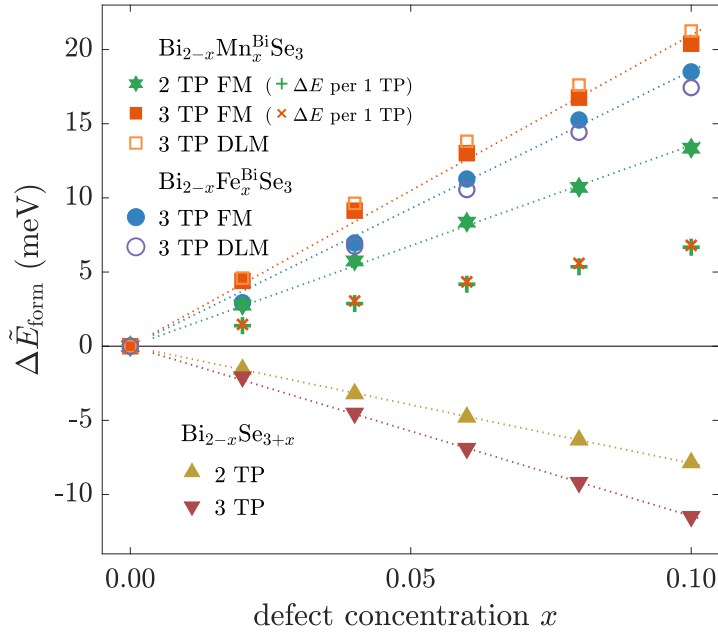


Figure 7.27: Dependence of the TP relative formation energy on the defect concentration. Bi_2Se_3 slabs of 20 QLs containing either two (\mathcal{T}_8^7 , \mathcal{T}_{13}^{12}) or three TPs (\mathcal{T}_5^4 , \mathcal{T}_{10}^9 , and \mathcal{T}_{17}^{16}) are used. Magnetic and native defects are used. (+) and (\times) denote relative formation energy contributions per single TP. (dotted lines) Linear fits.

To examine whether the TP formation energy is affected by the type of magnetic order, we attach calculations employing the DLM model representing a paramagnetic state (Fig. 7.27: empty points). The so far used FM ordering of magnetic dopants stands for a limit of a wholly ordered system, whereas the DLM state is related to an absolute disorder. However, the calculations reveal hardly any impact of magnetic ordering type on the evaluated concentration dependencies. Nevertheless, one can notice that the slope of relation formation energy

dependencies substantially differs for different magnetic dopants. Based on the ab-initio calculations, the Fe atoms in the used Bi_2Se_3 slab possess about $0.8 \mu_B$ smaller magnitudes of magnetic moments than Mn counterparts. It suggests that the TP formation energy might depend on the local exchange splitting.

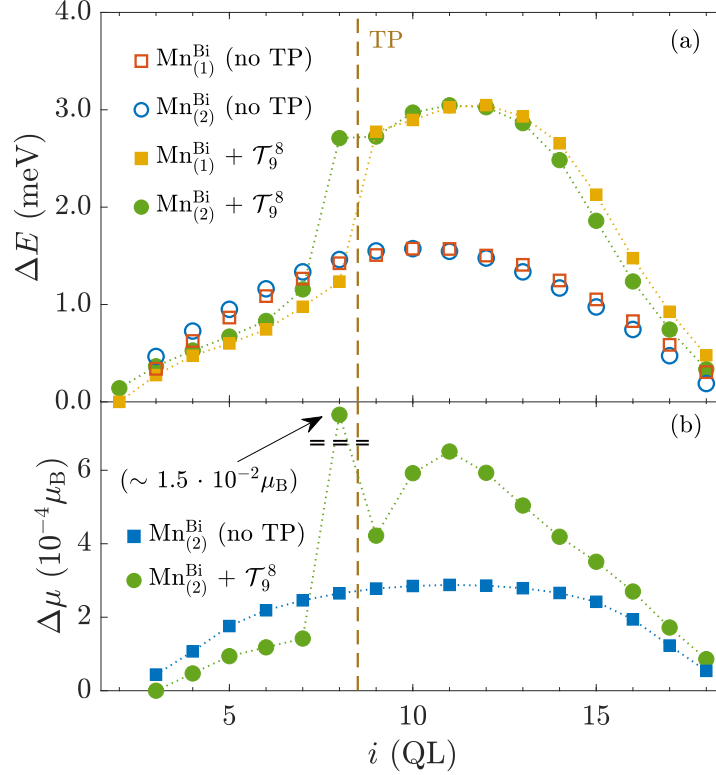


Figure 7.28: Local Mn^{Bi} magnetic doping in presence of a TP. (a) Relative Mn^{Bi} defects formation energy. (b) Relative change of the magnitude of Mn^{Bi} magnetic moments. Only a single Bi-layer is doped by 1 % of Mn^{Bi} . $\text{Mn}_{(1)}^{\text{Bi}}$ defects occupy Bi sites facing the top vacuum interface and vice versa. The Mn defect position is denoted by the number of the appropriate QL.

7.5.5 Magnetic dopants

In order to better determine the interplay between TPs and magnetic defects, we examine the influence of the TPs on the behavior of magnetic defects. Particularly, we focus on the Mn^{Bi} formation energy of Mn^{Bi} defects and the magnitudes of their magnetic moments (Fig. 7.28). We employ the larger Bi_2Se_3 slab of 20 QLs, where the magnetic doping is not homogeneous, but unlike previous sections, only a sole Bi-sublattice is doped by 1 % of Mn^{Bi} defects. Regarding a system with no TP, dependencies of the defects formation energy (Fig. 7.28a) and their magnitudes of magnetic moments (Fig. 7.28b) as functions of the Bi-sublattice position are near symmetric with respect to the layered structure of the slab. We point out that the positions of the Bi-sites are asymmetric concerning the center of the slab. Introducing a TP, modifications of the defects' formation energy and their magnitudes of magnetic moments occur. They are of the order of the finite slab size effects. According to the selected twin domain, there appear either more or less favorable sites for Mn^{Bi} defects compared to the initial state

with no TP. One can notice a correspondence between the change of the defect formation energy and the observed modification of the Mn spin splitting as the relatively enhanced magnitudes of magnetic moments are related to effectively increased defect formation energies and vice versa.

Let's introduce multiple TPs in the Bi_2Se_3 structure and evaluate their influence on the magnetic atoms' spin splitting in the homogeneously Mn^{Bi} doped slab with respect to the TP distribution (Fig. 7.29a). We find that the absolute modification of the magnitudes of Mn^{Bi} moments increases with the TP segregation (Figs. 7.29b,c). It suggests that the influence of TPs on the electronic structure is reduced for close TPs here. It might explain the tendency towards gathering of TPs in the case of magnetically doped systems.

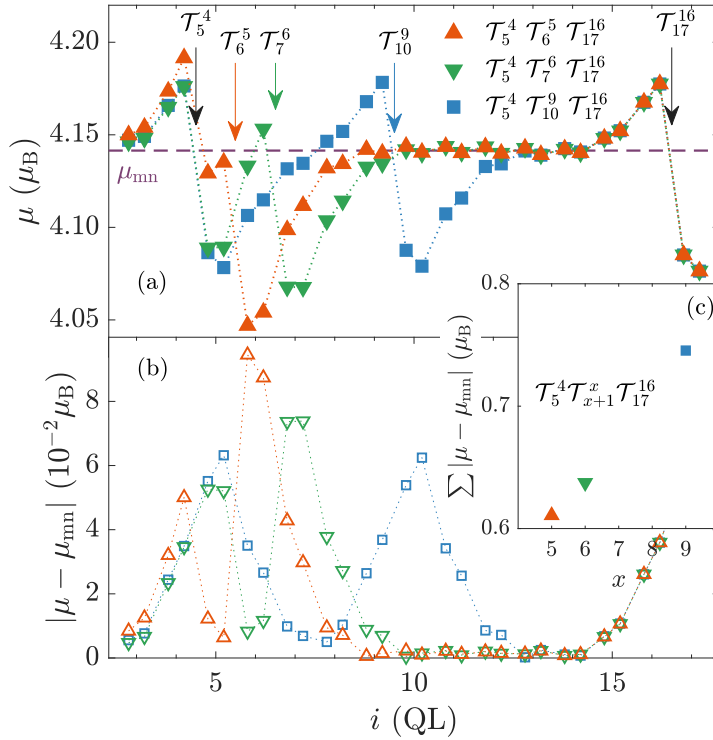


Figure 7.29: Influence of multiple TPs on Mn^{Bi} magnetic moments' magnitudes. Homogeneously doped $\text{Bi}_{1.98}\text{Mn}_{0.02}\text{Se}_3$ slab is used. (a) Distribution of magnitudes of magnetic moments within the slab with respect to TP positions. (b) Absolute change of the magnetic moments' magnitudes with respect to the mean value μ_{mn} . (c) Sums of the absolute magnetic moment changes as a function of the middle TP position.

7.5.6 Mixed TP orientation

So far, we have discussed TPs with the same orientation only. To examine the influence of non-identical TPs on the observed behavior, we recalculate the previously obtained relative formation energy of three TPs (Fig. 7.26) considering the inverted orientation of a single particular TP. Namely the foregoing identical three TPs of the α -type are replaced by the following sets of TPs with mixed TP orientations: $\{\alpha\alpha\beta, \alpha\beta\alpha, \beta\alpha\alpha\}$. Due to the mentioned artificial effects (Sec. 7.5.1), it is not possible to compare the formation energy of different types of TPs. Therefore, the comparison of the TP formation energies obtained for TPs of identical type with those containing a β -type TP is unfeasible. Nevertheless, one is able to mutually compare the formation energies in systems containing a single inverted TP.

Initially, let's consider the undoped Bi_2Se_3 system. Calculations reveal that the TP formation energy is strongly influenced by the TP-type order in the simulated structure (Fig. 7.30a). Based on the result, where structures including three TPs are employed, it appears that the local $(\beta\alpha)$ order of TP types is related to the lower formation energy than the $(\alpha\beta)$ one, and thus is more favorable. The types of TPs are ordered by means of the increasing QL index, which is numbered from the top vacuum interface. According to the Fig. 7.31, both TPs are located in the intermediate twin domain, in the case of the later $(\beta\alpha)$ order. Whereas, concerning the former one, TPs occur at the outer domains. One can notice that structures containing no $(\alpha\beta)$ TP sequence, the $\beta\alpha\alpha$ TP order, possess the lowest formation energy. Namely, the different formation energies of the $(\alpha\beta)$ and $(\beta\alpha)$ sequence are illustrated at the furthest points of the calculated dependencies, where adjacent TPs are introduced. The order of the α and β TPs is swapped there, and the $(\alpha\beta)$ sequence is interchanged for the $(\beta\alpha)$ (Fig. 7.31). It is evident that the lower formation energy belongs to the local $(\beta\alpha)$ sequence for both cases (Fig. 7.30a). Generally, the type of TP sequence is determined by the number of intermediate vdW gaps. Comparing to the $(\alpha\alpha)$ TP sequence, the $(\alpha\beta)$ one possesses an extra intermediate vdW gap, however the more favorable $(\beta\alpha)$ sequence misses one (Fig. 7.31).

Concerning TP orders with inverted border TP orientations – $\alpha\alpha\beta$ resp. $\beta\alpha\alpha$, the obtained dependencies of the formation energy as functions of the middle TP position nearly resemble the original energy curve belonging to the identical TPs (Fig. 7.30a). Particularly the shape of the dependence related to the $\beta\alpha\alpha$ TP order is almost the same. Regarding the $\alpha\alpha\beta$ order, a higher slope of the formation energy dependence might stem from the occurrence of the $(\alpha\beta)$ TP segment, which elongates as the middle TP approaches towards the top surface. The formation energy dependence related to the $\alpha\beta\alpha$ TP order bears more complicated behavior, which qualitatively differs from the preceding ones. Unlike the other dependencies, there occurs a noticeable local maximum for the middle β -type TP near the center of the slab. One might assume that it arises from a complex interplay given by the presence of the opposite $\alpha\beta$ and $\beta\alpha$ segments at the same time.

Thanks to the symmetry of the used Bi_2Se_3 slab and its vacuum interfaces (Fig. 7.21), we find that the $\alpha\alpha\beta$ TP order is equivalent to the $\alpha\beta\beta$ one due to the side inversion of the slab. Similarly, the $\beta\alpha\alpha$ order is equivalent to the $\beta\beta\alpha$ one. Regarding the later equivalence and the calculated formation energy

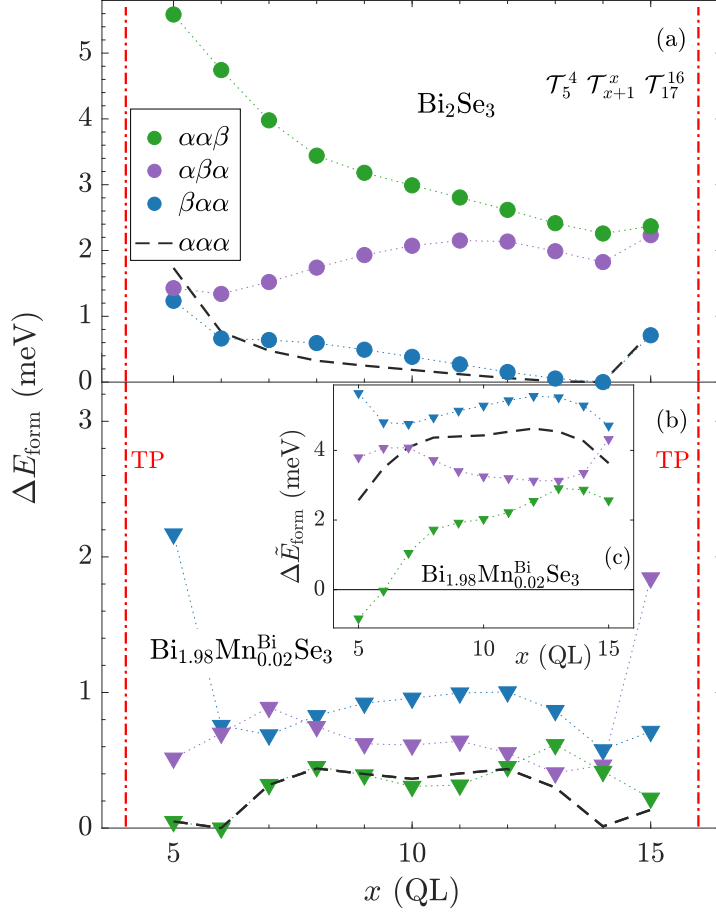


Figure 7.30: Influence of the mutual TP orientation on the relative formation energy. Relative formation energy of three TPs as a function of the position of the middle TP is depicted, different mutual orientations of the TPs are employed. (a) Pure Bi_2Se_3 structure. (b) Magnetically doped structure. (c) Change of the TP formation energy caused by magnetic doping with respect to the undoped case analogously to the Fig. 7.27. The relative formation energy curve of identical TPs serves only as a shape reference in panels (a), (b).

dependencies, it seems that the close alternation of TP types represented by the $\alpha\beta\alpha$ TP order is energetically unfavorable. Thus, considering all the calculated formation energy dependencies (Figs. 7.26a, 7.30a), one can assume that the TP distribution is hardly affected by TP orientations for pure Bi_2Se_3 systems.

Since the magnetically doped systems have been thoroughly discussed (Secs. 7.3.1 and 7.4), we examine the interplay of the mutual TP orientation and Mn^{Bi} defects likewise. Similar to the identical TPs, magnetic doping strongly modifies the formation energy curves (Fig. 7.30b). However, not only is their shape changed in comparison to the pure Bi_2Se_3 system, but also the preference of the order of TP types is rearranged. The calculated formation energy dependencies reveal that the magnetic doping still induces the gathering of TPs as local minima of the formation energy for close TPs occur (Fig. 7.30b). Regarding the $\beta\alpha\alpha$ and $\alpha\alpha\beta$ TP orders, the shape of the formation energy curves approaches that one of the identical TPs except for the part related to close TPs of different types. It indicates an interplay of the type of TP sequence and magnetic

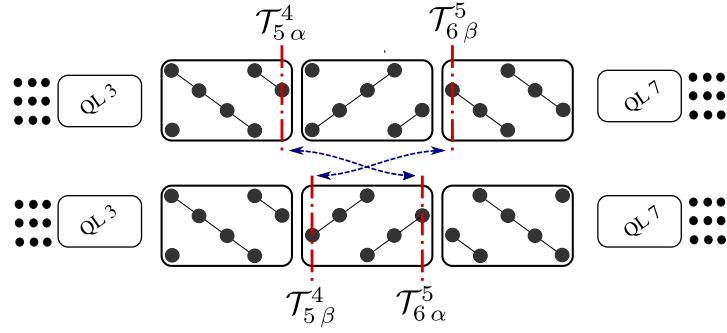


Figure 7.31: Interchange of TP orientation in the case of gathered TPs.

defects. Unlike the pure Bi_2Se_3 , it appears that the $(\alpha\beta)$ is more favorable than the $(\beta\alpha)$ one. However, the interplay between magnetic doping and TP type variation is rather complex. The TP formation energies are not clearly separated concerning different TP orders. They mostly overlap. Nevertheless, an increasing amount of magnetic dopants still suppress the TP formation except for special cases (Fig. 7.30c). The actual dependence is influenced by the TP orientations and TP distribution. We can conclude that the types of TPs concerning their orientations hardly qualitatively modify the TP behavior. Regarding either magnetically doped or pure Bi_2Se_3 system, the distribution related to identical TPs seems to be maintained. Similarly, an increase of the TP formation energy induced by magnetic defect does not disappear.

7.6 Results summary

Thin layer Bi_2Se_3 systems in presence of chemical and structural disorder have been studied in this chapter. We have focused on differences in the electronic structure between bulk and thin layer structures and examines the chemical doping influence on the surface Dirac states. Surface-induced modifications of magnetic pair exchange interactions have been discussed. Finally, motivated by layered structure and experimental data, behavior of twin planes, a sort of planar defects have been studied. Based on the obtained results, we can mention the main conclusions.

- Reliability of the Bi_2Se_3 surface states' description in the framework of the layer TB-LMTO-ASA method has been shown by comparison to the experimental data. Formation of the Dirac surface states in dependence on the thicknesses of Bi_2Se_3 slab and vacuum spacer has been discussed.
- Both magnetic as well as nonmagnetic impurity states are not strongly influenced by surface-induced effects. Mostly they nearly resemble the bulk counterparts. Furthermore, the employed chemical disorder induces in the surface layer modifications of the band gap similar to the bulk one. However, differences between the surface and bulk electronic structure naturally exist. It is reflected by small detected variations of the magnitudes of magnetic moments of magnetic dopants.
- Nonmagnetic defects, similar to the magnetic one, influence dispersion of the surface Dirac states. Defects as Vac^{Se} or Se^{Bi} , which substantially modify the electronic structure concerning the band gap, are able to suppress the Dirac states strongly. Regarding magnetic defects, particularly significant destruction of the Dirac surface states by the interstitial Mn^{i} defect even for tiny concentrations has been shown.
- According to the electronic structure, the magnetic exchange interactions substantially change with the increasing atomic layer's depth. Having implemented calculation of the exchange interactions within the layered formalism, it has been revealed that the magnitudes of magnetic exchange interactions substantially vary in the top QLs, although the character of the exchange interactions is hardly modified. Regarding the substitutional Mn^{Bi} defects, a substantial reduction of the related MFA Curie temperatures at surface atomic layers has been found. Despite small oscillation, their magnitudes converge in a distance of 4 – 5 QLs near the bulk Curie temperatures.
- Regarding undoped Bi_2Se_3 systems, the observed TP segregation over a distance of 3 – 4 QLs has been found, which corresponds to the experimental results. The distribution of the twin planes in Bi_2Se_3 structure seems to be strongly influenced by the magnetic disorder. It has been found that an increasing amount of magnetic Mn^{Bi} defects suppress TP formation, where a tendency towards TPs gathering has been observed. It likely indicates their annihilation. A thorough study has revealed an interplay between TPs' presence and modification of spin splitting of magnetic atoms. On the other hand, nonmagnetic disorder seems to make TPs more favorable.

Conclusions

The thesis covers the disorder's influence on the physical properties of well-known 3D TI Bi_2Se_3 employing the first-principle TB-LMTO-ASA calculations. A great emphasis is put on magnetic defects and related magnetic interactions. We proceed from the bulk compound and the impact of magnetic or native nonmagnetic defects' presence. Their influence on the Bi_2Se_3 electronic structure, particularly the character of the band gap is discussed. Distinct magnetic behavior of the substitutional and interstitial Mn dopants is studied in detail. Besides, the impact of native defects on the magnetism is demonstrated. A thorough study of Mn magnetic pair exchange interactions is performed to estimate magnetic ordering temperatures of magnetic dopants. Having discussed disorder in bulk, we focus on thin layer Bi_2Se_3 systems where surface metallic Dirac states, as a characteristic feature, can be observed. A simultaneous influence of the final Bi_2Se_3 slab size and chemical disorder on the electronic structure is examined. Notably, we concentrate on the impact on the surface Dirac states. The magnetic behavior of Mn defects in the bulk and thin layer systems is compared, focusing on the character of the exchange interactions and related magnetic ordering temperatures. Finally, motivated by the layered structure, the behavior of twin planes, a sort of planar defect, is inspected. We can introduce the following conclusions.

Regarding bulk Bi_2Se_3 systems, the chemical disorder is able to substantially modify electronic structure, namely, concerning the character of the band gap width. Particularly, it is shown there that closing of the band gap in either single or both spin channels can occur in presence of magnetic Mn^{i} defects resp. the native Vac^{Se} ones, which likely brings about a weak conductivity. Besides, considering substitutional Mn^{Bi} defects, the significance of the local relaxation is shown. It strongly affects the electronic structure and related magnetic behavior.

A thorough study of the Mn magnetic exchange interactions is provided. We discuss their dependence on the concentrations of both magnetic and native defects. Notably, a substantial strengthening of FM magnetic pair exchange interactions with the increasing concentration of Mn defects, as well as their strong dependence on co-doping, are observed for studied range of concentrations. Interestingly, enhancement of Mn^{Bi} FM interactions through Bi^{Se} atoms is found. It corresponds to the evaluated dependence of the magnetic exchange interactions' strength on the Fermi level shift. It predicts the enhancement in the case of p-doping, namely for the Fermi level shift exceeding -10 mRy. Besides, it reveals a significant contribution of conduction electrons and related RKKY-type interactions. The evaluated Curie temperatures reflect the behavior of exchange interactions. They almost linearly rise with increasing concentration of Mn^{Bi} magnetic defects. However, most of the studied co-dopants suppress their magnitudes, including also less favorable Mn^{i} dopants. It might explain the weak dependence of experimentally observed ordering temperatures on the Mn dopant concentration.

Then, employing thin layer Bi_2Se_3 systems, the influence of the vacuum interface is inspected in the framework of the layered TB-LMTO-ASA calculation. Modifications of the electronic structure in presence of disorder are evaluated, where particularly the impact on the surface Dirac states is examined. In the presence of a vacuum interface, the character of impurity states and their influence on the electronic structure is nearly preserved. It is shown that not only the magnetic Mn defects open surface gap, where Mn concentration dependence is discussed, but also a modification of the surface Dirac states' dispersion by native defects is described. In order to compare magnetic behavior in thin layer structures, the magnetic exchange interactions' calculation has been implemented in the layered framework. It reveals surface proximity induced modulation of magnitudes of exchange interactions in a few upper QLs, expressed mainly by the observed substantial reduction of Curie temperatures at the top QLs. In addition to chemical defects, structure defects in the thin layer Bi_2Se_3 systems are studied. Namely, we focus on the twin planes, a sort of planar defects. Their distribution in Bi_2Se_3 slabs and their interplay with chemical doping is discussed, where their mutual position is taken into account. It is found that TPs in the pure Bi_2Se_3 system are more than 3 QLs apart. However, TP segregation is strongly influenced by magnetic defects. Employed Mn^{Bi} defects induce gathering of TPs in the structure. It corresponds to the observed suppressed formation of TPs in presence of magnetic defects. It might reflect minimization of the electron structure modifications as TPs seems to influence the spin splitting of magnetic defects. By contrast, nonmagnetic Se^{Bi} defects suppress inter-TP interaction and make TPs more favorable.

Bibliography

- [1] K. Carva, P. Baláž, J. Šebesta, I. Turek, J. Kudrnovský, F. Máca, V. Drchal, J. Chico, V. Sechovský, and J. Honolka. Magnetic properties of Mn-doped Bi_2Se_3 topological insulators: Ab initio calculations. *Phys. Rev. B*, 101:054428, Feb 2020.
- [2] Jakub Šebesta, Karel Carva, Dominik Kriegner, and Jan Honolka. Twin domain structure in magnetically doped Bi_2Se_3 topological insulator. *Nanomaterials*, 10(10), Oct 2020.
- [3] Jakub Šebesta, Karel Carva, and Dominik Legut. Role of magnetism in the stability of the high-entropy alloy CoCrFeMnNi and its derivatives. *Phys. Rev. Materials*, 3:124410, Dec 2019.
- [4] Jakub Šebesta, Karel Carva, and Dominik Legut. Evolution of critical temperatures for substituted Cantor alloy. *submitted to Phys. Rev. B*, Aug 2020.
- [5] J.M. Wills, M. Alouani, P. Andersson, A. Delin, O. Eriksson, and O. Grechnev. *Full-Potential Electronic Structure Method: Energy and Force Calculations with Density Functional and Dynamical Mean Field Theory*. Springer Series in Solid-State Sciences. Springer Berlin Heidelberg, 2010.
- [6] Ilja Turek, Václav Drchal, Josef Kudrnovsky, Mojmír Sob, and Peter Weinberger. *Electronic Structure of Disordered Alloys, Surfaces and Interfaces*. Kluwer, Boston, 1997.
- [7] Stefan Blügel, Nicole Helbig, Volker Meden, and Daniel Wortmann, editors. *Computing Solids: Models, ab-initio methods and supercomputing*, volume 74 of *Schriften des Forschungszentrums Jülich Reihe Schlüsseltechnologien / Key Technologies*. Forschungszentrum Jülich GmbH Zentralbibliothek, Verlag, Jülich, Mar 2014. The Spring School was organized by the Institute for Advanced Simulation and the Peter Grünberg Institute of the Forschungszentrum Jülich.
- [8] A. Gonis. *Theoretical Materials Science: Tracing the Electronic Origins of Materials Behavior*. Materials Research Society, 2000.
- [9] B. Velický, S. Kirkpatrick, and H. Ehrenreich. Single-site approximations in the electronic theory of simple binary alloys. *Phys. Rev.*, 175:747–766, Nov 1968.
- [10] N.W. Ashcroft and N.D. Mermin. *Solid State Physics*. Cengage Learning, 2011.
- [11] B. Belhadji, L. Bergqvist, R. Zeller, P. H. Dederichs, K. Sato, and H. Katayama-Yoshida. Trends of exchange interactions in dilute magnetic semiconductors. *Journal of Physics: Condensed Matter*, 19(43):436227, Oct 2007.

- [12] P. Bruno and C. Chappert. Ruderman-Kittel theory of oscillatory interlayer exchange coupling. *Phys. Rev. B*, 46:261–270, Jul 1992.
- [13] Henrik Bruus and Karsten Flensberg. *Many-body quantum theory in condensed matter physics - an introduction*. Oxford University Press, United States, 2004.
- [14] Karol Szalowski and Tadeusz Balcerzak. RKKY interaction with diffused contact potential. *Phys. Rev. B*, 78:024419, Jul 2008.
- [15] C. H. Ziener, S. Glutsch, and F. Bechstedt. RKKY interaction in semiconductors: Effects of magnetic field and screening. *Phys. Rev. B*, 70:075205, Aug 2004.
- [16] E. Engel and S. H. Vosko. Wave-vector dependence of the exchange contribution to the electron-gas response functions: An analytic derivation. *Phys. Rev. B*, 42:4940–4953, Sep 1990.
- [17] K. L. Kliewer and Ronald Fuchs. Lindhard dielectric functions with a finite electron lifetime. *Phys. Rev.*, 181:552–558, May 1969.
- [18] Patrick Bruno. *Physical Origins and Theoretical Models of Magnetic Anisotropy*. Forschungszentrum Jülich, Verlag, Jülich, 1993.
- [19] Thomas Schäpers. *Topological Matter - Topological Insulators, Skyrmions and Majoranas*, volume 139 of *Schriften des Forschungszentrums Jülich Reihe Schlüsseltechnologien / Key Technologies*. Forschungszentrum Jülich GmbH Zentralbibliothek, Verlag, Jülich, Mar 2017.
- [20] T. Yildirim, A. B. Harris, A. Aharony, and O. Entin-Wohlman. Anisotropic spin hamiltonians due to spin-orbit and Coulomb exchange interactions. *Phys. Rev. B*, 52:10239–10267, Oct 1995.
- [21] J. Kudrnovský, I. Turek, V. Drchal, F. Máca, P. Weinberger, and P. Bruno. Exchange interactions in III-V and group-IV diluted magnetic semiconductors. *Phys. Rev. B*, 69:115208, Mar 2004.
- [22] I. Turek, J. Kudrnovský, V. Drchal, and P. Bruno. Exchange interactions, spin waves, and transition temperatures in itinerant magnets. *Philosophical Magazine*, 86(12):1713–1752, 2006.
- [23] M. Pajda, J. Kudrnovský, I. Turek, V. Drchal, and P. Bruno. Ab initio calculations of exchange interactions, spin-wave stiffness constants, and curie temperatures of Fe, Co, and Ni. *Phys. Rev. B*, 64:174402, Oct 2001.
- [24] L M Sandratskii. Symmetry analysis of electronic states for crystals with spiral magnetic order. II. connection with limiting cases. *Journal of Physics: Condensed Matter*, 3(44):8587–8596, Nov 1991.
- [25] A.I. Liechtenstein, M.I. Katsnelson, V.P. Antropov, and V.A. Gubanov. Local spin density functional approach to the theory of exchange interactions in ferromagnetic metals and alloys. *Journal of Magnetism and Magnetic Materials*, 67(1):65 – 74, 1987.

- [26] V.P Antropov, B.N Harmon, and A.N Smirnov. Aspects of spin dynamics and magnetic interactions. *Journal of Magnetism and Magnetic Materials*, 200(1):148 – 166, 1999.
- [27] A Oswald, R Zeller, P J Braspenning, and P H Dederichs. Interaction of magnetic impurities in Cu and Ag. *Journal of Physics F: Metal Physics*, 15(1):193–212, Jan 1985.
- [28] P. Lloyd and P.V. Smith. Multiple scattering theory in condensed materials. *Advances in Physics*, 21(89):69–142, 1972.
- [29] P. Bruno, J. Kudrnovský, V. Drchal, and I. Turek. Interlayer exchange coupling: The effect of substitutional disorder. *Phys. Rev. Lett.*, 76:4254–4257, May 1996.
- [30] Charles Kittel. *Introduction to Solid State Physics*. Wiley, 8 edition, 2004.
- [31] T.C Lubensky. Magnetic response functions I: Conserving systems. *Annals of Physics*, 64(2):424 – 451, 1971.
- [32] P.C. Hohenberg and A.P. Krekhov. An introduction to the Ginzburg–Landau theory of phase transitions and nonequilibrium patterns. *Physics Reports*, 572:1 – 42, 2015. An introduction to the Ginzburg–Landau theory of phase transitions and nonequilibrium patterns.
- [33] F. Ortmann, S. Roche, S.O. Valenzuela, and L.W. Molenkamp. *Topological Insulators: Fundamentals and Perspectives*. Wiley, 2015.
- [34] B.A. Bernevig and T.L. Hughes. *Topological Insulators and Topological Superconductors*. Princeton University Press, 2013.
- [35] M. Zahid Hasan and Joel E. Moore. Three-dimensional topological insulators. *Annual Review of Condensed Matter Physics*, 2(1):55–78, 2011.
- [36] Shuo-Ying Yang, Hao Yang, Elena Derunova, Stuart S. P. Parkin, Binghai Yan, and Mazhar N. Ali. Symmetry demanded topological nodal-line materials. *Advances in Physics: X*, 3(1):1414631, 2018.
- [37] Libor Šmejkal, Tomáš Jungwirth, and Jairo Sinova. Route towards Dirac and Weyl antiferromagnetic spintronics. *physica status solidi (RRL) – Rapid Research Letters*, 11(4):1700044, 2017.
- [38] K. v. Klitzing, G. Dorda, and M. Pepper. New method for high-accuracy determination of the fine-structure constant based on quantized hall resistance. *Phys. Rev. Lett.*, 45:494–497, Aug 1980.
- [39] Benoît Douçot, Vincent Pasquier, Bertrand Duplantier, and Vincent Rivasseau. *The Quantum Hall Effect*. Jan 2005.
- [40] Jürgen Schurr, Franz Ahlers, and Bryan P Kibble. The ac quantum Hall resistance as an electrical impedance standard and its role in the SI. *Measurement Science and Technology*, 23(12):124009, Nov 2012.

- [41] D. J. Thouless, M. Kohmoto, M. P. Nightingale, and M. den Nijs. Quantized hall conductance in a two-dimensional periodic potential. *Phys. Rev. Lett.*, 49:405–408, Aug 1982.
- [42] P.B. Allen. Chapter 6 Electron Transport. In Steven G. Louie and Marvin L. Cohen, editors, *Conceptual Foundations of Materials*, volume 2 of *Contemporary Concepts of Condensed Matter Science*, pages 165 – 218. Elsevier, 2006.
- [43] Michel Fruchart and David Carpentier. An introduction to topological insulators. *Comptes Rendus Physique*, 14(9):779 – 815, 2013. Topological insulators / Isolants topologiques.
- [44] F. D. M. Haldane. Model for a Quantum Hall Effect without Landau Levels: Condensed-Matter Realization of the "Parity Anomaly". *Phys. Rev. Lett.*, 61:2015–2018, Oct 1988.
- [45] M. Z. Hasan and C. L. Kane. Colloquium: Topological insulators. *Rev. Mod. Phys.*, 82:3045–3067, Nov 2010.
- [46] Jinying Wang, Shibin Deng, Zhongfan Liu, and Zhirong Liu. The rare two-dimensional materials with Dirac cones. *National Science Review*, 2(1):22–39, Jan 2015.
- [47] I. Pletikosić, M. Kralj, P. Pervan, R. Brako, J. Coraux, A. T. N’Diaye, C. Busse, and T. Michely. Dirac cones and minigaps for graphene on Ir(111). *Phys. Rev. Lett.*, 102:056808, Feb 2009.
- [48] R. Jackiw and C. Rebbi. Solitons with fermion number $\frac{1}{2}$. *Phys. Rev. D*, 13:3398–3409, Jun 1976.
- [49] C.L. Kane. Chapter 1 - Topological Band Theory and the \mathbb{Z}_2 Invariant. In Marcel Franz and Laurens Molenkamp, editors, *Topological Insulators*, volume 6 of *Contemporary Concepts of Condensed Matter Science*, pages 3 – 34. Elsevier, 2013.
- [50] H.B. Nielsen and M. Ninomiya. Absence of neutrinos on a lattice: (I). Proof by homotopy theory. *Nuclear Physics B*, 185(1):20 – 40, 1981.
- [51] B. Andrei Bernevig, Taylor L. Hughes, and Shou-Cheng Zhang. Quantum Spin Hall Effect and Topological Phase Transition in HgTe Quantum Wells. *Science*, 314(5806):1757–1761, 2006.
- [52] C. L. Kane and E. J. Mele. Quantum Spin Hall Effect in Graphene. *Phys. Rev. Lett.*, 95:226801, Nov 2005.
- [53] Liangzhi Kou, Yandong Ma, Ziqi Sun, Thomas Heine, and Changfeng Chen. Two-Dimensional Topological Insulators: Progress and Prospects. *The Journal of Physical Chemistry Letters*, 8(8):1905–1919, Apr 2017.
- [54] Ilya I. Klimovskikh, Mikhail M. Otrokov, Vladimir Yu. Voroshnin, Daria Sostina, Luca Petaccia, Giovanni Di Santo, Sangeeta Thakur, Evgueni V.

- Chulkov, and Alexander M. Shikin. Spin-orbit coupling induced gap in graphene on Pt(111) with intercalated Pb monolayer. *ACS Nano*, 11(1):368–374, Jan 2017.
- [55] Chi-Ho Cheung, Huei-Ru Fuh, Ming-Chien Hsu, Yeu-Chung Lin, and Ching-Ray Chang. Spin orbit coupling gap and indirect gap in strain-tuned topological insulator-antimonene. *Nanoscale Research Letters*, 11(1):459, Oct 2016.
- [56] O. A. Pankratov. Understanding surface states of topological insulators. *Physics-Uspexhi*, 61(11):1116–1126, Nov 2018.
- [57] Markus König, Steffen Wiedmann, Christoph Brüne, Andreas Roth, Hartmut Buhmann, Laurens W. Molenkamp, Xiao-Liang Qi, and Shou-Cheng Zhang. Quantum Spin Hall Insulator State in HgTe Quantum Wells. *Science*, 318(5851):766–770, 2007.
- [58] Yoichi Ando. Topological insulator materials. *Journal of the Physical Society of Japan*, 82(10):102001, 2013.
- [59] Xiao-Liang Qi and Shou-Cheng Zhang. Topological insulators and superconductors. *Rev. Mod. Phys.*, 83:1057–1110, Oct 2011.
- [60] G.M. Gusev, Z.D. Kvon, E.B. Olshanetsky, and N.N. Mikhailov. Mesoscopic transport in two-dimensional topological insulators. *Solid State Communications*, 302:113701, 2019.
- [61] Markus König, Matthias Baenninger, Andrei G. F. Garcia, Nahid Harjee, Beth L. Pruitt, C. Ames, Philipp Leubner, Christoph Brüne, Hartmut Buhmann, Laurens W. Molenkamp, and David Goldhaber-Gordon. Spatially Resolved Study of Backscattering in the Quantum Spin Hall State. *Phys. Rev. X*, 3:021003, Apr 2013.
- [62] Pietro Novelli, Fabio Taddei, Andre K. Geim, and Marco Polini. Failure of conductance quantization in two-dimensional topological insulators due to nonmagnetic impurities. *Phys. Rev. Lett.*, 122:016601, Jan 2019.
- [63] Xiao-Liang Qi and Shou-Cheng Zhang. The quantum spin Hall effect and topological insulators. *Physics Today*, 63(1):33–38, 2010.
- [64] Gerd Bergmann. *50 Years of Anderson Localization. Weak Localization And Its Applications As An Experimental Tool*. World Scientific, Jun 2010.
- [65] Wei Chen, Hai-Zhou Lu, and Oded Zilberberg. Weak localization and antilocalization in nodal-line semimetals: Dimensionality and topological effects. *Phys. Rev. Lett.*, 122:196603, May 2019.
- [66] Sudip Chakravarty and Albert Schmid. Weak localization: The quasiclassical theory of electrons in a random potential. *Physics Reports*, 140(4):193 – 236, 1986.

- [67] Michael Hilke, Mathieu Massicotte, Eric Whiteway, and Victor Yu. Weak Localization in Graphene: Theory, Simulations, and Experiments. *The Scientific World Journal*, 2014:737296, Jun 2014.
- [68] S.Q. Shen. *Topological Insulators: Dirac Equation in Condensed Matters*. Springer Series in Solid-State Sciences. Springer Berlin Heidelberg, 2013.
- [69] Vahid Sazgari, Gerard Sullivan, and İsmet İ. Kaya. Interaction-induced crossover between weak antilocalization and weak localization in a disordered InAs/GaSb double quantum well. *Phys. Rev. B*, 101:155302, Apr 2020.
- [70] D. Hsieh, D. Qian, L. Wray, Y. Xia, Y. S. Hor, R. J. Cava, and M. Z. Hasan. A topological Dirac insulator in a quantum spin Hall phase. *Nature*, 452(7190):970–974, Apr 2008.
- [71] Binghai Yan and Claudia Felser. Topological Materials: Weyl Semimetals. *Annual Review of Condensed Matter Physics*, 8(1):337–354, 2017.
- [72] N.P. Armitage, E. J. Mele, and Ashvin Vishwanath. Weyl and Dirac semimetals in three-dimensional solids. *Rev. Mod. Phys.*, 90:015001, Jan 2018.
- [73] Yoichi Ando and Liang Fu. Topological crystalline insulators and topological superconductors: From concepts to materials. *Annual Review of Condensed Matter Physics*, 6(1):361–381, 2015.
- [74] C. L. Kane and E. J. Mele. Z_2 topological order and the quantum spin Hall effect. *Phys. Rev. Lett.*, 95:146802, Sep 2005.
- [75] Liang Fu, C. L. Kane, and E. J. Mele. Topological insulators in three dimensions. *Phys. Rev. Lett.*, 98:106803, Mar 2007.
- [76] Liang Fu and C. L. Kane. Topological insulators with inversion symmetry. *Phys. Rev. B*, 76:045302, Jul 2007.
- [77] Liang Fu and C. L. Kane. Time reversal polarization and a Z_2 adiabatic spin pump. *Phys. Rev. B*, 74:195312, Nov 2006.
- [78] Shuichi Murakami. Phase transition between the quantum spin Hall and insulator phases in 3D: emergence of a topological gapless phase. *New Journal of Physics*, 9(9):356–356, Sep 2007.
- [79] B. Lenoir, M. Cassart, J.-P. Michenaud, H. Scherrer, and S. Scherrer. Transport properties of Bi-RICH Bi-Sb alloys. *Journal of Physics and Chemistry of Solids*, 57(1):89 – 99, 1996.
- [80] D. Hsieh, Y. Xia, L. Wray, D. Qian, A. Pal, J. H. Dil, J. Osterwalder, F. Meier, G. Bihlmayer, C. L. Kane, Y. S. Hor, R. J. Cava, and M. Z. Hasan. Observation of unconventional quantum spin textures in topological insulators. *Science*, 323(5916):919–922, 2009.

- [81] Haijun Zhang, Chao-Xing Liu, Xiao-Liang Qi, Xi Dai, Zhong Fang, and Shou-Cheng Zhang. Topological insulators in Bi_2Se_3 , Bi_2Te_3 and Sb_2Te_3 with a single Dirac cone on the surface. *Nature Physics*, 5(6):438–442, Jun 2009.
- [82] Y. Xia, D. Qian, D. Hsieh, L. Wray, A. Pal, H. Lin, A. Bansil, D. Grauer, Y. S. Hor, R. J. Cava, and M. Z. Hasan. Observation of a large-gap topological-insulator class with a single Dirac cone on the surface. *Nature Physics*, 5(6):398–402, Jun 2009.
- [83] D. Hsieh, Y. Xia, D. Qian, L. Wray, J. H. Dil, F. Meier, J. Osterwalder, L. Patthey, J. G. Checkelsky, N. P. Ong, A. V. Fedorov, H. Lin, A. Bansil, D. Grauer, Y. S. Hor, R. J. Cava, and M. Z. Hasan. A tunable topological insulator in the spin helical Dirac transport regime. *Nature*, 460(7259):1101–1105, Aug 2009.
- [84] Y. L. Chen, J. G. Analytis, J.-H. Chu, Z. K. Liu, S.-K. Mo, X. L. Qi, H. J. Zhang, D. H. Lu, X. Dai, Z. Fang, S. C. Zhang, I. R. Fisher, Z. Hussain, and Z.-X. Shen. Experimental realization of a three-dimensional topological insulator, Bi_2Te_3 . *Science*, 325(5937):178–181, 2009.
- [85] L. Plucinski, A. Herdt, S. Fahrendorf, G. Bihlmayer, G. Mussler, S. Döring, J. Kampmeier, F. Matthes, D. E. Bürgler, D. Grützmacher, S. Blügel, and C. M. Schneider. Electronic structure, surface morphology, and topologically protected surface states of Sb_2Te_3 thin films grown on $\text{Si}(111)$. *Journal of Applied Physics*, 113(5):053706, 2013.
- [86] Y. L. Chen, J.-H. Chu, J. G. Analytis, Z. K. Liu, K. Igarashi, H.-H. Kuo, X. L. Qi, S. K. Mo, R. G. Moore, D. H. Lu, M. Hashimoto, T. Sasagawa, S. C. Zhang, I. R. Fisher, Z. Hussain, and Z. X. Shen. Massive Dirac fermion on the surface of a magnetically doped topological insulator. *Science*, 329(5992):659–662, 2010.
- [87] Su-Yang Xu, Y. Xia, L. A. Wray, S. Jia, F. Meier, J. H. Dil, J. Osterwalder, B. Slomski, A. Bansil, H. Lin, R. J. Cava, and M. Z. Hasan. Topological phase transition and texture inversion in a tunable topological insulator. *Science*, 332(6029):560–564, 2011.
- [88] Su-Yang Xu, Madhab Neupane, Chang Liu, Duming Zhang, Anthony Richardella, L. Andrew Wray, Nasser Alidoust, Mats Leandersson, Thiagarajan Balasubramanian, Jaime Sánchez-Barriga, Oliver Rader, Gabriel Landolt, Bartosz Slomski, Jan Hugo Dil, Jürg Osterwalder, Tay-Rong Chang, Horng-Tay Jeng, Hsin Lin, Arun Bansil, Nitin Samarth, and M. Zahid Hasan. Hedgehog spin texture and Berry’s phase tuning in a magnetic topological insulator. *Nature Physics*, 8(8):616–622, Aug 2012.
- [89] Jeffrey C. Y. Teo, Liang Fu, and C. L. Kane. Surface states and topological invariants in three-dimensional topological insulators: Application to $\text{Bi}_{1-x}\text{Sb}_x$. *Phys. Rev. B*, 78:045426, Jul 2008.

- [90] Tomáš Rauch, Markus Flieger, Jürgen Henk, Ingrid Mertig, and Arthur Ernst. Dual topological character of chalcogenides: Theory for Bi_2Te_3 . *Phys. Rev. Lett.*, 112:016802, Jan 2014.
- [91] Hubert Steiner, Valentine Volobuev, Ondřej Čaha, Günther Bauer, Gunther Springholz, and Václav Holý. Structure and composition of bismuth telluride topological insulators grown by molecular beam epitaxy. *Journal of Applied Crystallography*, 47(6):1889–1900, Dec 2014.
- [92] Y. S. Hor, A. Richardella, P. Roushan, Y. Xia, J. G. Checkelsky, A. Yazdani, M. Z. Hasan, N. P. Ong, and R. J. Cava. p -type Bi_2Se_3 for topological insulator and low-temperature thermoelectric applications. *Phys. Rev. B*, 79:195208, May 2009.
- [93] D. O. Scanlon, P. D. C. King, R. P. Singh, A. de la Torre, S. McKeown Walker, G. Balakrishnan, F. Baumberger, and C. R. A. Catlow. Controlling bulk conductivity in topological insulators: Key role of anti-site defects. *Advanced Materials*, 24(16):2154–2158, 2012.
- [94] Agnieszka Wolos, Aneta Drabinska, Jolanta Borysiuk, Kamil Sobczak, Maria Kaminska, Andrzej Hruban, Stanisława G. Strzelecka, Andrzej Materna, Mirosław Piersa, Magdalena Romaniec, and Ryszard Diduszek. High-spin configuration of Mn in Bi_2Se_3 three-dimensional topological insulator. *Journal of Magnetism and Magnetic Materials*, 419:301 – 308, 2016.
- [95] Jian-Min Zhang, Wenmei Ming, Zhigao Huang, Gui-Bin Liu, Xufeng Kou, Yabin Fan, Kang L. Wang, and Yugui Yao. Stability, electronic, and magnetic properties of the magnetically doped topological insulators Bi_2Se_3 , Bi_2Te_3 , and Sb_2Te_3 . *Phys. Rev. B*, 88:235131, Dec 2013.
- [96] F.-T. Huang, M.-W. Chu, H. H. Kung, W. L. Lee, R. Sankar, S.-C. Liou, K. K. Wu, Y. K. Kuo, and F. C. Chou. Nonstoichiometric doping and Bi antisite defect in single crystal Bi_2Se_3 . *Phys. Rev. B*, 86:081104, Aug 2012.
- [97] D. L. Medlin and N. Y. C. Yang. Interfacial Step Structure at a (0001) Basal Twin in Bi_2Te_3 . *Journal of Electronic Materials*, 41(6):1456–1464, Jun 2012.
- [98] Y.F. Lee, S. Punugupati, F. Wu, Z. Jin, J. Narayan, and J. Schwartz. Evidence for topological surface states in epitaxial Bi_2Se_3 thin film grown by pulsed laser deposition through magneto-transport measurements. *Current Opinion in Solid State and Materials Science*, 18(5):279 – 285, 2014.
- [99] Dominik Kriegner, Petr Hrcuba, Jozef Veselý, Andreas Lesnik, Guenther Bauer, Gunther Springholz, and Václav Holý. Twin domain imaging in topological insulator Bi_2Te_3 and Bi_2Se_3 epitaxial thin films by scanning X-ray nanobeam microscopy and electron backscatter diffraction. *Journal of Applied Crystallography*, 50(2):369–377, Apr 2017.
- [100] Y. S. Hor, P. Roushan, H. Beidenkopf, J. Seo, D. Qu, J. G. Checkelsky, L. A. Wray, D. Hsieh, Y. Xia, S.-Y. Xu, D. Qian, M. Z. Hasan, N. P. Ong,

- A. Yazdani, and R. J. Cava. Development of ferromagnetism in the doped topological insulator $\text{Bi}_{2-x}\text{Mn}_x\text{Te}_3$. *Phys. Rev. B*, 81:195203, May 2010.
- [101] Joon Sue Lee, Anthony Richardella, David W. Rench, Robert D. Fraleigh, Thomas C. Flanagan, Julie A. Borchers, Jing Tao, and Nitin Samarth. Ferromagnetism and spin-dependent transport in n -type Mn-doped bismuth telluride thin films. *Phys. Rev. B*, 89:174425, May 2014.
- [102] Cui-Zu Chang and Mingda Li. Quantum anomalous hall effect in time-reversal-symmetry breaking topological insulators. *Journal of Physics: Condensed Matter*, 28(12):123002, Mar 2016.
- [103] Rui Yu, Wei Zhang, Hai-Jun Zhang, Shou-Cheng Zhang, Xi Dai, and Zhong Fang. Quantized anomalous Hall effect in magnetic topological insulators. *Science*, 329(5987):61–64, 2010.
- [104] Cui-Zu Chang, Jinsong Zhang, Minhao Liu, Zuocheng Zhang, Xiao Feng, Kang Li, Li-Li Wang, Xi Chen, Xi Dai, Zhong Fang, Xiao-Liang Qi, Shou-Cheng Zhang, Yayu Wang, Ke He, Xu-Cun Ma, and Qi-Kun Xue. Thin films of magnetically doped topological insulator with carrier-independent long-range ferromagnetic order. *Advanced Materials*, 25(7):1065–1070, 2013.
- [105] Yabin Fan, Pramey Upadhyaya, Xufeng Kou, Murong Lang, So Takei, Zhenxing Wang, Jianshi Tang, Liang He, Li-Te Chang, Mohammad Montazeri, Guoqiang Yu, Wanjun Jiang, Tianxiao Nie, Robert N. Schwartz, Yaroslav Tserkovnyak, and Kang L. Wang. Magnetization switching through giant spin-orbit torque in a magnetically doped topological insulator heterostructure. *Nature Materials*, 13(7):699–704, Jul 2014.
- [106] Wei Zhang, Rui Yu, Hai-Jun Zhang, Xi Dai, and Zhong Fang. First-principles studies of the three-dimensional strong topological insulators Bi_2Te_3 , Bi_2Se_3 and Sb_2Te_3 . *New J. Phys.*, 12(6):065013, 2010.
- [107] K. Carva, J. Kudrnovský, F. Máca, V. Drchal, I. Turek, P. Baláž, V. Tkáč, V. Holý, V. Sechovský, and J. Honolka. Electronic and transport properties of the Mn-doped topological insulator Bi_2Te_3 : A first-principles study. *Phys. Rev. B*, 93:214409, Jun 2016.
- [108] Yuri D Glinka, Sercan Babakiray, Mikel B Holcomb, and David Lederman. Effect of mn doping on ultrafast carrier dynamics in thin films of the topological insulator Bi_2Se_3 . *Journal of Physics: Condensed Matter*, 28(16):165601, Mar 2016.
- [109] R. Tarasenko, M. Vališka, M. Vondráček, K. Horáková, V. Tkáč, K. Carva, P. Baláž, V. Holý, G. Springholz, V. Sechovský, and J. Honolka. Magnetic and structural properties of Mn-doped Bi_2Se_3 topological insulators. *Physica B: Condensed Matter*, 481:262 – 267, 2016.
- [110] R. R. Urkude, Archana Sagdeo, R. Rawat, R. J. Choudhary, K. Asokan, S. Ojha, and U. A. Palikundwar. Observation of kondo behavior in the single crystals of Mn-doped Bi_2Se_3 topological insulator. *AIP Advances*, 8(4):045315, 2018.

- [111] A S Panfilov, G E Grechnev, A V Fedorchenko, K Conder, and E V Pomjakushina. Magnetic properties of Mn-doped Bi_2Se_3 compound: temperature dependence and pressure effects. *Journal of Physics: Condensed Matter*, 27(45):456002, Oct 2015.
- [112] V. Tkáč, K. Výborný, V. Komanický, J. Warmuth, M. Michiardi, A. S. Nганкеu, M. Vondráček, R. Tarasenko, M. Vališka, V. Stetsovych, K. Carva, I. Garate, M. Bianchi, J. Wiebe, V. Holý, Ph. Hofmann, G. Springholz, V. Sechovský, and J. Honolka. Influence of an anomalous temperature dependence of the phase coherence length on the conductivity of magnetic topological insulators. *Phys. Rev. Lett.*, 123:036406, Jul 2019.
- [113] Jian-Min Zhang, Wenguang Zhu, Ying Zhang, Di Xiao, and Yugui Yao. Tailoring magnetic doping in the topological insulator Bi_2Se_3 . *Phys. Rev. Lett.*, 109:266405, Dec 2012.
- [114] S.V. Chong, G.V.M. Williams, and R.L. Moody. The effect of manganese incorporation in Bi_2Se_3 on the thermal, electrical transport and magnetic properties. *Journal of Alloys and Compounds*, 686:245 – 251, 2016.
- [115] L. J. Collins-McIntyre, M. D. Watson, A. A. Baker, S. L. Zhang, A. I. Coldea, S. E. Harrison, A. Pushp, A. J. Kellock, S. S. P. Parkin, G. van der Laan, and T. Hesjedal. X-ray magnetic spectroscopy of MBE-grown Mn-doped Bi_2Se_3 thin films. *AIP Advances*, 4(12):127136, 2014.
- [116] E. D. L. Rienks, S. Wimmer, J. Sánchez-Barriga, O. Caha, P. S. Mandal, J. Růžička, A. Ney, H. Steiner, V. V. Volobuev, H. Groiss, M. Albu, G. Kothleitner, J. Michalička, S. A. Khan, J. Minár, H. Ebert, G. Bauer, F. Freyse, A. Varykhalov, O. Rader, and G. Springholz. Large magnetic gap at the dirac point in $\text{Bi}_2\text{Te}_3/\text{MnBi}_2\text{Te}_4$ heterostructures. *Nature*, 576(7787):423–428, Dec 2019.
- [117] Shuang Jia, Haim Beidenkopf, Ilya Drozdov, M. K. Fuccillo, Jungpil Seo, Jun Xiong, N. P. Ong, Ali Yazdani, and R. J. Cava. Defects and high bulk resistivities in the Bi-rich tetradymite topological insulator $\text{Bi}_{2+x}\text{Te}_{2-x}\text{Se}$. *Phys. Rev. B*, 86:165119, Oct 2012.
- [118] P. Ruleova, C. Drasar, A. Krejcova, L. Benes, J. Horak, and P. Lostak. Tuning the free electron concentration in Sr-doped Bi_2Se_3 . *Journal of Physics and Chemistry of Solids*, 74(5):746 – 750, 2013.
- [119] Alex Zunger. Practical doping principles. *Applied Physics Letters*, 83(1):57–59, 2003.
- [120] S. B. Zhang, Su-Huai Wei, Alex Zunger, and H. Katayama-Yoshida. Defect physics of the CuInSe_2 chalcopyrite semiconductor. *Phys. Rev. B*, 57:9642–9656, Apr 1998.
- [121] Jixia Dai, Damien West, Xueyun Wang, Yazhong Wang, Daniel Kwok, S.-W. Cheong, S. B. Zhang, and Weida Wu. Toward the intrinsic limit of the topological insulator Bi_2Se_3 . *Phys. Rev. Lett.*, 117:106401, Aug 2016.

- [122] D. West, Y. Y. Sun, Han Wang, Junhyeok Bang, and S. B. Zhang. Native defects in second-generation topological insulators: Effect of spin-orbit interaction on Bi_2Se_3 . *Phys. Rev. B*, 86:121201, Sep 2012.
- [123] Philipp Rübmann, Sanjoy K Mahatha, Paolo Sessi, Miguel A Valbuena, Thomas Bathon, Kai Fauth, Sylvie Godey, Aitor Mugarza, Konstantin A Kokh, Oleg E Tereshchenko, Pierluigi Gargiani, Manuel Valvidares, Erika Jiménez, Nicholas B Brookes, Matthias Bode, Gustav Bihlmayer, Stefan Blügel, Phivos Mavropoulos, Carlo Carbone, and Alessandro Barla. Towards microscopic control of the magnetic exchange coupling at the surface of a topological insulator. *Journal of Physics: Materials*, 1(1):015002, Sep 2018.
- [124] K. Sato, L. Bergqvist, J. Kudrnovský, P. H. Dederichs, O. Eriksson, I. Turek, B. Sanyal, G. Bouzerar, H. Katayama-Yoshida, V. A. Dinh, T. Fukushima, H. Kizaki, and R. Zeller. First-principles theory of dilute magnetic semiconductors. *Rev. Mod. Phys.*, 82:1633–1690, May 2010.
- [125] P. H. Dederichs, K. Sato, and H. Katayama-yoshida. Dilute magnetic semiconductors. *Phase Transitions*, 78(9-11):851–867, 2005.
- [126] S. Zimmermann, F. Steckel, C. Hess, H. W. Ji, Y. S. Hor, R. J. Cava, B. Büchner, and V. Kataev. Spin dynamics and magnetic interactions of Mn dopants in the topological insulator Bi_2Te_3 . *Phys. Rev. B*, 94:125205, Sep 2016.
- [127] Qin Liu, Chao-Xing Liu, Cenke Xu, Xiao-Liang Qi, and Shou-Cheng Zhang. Magnetic impurities on the surface of a topological insulator. *Phys. Rev. Lett.*, 102:156603, Apr 2009.
- [128] Annica M. Black-Schaffer and Alexander V. Balatsky. Subsurface impurities and vacancies in a three-dimensional topological insulator. *Phys. Rev. B*, 86:115433, Sep 2012.
- [129] S. H. Vosko, L. Wilk, and M. Nusair. Accurate spin-dependent electron liquid correlation energies for local spin density calculations: a critical analysis. *Canadian Journal of Physics*, 58(8):1200–1211, 1980.
- [130] P. A. Korzhavyi, A. V. Ruban, I. A. Abrikosov, and H. L. Skriver. Madelung energy for random metallic alloys in the coherent potential approximation. *Phys. Rev. B*, 51:5773–5780, Mar 1995.
- [131] Yang Xu, Ireneusz Miotkowski, Chang Liu, Jifa Tian, Hyoungdo Nam, Nasser Alidoust, Jiuning Hu, Chih-Kang Shih, M. Zahid Hasan, and Yong P. Chen. Observation of topological surface state quantum hall effect in an intrinsic three-dimensional topological insulator. *Nature Physics*, 10(12):956–963, Dec 2014.
- [132] I. A. Nechaev, R. C. Hatch, M. Bianchi, D. Guan, C. Friedrich, I. Aguilera, J. L. Mi, B. B. Iversen, S. Blügel, Ph. Hofmann, and E. V. Chulkov. Evidence for a direct band gap in the topological insulator Bi_2Se_3 from theory and experiment. *Phys. Rev. B*, 87:121111, Mar 2013.

- [133] P. Larson, V. A. Greanya, W. C. Tonjes, Rong Liu, S. D. Mahanti, and C. G. Olson. Electronic structure of Bi_2X_3 ($X = \text{S}, \text{Se}, \text{Te}$) compounds: Comparison of theoretical calculations with photoemission studies. *Phys. Rev. B*, 65:085108, Feb 2002.
- [134] Shifei Qi, Hualing Yang, Juan Chen, Xiaoyang Zhang, Yingping Yang, and Xiaohong Xu. Strain-modulated ferromagnetism and band gap of Mn doped Bi_2Se_3 . *Scientific Reports*, 6(1):29161, Jul 2016.
- [135] Geoffrey Tse and Dapeng Yu. The first principle study: Electronic and optical properties in Bi_2Se_3 . *Computational Condensed Matter*, 4:59 – 63, 2015.
- [136] Abdullahi Lawal, A. Shaari, R. Ahmed, and Norshila Jarkoni. First-principles many-body comparative study of Bi_2Se_3 crystal: A promising candidate for broadband photodetector. *Physics Letters A*, 381(35):2993 – 2999, 2017.
- [137] B. Alling, A. V. Ruban, A. Karimi, O. E. Peil, S. I. Simak, L. Hultman, and I. A. Abrikosov. Mixing and decomposition thermodynamics of $c\text{-Ti}_{1-x}\text{Al}_x\text{N}$ from first-principles calculations. *Phys. Rev. B*, 75:045123, Jan 2007.
- [138] G. Kresse and J. Furthmüller. Efficient iterative schemes for ab initio total-energy calculations using a plane-wave basis set. *Phys. Rev. B*, 54:11169–11186, Oct 1996.
- [139] G. Kresse and D. Joubert. From ultrasoft pseudopotentials to the projector augmented-wave method. *Phys. Rev. B*, 59:1758–1775, Jan 1999.
- [140] John P. Perdew, Kieron Burke, and Matthias Ernzerhof. Generalized gradient approximation made simple. *Phys. Rev. Lett.*, 77:3865–3868, Oct 1996.
- [141] Josef Kudrnovský, František Mácá, Ilja Turek, and Josef Redinger. Substrate-induced antiferromagnetism of a Fe monolayer on the Ir(001) surface. *Phys. Rev. B*, 80:064405, Aug 2009.
- [142] Juba Bouaziz, Manuel dos Santos Dias, Julen Ibañez Azpiroz, and Samir Lounis. Ab initio investigation of impurity-induced in-gap states in Bi_2Te_3 and Bi_2Se_3 . *Phys. Rev. B*, 98:035119, Jul 2018.
- [143] J. Sánchez Barriga, A. Varykhalov, G. Springholz, H. Steiner, R. Kirchschlager, G. Bauer, O. Caha, E. Schierle, E. Weschke, A. A. Ünal, S. Valencia, M. Dunst, J. Braun, H. Ebert, J. Minár, E. Golias, L. V. Yashina, A. Ney, V. Holý, and O. Rader. Nonmagnetic band gap at the Dirac point of the magnetic topological $(\text{Bi}_{1-x}\text{Mn}_x)_2\text{Se}_3$. *Nature Communications*, 7(1):10559, Feb 2016.
- [144] V. N. Antonov, L. V. Bekenov, S. Uba, and A. Ernst. Electronic structure and x-ray magnetic circular dichroism in Mn-doped topological insulators Bi_2Se_3 and Bi_2Te_3 . *Phys. Rev. B*, 96:224434, Dec 2017.

- [145] V.P. Antropov, M.I. Katsnelson, and A.I. Liechtenstein. Exchange interactions in magnets. *Physica B: Condensed Matter*, 237-238:336 – 340, 1997. Proceedings of the Yamada Conference XLV, the International Conference on the Physics of Transition Metals.
- [146] L. Udvardi, L. Szunyogh, K. Palotás, and P. Weinberger. First-principles relativistic study of spin waves in thin magnetic films. *Phys. Rev. B*, 68:104436, Sep 2003.
- [147] G. Bouzerar, J. Kudrnovský, L. Bergqvist, and P. Bruno. Ferromagnetism in diluted magnetic semiconductors: A comparison between ab initio mean-field, RPA, and Monte Carlo treatments. *Phys. Rev. B*, 68:081203, Aug 2003.
- [148] K Sato, P. H Dederics, and H Katayama-Yoshida. Curie temperatures of III–v diluted magnetic semiconductors calculated from first principles. *Europhysics Letters (EPL)*, 61(3):403–408, Feb 2003.
- [149] O. Eriksson, A. Bergman, L. Bergqvist, and J. Hellsvik. *Atomistic Spin Dynamics: Foundations and Applications*. OUP Oxford, 2017.
- [150] B Skubic, J Hellsvik, L Nordström, and O Eriksson. A method for atomistic spin dynamics simulations: implementation and examples. *J. Phys.: Cond. Mat.*, 20(31):315203, 2008.
- [151] D. Hinzke, U. Atxitia, K. Carva, P. Nieves, O. Chubykalo-Fesenko, P. M. Oppeneer, and U. Nowak. Multiscale modeling of ultrafast element-specific magnetization dynamics of ferromagnetic alloys. *Phys. Rev. B*, 92:054412, Aug 2015. 3.718.
- [152] J. Hellsvik, B. Skubic, L. Nordström, B. Sanyal, O. Eriksson, P. Nordblad, and P. Svedlindh. Dynamics of diluted magnetic semiconductors from atomistic spin-dynamics simulations: Mn-doped GaAs. *Phys. Rev. B*, 78:144419, Oct 2008.
- [153] Uppsala Atomistic Spin Dynamics (UppASD) code. Available under GNU General Public License. <http://physics.uu.se/uppasd/> and <http://github.com/UppASD/UppASD/>.
- [154] K. Binder. Finite size scaling analysis of ising model block distribution functions. *Zeit. Phys. B Cond. Mat.*, 43(2):119–140, 1981.
- [155] H. J. von Bardeleben, J. L. Cantin, D. M. Zhang, A. Richardella, D. W. Rench, N. Samarth, and J. A. Borchers. Ferromagnetism in Bi₂Se₃: Mn epitaxial layers. *Phys. Rev. B*, 88:075149, Aug 2013.
- [156] V.K. Maurya, C.L. Dong, C.L. Chen, K. Asokan, and S. Patnaik. High spin state driven magnetism and thermoelectricity in mn doped topological insulator Bi₂Se₃. *Journal of Magnetism and Magnetic Materials*, 456:1 – 5, 2018.

- [157] Sercan Babakiray, Trent A. Johnson, Pavel Borisov, Mikel B. Holcomb, David Lederman, Matthew A. Marcus, and Kartick Tarafder. Structural properties of $\text{Bi}_{2-x}\text{Mn}_x\text{Se}_3$ thin films grown via molecular beam epitaxy. *J. Appl. Phys.*, 118(4):045302, 2015.
- [158] P. Janíček, Č. Drašar, P. Lošt'ák, J. Vejpravová, and V. Sechovský. Transport, magnetic, optical and thermodynamic properties of $\text{Bi}_{2-x}\text{Mn}_x\text{Se}_3$ single crystals. *Physica B*, 403(19-20):3553–3558, October 2008.
- [159] M. G. Vergniory, M. M. Otrokov, D. Thonig, M. Hoffmann, I. V. Maznichenko, M. Geilhufe, X. Zubizarreta, S. Ostanin, A. Marmodoro, J. Henk, W. Hergert, I. Mertig, E. V. Chulkov, and A. Ernst. Exchange interaction and its tuning in magnetic binary chalcogenides. *Phys. Rev. B*, 89:165202, Apr 2014.
- [160] Paul Strange. *Relativistic Quantum Mechanics: With Applications in Condensed Matter and Atomic Physics*. Cambridge University Press, 1998.
- [161] Easo P. George, Dierk Raabe, and Robert O. Ritchie. High-entropy alloys. *Nature Reviews Materials*, 4(8):515–534, Aug 2019.
- [162] E. J. Pickering and N. G. Jones. High-entropy alloys: a critical assessment of their founding principles and future prospects. *International Materials Reviews*, 61(3):183–202, 2016.
- [163] Ming-Hung Tsai and Jien-Wei Yeh. High-entropy alloys: A critical review. *Materials Research Letters*, 2(3):107–123, 2014.
- [164] D.B. Miracle and O.N. Senkov. A critical review of high entropy alloys and related concepts. *Acta Materialia*, 122:448 – 511, 2017.
- [165] P.F. Yu, L.J. Zhang, H. Cheng, H. Zhang, M.Z. Ma, Y.C. Li, G. Li, P.K. Liaw, and R.P. Liu. The high-entropy alloys with high hardness and soft magnetic property prepared by mechanical alloying and high-pressure sintering. *Intermetallics*, 70:82 – 87, 2016.
- [166] Yi Zhang, Ke He, Cui-Zu Chang, Can-Li Song, Li-Li Wang, Xi Chen, Jin-Feng Jia, Zhong Fang, Xi Dai, Wen-Yu Shan, Shun-Qing Shen, Qian Niu, Xiao-Liang Qi, Shou-Cheng Zhang, Xu-Cun Ma, and Qi-Kun Xue. Crossover of the three-dimensional topological insulator Bi_2Se_3 to the two-dimensional limit. *Nature Physics*, 6(8):584–588, Aug 2010.
- [167] A. A. Kordyuk. ARPES experiment in fermiology of quasi-2D metals (Review Article). *Low Temperature Physics*, 40(4):286–296, Apr 2014.
- [168] P. Orgiani, C. Bigi, P. Kumar Das, J. Fujii, R. Ciancio, B. Gobaut, A. Galdi, C. Sacco, L. Maritato, P. Torelli, G. Panaccione, I. Vobornik, and G. Rossi. Structural and electronic properties of Bi_2Se_3 topological insulator thin films grown by pulsed laser deposition. *Applied Physics Letters*, 110(17):171601, 2017.

- [169] M. Vališka, J. Warmuth, M. Michiardi, M. Vondráček, A. S. Ngankeu, V. Holý, V. Sechovský, G. Springholz, M. Bianchi, J. Wiebe, P. Hofmann, and J. Honolka. Topological insulator homojunctions including magnetic layers: The example of n-p type (n-QLs $\text{Bi}_2\text{Se}_3/\text{Mn-Bi}_2\text{Se}_3$) heterostructures. *Applied Physics Letters*, 108(26):262402, 2016.
- [170] Mohammad Koleini, Thomas Frauenheim, and Binghai Yan. Gas doping on the topological insulator Bi_2Se_3 surface. *Phys. Rev. Lett.*, 110:016403, Jan 2013.
- [171] Joseph E. Brom, Yue Ke, Renzhong Du, Dongjin Won, Xiaojun Weng, Kalissa Andre, Jarod C. Gagnon, Suzanne E. Mohny, Qi Li, Ke Chen, X. X. Xi, and Joan M. Redwing. Structural and electrical properties of epitaxial Bi_2Se_3 thin films grown by hybrid physical-chemical vapor deposition. *Applied Physics Letters*, 100(16):162110, 2012.
- [172] D. L. Medlin, Q. M. Ramasse, C. D. Spataru, and N. Y. C. Yang. Structure of the (0001) basal twin boundary in Bi_2Te_3 . *Journal of Applied Physics*, 108(4):043517, 2010.
- [173] Hugo Aramberri, Jorge I. Cerdá, and M. Carmen Muñoz. Tunable Dirac electron and hole self-doping of topological insulators induced by stacking defects. *Nano Letters*, 15(6):3840–3844, Jun 2015.
- [174] N. V. Tarakina, S. Schreyeck, M. Luysberg, S. Grauer, C. Schumacher, G. Karczewski, K. Brunner, C. Gould, H. Buhmann, R. E. Dunin-Borkowski, and L. W. Molenkamp. Suppressing twin formation in Bi_2Se_3 thin films. *Advanced Materials Interfaces*, 1(5):1400134, 2014.

List of Figures

2.1	Antiferromagnetic superexchange geometry.	22
2.2	Ferromagnetic superexchange geometry	23
2.3	Friedel oscillations	27
4.1	Quantum Hall effect.	40
4.2	Chern insulator edge state.	42
4.3	Quasi 2D-model edge spectra.	45
4.4	HgTe and $\text{Hg}_{0.32}\text{Cd}_{0.68}\text{Te}$ band structures obtained by the Kane-Mele model.	46
4.5	HgTe topological phase transition.	46
4.6	Experimental evidence of QSHE in HgTe quantum well.	47
4.7	Schematic surface states.	48
4.8	Edge scattering.	48
4.9	Weak (anti-)localization magnetoconductivity sketch.	49
4.10	Clockwise – counterclockwise trajectory giving a backscattering contribution.	49
4.11	Temperature-induced WAL/WL crossover in a disordered InAs/GaSb double quantum well.	49
4.12	Transfer of the Wannier states along an insulating cylinder.	51
4.13	Switching of the spin partner	52
4.14	Time reversal polarization - projection of the TRIM points.	53
4.15	Bulk band gap evolution and topological phase in $\text{Bi}_{(1-x)}\text{Sb}_x$ systems as a function of the composition.	54
4.16	$\text{Bi}_{0.99}\text{Sb}_{0.01}$ surface states.	54
4.17	Sketch of the crystal structure of Bi_2Se_3 , Bi_2Te_3 and Sb_2Te_3 compounds.	56
4.18	Surface band structure of Bi_2Se_3 and Bi_2Te_3 experimentally measured by ARPES.	56
5.1	Examples of chemical disorder in the Bi_2Se_3 structure.	57
5.2	Band structure of the pure Bi_2Se_3 compound.	59
5.3	Densities of states of pure Bi_2Se_3	59
5.4	Dependence of the spin-resolved densities of states of Bi_2Se_3 doped by Mn^{Bi} acceptors on the structure relaxation.	60
5.5	Spin-resolved densities of states of magnetically doped Bi_2Se_3	61
5.6	Bulk band gap in magnetically doped Bi_2Se_3	62
5.7	Bulk band gap width as a function of the chemical defects' concentration.	63
5.8	Dependence of the Mn magnetic moments' magnitude on the Mn concentration x and the presence of other chemical defects.	63
5.9	Bi_2Se_3 system densities of states in presence of Se vacancies (Vac^{Se})	64
5.10	Bi_2Se_3 system densities of states in presence of Bi antisites (Bi^{Se})	65
5.11	Bi_2Se_3 system densities of states in presence of Se antisites (Se^{Bi})	66

5.12	Concentration dependence of the magnetic exchange interactions between Mn^{Bi} magnetic moments as a function of the mutual distance.	67
5.13	Relation of the Mn^{Bi} exchange interactions across the vdW gap and the crystal structure.	69
5.14	Magnetic exchange interactions between Mn^{Bi} magnetic moments as a function of the mutual distance in presence of other defects.	69
5.15	Concentration dependence of the magnetic exchange interactions between Mn^{i} magnetic moments as a function of the mutual distance.	70
5.16	Mn^{i} related magnetic exchange interactions as a function of the mutual distance in presence of other defects.	71
5.17	Relation between the Fermi level shift and magnitudes of magnetic exchange interactions.	72
5.18	MFA magnetic ordering temperature as a function of the concentration x of Mn magnetic defects in dependence on the presence of other chemical defects.	74
5.19	Temperature dependence of calculated MC simulations' quantities for a Bi-rich Mn-doped Bi_2Se_3 system.	75
5.20	Dependence of the MC Curie temperature on the concentration x of substitutional Mn^{Bi} atoms and the inclusion of extra chemical defects	76
6.1	Deviation of the Mn^{Bi} magnetic exchange interactions caused by the inclusion of the SO coupling.	82
6.2	Deviation of the Mn^{Bi} magnetic exchange interactions caused by the inclusion of the SO coupling and scaled by the factor $(r/a)^3$	83
6.3	Spatial distribution of the exchange interaction modification caused by the inclusion of the SO interaction.	84
6.4	MFA magnetic ordering temperature as a function of the Mn^{Bi} dopants concentration x depending of the inclusion of the SO interaction	85
6.5	Comparison of Mn^{Bi} magnetic moments' magnitudes in the case of scalar and fully relativistic approaches as a function of the dopants concentration.	85
6.6	Exchange interactions of the Mo-based CrMnFeCoNi derivatives.	89
6.7	RRKY-like oscillations of the Mo-based CrMnFeCoNi derivatives' exchange interactions calculated in the framework of the fully relativistic approach.	89
7.1	Layout of the calculated multilayer Bi_2Se_3 structure with a top vacuum surface.	91
7.2	Bloch spectral functions related to the top QL of a Bi_2Se_3 slab consisting of 10 QLs	92
7.3	Projected Bloch spectral function.	93
7.4	Formation of surface states with increasing thickness of the simulated Bi_2Se_3 slab.	94
7.5	Experimental Bi_2Se_3 thin-film ARPES spectra in dependence on the film thickness.	95

7.6	Surface states' dispersion as a function of the vacuum spacer thickness.	95
7.7	Evolution of the band gap at the 3 rd QL of the Bi ₂ Se ₃ slab.	96
7.8	Densities of states of the thin layer Bi ₂ Se ₃ system.	98
7.9	Densities of states of magnetically doped layered Bi ₂ Se ₃ systems.	99
7.10	Dependence of the Mn magnetic moments' magnitude on the Mn defects concentration x and the position of defects within the thin layer structure.	100
7.11	Surface QL BSFs of magnetically doped Bi ₂ Se ₃ systems.	100
7.12	Surface states in terms of the PBSF in presence of magnetic Mn ^{Bi} defects.	101
7.13	Surface states in terms of PBSF in presence of magnetic Mn ⁱ defects.	102
7.14	Densities of states of Bi ₂ Se ₃ systems in presence of Vac ^{Se} defects.	103
7.15	Densities of states of Bi ₂ Se ₃ systems in presence of Bi ^{Se} and Se ^{Bi} antisites.	104
7.16	BSFs of the surface QL in presence of native defects.	105
7.17	Surface states in terms of PBSF in presence of native defects.	105
7.18	Magnetic Mn ^{Bi} pair exchange interactions in thin layer systems as a function of the Mn ^{Bi} position in a doped Bi ₂ Se ₃ slab.	107
7.19	Magnetic Mn ^{Bi} pair exchange interactions in thin layer systems as a function of the Mn ⁱ position in a doped Bi ₂ Se ₃ slab.	109
7.20	MFA Curie temperatures as a function of the position of Mn dopants in a Bi ₂ Se ₃ slab.	109
7.21	Sketch of the simulated multilayer Bi ₂ Se ₃ slab including twin planes.	110
7.22	Relative formation energy of a single TP as a function of their position within the Bi ₂ Se ₃ slab.	111
7.23	Single TP induced charge transfer.	112
7.24	Mutual twin plane orientation.	113
7.25	Relative formation energy of two TPs as a function of their position.	114
7.26	Relative formation energy of three TPs as a function of the middle TP position.	115
7.27	Dependence of the TP relative formation energy on the defect concentration.	116
7.28	Local Mn ^{Bi} magnetic doping in presence of a TP.	117
7.29	Influence of multiple TPs on Mn ^{Bi} magnetic moments' magnitudes.	118
7.30	Influence of the mutual TP orientation on the relative formation energy.	120
7.31	Interchange of TP orientation in the case of gathered TPs.	121

List of Tables

6.1	MFA ferromagnetic Curie temperatures of Mo-based CrMnFeCoNi derivatives.	87
6.2	Element resolved magnetic moments magnitudes of Mo-based CrMnFeCoNi derivatives.	87
7.1	Relative difference of exchange interactions' strength at the inner QL with respect to bulk magnitudes.	108

List of Abbreviations

- 2DEG** 2D electron gas
- AFM** antiferromagnetic
- ARPES** angle-resolved photoemission spectroscopy
- ASA** atomic sphere approximation
- BCC** body-centered cubic
- BHZ** Bernevig–Hughes–Zhang (model)
- Bi^{Se}** Bi antisite
- BSF** Bloch spectral functions
- BZ** Brillouin zone
- CPA** coherent potential approximation
- DC** direct current
- DE** Dirac equation
- DFT** density functional theory
- DLM** disordered local moments
- DMI** Dzyaloshinskii–Moriya interaction
- DOS** density of states
- ES** empty sphere
- FCC** face-centered cubic
- FM** ferromagnetic
- FR** fully relativistic
- GGA** generalized gradient approximation
- HCP** hexagonal close-packed
- HF** Hartree-Fock
- KS** Kohn-Sham
- LDA** local density approximation

LSDA local spin density approximation

MC Monte-Carlo

MFA mean field approximation

Mn^{Bi} Mn substitutional defect

Mnⁱ Mn interstitial defect

PAW projector augmented wave

PBSF projected Bloch spectral function

QAHE quantum anomalous Hall effect

QHE quantum Hall effect

QL quintuple layer

QSH TI quantum spin Hall topological insulator

QSHE quantum spin Hall effect

RKKY Ruderman-Kittel-Kasuya-Yoshida

SE Schrödinger equation

Se^{Bi} Se antisite

SL septuple layer

SO spin-orbit

SOC spin-orbit coupling

SRA scalar-relativistic approximation

STI strong topological insulator

TB-LMTO tight-binding linear-muffin-tin (method)

TCI topological crystal insulators

TI topological insulators

TKKN Thouless-Kohmoto-Nightingale-den Nijs

TRIM time reversal invariant momenta (point)

TRP time reversal polarization

TRS time reversal symmetry

UppASD Uppsala Atomistic Spin Dynamics (package)

Vac^{Se} Se vacancies

VASP Vienna ab initio Simulation Package

vdW van der Waals

WAL weak anti-localization

WL weak localization

WTI weak topological insulator

xc exchange-correlation

List of Publications

(Published)

Jakub Šebesta, Karel Carva, Dominik Kriegner, and Jan Honolka. Twin domain structure in magnetically doped Bi_2Se_3 topological insulator. *Nanomaterials*, 10(10), Oct 2020

(Published)

K. Carva, P. Baláž, J. Šebesta, I. Turek, J. Kudrnovský, F. Máca, V. Drchal, J. Chico, V. Sechovský, and J. Honolka. Magnetic properties of Mn-doped Bi_2Se_3 topological insulators: Ab initio calculations. *Phys. Rev. B*, 101:054428, Feb 2020

(Published)

Jakub Šebesta, Karel Carva, and Dominik Legut. Role of magnetism in the stability of the high-entropy alloy CoCrFeMnNi and its derivatives. *Phys. Rev. Materials*, 3:124410, Dec 2019

(Submitted)

Jakub Šebesta, Karel Carva, and Dominik Legut. Evolution of critical temperatures for substituted Cantor alloy. *submitted to Phys. Rev. B*, Aug 2020

